

---

# On Shape and Structure in Biological Systems

## From Biopolymers to Cellular Organization

Karen Alim

---



München 2010



---

**On Shape and Structure in Biological Systems**  
**From Biopolymers to Cellular Organization**

**Karen Alim**

---

Doktorarbeit  
an der Fakultät für Physik  
der Ludwig-Maximilians-Universität  
München

vorgelegt von  
Karen Alim  
aus Hannover

München, den 28. April 2010

Erstgutachter: Prof. Dr. Erwin Frey

Zweitgutachter: Prof. Dr. Arezki Boudaoud

Tag der mündlichen Prüfung: 8. Juni 2010

# Contents

<b>Zusammenfassung</b>	<b>ix</b>
<b>Abstract</b>	<b>xi</b>
<b>1 Shapes and structures</b>	<b>1</b>
<b>2 Shape of semiflexible polymer rings</b>	<b>9</b>
2.1 Biopolymers . . . . .	10
2.2 Exploring configurations of biopolymers . . . . .	12
2.3 Semiflexible polymer model . . . . .	14
2.4 Quantification of shape . . . . .	16
2.5 Polymer ring conformations . . . . .	17
2.6 Outlook . . . . .	22
2.7 K. Alim and E. Frey, <i>Phys. Rev. Lett.</i> , <b>99</b> , 198102 . . . . .	23
2.8 K. Ostermeir, K. Alim, and E. Frey, <i>Phys. Rev. E</i> , <b>81</b> , 061802 . . . . .	27
2.9 K. Ostermeir, K. Alim, and E. Frey, <i>Soft Matter</i> , <b>6</b> , 3467 . . . . .	35
2.10 F. Drube, K. Alim, G. Witz, G. Dietler, and E. Frey, <i>Nano Lett.</i> , <b>10</b> , 1445 . . . . .	41
<b>3 Structuring tissue by mechanics and signals</b>	<b>49</b>
3.1 Plant development . . . . .	50
3.2 Tissue mechanics . . . . .	52
3.3 Auxin dynamics . . . . .	54
3.4 Pattern formation . . . . .	58
3.5 Vein initiation by polarization wave front . . . . .	60
3.6 Cell packing geometries in small groups of cells . . . . .	62
3.7 Outlook . . . . .	64
3.8 K. Alim and E. Frey, <i>Eur. Phys. J. E</i> , in press . . . . .	67
3.9 A. Piera Aberola, K. Alim, A.-K. Marel, E. Frey, J.O. Rädler, submitted . . . . .	83
<b>A Perturbation expansion for finite flexibility</b>	<b>109</b>
<b>Bibliography</b>	<b>113</b>
<b>Acknowledgements</b>	<b>129</b>
<b>Curriculum Vitae</b>	<b>131</b>



# List of Figures

1.1	Shapes representing equilibrium states I. . . . .	2
1.2	Shapes representing equilibrium states II. . . . .	4
1.3	Forms and structures arising out of non-equilibrium systems I. . . . .	5
1.4	Forms and structures arising out of non-equilibrium systems II. . . . .	7
2.1	Schematic drawing of the microscopic structure of biopolymers. . . . .	11
2.2	Biopolymers occurring in the topological constrained conformation of a ring. . . . .	12
2.3	Experimental measurements of polymer shapes employing DNA. . . . .	13
2.4	Simulation snap shots of free polymer ring conformations. . . . .	18
2.5	Simulation snap shots of spherically confined polymer ring conformations. . . . .	19
2.6	Simulation snap shots of phantom polymer and polymer with finite thickness. . . . .	21
3.1	Development of the model organism <i>Arabidopsis thaliana</i> . . . . .	51
3.2	Vertex model for tissue mechanics modeling. . . . .	53
3.3	Patterns of auxin flow in plants. . . . .	55
3.4	Illustration of auxin transport and feedback. . . . .	57
3.5	Patterns of polarly distributed PIN proteins during vein initiation. . . . .	61
3.6	Most probable packing states for cells confined to a square patch. . . . .	63





# Zusammenfassung

Die spezifische Form und Struktur geben biologischen Elementen ihre Funktion, sei es mikroskopisch innerhalb einer Zelle oder makroskopisch über ganze Zellverbände hinweg. Die Verknüpfung der Elemente selbst führt dann zur äußeren Form von biologischen Organismen. Die Ursachen der Formgebung dieser Bausteine des Lebens sind vielfältig. Einerseits gibt es Gleichgewichtszustände, die durch die Balance von Kräften, zum Beispiel elastische und/oder entropische, bestimmt werden. Andererseits bilden sich viele Strukturen durch andauernde Dissipation von Energie im Nichtgleichgewicht. In biologischen Systemen kommt es in letzterem Fall insbesondere durch die Rückkopplung verschiedener Komponenten zu vielfältigen Mustern.

Diese Arbeit beschäftigt sich mit beiden Arten der Formgebung. Gleichgewichtssysteme werden am Beispiel von semiflexiblen Biopolymeren und Zellverbänden untersucht, Nichtgleichgewichtssysteme anhand der Musterbildung des Pflanzenhormons Auxin.

Biopolymere sind wichtig für die Organisation und Funktionalität einer Zelle. Essentiell sind die DNA als Träger der Erbinformation und die Filamente des Zytoskeletts als Gerüst der Zelle. Um die Form dieser Biopolymere zu verstehen, betrachtet die Arbeit Polymerkonformationen im Kräftegleichgewicht in Abhängigkeit von inneren Faktoren wie Biegesteifigkeit, Topologie und Filamentdurchmesser, sowie unter dem Einfluss von äußeren Faktoren wie Confinement. Diese Aspekte sind wichtig für viele biologische Prozesse, bilden aber auch die Grundlage für biomimetische Anwendungen in Nanosystemen. Die Arbeit untersucht die Form von Polymeren mittels Monte-Carlo-Simulationen, die mit analytischen Argumenten belegt werden und so in direkte Aussagen zum Einfluss betrachteter Faktoren übersetzt werden. Die Erforschung des Einflusses des Filamentdurchmessers wird zudem von Experimenten von Guillaume Witz in der Gruppe von Prof. Giovanni Dietler, EPFL Lausanne, begleitet. So kann gezeigt werden, dass die Topologie eines Ringes im Wechselspiel zwischen elastischen und entropischen Kräften zu sehr unterschiedlichen Formen führt. Wenn elastische Kräfte dominieren, wird gezeigt, dass drei-dimensionale Ringe planar und elliptisch sind. Erst wenn entropische Kräfte die Polymerstruktur beherrschen, entstehen geknäuelte Zigarrenformen. In sphärischem Confinement der Größenordnung des Polymers hingegen führt die längliche Ausdehnung elastisch dominierter Polymerringe zu Euler-Knicken, entropischere Polymere verdrillen sich, wenn ihre Länge beschränkt ist. Ein größerer Filamentdurchmesser wiederum bewirkt, dass Polymerringe letztendlich sphärischer werden.

Auf der makroskopischen Ebene von Zellverbänden ist Strukturierung ein wichtiger Pro-

zess in der Entwicklung von Organismen. Zum einen zeigt sich dies in der Anordnung der Zellen zueinander zum anderen in der Differenzierung einiger Zellen eines Gewebes zu spezialisierteren Aufgaben. Die Entwicklung von Pflanzen wird hierbei durch den Nichtgleichgewichtsprozess des gerichteten Transports des Pflanzenhormons Auxin geprägt, welches die besondere Eigenschaft hat, dass es seine Richtung selbst durch eine Rückkopplung auf seine Effluxproteine bestimmt. Die Arbeit betrachtet in diesem Zusammenhang die Aderbildung in Blättern. Mit einer detaillierten Untersuchung der nichtlinearen Dynamik von Auxin und seinem Effluxprotein wird der Strukturbildungsmechanismus identifiziert, der es ermöglicht die Funktion der konstituierenden mikroskopischen Prozesse zu ermitteln. Analytische Berechnungen ergeben zudem die Abhängigkeit makroskopischer Observablen von der internen Dynamik. Deren Parameter werden somit messbar, ein wichtiger Aspekt für viele Strukturbildungsprozesse in Pflanzen.

Die Gesetzmäßigkeiten der geometrischen Struktur von Zellgewebe wird für kleine Zellverbände auf lithographischen beschränkten Oberflächen in Zusammenarbeit mit Experimenten von Alicia Piera Aberola und Anna-Kristina Marel in der Gruppe von Prof. Joachim O. Rädler, LMU München, untersucht. Die beobachteten Verteilungen der Zellgeometrien für zwei bis vier Zellen eröffnen neue Einblicke in die mechanischen Eigenschaften von Zellen. So zeigen wir, dass über die adhesiven Kräften zwischen Zellen und den kontraktilen Kräften innerhalb jeder einzelnen Zelle hinaus auch Kräfte, die der Zellanisotropie entgegenwirken, den Gleichgewichtszustand von Zellverbänden bestimmen.

Zusammenfassend zeigt die Arbeit wie aus einfachen physikalischen Kräften und der Rolle der Rückkopplung Form und Struktur in biologischen Systemen entstehen, sowohl innerhalb einer Zelle wie auch auf der Ebene von Zellverbänden. Diese Erkenntnisse sollen in Zukunft angewandt werden, um die Dynamik und Struktur innerhalb von wachsenden Zellgeweben zu untersuchen. Somit könnte dann von den physikalischen Kräften und der Rückkopplung auf der Zellebene auf die äußere Form von Geweben, Organen und Organismen geschlossen werden.

Die vorliegende Arbeit gliedert sich in drei Kapitel. Das erste Kapitel leitet in die Thematik der Arbeit ein und stellt verschiedene Form- und Strukturbildungsprozesse und deren grundlegende Prinzipien vor. Kapitel zwei befasst sich dann mit der Form von mikroskopischen, biologischen Bausteinen, den Biopolymerringen, unter unterschiedlichen inneren und äußeren Faktoren. In Kapitel drei werden dann Untersuchungen zur Struktur in Zellverbänden vorgestellt. Zum einen wird ergründet welche Prinzipien zur Aderstrukturierung in Blättern führen, zum anderen welche Gesetzmäßigkeiten die Anordnung von Zellen in Geweben beschreiben.

# Abstract

Specific form and structure provide functionality to biological elements, microscopically inside single cells as well as macroscopically within cell tissues. The combination of these elements then results in the outward appearance of biological organisms. The causes for the shape of these building blocks of life are manifold. On the one hand there are equilibrium states arising from the balance of for example elastic or/and entropic forces. On the other hand many structures develop by the continuous dissipation of energy in non-equilibrium. In the latter case biological systems often increase complexity by a feedback between constituting components resulting in diverse patterns.

This work is concerned with both types of structuring. Equilibrium states are investigated in the context of semiflexible biopolymers and cell packing geometries; non-equilibrium patterning is considered during the shaping of plants by their hormone auxin.

Biopolymers are important for the organization and functionality of cells. Prominent examples are the DNA as the carrier of the genetic code and the cytoskeletal filaments building the scaffold of the cell. To investigate the form of these biopolymers, this thesis investigates equilibrium polymer conformations depending on internal characteristics like flexibility, topology and filament diameter and external constraints such as confinement. These aspects are reoccurring themes in biological processes and form the basic principles for biomimetic applications in nanosystems. This work investigates polymer shape with Monte Carlo simulations which are substantiated by analytic arguments to transfer the influence of the considered factors into simple principles. Investigations of the impact of filament diameter are accompanied by experiments of DNA rings by Guillaume Witz in the group of Prof. Giovanni Dietler, EPFL Lausanne. Thus, it is shown that the topology of a ring yields a broad variety of shapes during the competition of elastic and entropic forces acting on semiflexible polymers. When elastic forces dominate, it is shown that the shape of three-dimensional polymer rings is in fact planar and elliptic. Only when entropic forces control polymer configurations, do crumpled, cigar-like conformations in three dimensions arise. In spherical confinement of the order of polymer size the elongated form of polymer rings dominated by elastic forces induces Euler buckling. More entropic polymers are found to writhe in order to store their length in confined spaces. An increasing filament diameter is shown to effectively stiffen the polymer leading to more spherical polymer shapes.

On the macroscopic level of cell tissues structuring is an important process during the development of organisms. Structuring proceeds by arranging cells relative to each other and by cell differentiation to specified functionality. In this aspect the development of

plants is ruled by the non-equilibrium process of the directed transport of the plant hormone auxin. This hormone shows the distinct characteristic to not only exhibit but also induce the direction of its oriented transport by feedback on its efflux proteins. This feedback governed structuring mechanism is studied in this work concerning vein initiation. A detailed analysis of the non-linear dynamics of auxin and its efflux protein identifies the structuring mechanism and thereby enables to characterize the role of each microscopic process. Analytic calculations predict the dependence of macroscopic observable on the underlying dynamics. Thus microscopic parameters become measurable, an important aspect for many developmental processes in plants.

The governing principles of geometric arrangements within cell tissue are studied for small groups of cells on lithographically patterned surfaces in collaboration with experiments by Alicia Piera Aberola and Anna-Kristina Marel in the group of Prof. Joachim O. Rädler, LMU Munich. The observed distributions of cell geometries for two to four cells open new insights into cell tissue mechanics. Beyond the contractile forces within each single cell and adhesive forces between cells we find that also forces counteracting cell shape anisotropy are important in determining the force balance states.

Summarizing, this work shows how simple laws of physics and the role of biological feedback give rise to form and structure in biological systems, both within individual cells and on the level of cell tissues. Future investigations based on these insights will concern the dynamics and structure within growing cell tissues. Such studies might be able to map the laws of physics and biological feedback mechanisms on the outward form of tissues, organs and organisms.

The present thesis is organized in three chapters. The first chapter familiarizes the topic of the thesis and introduces the principles of a range of processes that govern form and pattern formation. Chapter two then addresses the shape of microscopic biological building blocks, biopolymer rings, under the influence of different internal and external factors. Chapter three illustrates studies concerning structure formation in cell tissue. On the one hand the principles of vein initiation are discussed, on the other hand the governing laws of cell arrangements are investigated.

# 1 Shapes and structures

Our world displays a huge diversity of shapes and structures, continuously developing new ones. Non-living matter keeps surprising us, for instance, with the ordered structures in crystals and the marvelous variety of snow flakes. In the biological world we find numerous functionally well constructed entities such as proteins and protein assemblies that constitute whole organisms. Animals and plants again amaze us with their orchestrated development, their beautifully arranged structures, their sometimes even colorful patterns. All these phenomena emerge initially from the fundamental laws of physics. Hence, the conformation of a protein merely depends on electrostatic and entropic forces. By building covalent and non-covalent bonds a protein folds into its designated form. And still we discern biological systems from non-living matter. The utter difference between the shapes and structures in living and non-living matter lies not in how they employ the basic laws of physics, these are ultimately fixed. The difference is that biological systems reproduce themselves and evolved over numbers and numbers of generations. Living matter adapted to its environment and still is constantly optimizing to adapt even better. This optimization is encoded in the multiple layers of feedback emerging at the utmost level between chemical signals and the action of proteins. Feedback serves to couple otherwise unrelated factors and to increase or diminish their effect, thereby regulating even large scale patterns. Hence, to understand shapes and structures arising in biological systems two elements are important to study. On the one hand the laws of physics involved in the structuring processes, on the other hand the role and type of feedback regulating patterns.

As the kinds of shapes and structures and their origin varies largely throughout our world, there exists a long history of results and conjectures and an even more tremendous amount of open questions. This introduction may only give a flavor of the multitude of forms and structures that arise due to the principles of physics and the elaborate feedback rules present in biological systems.

Most generally we may distinguish shapes and structures as equilibrium states and non-equilibrium systems that are driven by a continuous dissipation of energy. Equilibrium governs to large extent the form of the basic entities that build biological matter and its functionality. As such the shape of a protein or a polymer as a concatenated chain of proteins is itself an equilibrium property. However, if energy dissipation is added, more elaborate structures may arise. Cytoskeletal polymers, for example, organize into asters or vortices if molecular motors drive them [132]. Most more complex biological shapes and structures arise in non-equilibrium systems organized by a network of feedback interactions. Their constituting building blocks are often formed by equilibrium properties only.

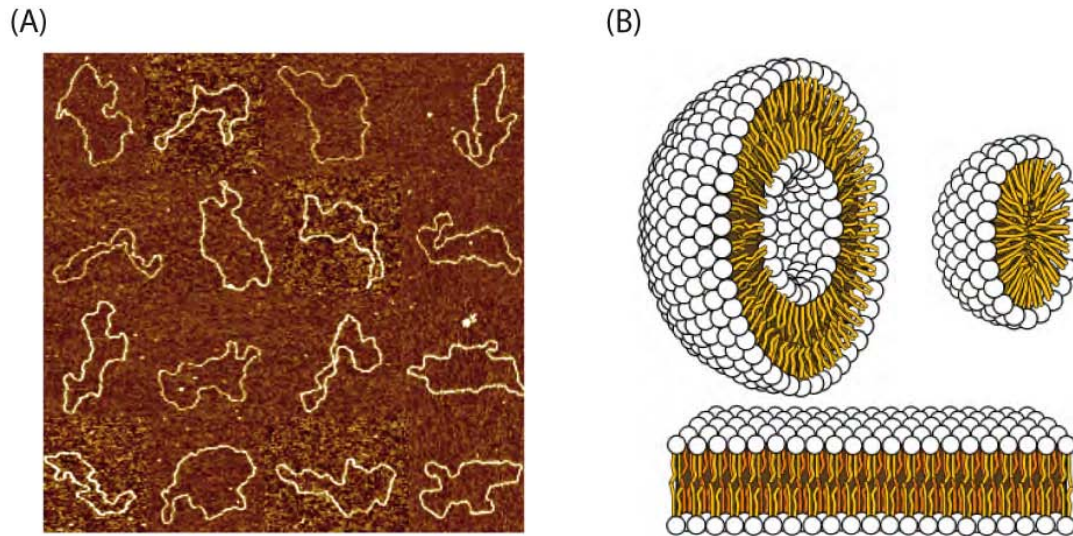


**Figure 1.1:** Shapes representing equilibrium states. (A) Atomic force microscopy scan of plasmid DNA pBR322 (2000nm length). The molecules shapes are governed by its elastic bending stiffness and the entropic forces arising due to thermal fluctuations. Courtesy of G. Witz, EPFL Lausanne. (B) Amphiphilic molecules assemble into various structures solely depending on their molecular geometry and concentration (modified from Wikipedia).

## Equilibrium shapes

In equilibrium the governing forces have elastic, electrostatic or entropic origin. The dominant shape of a system arises from the minimization of the free energy. For example the microscopic structure of a crystal is determined by the electronic properties of its constituting atoms and hence the physics of electrostatic forces. Similarly the basic building blocks of biological matter are governed by electrostatic interactions, which, for example, lead to the folding of proteins by establishing covalent and non-covalent bonds. Sometimes the free energy landscape of a protein is so rough that thermal fluctuations are too weak to guide the protein into its absolute minimal free energy in limited time. In such cases the designated structure of proteins is achieved by help of folding enzymes, so called chaperons [1].

The queen molecule of living matter, the DesoxyriboNucleic Acid (DNA), has microscopically a well defined free energy ground state. Covalent bonds between bases that are aligned along a sugar phosphate backbone yield DNA's double helical structure. This double helix is in fact a strand-like molecule that is often built to become a very long filament which then again may coil up into interesting shapes, see for example Fig. 1.1 (A). At this larger scale the conformation of the DNA filament is controlled by entropic forces arising from thermal fluctuations and elastic forces resulting from the steric hindrance against bending along the strand. Notable deviations of the helix occur only on a certain length scale of the

filament. Elastic forces dominate on short length scales, where the DNA behaves like an elastic rod. Entropic forces only exceed elastic forces on long length scales turning DNA's shape to look similar to a random walk trajectory. The broad length scales in between these two limits are dominated by an interplay of both forces. This turns the dominant shape let alone the distribution of conformations inaccessible to straight forward reasoning albeit its importance for biological processes.

Likewise the undulations of lipid bilayers which establish the numerous membranes within and around a cell are governed by elastic bending forces and entropic forces [25, 56, 88]. The building blocks of lipid membranes are amphiphilic molecules consisting of a hydrophilic polar head group and a hydrophobic non-polar tail. In water, amphiphilic molecules tend to assemble into structures where only the hydrophilic heads are exposed to water molecules shielding the hydrophobic tails. The form of the resulting aggregate depends on the molecular geometry of the amphiphile namely the head volume and tail length and volume [94]. The multitude of electrostatic, entropic and steric forces generates micelles, cylinders, vesicles and the prominent bilayers, as shown in Fig. 1.1 (B). Already vesicles, closed surfaces of bilayers encompassing water solvent, display an almost infinite variety of shapes ranging from prolate or oblate to dumbbell-like or pear shaped, see Ref. [176] for review. The different states of amphiphilic molecules are of ubiquitous application in *in vitro* experiments serving as supporting bilayer [118] or as envelopes to encapsulate molecules [115].

Amphiphiles are also the main molecules for the development of foams. Heuristically speaking a foam is an aggregation of “inverted” vesicles that enclose air. In a foam the hydrophobic tails of the amphiphiles are in contact with a droplet of air, while the hydrophilic heads of neighboring “inverted vesicles” caress the thin water film between them building the lamella. The shape of single soap bubbles is dominated by the surface tension within the liquid film. The surface tension causes the bubble to minimize its surface while keeping its total volume of air fixed, hence, generating a spherical object [149, 201]. Due to the gravitationally induced flow of liquid within the lamella the liquid film is thinned at the top, ultimately leading to the rupture of the bubble. Hence, a foam bubble is only metastable. It is, however, inspiring to note that the geometry of bubbles in a foam can solely be described by minimizing the energy composed of surface tension, given the constraint of fixed bubble volume. Thus, elastic tension alone characterizes the arrangement of individual soap bubbles within foams, see examples in Fig. 1.2 (A). Entropic forces only play a minor role concerning aggregates of this size.

Also the geometric arrangement of cells within epithelial tissue at an instant in developmental time is successfully described as a minimal elastic energy structure. The often two dimensional epithelial tissues dominate the anatomy of “higher” animals as they typically build the boundaries of compartments. Furthermore, epithelia are the first specialized tissue forming during the embryogenesis of metazoa, indicating the importance of this tissue type in development [40]. The models that describe epithelial cell geometry are inspired by foam structure descriptions, *e.g.*, Fig. 1.2 (A). Foam bubbles may, in fact, organize into deceivable similar arrangements. However, the mechanics that govern epithelial cells are

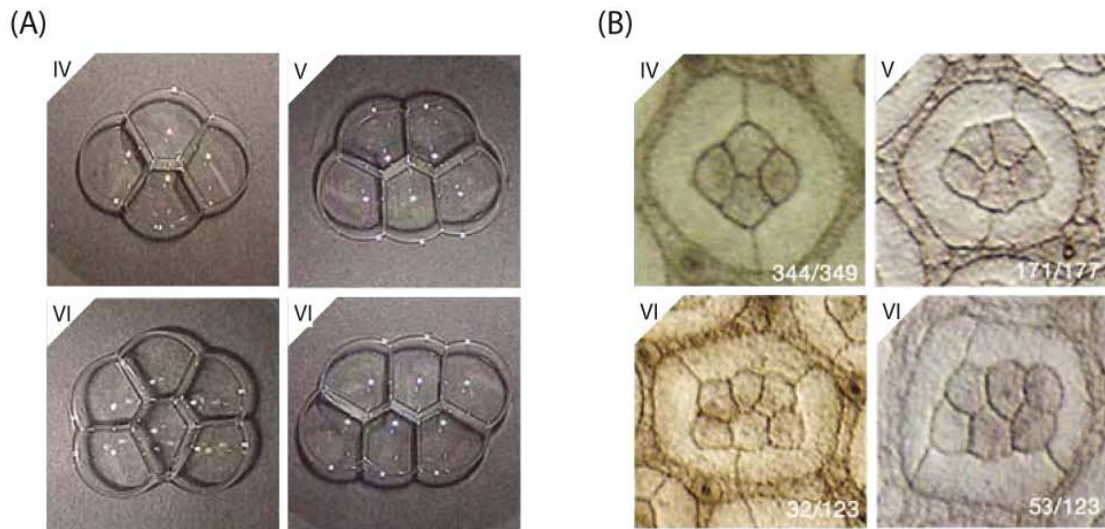


**Figure 1.2:** Shapes representing equilibrium states. (A) Soap bubble arrangements minimizing the overall surface area while keeping the total enclosed volume fixed. (B) Very similar in appearance the cell packing of photoreceptor cells in *Drosophila* eye, ommatidia. Cell cortex contractility and cell-cell adhesion explain the observed cell arrangements in this case [89, 98]. Reprinted by permission from Macmillan Publishers Ltd.: Nature [85], copyright 2004.

different [85, 89, 98]. In addition to an elastic bulk modulus two opposing forces drive tissue geometry and topology: The adhesion between cells mediated by cadherin proteins which favors cell-cell contact and the cell cortex contractility arising from the cytoskeleton diminishing cell perimeter. These mechanics account for cell packing in *Drosophila* wing disk [59]. Furthermore, variations in adhesion by modulated cadherin expression lies at the origin of the cell geometry of the photoreceptor cells that constitute the *Drosophila* eye, the ommatidia [85, 89, 98], reprinted in Fig. 1.2 (B). Additionally, alterations in cell cortex contractility govern germ-band elongation in *Drosophila* [13, 111, 153]. Hence, in a tissue of immobile cells with given topology, the geometry or slight changes in topology can be predicted on the basis of minimizing the elastic energy. However, the true biology lies in how the tissue grew to this arrangement and how differential cell cortex contractility of adhesion is patterned within the tissue. Patterning and growth itself are truly non-equilibrium processes that involve the huge network of feedback interactions.

## Non-equilibrium shapes and structures

Non-equilibrium processes may generate both purely non-living structures and biological patterns. For example the marvelous snowflakes grow purely due to physical forces occurring during the solidification of water molecules into ice. A beautiful example is shown in Fig. 1.3 (A). Starting from a small seed, growth of a snowflake is entirely governed



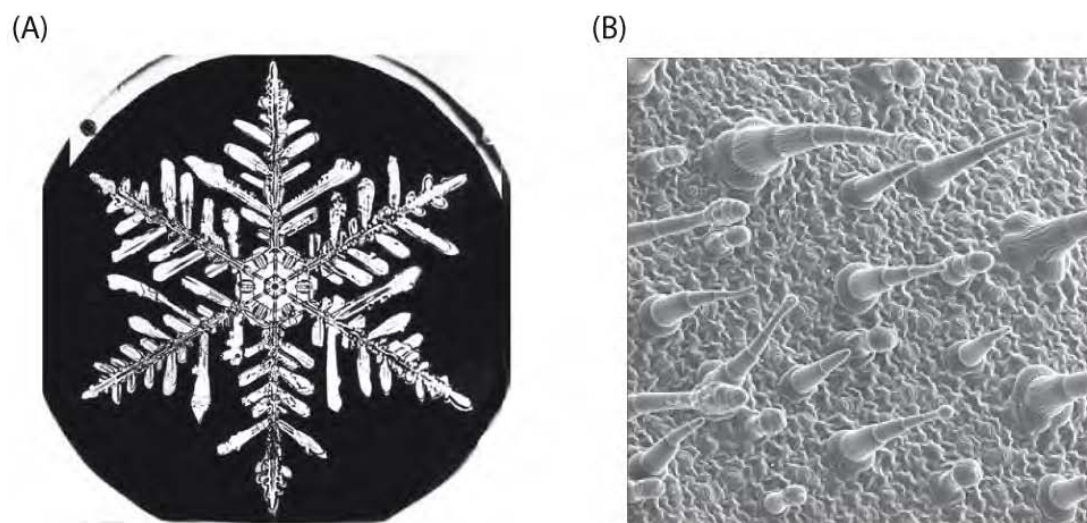


**Figure 1.3:** Forms and structures arising out of non-equilibrium systems. (A) The snowflake form is governed by the transport of heat that is generated during the phase transition from liquid/vapor to ice. Photograph of the late Wilson A. Bentley. (B) This scanning electron microscope image of *Nicotiana glauca* upper leaf surface shows the dotted pattern of hairs, trichomes. Protein interaction measurements suggest a Turing patterning to lie at its origin [93, 145]. Source: Wikipedia.

by external conditions and the structure of water molecules giving rise to the hexagonal symmetry of snowflakes [107]. During the phase transition from vapor/liquid to solid state a certain amount of latent heat is generated that has to be dissipated. Dendrites emerge as an increasing surface enhances heat transport. Experiments on the growth of artificial snowflakes showed that the growth velocity, the shape of the front most tip and the spacing between side branches depends only on the degree of undercooling of the solidifying medium [108]. Hence, the growth of snowflakes only depends on the local heat dissipation, there is no rule for emerging shapes and no control mechanism that supervises the growth of certain forms.

Development, however, relies on reproducible outcomes. Therefore, formation of macroscale structures and shapes in biology utilizes a whole network of regulatory interactions and feedbacks [74]. Regulatory interactions between proteins and signaling molecules can take place in various scenarios, involving different time scales. Long time scales are involved when a signal induces the up-regulation (activation) or down-regulation (inhibition) of the expression of a specific gene. As a result, a lot more or a lot less molecules of a certain protein may be synthesized. More directly a signal can also prevent protein folding, block functional sites of proteins or interfere with further protein activity, for example its mobility. More indirect signals may also activate or inhibit transmembrane channels and increase or decrease in this way molecule concentrations. Often, several pathways are employed to reach a given output for a certain input in order to increase robustness and reliability. Feedback takes place when a signaling molecule after a cascade of intermediate events

amplifies (positive feedback) or diminishes (negative feedback) its own concentration. Especially the multitude of feedbacks increases the robustness of an outcome against fluctuations in molecule concentrations. Feedback also lies at the basis of spatial structuring, the pattern formation that determines different cell fates for initially almost identical cells during development.

The seminal work of Turing [196] influenced the investigation of developmental patterns tremendously. He described a feedback mechanism which is able to predict spatial patterns of dots and stripes. Extensions of his work account for patterns observed in animal fur coats [129] and sea shells [122].

The model is based on two interacting substances; an activator molecule and an inhibitor molecule. The activator auto-activates (positive feedback) its own production and also increases the amount of the inhibitor. Thus, a site of high activator concentration is also a site of both activator and inhibitor production. The inhibitor on the other hand reduces the amount of activator (negative feedback). The key factor now is that the inhibitor diffuses a lot faster than the activator, which may even be immobile. Thereby, the amount of activator is reduced only on long ranges, remaining high at the site of local production and a pattern is generated.

Despite its powerful predictions research could only in a few systems identify activator and inhibitor molecules generating so-called Turing patterns. One presumable system is the dotted patterning of hair cells, trichomes, in plant leaves, precisely in the rosette leaves of the plant model organism *Arabidopsis* [146]. For reference, a trichome pattern is shown in Fig. 1.3 (B). Analysis of trichome patterning genes reveals groups of proteins that take the role of either an activator or an inhibitor in the feedback system. The difficulty in realizing and identifying Turing patterns lies usually in the requirement of two different scales of diffusion constants. Trichome patterns may arise due to a Turing mechanism as the activator is immobile and the inhibitor seems to be mobile [93, 145], alternative explanations, however, involve the depletion of the activator [48].

In plant development the universal trigger is the differential concentration of the hormone auxin. From the very beginning of plant development when auxin concentration induces the shoot-root orientation, auxin is part of almost every developmental process [66, 147]. The circulation of auxin, for example, patterns the helical ordering of leaves around the stem (phyllotaxis) and vein structures within leaves, see Fig. 1.4. The peculiarity about auxin is that it is transported throughout plants in a directed manner by help of polarly distributed proteins from the PIN family. The polar distribution of the PIN proteins within the cell membrane itself underlies the control of auxin. Hence, auxin induces via feedback its own orientation of transport. The true nature of this feedback is, however, under debate [182].

Although research is progressing fast there is still a tremendous amount of shapes and structures whose origin needs investigation. Especially questioning how shapes arise in biological systems only started to advance based on the recent discoveries in molecular biology and developmental biology. The study of shapes and structures requires, first of

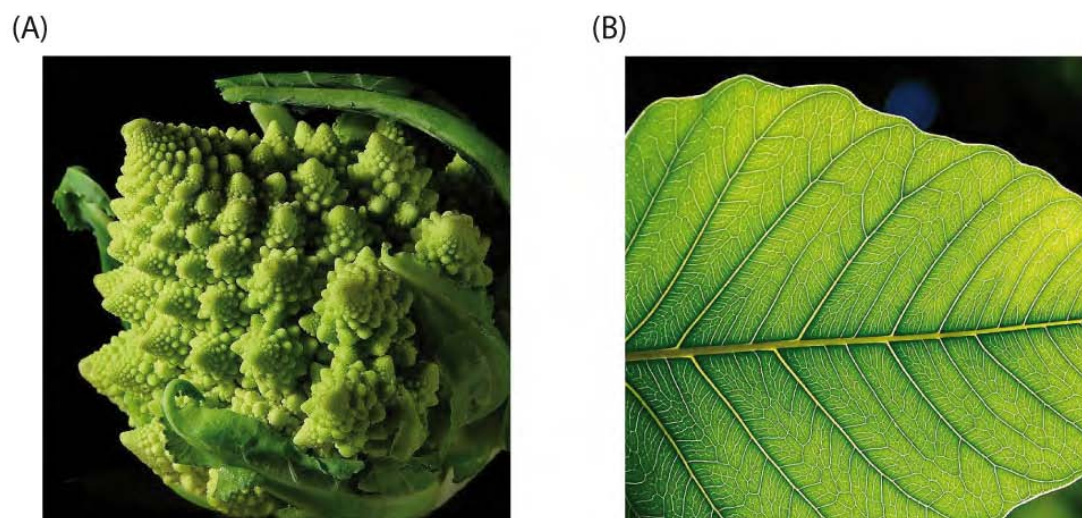


**Figure 1.4:** Forms and structures arising out of non-equilibrium systems. (A) Helical ordering of plant organs beautifully shown by romanesco broccoli is initiated by the accumulation of the plant hormone auxin at their sites of initiation along the plant stem. (B) Vein patterns in plant leaves represented here are initiated by the directed flow of the hormone auxin. Auxin itself feeds back onto its own transport, hence, governing the direction of its own flow. Source: Wikipedia.

all, the governing laws of physics and in many biological systems also a deep understanding of the ruling feedback relations. The present work investigates both aspects in two different settings as outlined in the following.

The first part concerns the shape of small biological building blocks, the conformations of biopolymers. Their form is an equilibrium state entirely controlled by the laws of physics, mainly the competition of elastic and entropic forces. We build an intuitive understanding of polymer shapes by translating observations from Monte Carlo simulations into heuristic and analytic arguments. The form of a biopolymer is especially multi-faceted as they occur in various different environments. We reflect this by investigating biopolymer shape not only in free three dimensional space but also under spherical confinement. The effect of changing filament diameter on polymer configurations is studied in the abstract scenario of two dimensional polymers. A setting which is also amenable to experimental investigation and therefore enables direct comparison between theoretical predictions and observations.

The second part investigates mechanisms of developmental processes giving rise to multicellular form and structure. Here, both aspects, physical laws that govern equilibrium form and biological feedback that structures cellular identity are considered. On the one hand, we analyze long-term cell geometries in finite size tissues as equilibrium state, arising from the balance of elastic forces generated within and between neighboring cells. On the other hand, we investigate the biological feedback of the plant hormone auxin and its efflux protein PIN during the initiation of veins in plant leaves. To fully grasp the auxin

dynamics we identify the non-linear mechanism behind and the role of each microscopic process in an analytically tractable model. Both studies concern ever reoccurring principles of development; the growth and rearrangement of cells within tissues and how a feedback mechanism orchestrates their differentiation. Eventually these principles lead to the elaborate structure of a fully grown, functional multicellular organism.

## 2 Shape of semiflexible polymer rings

The shape of biopolymers is governed by the laws of physics. On the small length scales of biopolymers the impact of thermal fluctuations is very strong. Thereby, a multitude of conformations emerges from the interplay of energy and entropy giving rise to a broad landscape of shapes, but also internal factors like topology and filament diameter and external constraints like confinement strongly govern polymer shapes.

As a polymer's configuration affects its function, investigations of the shape of biopolymers are relevant for many biological processes. Considering the most prominent examples of biopolymers, DNA and cytoskeletal filaments, their shape influences, for example, their mobility in heterogeneous environment such as the cytoplasm and the depletion forces between larger complexes mediated by such polymers. Concerning the recent developments of nano-biotechnological devices [19, 157] aiming at a lab on a chip [36] conformations of biopolymers become of technical importance. Furthermore, DNA as a carrier of the genetic code is subjected to an immense activity of proteins that regulate the transcription of genes by attaching to specific binding sites. This binding site search has recently been shown to be strongly affected by the polymer's configuration [197] turning DNA's shape a matter of gene regulation.

A biopolymer is successfully modeled as a semiflexible polymer by neglecting its microscopic architecture and describing it as a thermally fluctuating elastic rod. The specific properties of a biopolymer are subsumed in its elastic bending modulus  $\kappa$ . On which length scales a polymer bends depends on the cost of bending  $\kappa$  versus the energy provided by the thermal environment  $k_B T$ . This ratio is termed persistence length  $l_p = \kappa/k_B T$ . The total length of a polymer or more specifically the number of persistence lengths the total polymer encompasses then determines how many bends are on average observed. This flexibility  $L/l_p$  is the main lever to determine the shape of a polymer. The smaller the flexibility the stiffer the polymer. The larger the flexibility the more coiled is a polymer's configuration. For polymer rings we discern three different approximate regimes of flexibilities, stiff  $L/l_p < 5$ , semiflexible  $5 < L/l_p < 10$ , flexible  $L/l_p > 10$  [2]. Being successfully described as a thermally fluctuating elastic rod the shape of biopolymers is a truly physical question of statistics. Then again, even biopolymers are evolutionary optimized biological structures, ongoing optimization could concern the length of individual filaments regarding their specific requirements.

We study how the shape of semiflexible polymer rings is governed by inherent factors such as flexibility  $L/l_p$  and filament diameter and external constraints like confinement. Es-

pecially the topological constraint of a ring, ubiquitously occurring in biological systems as introduced in the following, results in astonishingly rich polymer configurations. It is the aim of our work to give an intuitive understanding of polymer shapes by rationalizing conformations observed within Monte Carlo Simulations with straightforward analytic arguments. Concerning the effect of filament diameter on polymer ring shape our results are substantiated with experimental data for DNA rings on mica surface from the Dietler group at the EPFL Lausanne.

## 2.1 Biopolymers

Filamentous structures are a ubiquitous entity of a functional biological organism. Most prominent examples of such long thin biopolymers are the carrier of our genetic code, DNA, and the elastic scaffold of each cell, the cytoskeletal filaments. Apart from the original definition of a polymer as a concatenated chain of many ( $\pi\omicron\lambda\nu$ , *poly*) identical building blocks ( $\mu\epsilon\rho\sigma$ , *meros*) the microscopic structure of biopolymers may be more subtle, see for illustration Fig. 2.1.

DNA consists of two strands of helically intertwined sugar phosphate backbones each carrying the bases adenine, thymine, guanine and cytosine that encode the genetic information, Fig. 2.1 (A). The famous base-pairing between those bases binds the two strands into a stable helix of about  $d = 2.4nm$  in diameter [165]. The length scales on which the helical chain bends, the persistence length, is about  $l_p \approx 50nm$  [23].

The main purpose of DNA is to store the genetic information and make it accessible for readout by enzymes. To fulfill this role the very long DNA of eukaryotes is folded by packing proteins such as nucleosomes into higher structures. On the other hand, there exists a huge amount of very short DNA such as viral DNA and plasmids, small supplemental pieces of genetic information, that may be transferred between individuals. These short nucleotide strands often occur in the topologically constrained state of a ring, presented in Fig. 2.2 (A). Especially the short DNA strands often experience confinement in viral or bacterial envelopes [1] or nanoscale devices that aim to analyze DNA properties [19, 185]. In recent years DNA has been discovered as a building block to generate designed lattices [204] and compounds [31]. Here the exploration of new bio-nanomaterials is including more and more physical properties of DNA beyond its base-pairing mechanism.

The cell's cytoskeleton comprises three different types of biopolymers; actin and intermediate filaments as well as microtubules. The most flexible of all are actin filaments, which are built by intertwined protein chains to a mere thickness of  $d = 7nm$  exhibiting a persistence length of  $l_p = 17\mu m$  [75, 110], Fig. 2.1 (B). Intermediate filaments are a bundle of eight protein strands so called protofilaments in total about  $d = 10nm$  in diameter with a persistence length of  $l_p = 2\mu m$  [21]. Microtubules on the other hand are hollow cylinders composed of circularly arranged tubulin protofilaments about  $d = 25nm$  wide,

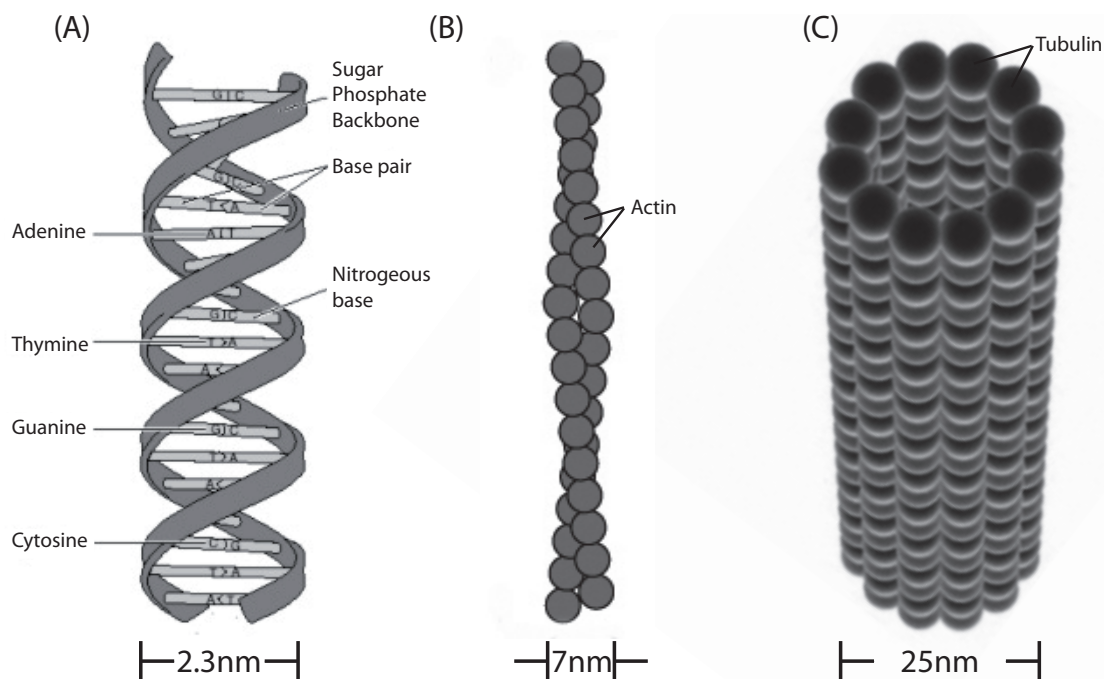


**Figure 2.1:** Schematic drawing of the microscopic structure of (A) DNA, (B) an actin filament and (C) a microtubule. All these biopolymers show bending on different orders of length scales as their persistence length varies from  $l_p = 50nm$  for DNA, via  $l_p = 17\mu m$  for actin filaments to about  $l_p = 6mm$  for microtubules. All filaments occur on broad filament length  $L$  scales, such that the flexibility  $L/l_p$  changes for each polymer over orders of magnitude.

Fig. 2.1 (C). Their persistence length is usually cited with  $l_p = 6mm$  [54, 75] but it is in fact dependent on the microtubule's total length decreasing down to  $l_p = 0.1mm$  for very short molecules [143].

Together these biopolymers are the main constituents of a cell's cytoskeleton, which establishes and maintains the shape of a cell, takes an active part in cell motion and cell division and also serves as the scaffold for intracellular transport. The prominent state of the cytoskeletal filaments is one where they are interwoven and connected to build an active elastic network. Beyond this multi-filament state the role of single cytoskeletal filaments on their own may be very distinguished. For example the conformation of single microtubules are pronounced in the chromosome sorting during mitosis. Furthermore, in red blood cells, erythrocytes, of birds and reptiles a single microtubule bundle forms into a ring [116], see Fig. 2.2 (C). Beyond their role in biological processes cytoskeletal filaments are often studied in *in vitro* experiments to learn about their behavior in flow [175] and their polyelectrolyte nature [192]. Prominently, actin forms rings either due to counterions [171, 193] or with help of cross-linking proteins [33], shown in Fig. 2.2 (B). Therefore, actin is a versatile polymer which aspires to be a frequent molecule in the study of biomaterials and biomimetic devices. Here again the effect of confinement is eminent.

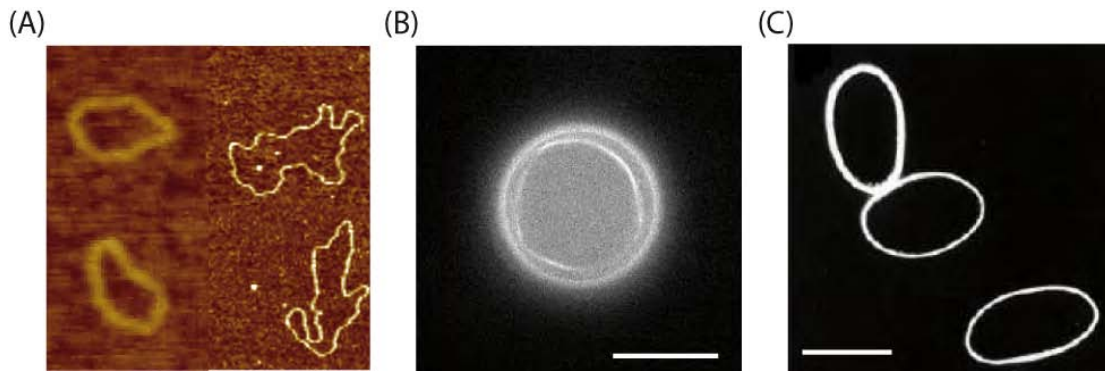


**Figure 2.2:** Many biopolymers occur in the topological constrained conformation of a ring. The shown examples are (A) DNA rings of different total length (80nm and 2000nm) in an atomic force microscopy image. Courtesy of G. Witz, EPFL Lausanne, and (B) actin filaments which assembled within an emulsion droplet build of phospholipids by addition of actin linker proteins. Scale bar 10  $\mu$ m. Courtesy of M.M.A.E. Claessens, University of Twente. (C) The last example shows microtubule bundle rings within bird erythrocytes [116], reprinted with permission of John Wiley & Sons, Inc., scale bar 10  $\mu$ m.

Although all introduced biopolymers differ fundamentally in their microscopic structure their conformations on the scale of their persistence length or larger can to large extent be described by just a single parameter: their flexibility, the ratio of total length to persistence length. Furthermore, both DNA and cytoskeletal filaments have the capacity to occur on hugely varying scales of length turning the flexibility to change over broad ranges. As characteristic conformations strongly depend on flexibility the study of polymer configurations is a fascinating endeavor both by theoretical considerations and experimental imaging.

## 2.2 Exploring configurations of biopolymers

The imaging of biopolymers had its first climax with the decryption of DNA's microscopic structure by Watson and Crick [200] based on X-ray data by Franklin. Afterwards X-ray diffraction was further employed to study the conformation of DNA polymers under strong confinement in viral capsids [53]. This effort was supported by electron microscopy [29, 113], which led to the observation of highly ordered polymer alignment as the nucleotides approach optimal packing.

The drawback of electron microscopy is, however, that samples have to be dehydrated. Biological specimen are therefore deprived of their natural condition and ranges of polymer configurations arising due to thermal activation cannot be quantitatively imaged. The



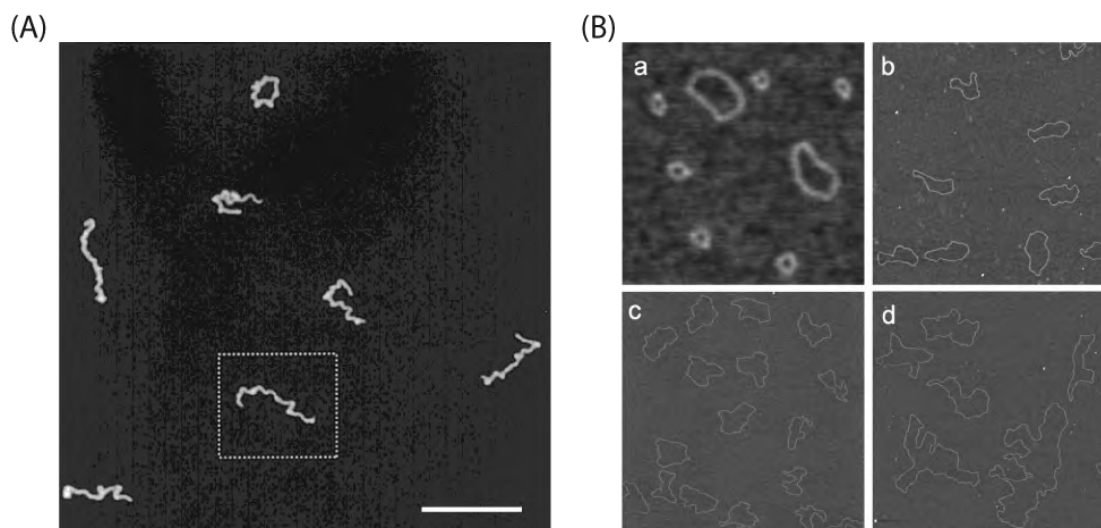


**Figure 2.3:** Experimental measurements of polymer shapes employing DNA. In both cases the biopolymer is confined to two dimensions such that it may still fluctuate within the plane and, hence, obey true two dimensional statistics. (A) Long linear DNA on fluid cationic supported membrane establishing the shape of flexible polymers, reprinted with permission from [119]. Copyright 2001 American Chemical Society. Scale bar 10  $\mu\text{m}$ . (B) Circular DNA on mica surface, reproduced from [206]. Copyright (2008) by The American Physical Society. As the DNA rings are prepared to be of different length the shape along the full regime of flexibilities from stiff to flexible (a-d) can be studied [51]. Scales (a) 350nm, (b) 2  $\mu\text{m}$ , (c) 3  $\mu\text{m}$  and (d) 2.5  $\mu\text{m}$ .

better alternative is optical imaging, which is limited in resolution but can be improved by successful image analysis [20] especially since the invention of fluorescent marker GFP [30, 86, 178]. Optical microscopy has been successfully employed to determine the persistence length of the relatively stiff cytoskeletal actin filaments and microtubules by tracking polymer configurations and comparing them to the semi-flexible polymer model wormlike chain [75]. Avoiding the yet erroneous tracking of filaments persistence length measurement were also performed by observing the fluctuations of the end-to-end distance of a polymer attached to a wall [110, 143].

A remaining problem is, however, that imaging is only two-dimensional. The shape observed is hence only the two dimensional projection of a three dimensional object [19, 81]. Three dimensional scans are in principle possible but fluctuations take usually place on timescales faster than scan velocity. Undesirable projections into two dimensions can be prevented by preparing polymers that are truly fluctuating in a plane as achieved for DNA on fluid supported bilayers by Maier and Radler [118], shown in Fig. 2.3. With this setup first shape measurements were obtained [119] in accordance with theoretical predictions for flexible polymers [7]. Due to the limit in optical resolution only very long and, hence, very flexible DNA could be observed.

Higher resolution of biopolymer configurations is generally possible with atomic force microscopy scans. In this experimental setup the challenge is to attach the object tightly to a surface but still allow relaxation dynamics on the plane to observe polymers in two dimensions. A successful implementation has been achieved for DNA on mica surfaces [159]. Because of the fine resolution now also short DNA strands could be observed in their semiflexible regime, enabling the characterization of small DNA rings in two dimensions [206], see Fig. 2.3 (B). In collaboration with Guillaume Witz and Giovanni Dietler from the EPFL Lausanne we analyzed the shape of small DNA rings both theoretically and by experiment to find a distortion in shape due to an effective stiffening by the finite diameter of DNA [51].

For optical microscopy actin filaments are a popular object not only because of their important role in cell cytoskeleton. The persistence length of actin filaments is more than three hundred fold larger than the one of DNA and, hence, semiflexible properties are important on much larger polymer length turning optical resolution sufficiently high. Here, recent experiments involve single actin polymer conformations in an entangled network established by fellow actin filaments [161] and actin confined to nano-channels [99]. Especially the study of actin polymers in confined geometries contributes to the highly active research field on biomimetic devices. The configuration of actin condensates most prominently into actin rings [33, 34, 109, 115, 171, 193] is also energetically investigated with respect to the development of new bio-nanomaterials.

Recent experiments also indicate an important role for polymer shape during genetic processes [197]. While a protein tries to locate its specific target along the DNA, it slides in one-dimensional diffusion along the polymer interspersed by dissociation/association events into the three dimensional surrounding volume [12]. When dissociated the protein can diffuse long distances in the three dimensional volume or significantly speed up its target search by hopping just a short distance along the DNA contour or jumping to a spatially close, but along the polymer's contour distant, DNA segment. Especially for those intrasegmental jumps the study of polymer shapes may give promising insights.

## 2.3 Semiflexible polymer model

The study of single biopolymers is one of the blessed topics in the field of biological systems where theoretical models and experimental observations do result in exact matching. An example shown in this work is the measurement of the shape of small DNA circles on mica surfaces in collaboration with the Dietler Group at EPFL Lausanne [51]. Surely, also models for biopolymers employ rigorous abstractions of the real microscopic constituents. The key is to choose the level of abstraction appropriate for the question to answer.

For flexible biopolymers which are very long with respect to their persistence length the polymer's stiffness against bending can be neglected and a simple random walk may ex-

plain the observed conformations. However, in many biological or in vitro settings this assumption is not true and a model for semiflexible polymers such as the wormlike chain model is desired. The wormlike chain model describes a polymer as a infinitely thin slender, elastic rod whose space curve  $\mathbf{r}(s)$  is parametrized by an arc length  $s \in [0, L]$ . The elastic energy of the rod increases proportional to its elastic bending modulus  $\kappa$  with the total curvature, measured by the derivative of the tangent of the rod  $\mathbf{t} = \partial\mathbf{r}(s)/\partial s$  [106].

$$E = \frac{\kappa}{2} \int_0^L ds \left( \frac{\partial\mathbf{t}(s)}{\partial s} \right)^2. \quad (2.1)$$

The energy required to fulfill bending is supplied by the thermal environment  $k_B T$  and depends on the actual temperature. At zero temperature no bending is possible at all, at higher temperature, the length scale on which bending becomes possible is just the persistence length defined by  $l_p = \kappa/k_B T$ . The notion that biopolymers are hardly extensible is respected by setting the magnitude of the tangent vector equal one  $|\mathbf{t}(s)| = 1$ .

The wormlike chain model is to some extent amenable to analytic calculations. For open polymer chains besides the trivial results for the mean radius, higher moments of the end-to-end distance [170], the pair correlation function [6] and the radial distribution function [39, 203] are resolved. Analytical results for polymer rings are much more scarce, *e.g.*, analytical results for the mean square diameter as a measure of size only exist in the very flexible limit [209] and the very stiff limit [2].

Dating back to Kratky and Porod [102] the original notation of the wormlike chain model is in its discrete version, where the curved rod is build of  $N$  segments of length  $\ell$ ,  $L = N\ell$ .

$$E = k_B T N \frac{l_p}{L} \sum_{i=1}^N (1 - \mathbf{t}_i \mathbf{t}_{i+1}). \quad (2.2)$$

This is also the formulation that is exploited in our Monte Carlo simulations where a semiflexible polymer ring is discretized into a polygon.

On a closer level of abstraction it can also be desirable to consider an elastic rod with asymmetric bending stiffnesses  $a_1$ ,  $a_2$  and torsional stiffness  $a_3$ . Although more demanding both in simulations and analytical treatment, such ribbon models might need to be considered when the helical structure of DNA or actin becomes important. The elastic energy of a ribbon is analogously defined

$$E = \frac{k_B T}{2} \int_0^L ds (a_1 \omega_1^2 + a_2 \omega_2^2 + c \omega_3^2), \quad (2.3)$$

where  $\omega_i$ ,  $i = 1, 2, 3$  denote the respective curvature or helical deformation density as assigned by the generalized Frenet equations,  $d\mathbf{t}/ds = \boldsymbol{\omega} \times \mathbf{t}_i$ ,  $i = 1, 2, 3$ . and  $\{\mathbf{t}_1, \mathbf{t}_2, \mathbf{t}_3\}$  denote the local body coordinate system of the ribbon. Such ribbon models have been under consideration in earlier work of us [2].

On an even closer step of abstraction the filament diameter of real polymers is respected by introducing the notion of excluded volume [63]. While the pure wormlike chain model, a so called phantom polymer model, allows polymer segments to overlap, the concept of excluded volume introduces a finite shell around each segment of a polymer whose volume is impenetrable for any other segment. This excluded volume forces polymer chain segments to be further apart resulting in an overall swelling of the polymer in size. This work shows that the growth in size is also accompanied by an anisotropic change in shape [51].

## 2.4 Quantification of shape

The search for a measure of shape dates back to 1934 when Kuhn [104] realized that the shape of long flexible polymer coils is overall prolate. Intuition would let us leap to the conclusion that an object, whose consecutive segment can take any direction with equal probability, fills a spherically symmetric space. However, this reasoning implies rotational averaging. And in fact, entropy is maximized for a single trajectory of a polymer if the number of segments in each direction is inhomogeneous and, hence, not spherically symmetric.

To capture the inhomogeneity of a polymer's extent in space initial work was devoted to measure the average length along each principal axis using simulations [16, 57, 184]. The spatial dimensions of a single polymer trajectory are measured by the radius of gyration tensor  $Q$

$$Q_{ij} = \frac{1}{L} \int_0^L ds \mathbf{r}_i(s) \mathbf{r}_j(s) - \frac{1}{L^2} \int_0^L ds \mathbf{r}_i(s) \int_0^L d\tilde{s} \mathbf{r}_j(\tilde{s}), \quad (2.4)$$

whose eigenvalues define the spatial extent. Analytical calculations of shape became possible when Aronovitz and Nelson [7] and Rudnick and Gaspari [163] defined a measure for the asymmetric extent in space, the asphericity  $\Delta$ . This length-independent measure is defined as the normalized variance of the eigenvalues of the radius of gyration tensor

$$\Delta = \frac{d}{d-1} \frac{\text{Tr} \hat{Q}^2}{(\text{Tr} Q)^2}, \quad (2.5)$$

where  $\hat{Q}_{ij} = Q_{ij} - \delta_{ij} \text{Tr} Q / d$  and  $d$  denotes the dimension of space. The asphericity takes values between  $0 \leq \Delta \leq 1$ , where  $\Delta = 0$  corresponds to a spherically symmetric object. For  $\Delta = 1$  the object resembles a rigid rod. Extensive field theoretic renormalization group methods led to the calculation of the asphericity of open flexible polymers, flexible polymer rings and flexible star polymers [47, 95, 96]. We employ a perturbation expansion to extend investigations beyond flexible polymers and determine the asphericity of semiflexible polymers in [3], see also Appendix A.

In two dimensions a polymer's form is fully defined by two independent measures; the intensive quantity asphericity  $\Delta$  and the extensive quantity squared radius of gyration  $R_g^2$

as a measure of size.  $R_g^2$  is defined as the sum of the spatial extent of the principal axes,  $R_g^2 = \text{Tr } Q$ . In three dimensions a third intensive quantity is necessary to fully define an object's form, the nature of asphericity  $\Sigma$  given by [26]

$$\Sigma = \frac{4 \text{Det } \widehat{Q}}{\left(\frac{2}{3} \text{Tr } \widehat{Q}^2\right)^{3/2}}. \quad (2.6)$$

The nature of asphericity specifies the prolateness or oblateness of an object by measuring the normalized skewness of the eigenvalues of the radius of gyration tensor.  $\Sigma$  is bounded between  $-1 \leq \Sigma \leq 1$ .  $\Sigma = -1$  is obtained for a fully oblate object such as a disk, while  $\Sigma = 1$  is the result for a prolate object as a rigid rod.

In our work we utilize these well-established measures to determine the conformations of semiflexible biopolymers. The lever that controls such a polymers shape is intrinsically its flexibility, but also extrinsic factors such as confinement and solvent condition have a huge impact on biopolymer's final form.

## 2.5 Polymer ring conformations

What is the shape of a biopolymer ring? We answer this question by characterizing the form of polymer rings over the full range of flexibilities from stiff almost rigid ring like states via semiflexible to flexible conformations. Three different scenarios are considered to understand the effects of topology, confinement and filament diameter on polymer shape. First, the conformations of polymers topologically constrained to a ring, fluctuating freely in three dimensional space, are considered; a work that has been published under the title "Shapes of semiflexible polymer rings" in *Physical Review Letters* [3], reprinted in section 2.7 of this work. Second, we analyze the impact of spherical confinement to the available states of a ring polymer in the stiff and the semiflexible regime; the results concerning stiff polymer rings are published under the title "Buckling of stiff polymer rings in weak spherical confinement" in *Physical Review E* [140], reprinted in section 2.8, the part on semiflexible confined polymer rings is published under the title "Confinement induces conformational transition of semiflexible polymer rings to figure eight form" in *Soft Matter* [141], reprinted in section 2.9. At last, we focus on the effect of a finite filament diameter on ring polymer's shape by investigating semiflexible polymers on a two-dimensional plane, published under the title "Excluded volume effects on semiflexible ring polymers" in *Nano Letters* [51] and reprinted along with the accompanying supporting information in section 2.10. This last work is accompanied by experimental results of DNA rings on mica surfaces by the Dietler Group, EPFL Lausanne.

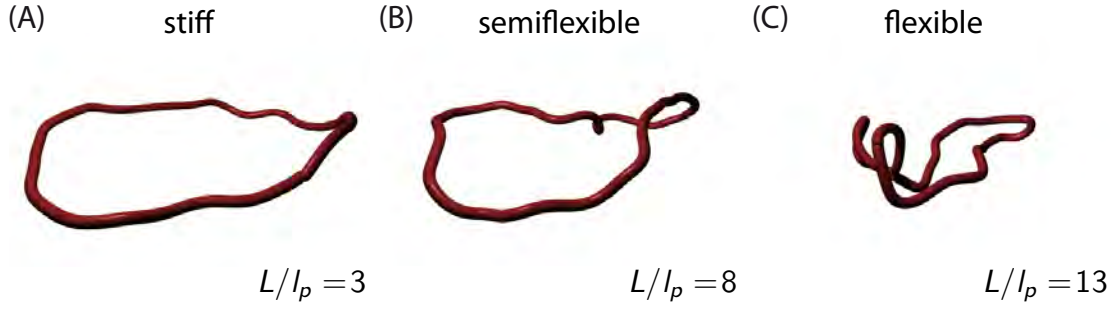


**Figure 2.4:** Simulation snap shots of polymer ring conformations in the stiff  $L/l_p = 3$  (A), semiflexible  $L/l_p = 8$  (B) and flexible regime  $L/l_p = 13$  (C). Starting from a rigid ring thermal fluctuations first induce a simple bending mode which leads to a planar elliptical form. Only at larger flexibilities do polymers crumple up yielding compact, prolate shapes.

## Free polymers

At zero temperature or equivalently zero flexibility defined by  $L/l_p = k_B T L / \kappa = 0$  the conformation of an open polymer is a rigid rod. If one now increases the flexibility by raising the temperature or the total length of the polymer, a first bending mode can be excited. The polymer turns into a two dimensional object. Only when higher and higher bending modes set in the whole polymer crumples up to fill a prolate ellipsoid.

Analogously polymer rings are characterized by their first bending mode in the stiff regime, which is a planar ellipse. However, the topological constraint of a ring effectively stiffens the polymer's behavior relative to the ones of an open polymer chain [2, 171]. Hence, the planar elliptical shape dominates the polymer's appearance for large flexibilities until about  $L/l_p \approx 5$ . Only then higher modes set in that finally crumple the polymer up into a prolate coil-like ellipsoid, considerably later than for linear polymers, which transition at  $L/l_p \approx 1$ . Our detailed study of the polymer's shape in configuration space substantiates that in the stiff regime only ellipses are populated whose degree of eccentricities increases with flexibility. For an illustration of typical polymer configuration observe the simulation snap shots in Fig. 2.4.

Analyzing the mean asphericity and the mean nature of asphericity the above observations stemming from density profiles in the configuration space obtained with Monte Carlo simulations are confirmed by analytical arguments. In the stiff limit the mean amplitude of the fluctuations  $\langle a \rangle$  is analytically calculated to grow with the square-root of the flexibility  $\langle a \rangle \propto L \sqrt{L/l_p}$  [136]. Assuming now an elliptical configuration where the major axis grows and the minor axis shrinks due to the fluctuations [24, 177] a linear increase of the mean asphericity and the mean nature of asphericity with flexibility is forecasted. These predictions are in accordance with our simulation results substantiating the shape of an ellipse in the extended stiff regime.

While exact results for the mean asphericity of an infinitely flexible polymer ring exist

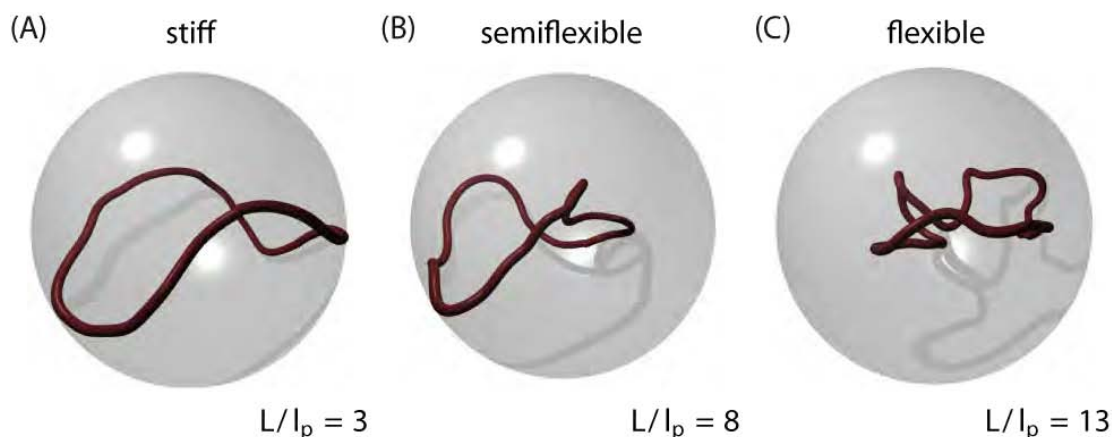


**Figure 2.5:** Simulation snapshots of polymer ring conformations in spherical confinement in the stiff  $L/l_p = 3$  (A), semiflexible  $L/l_p = 8$  (B) and flexible regime  $L/l_p = 13$  (C). The planar ellipse of a free stiff polymer ring cannot be accommodated within the spherical confinement. Therefore, the ellipse buckles into the banana-like shape in (A). In the semiflexible regime the higher bending modes induce a writhing of the ring to arrange the even more elongated polymer within the confinement (B). In the flexible regime the influence of the confinement on polymer conformation ceases, as the polymer crumples up in the vicinity of the sphere's center (C).

[47, 72], we compute that the asphericity of a semiflexible polymer ring approaches its limit of infinite flexibility from above by employing a perturbation expansion, see Appendix A. This result is again in agreement with our numerical data and clarifies numerically limited previous work [24, 135].

All in all our analytical results confirm that a polymer ring has the shape of an ellipse for small flexibilities. As the ellipse's eccentricity grows with increasing flexibility the polymer becomes more and more aspherical and prolate until higher modes lead to crumpling which then decreases the asphericity again slowly.

## Spherically confined polymers

Confinement restricts attainable modes of a thermally fluctuating polymer and thereby alters a polymer's overall shape. We study polymer rings in weak spherical confinement where the radius of the shell is of the same order as the radius of the enclosed polymer ring, such that an infinitely stiff rigid ring is just accommodated within the sphere. According to its first bending mode a polymer ring would take an elliptical shape in the stiff regime, whose major axis would, however, exceed the spatial extension provided by the spherical confinement. Therefore, already shallow confinement induces major changes to the shape of polymer rings.

Thermal fluctuations excite a stiff polymer ring to bend as much as the provided thermal

energy versus elastic bending energy permits. Initially, in the competition of entropy and energy an elliptical shape arises. In the steric confinement of a spherical shell, the major axis of the ellipse pushes against the rigid walls. The walls compress the ellipse such that the polymer ellipse buckles into a banana-like shape. The height of the resulting dome increases as the major axis grows with the square-root of the flexibility until, at high enough flexibilities, bends on length scales smaller than the curvature of the confining sphere arise, see Fig. 2.5. The buckling in the stiff limit observed in Monte Carlo Simulations is in accordance with a scaling argument developed on the basis of an Euler buckling ellipse [106, 112], where the length of the minor and major axis depend on the flexibility of the polymer. Taking into account that entropy is maximized if the ellipse's apices do not lie on the same equatorial plane our scaling argument explains the observed mean asphericity and nature of asphericity for all radii of spherical confinement larger or equal to the radius of the polymer's corresponding rigid ring.

In the semiflexible regime beyond the stiff range, the lower elastic energy allows bends on length scales smaller than the radius of the confining sphere. Simultaneously the dominant elliptical shape has a yet with flexibility increasing major axis. Hence, an even longer object has to be accommodated within the shell. The semiflexible polymer ring stores this length by winding up into a figure eight shape, see Fig. 2.5 (B) for a simulation snap shot. This result follows from the behavior of two observables: The tangent-tangent correlation, which reflects the relative orientation of polymer segments along the polymer backbone and the mean winding number, the writhe  $Wr$ , which characterizes how much a polymer trajectory is twined about itself. The mean writhe of confined polymer rings shows a strong increase in the semiflexible region in comparison to unconfined polymer rings due to additional polymer configurations centered around a distinct writhe of  $|Wr| = 0.8$ . Simultaneously the tangent-tangent correlation exhibits the characteristics of correlations along a figure eight. Analysis of the writhe distribution of confined polymer rings at different flexibilities enables to quantify the percentage of writhed configurations provoked by confinement, amounting up to over 50%. Only even higher bending modes yield a crumpling of the whole polymer ring turning the impact of spherical confinement less and less, Fig. 2.5 (C).

## Polymers with finite thickness

Up to now polymers have been modeled as infinitely thin space curves. This is a good approximation as polymer chains almost never get so close in the vast space of three dimensions that alterations in their conformations occur due to a steric self-hindrance. However, this space curve approximation fails if polymers are subjected to strong confinement or are constrained to two dimensions. Here the finite cross-sectional diameter  $d$  of filaments induces in addition to Flory's predicted swelling in size [63] an anisotropic distortion of the polymers shape and an effective stiffening of the polymer. We show this by comparing a two dimensional phantom polymer ring, where self-crossings are allowed, to a two dimensional polymer ring with finite diameter. Our simulation results are in



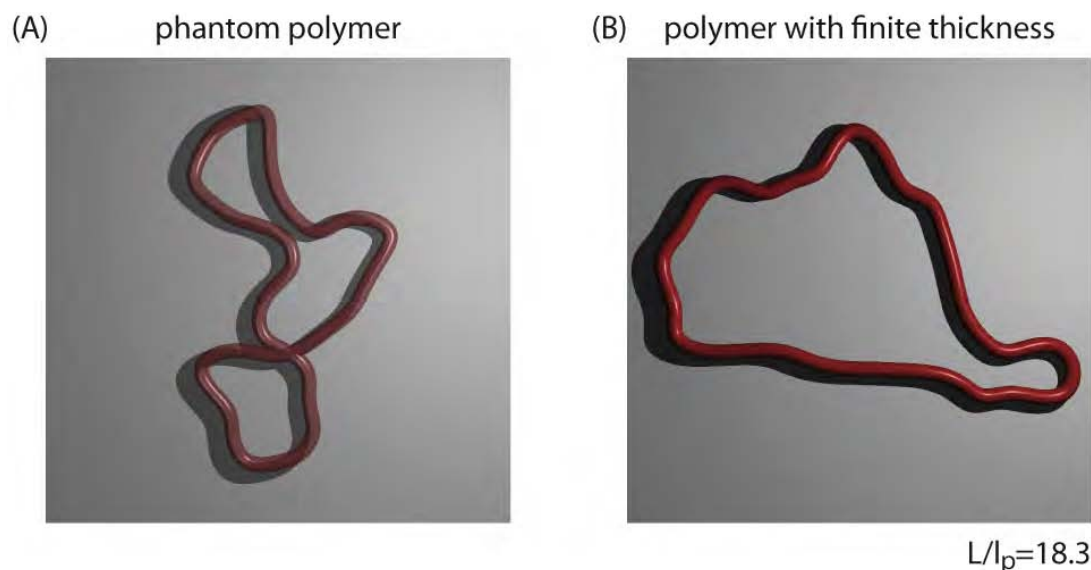


**Figure 2.6:** Simulation snap shot of a phantom polymer (A) and a polymer with finite thickness (B) on a plane. Phantom polymers bear overlaps and kink-like bending resulting in smaller more aspherical shapes than polymers with finite thickness, where effective stiffness governs the not self-intersecting polymer chain.

good agreement with experimental measurements of circular DNA conformations on mica surfaces.

Considering a polymer trajectory as a curved tube with cross-sectional diameter  $d$  large deformations on small length scales are forbidden since self-crossing would result. Hence, the polymer with finite diameter is effectively stiffer than a phantom polymer. We observe this effective stiffening by an enhanced correlation in the tangent-tangent correlation and an extended stiff behavior in the mean size of two dimensional polymer rings.

Due to the finite diameter polymer segments cannot get as close to each other as for phantom polymers. Hence, the overall size of a polymer with finite diameter is larger, the polymer is swollen. We find that this increase in size is asymmetric, the polymer is distorted in shape due to the increase in cross-sectional diameter. Two dimensional polymer rings are aspherical, hence, one principal axis is longer than the other much like in an ellipse. In the apices of the ellipse neighboring segments tend to overlap while in the convex part segments being separated approximately half the contour length apart are prone to overlap. The finite thickness now effectively stiffens the polymer inducing less bending at the apices and it increases the minor principle axis by pushing segments apart in the convex region. In total the finite thickness leads to a more spherical shape.

## 2.6 Outlook

Our work builds an intuitive understanding on how internal polymer characteristics such as flexibility, topology and filament diameter as well as external confinement constraints affect the shape of biopolymers. Based on this characterization it is possible to build more coarse-grained models for more complex biological processes involving several objects. To investigate for example the depletion forces mediated by polymers in polymer solution [195, 198] an approximation of polymers by their dominating shape could be a successful approach. Likewise a coarse-grained description of polymers could be desirable concerning the design of nano-biotechnological devices [19, 157] aiming at a lab on a chip [36]. However, in biomimetic devices polymer properties neglected in our study may become of dominating importance. As such we neglected the polyelectrolyte character of most polymers in particular DNA. In many biological settings the charges associated with polymers are screened by positive ions resulting in a neutral state. Net effects of the charges and their counter ions do, however, occur when electrical fields are applied driving the movement of a polymer. Additionally, many bio-mimetic devices use pumping of the surrounding solution to arrange objects by flow turning hydrodynamic forces dominant [22].

In our study of polymer shapes we focused on the equilibrium properties. Besides these fundamental insights it is desirable to understand the dynamic [78, 82, 110] aspect of polymer shapes. What is the path taken within the configuration space? Is the polymer performing a mere random walk or are there certain favored transitions from one state to another? Concerning the target search problem of proteins along DNA valuable insight could be obtained from how fast spatial neighbor relations change.

Our scaling arguments in the stiff limit do explain the whole dominant polymer trajectory. However, beginning from the semiflexible regime onwards the shape parameters mainly describe the form of an enveloping ellipse. The internal structure is so far merely reflected in observables such as the writhe and the tangent-tangent correlation. Measures beyond these would be desirable to understand the internal polymer organization for example by the surface to bulk ratio of chain segments.

Despite a long tradition polymer science is still rich in challenging question to be answered to unravel the multitude of processes in biological systems.

## Shapes of Semiflexible Polymer Rings

Karen Alim and Erwin Frey

*Arnold Sommerfeld Center for Theoretical Physics and Center for NanoScience, Department of Physics,  
Ludwig-Maximilians-Universität München, Theresienstrasse 37, D-80333 München, Germany*

(Received 5 March 2007; published 7 November 2007)

The shape of semiflexible polymer rings is studied over their whole range of flexibility. Investigating the joint distribution of asphericity and the nature of asphericity as well as their respective averages, we find two distinct shape regimes depending on the flexibility of the polymer. For a small perimeter to persistence length the fluctuating rings exhibit only planar, elliptical configurations. At higher flexibilities three-dimensional, crumpled structures arise. Analytic calculations confirm the qualitative behavior of the averaged shape parameters and the elliptical shape in the stiff regime.

DOI: [10.1103/PhysRevLett.99.198102](https://doi.org/10.1103/PhysRevLett.99.198102)

PACS numbers: 87.17.Aa, 05.20.Gg, 36.20.Ey, 87.14.Gg

It is a well-known fact dating back to 1934 that the shape of a flexible coil is overall prolate [1]. From the isotropy of space, the intuitive expectation would be a spherically symmetric conformation. However, this idea implies rotational averaging and, in fact, entropy is maximized for a single trajectory of a polymer if the number of segments in each direction is inhomogeneous.

After a series of theoretical investigations, based on both analyses [2–4] and simulations [5,6], only with the onset of single molecule techniques, experiments could prove the asymmetric shape of a flexible polymer [7,8] and address the relevance of a polymer's shape in biology. The overall shape of a polymer is important for its mobility in heterogeneous media such as cytoplasm and the depletion forces between larger complexes in polymer solution [9,10]. For the transcription of viral genome or plasmids, the shape of its DNA might enhance or reduce the accessibility for enzymes depending on the spatial distance between DNA segments [11]. DNA as many biopolymers is semiflexible, behaving like a thermally fluctuating elastic rod on length scales of the order of its persistence length. Considering the shape of viral DNA and plasmids, this limit is applicable and deserves investigation. In fact, most of the short genomes as well as plasmids are circular, yielding an even stronger constraint for the polymer's shape. To obtain a complete picture for any circular DNA, it is desirable to understand the shape of semiflexible rings as their flexibility is varied. A polymer's shape is well characterized by the asphericity [2] as the deviation from spherical symmetry. The degree of prolateness or oblateness is captured by the independent nature of asphericity [5]. Measurements of both their mean values give a good indication of how the average outline looks, but fail to reflect the total ensemble of configurations that can only be accessed via the shape parameter's distribution.

We employ Monte Carlo simulations to study the shape of semiflexible polymer rings over a large range of flexibility. To give a complete picture of the polymer's change of shape as its flexibility increases, the joint distribution of asphericity and nature of asphericity as well as their re-

spective averages will be presented. We find two different shape regimes. In the first, the flexibilities are small, resulting in dominantly planar polymer ring configurations. In the second, at large flexibilities, crumpled three-dimensional (3D) structures prevail. In both the stiff and the flexible limit analytic calculations explain the observed behavior.

Characterizations of the shape of a polymer's trajectory  $\{\mathbf{r}(s)\}$ ,  $s \in [0, L]$ , are based on the radius of gyration, primarily a measure for the spatial extent. Generalizing to a radius of gyration tensor  $Q$ ,

$$Q_{ij} = \frac{1}{L} \int ds \mathbf{r}_i(s) \mathbf{r}_j(s) - \frac{1}{L^2} \int ds \mathbf{r}_i(s) \int d\tilde{s} \mathbf{r}_j(\tilde{s}), \quad (1)$$

the eigenvalues  $\lambda_i$  of the tensor describe the spatial extent along each principal axis. Measuring the variance of the eigenvalues, the deviation from a fully symmetric object is obtained, denoted asphericity,  $\Delta$ . Furthermore, prolateness or oblateness of the object is specified by the nature of asphericity,  $\Sigma$ , measuring the skewness of the eigenvalues. Choosing the normalization such that the quantities are independent of the total length, the asphericity of a polymer is defined by [2]

$$\Delta = \frac{3}{2} \frac{\text{Tr} \hat{Q}^2}{(\text{Tr} Q)^2}, \quad (2)$$

where  $\hat{Q}_{ij} = Q_{ij} - \delta_{ij} \text{Tr} Q / 3$ . The nature of asphericity is given by [5]

$$\Sigma = \frac{4 \det \hat{Q}}{(\frac{2}{3} \text{Tr} \hat{Q}^2)^{3/2}}. \quad (3)$$

The asphericity takes values  $0 \leq \Delta \leq 1$ , where  $\Delta = 0$  corresponds to a spherically symmetric object. For  $\Delta = 1$ , the polymer is fully extended, forming a rigid rod. The nature of asphericity is bounded between  $-1 \leq \Sigma \leq 1$ .  $\Sigma = -1$  is obtained for a fully oblate object such as a disk, while  $\Sigma = 1$  is the result for a prolate object as a rigid rod. As the asphericity and the nature of asphericity are independent, a joint distribution yields a thorough classification

of stochastic objects such as thermally fluctuating polymers. For reasons of comparison, we will adopt the parameters  $\rho = 2\sqrt{\Delta} \in [0, 2]$  and  $\theta = \arccos \Sigma/3 \in [0, \pi/3]$  for the joint distribution defined by Cannon *et al.* [5].

Those parameters are directly connected to the eigenvalues of the radius of gyration tensor by  $\lambda_1 = \bar{\lambda}[1 + \rho \cos(\theta)]$ ,  $\lambda_2 = \bar{\lambda}[1 + \rho \cos(\theta - 2\pi/3)]$ , and  $\lambda_3 = \bar{\lambda}[1 + \rho \cos(\theta + 2\pi/3)]$ , where  $\lambda_1 \geq \lambda_2 \geq \lambda_3$  and  $\bar{\lambda}$  denotes the mean eigenvalue. Using these relations, the shape diagram presented in Fig. 1 is constructed. In the region of both large  $\rho$  and large  $\theta$ , one eigenvalue becomes negative, excluding these parameter sets for real structures. Along the solid line separating the excluded conformations from possible ones, at least one eigenvalue is zero. Hence, the solid line represents all planar configurations ranging from the fully oblate geometry of a rigid ring with  $\theta = \pi/3$  via elliptical shapes to the fully prolate structure of a rigid rod at  $\theta = 0$ . Below the solid line, 3D conformations are exhibited as all eigenvalues are now greater than zero. The shape is rather oblate for  $\theta > \pi/6$  or comparatively prolate for  $\theta < \pi/6$  as illustrated by the ellipsoids enclosing a polymer's trajectory. Towards smaller  $\rho$ , the structure becomes less and less aspherical resulting in a spherically symmetric conformation for  $\rho = 0$ .

For flexible open polymers the shape distribution is known to be almost exclusively prolate and highly aspherical being peaked around  $\theta = \pi/40$  and  $\rho = 1.55$  [5] as indicated by the diamond in Fig. 1. However, the conformation of a rigid ring lies just at the opposite end of the shape diagram at  $\theta = \pi/3$  and  $\rho = 1$ . As the states of a highly flexible ring polymer can be assumed to be similar to those of flexible open polymers, a strong crossover between a stiff and a flexible regime seems inevitable.

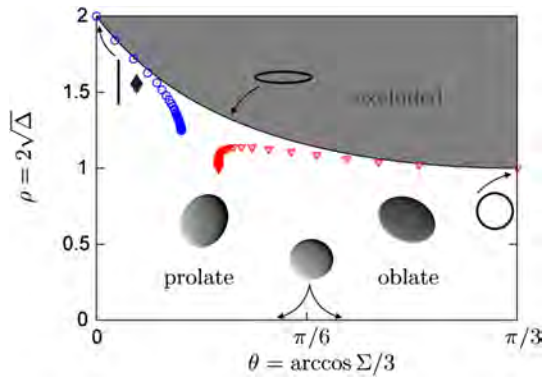


FIG. 1 (color online). The overall shape of polymer configurations depending on the asphericity  $\Delta$  and the nature of asphericity  $\Sigma$ . Along the solid line the structures are planar; configurations beyond that line are excluded as they do not correspond to real structures. The diamond indicates the peak in the distribution of flexible open polymers. The sequences of circles and triangles denote the mean shapes of open and ring polymers at integer flexibilities starting from  $L/l_p = 0$  at  $(0, 2)$  and at  $(\pi/3, 1)$ , respectively.

Heuristically, we may argue that the shape of the tight fluctuating ring in the stiff limit is expected to be dominated by the first modes since higher modes are almost not thermally excited. Both the first in-plane “breathing” mode and the first transverse bending mode yield an elliptical conformation as can be illustrated by deforming a strip of paper connected to form a ring. Although the ring rotates in space when fluctuating, the elliptical shape itself remains planar, being oblate for small eccentricities and becoming prolate for large eccentricities of the ellipse. Towards the flexible limit also higher modes are excited resulting in a crossover to the flexible regime where the conformations are three dimensional and crumpled as expected for a closed random walk.

The METROPOLIS Monte Carlo method was employed to simulate a discretized semiflexible ring of total length  $L$  and persistence length  $l_p$ . The ring is described as a polygon composed of  $N$  tethers of fixed length  $a = (L/\pi) \times \sin(\pi/N)$  and direction  $\mathbf{t}$ . The energy assigned to an individual configuration is given by the elastic energy,  $E = Nk_B T (l_p/L) \sum_{i=1}^N (1 - \mathbf{t}_i \cdot \mathbf{t}_{i+1})$ , imposing periodic boundary conditions,  $\mathbf{t}_{N+1} = \mathbf{t}_1$ . New conformations are achieved by pivot moves [12], performing  $10^6$  Monte Carlo steps per segment. Measured expectation values of the mean square diameter  $\langle D^2 \rangle$  were in accordance with analytical expressions [13] up to the estimated statistical error. The effect of self-avoidance is neglected, as its impact on the shape of even flexible polymers was shown to be only of the order of 1% [2].

The change of shape as the flexibility increases is best studied when analyzing the shape distribution at different flexibilities as plotted in Fig. 2. We distinguish between a stiff regime exemplified by  $L/l_p = 1, 4$  and a flexible regime represented by  $L/l_p = 16, 32$ . The geometry of a ring induces an apparent stiffening of the fluctuating polymer to approximately 5 times its unconstrained flexibility [13]. Therefore, even  $L/l_p = 4$  belongs to the stiff limit. By comparison with the shape diagram in Fig. 1 polymer ring configurations in the stiff regime are identified to be almost exclusively planar ranging from totally oblate to comparatively prolate shapes. In the flexible regime, crumpled structures that fill 3D space dominate the broader configuration space. The distribution changes from rimlike being strongly peaked in the asphericity to lenslike with the major weight on prolate and highly aspherical conformations, although less rodlike than observed for *open* polymers. In agreement with experimental observations [7,8], the distribution of shapes is very broad, yielding also very extended conformation close to  $\rho = 2$ .

In between the two asymptotic shape regimes a crossover is observed represented by  $L/l_p = 8$  in Fig. 2. During this crossover both crumpled, 3D configurations and planar structures are almost equally probable, yielding the largest spread of well-occupied conformations in the configuration space. Beyond the stiff regime in Fig. 2 the mean of

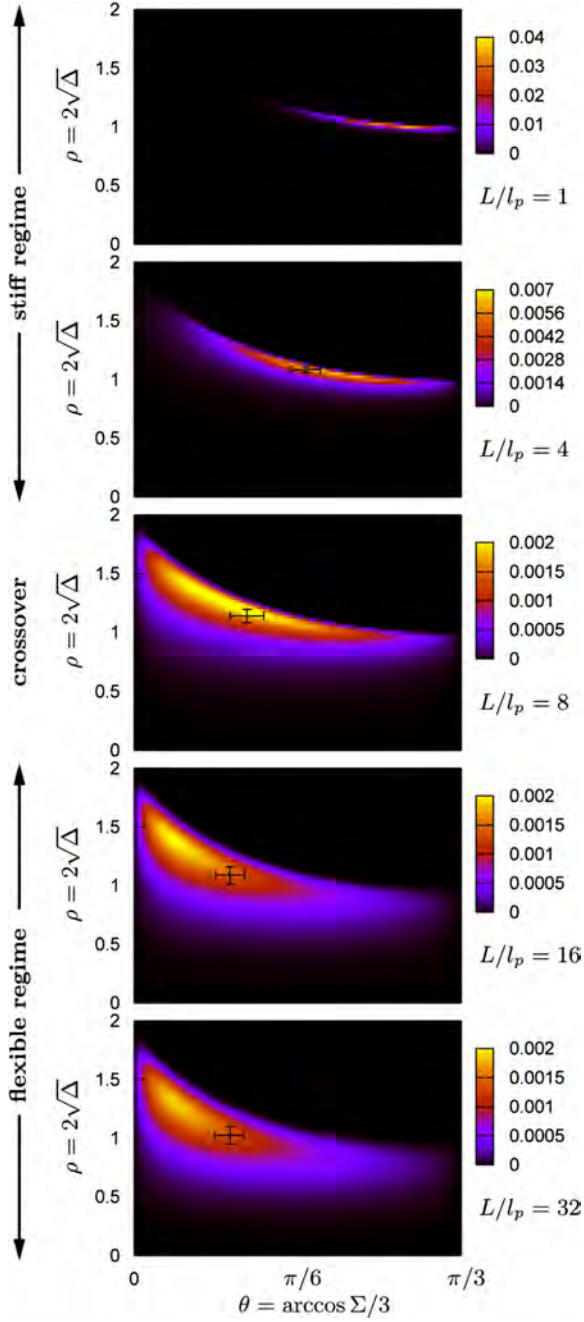


FIG. 2 (color online). The distribution of asphericity  $\Delta$  and the nature of asphericity  $\Sigma$  at different levels of flexibility. For tight rings,  $L/l_p < 5$ , planar conformations dominate, while the configurations become truly 3D beyond  $L/l_p$  of the order of 10. The crosses indicate mean and variance of each single shape parameter deviating from the most probable state. Note the change of the color scaling as the distribution spreads out.

each single shape parameter deviates from the states with the largest joint probability, showing its limitation in identifying a polymer's configurations. Identification of the conformations and insight into the width and the form of

the density of states are only attainable by the distribution of the shape parameters, highlighting their importance for studying polymer shapes.

Investigating the mean asphericity and the mean nature of asphericity, qualitative arguments can be quantified and compared to previous results in the limit of infinite flexibility. The change of both shape parameters on increasing flexibility  $L/l_p$  is depicted in Fig. 3. For a rigid ring, the asphericity is given by  $\Delta = 0.25$ , being fully oblate:  $\Sigma = -1$ . Up to  $L/l_p \approx 5$  both asphericity and the nature of asphericity grow linearly with the flexibility, obeying  $\langle \Delta \rangle_{\text{stiff}} = 0.25 + 0.01L/l_p$ ,  $\langle \Sigma \rangle_{\text{stiff}} = -1 + 0.3L/l_p$ . This linear dependence classifying the stiff regime is explained by the shape of an ellipse whose axes grow and shrink with the square root of the flexibility, respectively, as will be discussed in the next paragraph. A similar scaling argument has been given by Camacho *et al.* [14] analyzing planar rings. Beyond this stiff regime a maximum of the mean asphericity is reached. Increasing the flexibility further, higher modes become accessible. These undulations contract particularly the major axis of the “ellipse,” decreasing the variance of the eigenvalues of the radius of gyration tensor and hence yielding a declining asphericity. The asphericity approaches the exact value for an infinitely flexible polymer ring, a closed Gaussian chain,  $\langle \Delta \rangle_{\text{fl,c}} = 0.2464$ , derived by Diehl and Eisenriegler [3] in a power law with exponent  $\nu = -1.3$ . Compared with a flexible open polymer with  $\langle \Delta \rangle_{\text{fl,o}} = 0.396(5)$  [5], a polymer ring is much more spherical. Analytic calculations based on a perturbation expansion of a closed Gaussian chain for finite flexibility forecast a positive correction in first order [15],

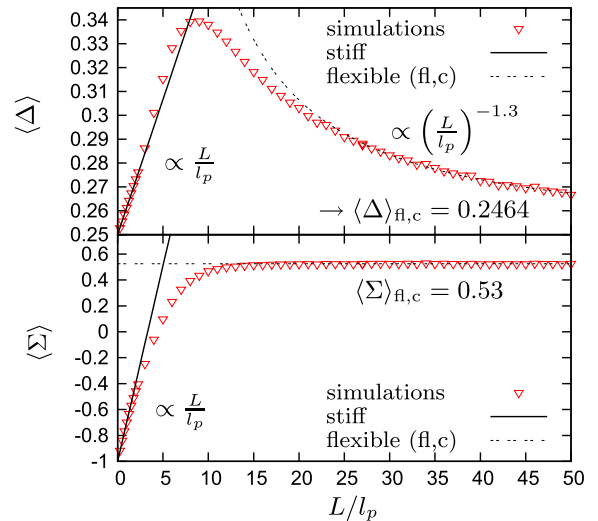


FIG. 3 (color online). Monte Carlo simulation data for the mean asphericity  $\langle \Delta \rangle$  and the mean nature of asphericity  $\langle \Sigma \rangle$  versus increasing flexibility  $L/l_p$ . Both grow linearly with raising flexibility for tight rings (solid line). Then,  $\langle \Sigma \rangle$  saturates at a prolate shape, while the asphericity decreases in a power law (dashed line). Error bars are of the size of the symbols.

and, hence, explain why the asphericity approaches its Gaussian limit from above. Also for two-dimensional polymer rings our analytic arguments predict a linear increase of the asphericity in the stiff limit and a monotonic decrease in the flexible limit explaining the nonmonotonic behavior of the shape parameter observed in previous simulations in two dimensions [14,16]. Experiments found a slight increase of the asphericity versus  $L/l_p$  in the flexible regime for linear DNA [7] not to be justified with our predictions of the shape of semiflexible polymers discarding for the sake of simplicity additional DNA effects, such as twist, nicks, or supercoils. Although DNA rings make up a huge field of biological processes where shape matters, resolving their 3D shapes is a challenge due to their small size and rate of change. Ring polymers of larger persistence length  $l_p$  such as cytoskeletal filaments as in [17] or mesoscopic polymer materials are feasible to measure our results. The nature of asphericity increases monotonically saturating at a value of  $\langle \Sigma \rangle_{n,c} = 0.53$  at  $L/l_p \approx 15$ , being less prolate than flexible open polymers with  $\langle \Sigma \rangle_{n,o} = 0.745$  [5]. Towards the Gaussian limit the sequences of averaged shape parameters of ring and open polymer as depicted in Fig. 1 can neither cross nor depart from each other. Therefore, both their  $\langle \Sigma \rangle$  approach their limiting value monotonically. Overall, the geometric constraint induces a bias towards more spherical and oblate structures.

The linear growth of  $\langle \Delta \rangle$  and  $\langle \Sigma \rangle$  for tight rings is analytically predictable based on the assumption of a planar shape. Because of the first bending modes, the ring of radius  $R_c$  becomes an ellipse, where the major and minor axes are the radius  $R_c$  increased and decreased, respectively, by  $\sqrt{\langle \mathbf{r}_\perp^2 \rangle}$ , the amplitude of the undulations of a weakly bending rod. In the weakly bending limit fluctuations parallel to the average axis of the contour are second order to undulations perpendicular, resulting in the approximate bending energy  $E = \frac{1}{2} k_B T l_p \int_0^L ds \mathbf{r}_\perp''(s)^2$ , and yielding  $\sqrt{\langle \mathbf{r}_\perp^2 \rangle} = \gamma R_c^{3/2} l_p^{-1/2}$  [14,18,19], where  $\gamma$  denotes a numerical constant. Hence, the asphericity and the nature of asphericity are equated in the limit of small flexibilities  $L/l_p$ , where the first modes truly dominate

$$\Delta_{\text{ellipse}} = 0.25 + 2\gamma L/l_p + \mathcal{O}((L/l_p)^2), \quad (4)$$

$$\Sigma_{\text{ellipse}} = -1 + 54\gamma L/l_p + \mathcal{O}((L/l_p)^2). \quad (5)$$

These analytic results forecast the observed behavior.

In conclusion, we have employed the joint distribution of asphericity and the nature of asphericity and their respective means as well as analytic arguments to show that the shape of semiflexible polymer rings exhibits two distinct regimes depending on their flexibility. Tight rings are planar “ellipses,” while flexible rings are 3D, crumpled structures. These two regimes may have implications for a variety of biological processes such as the flow behavior or the accessibility of DNA rings to enzymes. As the shape of

stiff, elliptical rings may not be considerably changed by hydrodynamic forces since they will behave as rigid disks, rings in the flexible regime may undergo tumbling motion with alternating collapse and stretching as observed for flexible open polymers [20]. Similarly, the time it takes an enzyme to find its assigned binding site on a DNA strand should be larger if the DNA conformation is planar, as the enzyme cannot easily travel to DNA segments separated afar along the backbone by 3D diffusion as in coiled up 3D structures. In this context of opposed behavior in the two shape regimes, polymers in the crossover region where both shapes are equally probable may show striking properties. Depending on the manner in which a polymer changes between a planar and a crumpled shape, e.g., randomly or following a particular trajectory, and its time scale, a broad variety of biological functionality can emerge. The characterization of a semiflexible polymer by its shape can therefore enable a coarse-grained modeling of complex biological processes.

Financial support of the German Excellence Initiative via the program “Nanosystems Initiative Munich (NIM)” and of the Deutsche Forschungsgemeinschaft through SFB 486 is gratefully acknowledged.

- 
- [1] W. Kuhn, *Kolloid Z.* **68**, 2 (1934).
  - [2] J. A. Aronovitz and D. R. Nelson, *J. Phys. (France)* **47**, 1445 (1986).
  - [3] H. W. Diehl and E. Eisenriegler, *J. Phys. A* **22**, L87 (1989).
  - [4] K. Solc, *J. Chem. Phys.* **55**, 335 (1971).
  - [5] J. W. Cannon, J. A. Aronovitz, and P. Goldbart, *J. Phys. I* **1**, 629 (1991).
  - [6] M. Bishop and J. H. R. Clarke, *J. Chem. Phys.* **90**, 6647 (1989).
  - [7] C. Haber, S. A. Ruiz, and D. Wirtz, *Proc. Natl. Acad. Sci. U.S.A.* **97**, 10792 (2000).
  - [8] B. Maier and J. O. Rädler, *Macromolecules* **34**, 5723 (2001).
  - [9] R. Verma *et al.*, *Phys. Rev. Lett.* **81**, 4004 (1998).
  - [10] M. Triantafillou and R. D. Kamien, *Phys. Rev. E* **59**, 5621 (1999).
  - [11] T. Hu, A. Y. Grosberg, and B. I. Shklovskii, *Biophys. J.* **90**, 2731 (2006).
  - [12] K. V. Klenin *et al.*, *J. Mol. Biol.* **217**, 413 (1991).
  - [13] K. Alim and E. Frey, arXiv:q-bio.BM/0703049 [*Eur. Phys. J. E* (to be published)].
  - [14] C. J. Camacho, M. E. Fisher, and R. R. P. Singh, *J. Chem. Phys.* **94**, 5693 (1991).
  - [15] K. Alim and E. Frey (unpublished).
  - [16] R. E. Norman, G. C. Barker, and T. J. Sluckin, *J. Phys. II* **2**, 1363 (1992).
  - [17] M. M. A. E. Claessens *et al.*, *Nature Mater.* **5**, 748 (2006).
  - [18] J. Shimada and H. Yamakawa, *Biopolymers* **27**, 657 (1988).
  - [19] T. Odijk, *J. Chem. Phys.* **105**, 1270 (1996).
  - [20] C. M. Schroeder, R. E. Teixeira, E. S. G. Shaqfeh, and S. Chu, *Phys. Rev. Lett.* **95**, 018301 (2005).

## Buckling of stiff polymer rings in weak spherical confinement

Katja Ostermeir, Karen Alim, and Erwin Frey

*Arnold Sommerfeld Center for Theoretical Physics and Center for NanoScience, Department of Physics,  
Ludwig-Maximilians-Universität München, Theresienstraße 37, D-80333 München, Germany*

(Received 24 March 2010; published 23 June 2010)

Confinement is a versatile and well-established tool to study the properties of polymers either to understand biological processes or to develop new nanobiomaterials. We investigate the conformations of a semiflexible polymer ring in weak spherical confinement imposed by an impenetrable shell. We develop an analytic argument for the dominating polymer trajectory depending on polymer flexibility considering elastic and entropic contributions. Monte Carlo simulations are performed to assess polymer ring conformations in probability densities and by the shape measures asphericity and nature of asphericity. Comparison of the analytic argument with the mean asphericity and the mean nature of asphericity confirm our reasoning to explain polymer ring conformations in the stiff regime, where elastic response prevails.

DOI: [10.1103/PhysRevE.81.061802](https://doi.org/10.1103/PhysRevE.81.061802)

PACS number(s): 82.35.Lr, 87.17.Aa, 36.20.Ey, 05.20.Gg

### I. INTRODUCTION

It is the interplay of elastic energy and entropy that governs the equilibrium form and the dynamics of semiflexible biopolymers. Their competition determines the shape and consequently the function of a biopolymer as a building block in the cytoskeleton [1,2] or as an accessible storage medium for genetic information [3]. Experimental quantification of the elastic and entropic properties of biopolymers often employ confinement, may it be by clamping one end of the polymer [4,5] or confining the whole polymer into a channel [6–8] or microchamber [9]. In natural conditions the confinement imposed by cell walls and membranes, cell nucleus or viral capsids is approximately spherical. This inspired to use the rather *weak* confinement of artificial giant vesicles as a versatile and well-controllable model system for the investigation of polymer and polymer bundle characteristics [10–12]. Especially but not only in these biomimetic systems, that investigate both biological processes and new nano-biomaterials, polymer rings become of larger and larger importance, stirring theoretical studies of semiflexible polymer rings [13–20]. DNA on the one hand naturally occurs in ring form [21,23] while actin and actin bundles self-assemble into rings under various conditions [11,12,22,24,25]. Polymer rings are an ideal object to investigate entropic and elastic effects as their topology induces Euler buckling even in weak confinement, where the confining cavity is just equal or a little larger than the average size of the polymer, see Fig. 1. Therefore, spherical confinement serves indeed as an excellent tool to investigate the mechanical properties of semiflexible polymer rings and how they are affected due to biological processes under well-defined conditions.

Within the wormlike chain model semiflexible polymers are characterized by their bending elasticity that opposes the excitation of undulations from thermal fluctuations [26]. Representing a polymer of bending modulus  $\kappa$  as a differential space curve  $\mathbf{r}(s)$  of length  $L$  parametrized by an arc

length  $s$ , its statistical properties are determined by the elastic energy

$$\mathcal{H} = \frac{\kappa}{2} \int_0^L ds \left[ \frac{\partial \mathbf{t}(s)}{\partial s} \right]^2, \quad (1)$$

where  $\mathbf{t}(s) = \partial \mathbf{r}(s) / \partial s$  denotes the tangent vector. The competition of elastic against entropic contributions is reflected in the material specific persistence length,  $l_p = \kappa / k_b T$ , which is just the ratio of elastic bending modulus and thermal energy. Comparing this length scale to the total length of the polymer gives a measure of polymer flexibility  $L / l_p$ . Polymer flexibility easily varies; therefore, our present study takes it as a variable parameter within the region of stiff polymers. It was shown that polymer rings due to their topology effectively behave about five times stiffer than linear polymers, i.e., their stiff regime extends up to  $L / l_p \approx 5$  [18] rendering polymer rings advantageous to study elastic responses.

Semiflexible polymers have previously been the subjects of investigations under conditions of strong confinement where the confining cavity is much smaller than the equilibrium size of the polymer. These conditions arise in viral capsids and bacterial envelopes and provoked both analytical

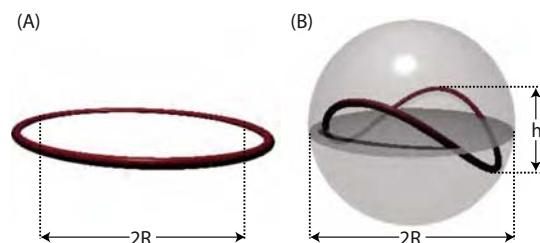


FIG. 1. (Color online) Dominant shape of a stiff polymer ring without (a) and with (b) spherical confinement. (a) Without confinement the first order bending mode excited by thermal fluctuations induces a planar ellipse that exceeds along its major axis the radius of the corresponding rigid ring. (b) Enclosed by spherical confinement the otherwise planar ellipse is compressed and Euler buckles into a bananalike shape.

[27–31] and simulation studies [32–36]. While most studies focus on linear polymers viral DNA may indeed be circular as taken into account for the investigation of knotting probabilities of polymer rings in strong confinement [37]. Motivated by nanotechnological advances to study polymers in biomimetic systems semiflexible polymers have furthermore been theoretically investigated in channels [38–42] on spherical surfaces [43–46] and on two-dimensional (2D) planes [47,48]. Concerning equilibrium properties it is usually the most likely polymer conformation that is relevant for biological processes and nanotechnological applications.

Polymer configuration and form are well accessible by shape parameters based on the radius of gyration tensor  $Q$ , given by

$$Q_{ij} = \frac{1}{L} \int_0^L ds \mathbf{r}_i(s) \mathbf{r}_j(s) - \frac{1}{L^2} \int_0^L ds \mathbf{r}_i(s) \int_0^L ds' \mathbf{r}_j(s'). \quad (2)$$

The eigenvalues  $\lambda_i$  and the direction of the eigenvectors  $\Lambda_i$ ,  $i=1,2,3$ , of the radius of gyration tensor determine the spatial extent of a polymer in space. The degree of asymmetry, denoted asphericity  $\Delta$ , is proportional to the normalized variance of the eigenvalues  $\lambda_i$  of  $Q$  [49],

$$\Delta = \frac{\sum_{i=1}^3 [\lambda_i - \bar{\lambda}]^2}{2 \left( \sum_{i=1}^3 \lambda_i \right)^2}, \quad (3)$$

where  $\bar{\lambda} = \sum_{i=1}^3 \lambda_i / 3$  denotes the mean extent. While a spherical symmetric object with  $\lambda_i = \bar{\lambda}$  is characterized by the minimal value of the asphericity  $\Delta=0$ , a spherical asymmetric rodlike object is represented by its maximal value  $\Delta=1$ . To measure the degree of prolateness or oblateness of an object, the nature of asphericity  $\Sigma$  is defined by [50]:

$$\Sigma = \frac{4(\lambda_1 - \bar{\lambda})(\lambda_2 - \bar{\lambda})(\lambda_3 - \bar{\lambda})}{\left( \frac{2}{3} \sum_{i=1}^3 [\lambda_i - \bar{\lambda}]^2 \right)^{3/2}}. \quad (4)$$

The sign of the nature of asphericity is determined by the product of the deviations of the eigenvalues from their mean and is negative for oblate objects and positive for prolate ones. Ranging from  $\Sigma=-1$  to  $\Sigma=1$  the minimal value of the nature of asphericity is attributed to a fully oblate object such as a disk, while the maximal one is assigned to a fully prolate one such as a rigid rod.

We use these shape measures to investigate the form of stiff polymer rings in weak spherical confinement imposed by an impenetrable shell. Employing both Monte Carlo simulations and analytical calculations we discern elastic and entropic contributions and faithfully describe the dominant polymer conformation depending on polymer flexibility. In Sec. II we develop an analytic argument for the trajectory of the dominant polymer conformation considering both entropic and elastic effects. In Sec. III we assess polymer configurations in spherical confinement over ranges of flexibili-

ties by simulation generated probability densities. Finally, we compare asphericity and nature of asphericity calculated from our analytic argument to their mean values obtained from simulations in Sec. IV. In the desired stiff regime our analytic argument explains the observed polymer configurations for any weak spherical confinement. We conclude in Sec. V.

## II. BUCKLING OF AN ELASTIC ELLIPSE

To understand the form of polymer rings in spherical confinement it is insightful to have a description of the mean polymer conformation. As the distribution of stiff polymer configurations is indeed sharply centered around the mean, we develop an analytic argument for the space curve of this dominant polymer configuration depending on the strength of the confinement and polymer flexibility. Based on this dominant space curve (DSC) the governing polymer form can be understood and assessed by calculating its shape parameters. The successful mapping between DSC and simulation results then also ascertains our fruitful insights into the whole polymer configuration. The DSC of a fluctuating stiff polymer ring arises from the interplay of elastic and entropic forces. We analyze their influence subsequently. To derive the DSC of a stiff semiflexible polymer ring in weak confinement it is instructive to consider first the DSC of an unconfined polymer ring.

A completely rigid polymer ring of contour radius  $R_c$  is circular. Subjected to thermal fluctuations, it assumes the shape of a planar ellipse [51], the conformation induced by the first bending mode. Increasing flexibility enhances the eccentricity of the ellipse within the stiff regime. While the major axis of the ellipse grows, the minor axis decreases with the square root of the flexibility  $\sqrt{L/l_p}$  [13–15]. As spherical symmetry is broken, this change in shape yields an increase of entropy and, hence, minimizes the free energy. Thus the DSC of the planar stiff polymer ring can be parameterized by

$$\begin{aligned} x(s) &= R_c \left( 1 - \gamma \sqrt{\frac{L}{l_p}} \right) \sin\left(\frac{s}{R_c}\right), \\ y(s) &= R_c \left( 1 + \gamma \sqrt{\frac{L}{l_p}} \right) \cos\left(\frac{s}{R_c}\right), \\ z(s) &= 0, \end{aligned} \quad (5)$$

where  $s/R_c \in [0, 2\pi]$  here represents the polar angle of the trajectory and  $\gamma$  denotes a dimensionless parameter that measures the influence of flexibility. The DSC describes a polymer ring that is deformed from an oblate circle to a more and more eccentric ellipse as the flexibility increases. During this growth of eccentricity the total length of the space curve is not conserved, hence, the model does not predict the overall size of a polymer. This caveat does, however, not prevent successful predictions of the shape parameters. As length-invariant measures the asphericity and the nature of asphericity are only affected by the aspect ratio of the axes. In summary, the elliptical form of a free polymer is an entropic



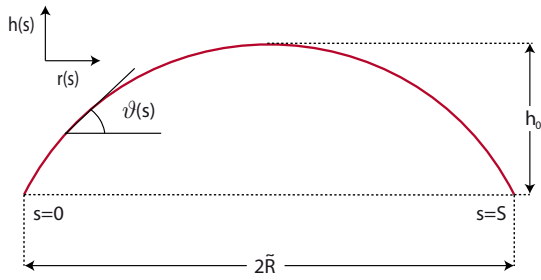


FIG. 2. (Color online) Buckled rod of length  $S$  with maximal height  $h_0$ . The distance between its hinged ends  $2\tilde{R}$  determines the rod trajectory parameterized by  $\vartheta(s)$ ,  $s \in [0, S]$  and the maximal height  $h_0$ .

effect that can, however, be translated into an elastic response in confinement.

Confining a stiff polymer ring inside an impenetrable sphere induces a change in its shape. If the major axis of length  $S=2R_c(1+\gamma\sqrt{L/l_p})$  exceeds the diameter of the sphere  $2R$ , no planar ellipse can develop inside a sphere. Instead the major axis and therefore the whole polymer ring is compressed by the rigid confining walls of the sphere into a curved bananalike ellipse as shown in Fig. 1. This elastic response of the stiff polymer ring to the confinement results in a  $z$  component of the DSC. This additional component generates a bananalike polymer ring that can be computed by drawing the analogy to the buckling of an elastic rod.

The conformation of a rod of length  $S$  pushing against rigid walls a distance  $2\tilde{R}$  apart is equivalent to the shape of a rod of length  $S$  being compressed by a constant force  $f$  at its hinged ends. As illustrated in Fig. 2, the configuration of a buckled rod of length  $S$  can be parameterized by the angle  $\vartheta(s)$  between the tangent vector  $\mathbf{t}(s)$  and the direction  $\hat{\mathbf{r}}$  parallel to the compressing force, where the arc length  $s$  runs from 0 to the length  $S$  of the rod. Note, that the rod can rotate and move freely perpendicular to the axis of the force. Reflecting the mirror symmetry of the conformation, the absolute value of the angles at both ends of the rod is equal:  $\vartheta(0) \equiv \vartheta_0 = -\vartheta(S)$ . Euler-Lagrange theory predicts the optimal shape of a compressed rod as the state of minimal elastic energy. The compressive force  $f$  adds a potential term to the bending energy of an elastic rod [52],

$$\mathcal{H} = \int_0^S ds \left\{ k_b T \frac{l_p}{2} \left[ \frac{d\vartheta(s)}{ds} \right]^2 - f \cos[\vartheta(s)] \right\}, \quad (6)$$

where we already replaced the bending modulus by its relation to the polymer specific persistence length. As shown in Ref. [53] the minimization of the above elastic energy Eq. (6) under the given constraints results in a Euler-Lagrange equation. The minimizing two-dimensional space curve describing the optimal filament shape is then given by its component  $r(s)$  along the direction of the force and the component  $h(s)$  perpendicular to it, see Fig. 2,

$$r(s) = -s + \frac{S}{2} + \frac{S}{K(\sigma)} E \left[ \left( \frac{2s-S}{S} \right) K(\sigma^2), \sigma^2 \right],$$

$$h(s) = \frac{S\sigma}{K(\sigma^2)} \left\{ 1 - \text{cn} \left[ \left( \frac{2s-S}{S} \right) K(\sigma^2), \sigma^2 \right] \right\}, \quad (7)$$

where  $\sigma$  denotes  $\sin(\vartheta_0/2)$  and  $K$ ,  $E$ , and  $\text{cn}$  are the elliptic integral of the first and second kind and the Jacobi elliptic function, respectively. When the spatial constraint  $r(0)-r(S)=2\tilde{R}$  is respected and the elliptic integrals are expanded for small opening angles  $\vartheta_0$ , the maximal height  $h_0=|h(S/2)-h(0)|$  depends on the distance between the confining walls  $2\tilde{R}$  and the length of the elastic rod  $S$  only,

$$h_0(S, \tilde{R}) \approx \frac{2}{\pi} S \sqrt{2 \left( 1 - \frac{2\tilde{R}}{S} \right)}, \quad (8)$$

see Fig. 2. Based on this result the  $z$  component of the DSC due to elastic forces can be predicted. Respecting the differential continuity of a buckled ellipse the height modulation function is taken to be a squared sine resulting in the following  $z$  component for the DSC in confinement

$$z(s) = h_0(S, \tilde{R}) \sin^2 \left( \frac{s}{R_c} \right). \quad (9)$$

In addition to the elastic response due to compression also entropic forces contribute to the DSC of a spherically confined polymer ring. For simplicity, we first assume the confining sphere to be of the same radius  $R=R_c$  as the contour radius of the confined polymer ring. In this case any finite temperature causes the major axis of the ensuing ellipse to exceed with its apices the spherical confinement and, hence, forces the polymer to buckle. The elastic bending energy would be smallest if the ellipse's apices both rest on an equatorial plane. Namely, such a configuration maximizes the distance between the apices and, hence, minimizes the curvature of the state. Disregarding rotational symmetry, there is only a single equatorial plane. However, entropy increases if the apices may rest on any plane instead of just a single equatorial plane. This increase in entropy clearly goes at the expense of stronger bending. Therefore, the magnitude in deviation from the equatorial plane should be related to polymer flexibility. As a good estimate we take the DSC of a polymer ring to nestle half its total height  $h_0(S, \tilde{R})$  below an equatorial plane and the other half above. Employing Pythagoras law the total length of the major axis is then confined to  $\sqrt{R^2 - (h_0/2)^2}$ . Hence, the  $y$ -component of the DSC follows as

$$y(s) = \sqrt{R^2 - (h_0/2)^2} \cos \left( \frac{s}{R_c} \right). \quad (10)$$

Surely, this nestling below the equatorial plane has also an effect on the buckling height itself, but it is only of second order and, therefore, neglected in the following.

The above equations for the polymer ring's DSC already allow a successful prediction of the mean shape of a polymer ring when the confining radius equals the contour radius  $R=R_c$ . Next our analysis is extended to larger radii to enable

a full description for any kind of confining radius between  $R=R_c$  and  $R=\infty$ . At small flexibilities the DSC of a polymer ring is not supposed to be affected by spherical confinement. As the major axis of the ensuing ellipse does not yet stretch beyond the confining walls, a planar ellipse forms as described by Eq. (5). Intuitively one would guess that confinement effects become noticeable once the length of the DSC's major ellipse equals the radius of the sphere  $R_c(1+\gamma\sqrt{L/l_p})=R$ . However, the broadness of the distribution of states makes confinement affect the DSC even before the major vertices of the DSC's planar ellipse encounter the sphere's shell. So far our considerations only described the DSC as the mean space curve irrespective of the broadness of the distribution of states. However, the fraction of configurations with longer major axis forces the DSC to buckle at lower flexibilities than expected. This results in an effectively reduced radius of the sphere, which we account for by choosing  $\tilde{R}=R-(1-\alpha)(R-R_c)$ . For the lower limiting case  $\alpha=0$  the effective confinement  $\tilde{R}=R_c$  instantaneously affects the DSC irrespective of the true radius  $R$ , while for the upper limiting case  $\alpha=1$  only the encounter of the DSC major axis with the real confinement  $\tilde{R}=R$  causes an elastic response. Hence,  $\alpha$  denotes the percentage of how much below the real confinement radius  $R$  statistically confinement affects the DSC.  $\alpha$  is like  $\gamma$  a numerical parameter to be determined from simulation data.

Together these two entropic effects and the elastic buckling determine the DSC of a polymer ring of contour radius  $R_c$  in spherical confinement of radius  $R\geq R_c$ . For small flexibilities a planar ellipse develops described by Eq. (5), that is unaffected by the confinement. This regime extends up to  $R_c(1+\gamma\sqrt{L/l_p})\leq R-(1-\alpha)(R-R_c)$ . For larger flexibilities this inequality topples over  $R_c(1+\gamma\sqrt{L/l_p})>R-(1-\alpha)(R-R_c)$  and the DSC is described by

$$\begin{aligned}
 x(s) &= R_c \left( 1 - \gamma \sqrt{\frac{L}{l_p}} \right) \sin\left(\frac{s}{R_c}\right), \\
 y(s) &= R_c \sqrt{\frac{R^2}{R_c^2} - \frac{8}{\pi^2} \left( 1 + \gamma \sqrt{\frac{L}{l_p}} \right) \left( \alpha \left( 1 - \frac{R}{R_c} \right) + \gamma \sqrt{\frac{L}{l_p}} \right)} \\
 &\quad \times \cos\left(\frac{s}{R_c}\right), \\
 z(s) &= \frac{4\sqrt{2}}{\pi} R_c \sqrt{\left( 1 + \gamma \sqrt{\frac{L}{l_p}} \right) \left( \alpha \left( 1 - \frac{R}{R_c} \right) + \gamma \sqrt{\frac{L}{l_p}} \right)} \\
 &\quad \times \sin^2\left(\frac{s}{R_c}\right). \tag{11}
 \end{aligned}$$

Based on this analytic argument for the DSC of a stiff polymer ring the corresponding shape parameters can be calculated and compared to results from Monte Carlo simulations. Qualitative accordance with our assumptions for the elastic and entropic forces is gained from projections of polymer configurations into two-dimensional planes.

### III. 2D PROJECTIONS OF POLYMER CONFIGURATIONS

A discretization of the space curve of the polymer ring enables Monte Carlo simulations, which open insights into the governing conformations of polymer rings at different flexibilities. To simulate a polymer ring of circumference  $L$  the Metropolis Monte Carlo method has been employed. The polymer ring is modeled as a discrete polygon, that consists of  $N$  segments of fixed length  $l$  pointing in the direction  $\mathbf{t}$ . The elastic energy of a single conformation depends on the direction between successive segments:  $\mathcal{H}=Nk_bT(l_p/L)\sum_{i=1}^N(1-\mathbf{t}_i\cdot\mathbf{t}_{i+1})$ , where the closure of the ring is implemented by periodic boundary conditions  $\mathbf{t}_1=\mathbf{t}_{N+1}$ . The polymer ring moves through phase space by performing crankshaft moves, restricted by the spherical confinement: Only configurations, which are located entirely inside the rigid walls of the sphere, are considered for averaging. To collect uncorrelated data, only every  $10^5$ th of those configurations is considered. We sample  $10^5$  configurations for each averaged data point, such that the statistical error lies within the ranges of the symbols depicted in our graphs.

To illustrate the form of the polymer rings of radius  $R_c$  in spheres with  $R=R_c$  at different flexibilities, the probability density of polymer configurations are shown in Fig. 3. The position vectors of all samples of polymer configurations are mapped on two-dimensional planes spanned by two principal axes of the radius of gyration tensor in Eq. (2), respectively. Ordering the principal axes  $\Lambda_i$ ,  $i=1,2,3$ , by the magnitude of their corresponding eigenvalues the largest axis  $\Lambda_1$  is taken as reference axis, and the planes spanned together with the intermediate  $\Lambda_2$  and the smallest axis  $\Lambda_3$  are considered, respectively, to gain insight into the three-dimensional configuration space. Considering a planar ellipse that buckles due to confinement as discussed in Sec. II, the plane spanned by the two largest eigenvalues represents the planar ellipse and the plane spanned by the smallest and the largest principal axis corresponds to the height of the buckling polymer relative to the major axis.

The probability density of polymer configurations in the plane spanned by the largest and the intermediate principal axis in Figs. 3(A)–3(C) reveals the elliptical character of the mean shape of the polymer ring. At small flexibilities, Figs. 3(A) and 3(B), the polymer trajectories are confined to a narrow rim close to the spherical shell that broadens with increasing flexibility. With growing undulations along the polymer their intermediate axis shortens stronger than the larger one. Hence, polymer configurations resembling an ellipse with higher eccentricity become more probable. Beyond the stiff regime at large flexibilities, Fig. 3(C), the polymer ring exhibits compact configurations and looses the character of a planar ellipse. In this semiflexible region, the polymer configurations take a figure-eight shape as indicated by the two yellow semicircles in Fig. 3(C). Due to entropic reasons the eight consists of two circles with different sizes for each single polymer configuration [54], therefore, the density distribution is smoothed out in the overlap region of the figure-eight. In the flexible regime, the principal axes shrink further with growing flexibility (data not shown). However, their ratio remains asymmetric to maximize entropy [55].

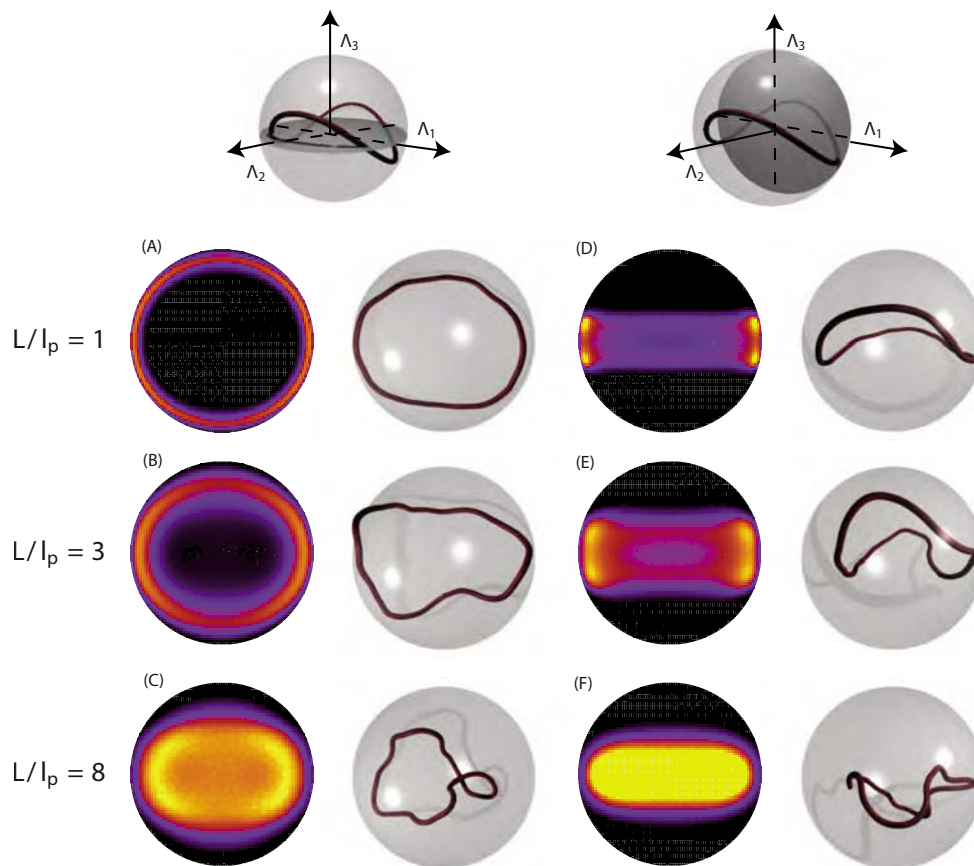


FIG. 3. (Color online) Probability density and representative snapshots of polymer rings from Monte Carlo simulation data for the flexibilities  $L/l_p=1, 3$  and  $8$ . As indicated by the cartoons on top, the polymer configurations in the first column (A–C) are projected onto the plane spanned by the intermediate  $\Lambda_2$  and the largest principal axis  $\Lambda_1$ . In the second column polymer configurations (D–F) are projected onto the plane spanned by the smallest  $\Lambda_3$  and the largest principal axis  $\Lambda_1$ . The gradient in the density of states from high to low is color coded from bright (yellow) to dark (black), the absolute scale of the probability density halves starting from  $0.0016$  onward as the flexibility increases. The snapshots are chosen such that their asphericity matches the mean configuration of the observed ensemble.

Studying the density distribution in the plane spanned by the largest and the smallest principal axis we observe bone-shaped probability densities of polymer configurations, see Figs. 3(D) and 3(E). In these projections the density peaks close to the sphere's rim indicate the position, where the elliptically shaped polymer configurations encounter the sphere's shell relative to the equatorial plane. While the largest and intermediate principal axis of the elliptically shaped polymer rings in the stiff regime map onto the major and minor axis of a buckling ellipse, the smallest principal axis points toward the height of the buckling ellipse. Hence, the width of the probability density along the  $\Lambda_3$  axis in Figs. 3(D) and 3(E) indicates the maximal buckling height, which in the stiff regime is growing with increasing flexibility. An entirely rigid circular polymer ring would be located in the equatorial plane. With growing flexibility thermal fluctuations force the ensuing ellipse to arch out of the horizontal equatorial plane, forming a bend. Thereby, the major axis of the elliptical polymer ring is clamped below or above the equatorial plane. The position of the ellipses' apices, which pushes against the confining sphere, is marked by the density peaks in the bone-shaped density distribution. The movement of apices' positions away from the equatorial plane with in-

creasing flexibility is an entropic effect taken into account in our analytic argument in Eq. (11). Beyond the stiff regime, undulations contract the polymers to a degree that they are no longer forced to undergo Euler buckling but form more and more crumpled configurations also diminishing the polymers' extent along the smallest principal axis.

The entropic and elastic effects observed in the density distributions are in agreement with the analytic argument presented in Sec. II. To substantiate these qualitative observations, the observed shapes of polymer rings at different flexibilities in spherical confinement are quantified by the asphericity and the nature of asphericity.

#### IV. SHAPES IN SPHERICAL CONFINEMENT

The shape of polymer rings is best captured by the asphericity and the nature of asphericity as measures of the extent of asymmetry and the degree of prolateness and oblateness, respectively. Comparing the mean values of these shape parameters for free and confined polymer rings displays the dramatic changes in polymer shape due to weak confinement, as shown in Fig. 4. Based on our analytic description for the dominant space curve (DSC) the shapes of polymer

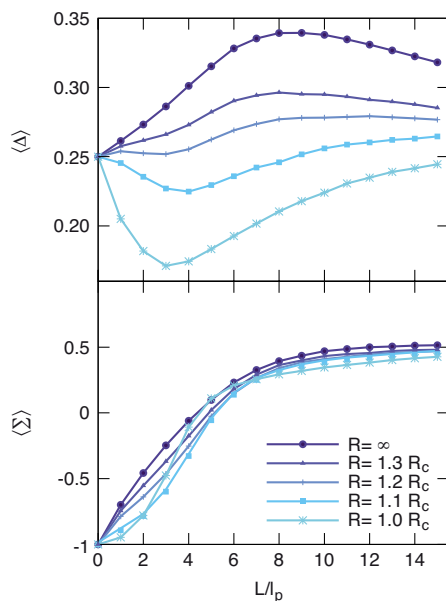


FIG. 4. (Color online) Monte Carlo simulation data for the mean asphericity  $\langle \Delta \rangle$  and the mean nature of asphericity  $\langle \Sigma \rangle$  versus flexibility  $L/l_p$  for polymer rings of contour radius  $R_c$ , that are confined by impenetrable spheres of radii  $R=1.0R_c$  to  $R=\infty$ . Relatively weak confinement already induces dramatic changes in the shape of polymer rings.

rings are rationalized, and by calculating exact values for shape parameters of the DSC we now show that our analytic argument is in agreement with the corresponding Monte Carlo data in the stiff limit, see Fig. 5.

Starting from  $\Delta=0.25$  and  $\Sigma=-1$  for a rigid ring the mean asphericity  $\langle \Delta \rangle$  and the mean nature of asphericity  $\langle \Sigma \rangle$  of a free polymer ring first grow linearly with flexibility  $L/l_p$  in the stiff regime due to the increase of the eccentricity of the ensuing planar ellipse [51], see Fig. 4. In the semiflexible regime, the free polymer evolves into three-dimensional configurations and undulations lead to crumpling that decreases the variance in spatial extent. Thereby, the mean asphericity finally decays to the exact value for an infinitely flexible closed Gaussian chain of  $\langle \Delta \rangle=0.2464$  [56]. In the course of this transition the polymer form saturates to a prolate, hence,

cigarlike shape. In contrast, spherical confinement that is small enough to clamp the largest axis of a polymer ring provokes the mean asphericity to decline in the stiff regime. Only beyond the stiff regime the mean asphericity is observed to grow with increasing flexibility slowly approaching the value of a free polymer ring. Also the linear increase of the mean nature of asphericity  $\langle \Sigma \rangle$  of a free polymer in the stiff limit is modified by the confinement and results in a sigmoidal curve progression toward the plateau in the flexible regime.

The decrease in the mean asphericity for confined polymer rings sets in as the ensuing planar ellipse is restricted by the confining shell and buckles into the third dimension. As the major axis of the polymer increases with flexibility, the buckled polymer conformation gains height and, therefore, loses asphericity. This process progresses up to flexibilities of  $L/l_p \approx 3$ . This marks the end of the stiff regime defined by an elastic buckling. The nature of asphericity displays that in the stiff regime the cigarlike character of the free polymer rings is suppressed by the confinement in favor of more oblate conformations. The inflection point of the mean nature of asphericity reflects the minimum of the asphericity. Increasing the size of the spherical confinement from  $R=1.0R_c$  to  $R=1.3R_c$  reduces the absolute change in asphericity compared to the free polymer case. With weaker confinement the onset of the decline of the asphericity is shifted to larger values of flexibility, as the ensuing planar ellipse encounters the shell only at higher flexibilities. As the distribution of polymer extents is broadening with increasing flexibilities this transition is smoothed out more if the buckling sets in at higher flexibilities. Also the character of the nature of asphericity changes at the transition, as clearly shown by the Monte Carlo data in Fig. 5. If the extension of the polymer rings is smaller than the diameter, the nature of asphericity grows linearly. Its sigmoidal character commences at the transition to buckling.

Beyond the stiff regime,  $L/l_p > 3$ , undulations start contracting the buckled ellipse inducing crumpling to increasingly compact configurations. Thereby, the polymer configurations become less affected by their confinement and both shape measures increase toward the value of unconfined polymer rings. However, over the range of flexibilities observed, even the values in the flexible regime remain distinct.

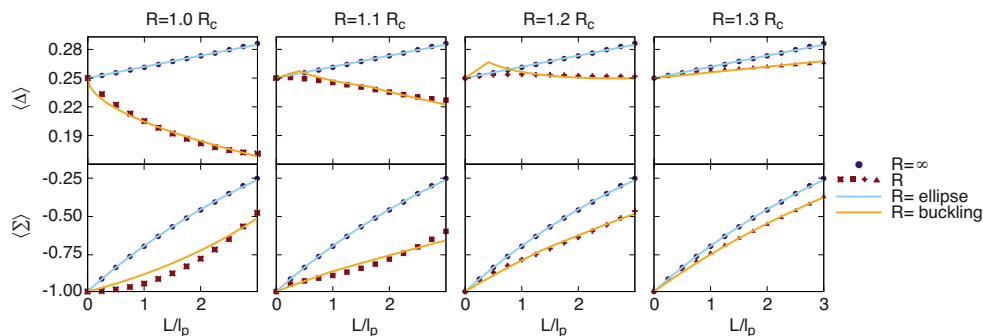


FIG. 5. (Color online) Comparison of the mean asphericity  $\langle \Delta \rangle$  and mean nature of asphericity  $\langle \Sigma \rangle$  versus flexibility  $L/l_p$  calculated from our analytical description in Eqs. (5) and (11) (light colors) and from Monte Carlo simulation data (dark symbols) for polymer rings of contour radius  $R_c$  inside spheres of radii  $R=1.0R_c$  to  $1.3R_c$  (lower red series). For reference data and analytical predictions for a free polymer ring are displayed in each diagram as well (upper blue series).

Although the majority of polymer conformations is coiled up within the sphere, very elongated configurations are still discarded and the mean values differ from the unconfined case.

Apart from these qualitative considerations on polymer shape our analytical predictions for the dominant space curve (DSC) in Sec. II can be quantitatively assessed by comparison to the shape parameters asphericity and nature of asphericity. Our predictions for the shape parameters depend on two parameters,  $\gamma$  and  $\alpha$ , as given by Eqs. (5) and (11); in the case of  $R=R_c$  only a single parameter  $\gamma$  is needed, as  $\alpha=0$  by definition. The results shown in Fig. 5 are obtained by fitting the parameters  $\gamma$  [57] and  $\alpha$  [58] to both observables for all degrees of confinement. Different values for  $\gamma$  are obtained for the asphericity and the nature of asphericity. Such as the mean asphericity represents the average shape of all polymer configurations such does the fitted parameter  $\gamma$  only reflect an average of a whole distribution of parameters. Now both asphericity and nature of asphericity have differently shaped, broad and highly skewed distributions. Therefore, the different results for the fitted  $\gamma$  reflect only a range of possible values. However, the fit to the stronger peaked asphericity may resemble the average growth with flexibility sufficiently well. Altogether, the fitted curve for the DSC of polymer rings in spheres with radius  $R=1.0R_c$  and  $R=1.3R_c$  is in good agreement with the simulation results. As our analytical argument does not capture the distribution of states, the smooth transition from planar to buckled ellipses for  $R \gg R_c$  shows deviations. There, our argument exaggerates the transition in a kink for  $R=1.1R_c$  and  $R=1.2R_c$ . Confirming the quality of our DSC prediction the analytic argument for the nature of asphericity even forecasts its sigmoidal character. In the range between  $R=1.1R_c$  and  $R=1.3R_c$  the transition is again not fully captured due to the broad distribution of states, however, the dominant character of the nature of asphericity is well reflected. Based on our fitted parameters the magnitude of all three principal axes of the DSC can be calculated for all flexibilities up to  $L/l_p=3$ . Having two different parameters sets at hand only an estimate of the magnitude is accessible. Recalling that we attribute the fitting results for the stronger peaked asphericity a better representation of all possible polymer states, we employ this value of  $\gamma$  to predict for example for  $R=R_c$  a maximal buckling height at  $L/l_p=3$  of about  $h_0/R_c \approx 0.7$ . If one extends the polymer model to account for further microscopic properties as for instance for torsional stiffness, the maximal buckling height is expected to be smaller since torsional stiffness increases the elastic energy of out-of-plane deformations leaving in-plane bending unaffected. Hence, polymers with noticeable torsional stiffness would form elliptical shapes due to in-plane modes as observed for worm-

like chain polymers and thus be compressed by confining walls, but the resulting buckling would be to less extend.

## V. CONCLUSION

In summary, the shape and conformation of stiff polymer rings of contour radius  $R_c$  in any weak spherical confinement  $R \geq R_c$  imposed by an impenetrable shell has been analyzed for varying flexibility  $L/l_p$ . We find that confining a polymer ring induces buckling due to the polymers elastic properties for finite flexibilities  $L/l_p \lesssim 3$ . We discern elastic and entropic contributions to the form of polymer rings by simulation-derived probability densities and an analytic argument for the dominating polymer trajectory. While the elastic response can be summarized to Euler buckling, the entropic contribution that broadens the number of accessible states, induces three main effects in the stiff regime. First, entropy promotes planar ellipses for any nonzero flexibility, which increase in eccentricity with growing flexibility. If eventually the major axis is compressed by the confining cavity the polymer ring buckles as an elastic response. Here entropy again takes action as it shifts the plane in which the ring is compressed from the energetically favorable equatorial plane to smaller radii. At last, due to the broad distribution of polymer configurations the transition to buckling is premature and smooth. These four effects are sufficient to explain the form of polymer rings in weak spherical confinement as shown by comparison of shape parameters calculated from our analytic description and averaged simulation data.

Our analytic description, hence, gives a faithful representation of stiff polymer ring conformations and the scaling of the principal polymer axes, especially the scaling of the buckling height, with polymer flexibility. As our analytic argument accounts beyond polymer flexibility for different radii of confinement, the dominant polymer conformation is now available for active control by these two experimentally adjustable factors. Employing our results in biomimetic experiments, biological processes, that are strongly dependent on polymer configuration, can be investigated under well-defined conditions. Furthermore, the knowledge of full polymer conformations is one of the first steps to build nanostructures based on biopolymers.

## ACKNOWLEDGMENTS

The financial support of the Deutsche Forschungsgemeinschaft through SFB 863 and of the German Excellence Initiative via the program ‘‘Nanosystems Initiative Munich (NIM)’’ is acknowledged. K.A. also acknowledges funding by the Studienstiftung des deutschen Volkes.

- [1] D. H. Boal, *Mechanics of the Cell* (Cambridge University Press, Cambridge, England, 2002).  
 [2] J. Howard, *Mechanics of Motor Proteins and the Cytoskeleton* (Sinauer Associates, Sunderland, MA, 2001).

- [3] B. van den Broek, M. A. Lomholt, S.-M. J. Kalisch, R. Metzler, and G. J. L. Wuite, *Proc. Natl. Acad. Sci. U.S.A.* **105**, 15738 (2008).  
 [4] M. E. Janson and M. Dogterom, *Phys. Rev. Lett.* **92**, 248101

- (2004).
- [5] F. Pampaloni, G. Lattanzi, A. Jonás, T. Surrey, E. Frey, and E.-L. Florin, *Proc. Natl. Acad. Sci. U.S.A.* **103**, 10248 (2006); K. M. Taute, F. Pampaloni, E. Frey, and E.-L. Florin, *Phys. Rev. Lett.* **100**, 028102 (2008).
- [6] M. C. Choi, C. D. Santangelo, O. Pelletier, J. H. Kim, S. Y. Kwon, Z. Wen, Y. Li, P. A. Pincus, C. R. Safinya, and M. W. Kim, *Macromolecules* **38**, 9882 (2005).
- [7] W. Reisner, K. J. Morton, R. Riehn, Y. M. Wang, Z. Yu, M. Rosen, J. C. Sturm, S. Y. Chou, E. Frey, and R. H. Austin, *Phys. Rev. Lett.* **94**, 196101 (2005).
- [8] S. Köster, J. Kierfeld, and T. Pfohl, *Eur. Phys. J. E* **25**, 439 (2008).
- [9] M. Cosentino Lagomarsino, C. Tanase, J. W. Vos, A. M. C. Emons, B. M. Mulder, and M. Dogterom, *Biophys. J.* **92**, 1046 (2007).
- [10] M. Elbaum, D. Kuchnir Fyngenson, and A. Libchaber, *Phys. Rev. Lett.* **76**, 4078 (1996).
- [11] L. Limozin and E. Sackmann, *Phys. Rev. Lett.* **89**, 168103 (2002).
- [12] M. M. A. E. Claessens, M. Bathe, E. Frey, and A. R. Bausch, *Nature Mater.* **5**, 748 (2006).
- [13] J. Shimada and H. Yamakawa, *Biopolymers* **27**, 657 (1988).
- [14] C. J. Camacho, M. E. Fisher, and R. R. P. Singh, *J. Chem. Phys.* **94**, 5693 (1991).
- [15] T. Odijk, *J. Chem. Phys.* **105**, 1270 (1996).
- [16] S. Panyukov and Y. Rabin, *Phys. Rev. E* **64**, 011909 (2001).
- [17] S. M. Rappaport, Y. Rabin, and A. Y. Grosberg, *J. Phys. A* **39**, L507 (2006).
- [18] K. Alim and E. Frey, *Eur. Phys. J. E* **24**, 185 (2007).
- [19] D. Norouzi, F. Mohammad-Rafiee, and R. Golestanian, *Phys. Rev. Lett.* **101**, 168103 (2008).
- [20] H. Wada, *Eur. Phys. J. E* **28**, 11 (2009).
- [21] B. Alberts, *Molecular Biology of the Cell* (Taylor & Francis, New York, 2010).
- [22] T. Sanchez, I. M. Kulic, and Z. Dogic, *Phys. Rev. Lett.* **104**, 098103 (2010).
- [23] G. Witz, K. Rechenndorff, J. Adamcik, and G. Dietler, *Phys. Rev. Lett.* **101**, 148103 (2008).
- [24] J. X. Tang, J. A. Käs, J. V. Shah, and P. A. Janmey, *Eur. Biophys. J.* **30**, 477 (2001).
- [25] A. W. C. Lau, A. Prasad, and Z. Dogic, *EPL* **87**, 48006 (2009).
- [26] M. Rubinstein and R. H. Colby, *Polymer Physics* (Oxford University Press, Oxford, 2003).
- [27] T. Odijk, *Philos. Trans. R. Soc. London, Ser. A* **362**, 1497 (2004).
- [28] R. Metzler and P. G. Dommersnes, *Eur. Biophys. J.* **33**, 497 (2004).
- [29] E. Katzav, M. Adda-Bedia, and A. Boudaoud, *Proc. Natl. Acad. Sci. U.S.A.* **103**, 18900 (2006).
- [30] T. Sakaue, *Macromolecules* **40**, 5206 (2007).
- [31] G. Morrison and D. Thirumalai, *Phys. Rev. E* **79**, 011924 (2009).
- [32] J. Kindt, S. Tzllil, A. Ben-Shaul, and W. M. Gelbart, *Proc. Natl. Acad. Sci. U.S.A.* **98**, 13671 (2001).
- [33] J. C. LaMarque, T.-V. L. Le, and S. C. Harvey, *Biopolymers* **73**, 348 (2004).
- [34] I. Ali, D. Marenduzzo, and J. M. Yeomans, *Phys. Rev. Lett.* **96**, 208102 (2006).
- [35] S. Jun and B. Mulder, *Proc. Natl. Acad. Sci. U.S.A.* **103**, 12388 (2006).
- [36] A. S. Petrov, M. B. Boz, and S. C. Harvey, *J. Struct. Biol.* **160**, 241 (2007).
- [37] C. Micheletti, D. Marenduzzo, E. Orlandini, and D. W. Summers, *Biophys. J.* **95**, 3591 (2008).
- [38] D. J. Bicout and T. W. Burkhardt, *J. Phys. A* **34**, 5745 (2001).
- [39] F. Wagner, G. Lattanzi, and E. Frey, *Phys. Rev. E* **75**, 050902(R) (2007).
- [40] Y. Yang, T. W. Burkhardt, and G. Gompper, *Phys. Rev. E* **76**, 011804 (2007).
- [41] P. Cifra, *J. Chem. Phys.* **131**, 224903 (2009).
- [42] F. Thüroff, F. Wagner, and E. Frey, e-print arXiv:1002.1826.
- [43] J. J. Cerdà, T. Sintes, and A. Chakrabarti, *Macromolecules* **38**, 1469 (2005).
- [44] C.-H. Lin, Y.-C. Tsai, and C.-K. Hu, *Phys. Rev. E* **75**, 031903 (2007).
- [45] T. Odijk, *Macromolecules* **26**, 6897 (1993).
- [46] A. J. Spakowitz and Z. G. Wang, *Phys. Rev. Lett.* **91**, 166102 (2003).
- [47] Y. Liu and B. Chakraborty, *Phys. Biol.* **5**, 026004 (2008).
- [48] F. Drube, K. Alim, G. Witz, G. Dietler, and E. Frey, *Nano Lett.* **10**, 1445 (2010).
- [49] J. A. Aronovitz and D. R. Nelson, *J. Phys. (Paris)* **47**, 1445 (1986).
- [50] J. W. Cannon, J. A. Aronovitz, and P. Goldbart, *J. Phys. I* **1**, 629 (1991).
- [51] K. Alim and E. Frey, *Phys. Rev. Lett.* **99**, 198102 (2007).
- [52] L. Landau and E. Lifschitz, *Theory of Elasticity* (Pergamon Press, Oxford, 1970).
- [53] N.-K. Lee, A. Johner, and S.-C. Hong, *Eur. Phys. J. E* **24**, 229 (2007).
- [54] R. Metzler, T. Ambjörnsson, A. Hanke, Y. Zhang, and S. Levne, *J. Comput. Theor. Nanosci.* **4**, 1 (2007).
- [55] W. Kuhn, *Kolloid-Z.* **68**, 2 (1934).
- [56] H. W. Diehl and E. Eisenriegler, *J. Phys. A* **22**, L87 (1989).
- [57] asphericity:  $R=1.0R_c$ ,  $\gamma=0.070$ ;  $R=1.1R_c$ ,  $\gamma=0.077$ ;  $R=1.2R_c$ ,  $\gamma=0.117$ ;  $R=1.3R_c$ ,  $\gamma=0.045$ ; nature of asphericity:  $R=1.0R_c$ ,  $\gamma=0.134$ ;  $R=1.1R_c$ ,  $\gamma=0.052$ ;  $R=1.2R_c$ ,  $\gamma=0.065$ ;  $R=1.3R_c$ ,  $\gamma=0.071$ ;
- [58]  $R=1.0R_c$ ,  $\alpha=0.0$ ;  $R=1.1R_c$ ,  $\alpha=0.5$ ;  $R=1.2R_c$ ,  $\alpha=0.375$ ;  $R=1.3R_c$ ,  $\alpha=0.5$ .

# Confinement induces conformational transition of semiflexible polymer rings to figure eight form

Katja Ostermeir,\* Karen Alim,\* and Erwin Frey

Arnold Sommerfeld Center for Theoretical Physics and Center for NanoScience, Department of Physics,  
Ludwig-Maximilians-Universität München, Theresienstraße 37, D-80333 München, Germany<sup>†</sup>

(Dated: April 27, 2010)

Employing Monte Carlo simulations of semiflexible polymer rings in weak spherical confinement a conformational transition to figure eight shaped, writhed configurations is discovered and quantified.

The conformation of biopolymers is an important aspect for their functionality. For DNA, transcription and replication are governed by specific binding of proteins, a mechanism strongly connected to polymer configuration [1, 2]. Furthermore, conformational transitions of cytoskeletal filaments represent small engines [3], an idea that might be transferable to build biomimetic nano-actuators. Both biological processes and technological applications of biopolymers are well-studied in *in vitro* setups. Inevitably and sometimes also desirably accompanied with these experiments is the confinement of polymers, for instance, into channels [4] or micro-chambers [5]. Confinement is an effect that also arises ubiquitously in biological systems due to cellular compartments and bacterial or viral envelopes. Indeed, confinement affects polymer conformation and induces conformational transitions as shown by the present work concerning semiflexible polymer rings. As an omnipresent form for DNA [6] and as a new nano-biomaterial building block [7, 8], semiflexible polymer rings are recently an object of growing interest. Especially biopolymer's resistance against bending on length scales of their persistence length  $l_p$ , their semiflexibility, turns them into an interesting material, as the degree of overall bending can be tuned by changing their absolute length  $L$ . The internal structure of polymers can be well characterized by the “self-crossing number”, the writhe [9, 10] or by correlation functions along the polymer backbone [11]. Thus, we can assess conformational transitions due to confinement.

In this work we investigate the internal structure of semiflexible polymer rings in spherical confinement established by an impenetrable shell. Employing Monte Carlo simulations we compare unconfined polymer rings and polymer rings restricted by different degrees of spherical confinement over the full range of flexibilities. A conformational transition is observed to arise in the semiflexible regime within weak confinement, non-existing in the stiff regime; the mean absolute writhe exhibits a sharp growth to up to two and a half times the unconstrained value. Evaluation of the writhe distribution for different flexibilities reveals from the semiflexible regime onwards a tremendous increase of polymer configura-

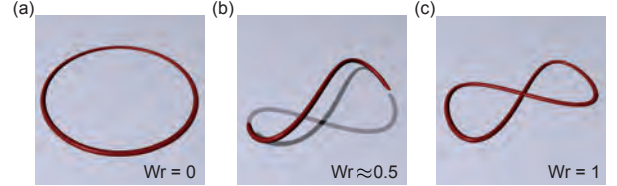


FIG. 1: Writhe of exemplary polymer ring conformations. (a) When no angular perspective reveals any self-crossings as for a fully symmetric ring the writhe is zero. (b) Writhing occurs when for example an ellipse is twined about itself, here to the degree of  $Wr \approx 0.5$ . (c) A point of self-intersection increases the writhe by one as in the case of this planar figure eight shaped trajectory.

tions with writhing numbers specifically centered around  $|Wr| = 0.8$  within confinement. Finally, the tangent-tangent correlation discloses the conformational transition to figure eight shaped polymer rings due to spherical confinement.

Semiflexible polymers are well described as a concatenated chain of  $N$  segments, with tangent vector  $\mathbf{t}$ , where the range of the angle between successive bonds is narrowed by the elastic bending energy  $E = Nk_bT(l_p/L) \sum_{i=0}^N (1 - \mathbf{t}_i \mathbf{t}_{i+1})$  in the worm-like chain model [12]. The flexibility  $L/l_p$  therein determines the stiffness against bending undulations provoked by thermal energy  $k_B T$ . A polymer ring is considered stiff, *i.e.*, dominated by elastic forces, for flexibilities up to  $L/l_p \approx 5$  [8, 13], beyond semiflexible behavior smoothly crosses over into the entropic, flexible regime for large  $L/l_p$ . Polymer conformations are investigated by a Metropolis Monte Carlo simulation, where successive configurations of a closed polygon are generated by crankshaft moves. To collect uncorrelated data only every  $10^5$ th of successive configurations is considered. Polymer conformations that violate the spherical confinement are excluded when sampling a set of  $10^5$  uncorrelated polymer configurations. The statistical error of these ensembles lies within the ranges of the symbols of all data shown.

The internal structure of polymers can be assessed by the correlation of two tangent vectors separated a distance  $s \in [0, L]$  along the polymer backbone  $\langle \mathbf{t}(s) \mathbf{t}(0) \rangle$ . This observable provides details about the relative orientation of the whole contour line of a polymer, however, it fails to reflect the position of polymer segments with

\*Authors contributed equally.

<sup>†</sup>Electronic address: frey@lmu.de

regard to each other in space. This aspect is considered by the writhe  $Wr$  [14], which measures the degree of coiling of a polymer by counting the number of crossings of the polymer with its own axis. Projecting a three-dimensional polymer trajectory into a plane defined by a normal vector  $\mathbf{n}$  results in a two-dimensional curve, which may exhibit crossings. Counting these crossings with  $\pm 1$  according to their handedness and averaging the number of crossings over all angular perspectives given by all possible normal vectors  $\mathbf{n}$  defines the writhe  $Wr$  of the three-dimensional trajectory. Hence, a two dimensional curve always exhibits integer writhing numbers, *i.e.*,  $Wr = 0$  for a circle and  $Wr = 1$  for a figure eight shaped trajectory, while three dimensional objects in general are characterized by a real number as shown in Fig. 1. As only the orientation in which a trajectory is traced decides if the writhe is positive or negative, any writhe distribution is symmetric about the origin with the mean writhe being equal to zero. Insights are therefore gained when measuring the mean absolute writhe  $\langle |Wr| \rangle$  of a writhe distribution. To calculate the writhe of polymer configurations generated by Monte Carlo simulations we follow Klenin and Langowski [15]. Originally, the writhe has been employed to characterize the supercoiled state of nicked DNA [16, 17], recently, it has been extended as a measure for the increased complexity of random polygons due to knotting in strong confinement [18]. Our work considers non-nicked, *i.e.*, zero linking number, polymer rings in the semiflexible regime, where knotting is prevented by high bending energy cost. In addition, the confinement imposed in our study is very weak: The radius  $R$  of the restricting sphere is greater or equal than the contour radius  $R_c = L/2\pi$  of the polymer's corresponding rigid ring. Thus, the writhe is expected to reflect only the increase in undulations by a linear growth with flexibility  $L/l_p$ , as predicted for stiff, unconfined polymer rings [19, 20].

Despite the weak confinement considered, the mean absolute writhe of semiflexible polymer rings displays a strong increase proportional to the degree of confinement for flexibilities  $L/l_p > 4$  as shown in Fig. 2. The mean writhe grows roughly linearly for stiff, unconfined polymer rings [23] in agreement with previous considerations [19, 20]. Irrespective of the degree of confinement all curves collapse on the unconfined state in the very stiff regime up to  $L/l_p \approx 3$ . From there on the curves of confined polymer rings start to deviate from the unconstrained case, with strongest confinement rising first. The increase in writhe is very sharp and only saturates on an almost linear growth for higher flexibilities. Towards even higher flexibility we expect the absolute writhe to grow with the square root of polymer length  $\sqrt{L}$  as found for the flexible limit of random polygons in spherical confinement [21]. The deviation in mean absolute writhe between the different degrees of confinement decreases slightly with growing flexibility.

To understand the sharp increase in mean absolute writhe for confined polymer rings we compare the full

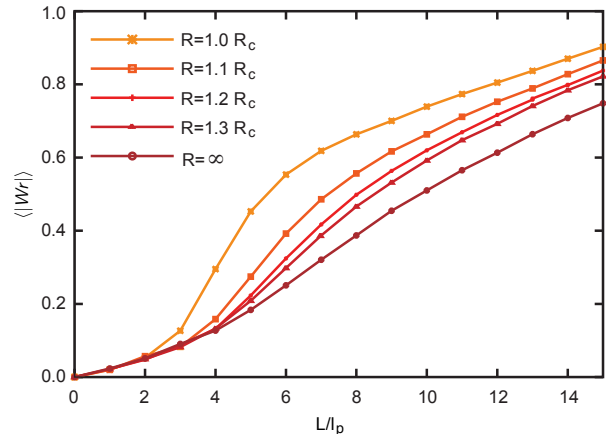


FIG. 2: Mean absolute writhe versus flexibility  $L/l_p$  for unconfined polymer rings  $R = \infty$  and polymer rings in weak spherical confinement  $R = 1.3R_c, \dots, 1.0R_c$  of the order of the extent of the polymer's corresponding rigid ring  $R_c = L/2\pi$ . From flexibilities of about  $L/l_p \approx 4$  onwards the confinement induces a sharp increase in absolute writhe proportional to the degree of confinement.

distribution of the absolute writhe in both extreme cases considered, unconfined and spherical confinement with radius  $R = R_c$  as shown in Fig. 3. The writhe distribution of a free semiflexible polymer ring is monotonically decaying from  $Wr = 0$  continuously spreading out with increasing flexibility [19].

In contrast, the writhe distribution of a confined polymer ring displays a very different behavior. While the writhe distributions decay from  $Wr = 0$  in the stiff limit like in the unconfined case, the distributions from  $L/l_p \approx 3$  onwards become bimodal exhibiting a second maximum at  $|Wr| = 0.8$ . This maximum gains statistical weight at the expense of the first at  $Wr = 0$  as flexibility grows. At sufficiently high flexibilities both maxima have spread out so much that they overlap to form a plateau that extends up to the maximum at  $|Wr| = 0.8$  before the writhe distribution decays for large absolute writhe. These qualitative observations can also be quantified by extracting the contributing polymer configurations as shown in Fig. 4. Assuming that free  $P_\infty(|Wr|)$  and confined  $P_{R_c}(|Wr|)$  polymer ensembles show the same decay from  $Wr = 0$ , the contributing configurations from this decay can be subtracted from the full absolute writhe distribution of confined polymer rings by  $P_{R_c}(|Wr|) - \frac{P_{R_c}(0)}{P_\infty(0)} P_\infty(|Wr|)$ . This discloses the underlying contributing polymer conformations, in particular a distribution centered around  $\langle |Wr| \rangle = 0.8$  that is well approximated by a Gaussian  $\mathcal{N}(\mu, \sigma^2)$ . Table I displays for different flexibilities the total number of configurations and the variance of the Gaussian distribution that was fitted to extract this information from the data. In addition, at lower absolute writhe Gaussian shaped distributions are observed centered around  $\langle |Wr| \rangle = 0.17$  for  $L/l_p = 3$  then shifting to  $\langle |Wr| \rangle = 0.23$  for  $L/l_p = 4$  and  $\langle |Wr| \rangle = 0.3$  for



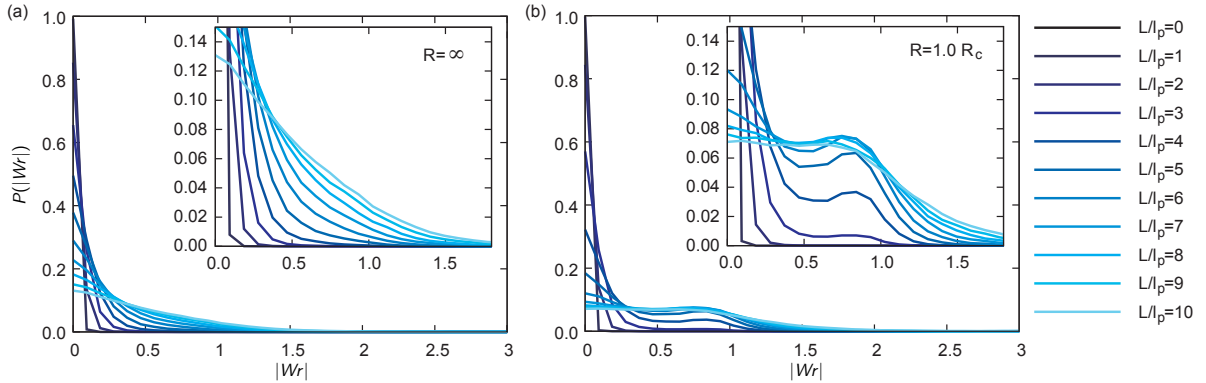


FIG. 3: Distribution of the absolute writhe for an unconfined polymer ring (a) and a polymer ring within weak spherical confinement of radius  $R = R_c$  (b). Displayed are integer flexibilities from  $L/l_p = 1$  to  $L/l_p = 10$ . The writhe distribution is a monotonically decaying function of the absolute writhe for unconfined semiflexible polymer rings. In contrast, in spherical confinement polymers becomes bimodal by developing in addition to the maximum at  $Wr = 0$  a well visible local maximum around  $|Wr| = 0.8$  from  $L/l_p \approx 3$  onwards. For sufficiently high flexibilities the two maxima overlap to form a plateau extending up to  $|Wr| = 0.8$ .

$4 < L/l_p \leq 6$ . Their percentage amounts at most to 20% and decays strongly for progressing flexibility. The distribution centered around  $\langle |Wr| \rangle = 0.8$  is fixed in its mean only spreading in variance for increasing flexibilities. Moreover, the absolute percentage of polymer conformations centered around  $\langle |Wr| \rangle = 0.8$  grows up to over 50% very slowly decaying in the flexible regime for  $L/l_p > 8$ . Thus, confinement provokes at flexibilities larger than  $L/l_p \approx 3$  additional writhed polymer configuration whose portion amounts up to over 50% of all states.

As a first step towards an understanding of these observations we consider overall polymer shape. In the limit-

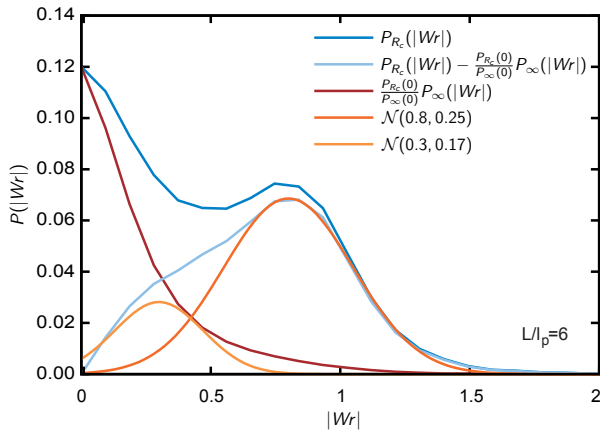


FIG. 4: Polymer conformations contribution to the writhe distribution of a confined polymer ring  $P_{R_c}(|Wr|)$  exemplarily shown for  $L/l_p = 6$ . Subtracting from the confined distribution the decay in writhe from  $Wr = 0$  as exhibited by the unconfined writhe distribution  $P_{\infty}(|Wr|)$  reveals additional states, which can be attributed to two normal distributions  $\mathcal{N}(\mu, \sigma^2)$  centered at  $|Wr| = 0.3$  and  $|Wr| = 0.8$ .

ing case of zero flexibility a polymer ring is a rigid planar ring with zero writhe. For slightly higher flexibility the first bending mode deforms the free polymer ring into a planar, elliptical shape [13], whose axes grow and shrink, respectively, with the square root of the flexibility, up to  $L/l_p \approx 5$ . Surely, the writhe of any truly two-dimensional ellipse is zero as well. However, thermal fluctuations do excite small deviations out of the plane such that the actual ensemble of free, stiff polymer rings does exhibit crossings in a small fraction of angular perspectives and, hence, displays a small writhing number. As flexibility grows the writhing number slowly increases.

In contrast, even weakly confined polymer rings cannot form the desired elliptical configuration of free polymers as soon as the major axis of the ellipse exceeds the spherical confinement. Instead they buckle into a banana-like ellipse [22]. Any symmetrically buckled ellipse again has zero writhe as the mirror plane through the ellipse's apices ensures that any crossing observed from a certain perspective cancels in the summation with a crossing of the opposite sign from the mirror perspective. Hence, very stiff, weakly confined polymer rings only show a small writhe due to undulations about the buckled curve as in the unconfined case. In both cases the absolute writhe grows with flexibility as the undulations increase with  $L/l_p$ ; see Note [23]. Thus, writhe distribution and mean absolute writhe collapse in the stiff regime.

To understand the structural transition which is provoked by the spherical confinement beyond the stiff

$L/l_p$	3	4	5	6	7	8	9	10
%	3	18	34	47	54	55	50	49
$\sigma^2$	0.16	0.19	0.21	0.25	0.31	0.35	0.40	0.47

TABLE I: Percentage and variance  $\sigma^2$  of structural distinct polymer states centered around  $\langle |Wr| \rangle = 0.8$ . Error of 3% in percentage and 0.03 in variance.

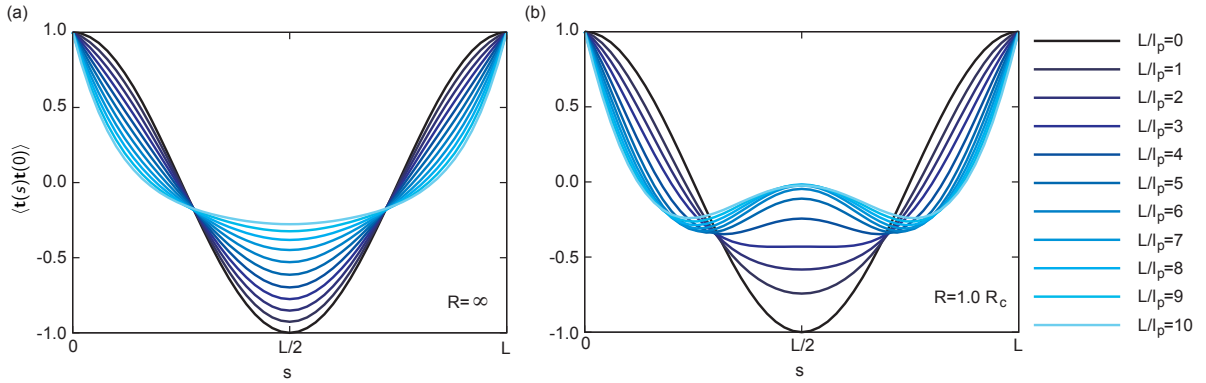


FIG. 5: Mean tangent-tangent correlation  $\langle \mathbf{t}(s)\mathbf{t}(0) \rangle$  along the whole polymer backbone  $s \in [0, L]$  for a free (a) and a spherically confined  $R = R_c$  (b) semiflexible polymer ring over flexibilities  $L/l_p = 0, \dots, 10$ . The correlation of an unconfined polymer ring smoothly crosses over from the tangent-tangent correlation along an “ellipse” in the stiff regime to an exponential decay with periodic boundary conditions in the flexible limit. In contrast the correlation of a spherically confined polymer ring displays the correlation of a “figure eight” shaped trajectory from  $L/l_p > 3$  onwards, only slowly saturating for large flexibilities.

regime the tangent-tangent correlation  $\langle \mathbf{t}(s)\mathbf{t}(0) \rangle$  along the polymer backbone  $s \in [0, L]$ , is considered in the cases  $R = \infty$  and  $R = R_c$ , see Fig. 5. The symmetry of the correlation function about the point of anti-correlation situated at half the distance along the polymer backbone  $s = L/2$  arises due to the topology of a ring. For example, the tangent-tangent correlation of a rigid ring yields  $\langle \mathbf{t}(s)\mathbf{t}(0) \rangle = \cos(2\pi s/L)$ . In the event of no confinement the elliptically shaped polymers in the stiff regime  $L/l_p < 5$  display a tangent-tangent correlation that resembles the correlations along an elliptical trajectory in agreement with analytic calculations [24]. In contrast to the correlations of a real ellipse the anti-correlations do not reach down to  $\langle \mathbf{t}(L/2)\mathbf{t}(0) \rangle = -1$  due to fluctuations which distort the direction of mirror polymer segments half the backbone distance apart. At higher flexibilities beyond the stiff regime the elliptical character is lost as higher modes crumple up the polymer configuration. This fact is also marked by a change in the initial curvature of the correlation function from convex to concave. With increasing flexibility the topological constraint becomes locally less and less important, thus the correlation function gradually approaches a symmetric exponential decay similar to an open semiflexible polymer. Quite strikingly the tangent-tangent correlations for all flexibilities intersect at  $s/L = 0.2744 \dots, 0.7744 \dots$  as calculated from the analytic result for the correlation function in the stiff regime presented in Note [24]. This suggests a certain symmetry in the undulations excited in an unconfined semiflexible polymer ring, they all seem to be superpositions of those generated in the stiff limit. This symmetry is, however, broken for spherically confined polymer rings. In the very stiff regime up to  $L/l_p \approx 3$  the tangent-tangent correlation of a polymer ring in spherical confinement of  $R = R_c$  displays an elliptical character, but compared to the unrestricted case the anti-correlation is notably less pronounced. As the confined polymer ring

is forced to extend in three dimensional space due to buckling, the probability for deviating directions between mirror segments along the polymer backbone is considerably higher than for an unconstrained planar polymer. Beyond the stiff range the tangent-tangent correlation reveals the internal structure corresponding to the new polymer configurations induced by confinement. For  $L/l_p > 3$  the correlation function displays decay and increase with twice the frequency as observed for elliptically shaped polymers. In fact, a figure eight shaped trajectory exhibits a correlation function of that frequency given by  $\langle \mathbf{t}(s)\mathbf{t}(0) \rangle = \cos(4\pi s/L)$ . Indeed an elliptical trajectory that is twined about its longest axis could account for both the correlation function and a writhe number around  $\langle |Wr| \rangle = 0.8$ . The states of smaller writhe are again hidden in the full distribution due to their small percentage in number. The figure eight correlation becomes most pronounced around  $L/l_p = 7$ , when the percentage of  $\langle |Wr| \rangle = 0.8$  is largest. For higher flexibilities the function smoothes out, as the distribution of states broadens in accordance with observations from the writhe distribution.

Altogether our observations confirm that weak spherical confinement imposed by an impenetrable shell induces a conformational transition to polymer rings above a certain flexibility. Very stiff polymer rings below  $L/l_p \approx 3$  exhibit very symmetric conformations whose mean trajectory obeys zero linking number. Only small undulations around this mean trajectory yield a finite mean writhe increasing identically with flexibility for weakly confined and unrestricted polymer rings. Differences in internal structure are only visible by the tangent-tangent correlation reflecting the planar configuration of unconfined and buckled three-dimensional state of confined polymers. Increasing flexibility further beyond this stiff regime induces more and more undulations. For a free polymer ring these lead to more and more crossings in projec-

tion planes broadening the writhe distribution. Crumpled configurations do not exhibit the symmetry of an elliptical trajectory any more, which in the stiff limit provoked cancelations in the sum over crossings, hence yielding smaller writhing numbers. Thus, beyond the stiff regime the mean absolute writhe shows a steeper increase with flexibility. In confinement, however, it is not only the increase in undulations that raises the mean writhe with flexibility. In addition, there is a qualitative change in the writhe distribution. From  $L/l_p \approx 3$  onwards the writhe distribution becomes bimodal as polymer configurations with a writhing number distinctly distributed around  $\langle |Wr| \rangle = 0.8$  start to develop. Also the tangent-tangent correlation shows from this threshold onwards the characteristics of a figure eight trajectory. We, therefore, deduce that confinement induces a conformational change to figure eight shaped polymers with  $\langle |Wr| \rangle = 0.8$ . Additional polymer states centered around  $\langle |Wr| \rangle = 0.17, 0.23, 0.3$  are few in number and only transiently occur between  $3 \leq L/l_p \leq 6$ . Configurations centered around  $\langle |Wr| \rangle = 0.8$  grow strongly in percentage with flexibility and only slowly decay from  $L/l_p > 8$  onwards. In fact, the first bending mode induces an elliptical polymer form that has to buckle transversely within spherical confinement. Thus, it seems plausible that an increase in flexibility and, hence, in ellipse eccentricity but also in possible curvature results in a polymer conformation, where the free energy to bend a polymer into a writhed state is equal or less than the free energy of stronger transverse bending. Therefore, a polymer ring chooses to intertwine with itself as an alternative way to

fit inside a sphere. This picture is also in agreement with the subsequent and less pronounced increase in mean absolute writhe for larger cavities. In larger confinement the energy for buckling becomes comparable to the bending energy paid for writhing at higher flexibility and also to less extend. It is, however, quite remarkable that the structural transition selects specific writhing numbers. Already the tangent-tangent correlation of free polymer rings suggests a selection of bending modes, which might be extended to a selection of “writhing modes” within confinement. Surely regarding the specific writhing number the exact geometry and strength of confinement enters.

In summary, our work discloses the occurrence and kind of conformational transitions in semiflexible polymers due to an impenetrable shell. The probability curve and the absolute quantity of the restructured state for a given flexibility is accessible from the writhe distribution presented. This turns the conformational transition due to confinement a predictable event to be employed in *in vitro* investigations. Thus, polymer conformations influence on gene regulation or controlled dynamics of conformational transitions due to administered changes in confinement become accessible opening up new perspective both concerning the study of biological process as well as the invention of biomimetic devices.

The financial support of the Deutsche Forschungsgemeinschaft through SFB 863 and of the German Excellence Initiative via the program “Nanosystems Initiative Munich (NIM)” is acknowledged. K.A. also acknowledges funding by the Studienstiftung des deutschen Volkes.

- 
- [1] D. M. Gowers and S. E. Halford, *EMBO J.* **22**, 1410 (2003).
- [2] B. van den Broek, M. A. Lomholt, S.-M. J. Kalisch, R. Metzler, and G. J. L. Wuite, *Proc. Natl. Acad. Sci. U.S.A.* **105**, 15738 (2008).
- [3] M. F. Schmid, M. B. Sherman, P. Matsudaira, and W. Chiu, *Nature* **431**, 104 (2004).
- [4] W. Reisner, K. J. Morton, R. Riehn, Y. M. Wang, Z. N. Yu, M. Rosen, J. C. Sturm, S. Y. Chou, E. Frey, and R. H. Austin, *Phys. Rev. Lett.* **94**, 196101 (2005).
- [5] M. Cosentino Lagomarsino, C. Tanase, J. W. Vos, A. M. C. Emons, B. M. Mulder, and M. Dogterom, *Biophys. J.* **92**, 1046 (2007).
- [6] G. Witz, K. Rechendorff, J. Adamcik, and G. Dietler, *Phys. Rev. Lett.* **101**, 148103 (2008).
- [7] J. X. Tang, J. A. Käs, J. V. Shah, and P. A. Janmey, *Eur. Biophys. J.* **30**, 477 (2001).
- [8] T. Sanchez, I. M. Kulic, and Z. Dogic, *Phys. Rev. Lett.* **104**, 098103 (2010).
- [9] S. Panyukov and Y. Rabin, *Phys. Rev. E* **64**, 011909 (2001).
- [10] D. Norouzi, F. Mohammad-Rafiee, and R. Golestanian, *Phys. Rev. Lett.* **101**, 168103 (2008).
- [11] G. Morrison and D. Thirumalai, *Phys. Rev. E* **79**, 011924 (2009).
- [12] O. Kratky and G. Porod, *Recl. Trav. Chim. Pay. B* **68**, 1106 (1949).
- [13] K. Alim and E. Frey, *Phys. Rev. Lett.* **99**, 198102 (2007).
- [14] F. B. Fuller, *Proc. Natl. Acad. Sci. U.S.A.* **68**, 815 (1971).
- [15] K. Klenin and J. Langowski, *Biopolymers* **54**, 307 (2000).
- [16] W. R. Bauer, F. H. C. Crick, and J. H. White, *Sci. Am.* **243**, 100 (1980).
- [17] J. H. White and W. R. Bauer, *J. Mol. Biol.* **189**, 329 (1986).
- [18] J. Arsuaga, M. Vázquez, S. Trigueros, D. W. Summers, and J. Roca, *Proc. Natl. Acad. Sci. U.S.A.* **99**, 5373 (2002).
- [19] I. Tobias, *J. Chem. Phys.* **113**, 6950 (2000).
- [20] A. C. Maggs, *J. Chem. Phys.* **114**, 5888 (2001).
- [21] C. Micheletti, D. Marenduzzo, E. Orlandini, and D. W. Summers, *J. Chem. Phys.* **124**, 64903 (2006).
- [22] K. Ostermeir, K. Alim, and E. Frey, arXiv:1003.4267 (2010).
- [23] Expressing the continuous version of the wormlike chain model in Euler angles  $\varphi(s), \vartheta(s)$ ,  $E = l_p k_B T / 2 \int_0^L ds \{ (\partial_s \varphi(s))^2 \sin^2 \vartheta(s) + (\partial_s \vartheta(s))^2 \}$  with  $\partial_s = \partial / \partial s$ , statistics of stiff, unconfined polymer rings are amenable to calculations by expanding the elastic energy around a rigid ring, *i.e.*,  $\varphi(s) = 2\pi s / L + \delta\varphi(s)$ ,  $\vartheta(s) = \pi/2 + \delta\vartheta(s)$ . Taking the Fourier transform and respecting the

periodic boundary conditions then yields,  $E = k_B T 2\pi^2 l_p / L \sum_{n=2}^{\infty} \{n^2 |\delta\varphi^2(n)| + (n^2 - 1) |\delta\vartheta^2(n)|\}$ .

Applying the equipartition theorem the correlations of the Euler angles are calculated  $\langle \delta\varphi(s)\delta\varphi(0) \rangle$ ,  $\langle \delta\varphi(s)\delta\varphi(0) \rangle$ . Transferring the reasoning of Panyukov and Rabin [9] forecasting  $\langle W r^2 \rangle = \sum_{n=2}^N n^2 \{ \langle \delta\varphi^2(n) \rangle \langle \delta\vartheta^2(n) \rangle - \langle \delta\varphi(n)\delta\vartheta(n) \rangle^2 \}$ , the second moment of the writhe fluctuations of a stiff polymer ring are calculated to grow with the square of the flexibility  $\langle W r^2 \rangle = \frac{3}{16\pi^4} \left(\frac{L}{l_p}\right)^2$ .

[24] Employing the calculations of Note [23] the correlation functions of the tangent vector  $\langle \mathbf{t}(s)\mathbf{t}(0) \rangle$  are

calculated based on its definition in Euler angles  $\mathbf{t}(s) = (\sin\vartheta(s)\sin\varphi(s), -\sin\vartheta(s)\cos\varphi(s), \cos\vartheta(s))$ . Expanding the tangent product for small angles  $\delta\varphi$  and  $\delta\vartheta$  and inserting the correlations of the relative Euler angles then yields  $\langle \mathbf{t}(s)\mathbf{t}(0) \rangle = \cos(2\pi s/L) [1 + \frac{1}{2\pi^2} \frac{L}{l_p} (g(s) - g(0) - f(0))] + \frac{1}{2\pi^2} \frac{L}{l_p} f(s)$  with  $g(s) = (\pi - 2\pi s/L)^2/4 - \pi^2/12 - \cos(2\pi s/L)$  and  $f(s) = \frac{1}{4} [2 + \cos(2\pi s/L) + 2\pi(2s-1)\sin(2\pi s/L)]$ . Perfect agreement with Monte Carlo simulation data is obtained for flexibilities up to  $L/l_p < 5$  thus describing the full stiff limit.

# Excluded volume effects on semiflexible ring polymers

Fabian Drube,<sup>1</sup> Karen Alim,<sup>1</sup> Guillaume Witz,<sup>2</sup> Giovanni Dietler,<sup>2</sup> and Erwin Frey<sup>1</sup>

<sup>1</sup>*Arnold Sommerfeld Center for Theoretical Physics and Center for NanoScience, Department of Physics, Ludwig-Maximilians-Universität München, Theresienstraße 37, D-80333 München, Germany*

<sup>2</sup>*Laboratoire de Physique de la Matière Vivante, Ecole Polytechnique Fédérale de Lausanne (EPFL), CH-1015 Lausanne, Switzerland*

(Dated: April 15, 2010)

Two-dimensional semiflexible polymer rings are studied both by imaging circular DNA adsorbed on a mica surface and by Monte Carlo simulations of phantom polymers as well as of polymers with finite thickness. Comparison of size and shape of the different models over the full range of flexibilities shows that excluded volume caused by finite thickness induces an anisotropic increase of the main axes of the conformations, a change of shape, accomplished by an enhanced correlation along the contour.

DNA is one of the most versatile building blocks for the self-assembly of nanoscale structures [1]. The complementary base-pairs enables almost unlimited possibilities in designing highly tailored constructs [2]. But even without specially designing sequences for specific base-pairing, biopolymers such as DNA or cytoskeletal filaments self-assemble in their natural environment. DNA occurs both in linear and circular forms and condenses into toroidal structures [3, 4]. Actin assembles into filaments and bundles [5] and also builds ring [6–8], and racket like [9, 10] complexes. From a geometrical perspective filaments denote the simplest building blocks. The next level of complexity is reached when topological constrained forms as in rings arise. Considering polymer rings as building blocks their size and shape are of eminent importance. Both size and shape strongly depend on two internal biopolymer properties: the ability to bend and the effective diameter of the polymer. Indeed the shape of polymer rings has been investigated theoretically regarding the influence of the polymers flexibility  $L/l_p$ , given by the ratio of total polymer length  $L$  and its persistence length  $l_p$  [11]. However, our experimental observations show that the previously neglected finite thickness not only regulates the absolute size [12] of a polymer configuration but also its shape. This observation is especially important in confined geometries utilized in the preparation of biopolymer assemblies of higher order [10].

Coarse grained polymer models rely on phantom chains, which allow segments to overlap. To describe real polymers with finite thickness, the excluded volume of a polymer chain is accurately accounted for by tube models [13], where the tube imposes a hard core potential, see Fig. 1. To access the effects of finite thickness and topology experimentally in a well-defined setup, we investigate circular DNA adsorbed on a mica surface, which has previously been shown to obey two dimensional worm-like chain statistics [14, 15]. Our data verifies Flory’s predicted growth in size due to polymer’s finite thickness [12], as has also been accomplished experimentally in different contexts [16–18] and theoret-

cally by self-consistent and renormalization group theories [19]. Since DNA can be produced in different lengths, it serves as a model system to investigate the shape over the full range of flexibility, which so far has only been forecasted theoretically for phantom polymers in three dimensions [11].

Here we study the effects of excluded volume caused by finite thickness on semiflexible polymer rings by imaging circular DNA on a mica surface and performing Monte Carlo simulations of semiflexible phantom polymers and polymers with finite thickness. Calibrating the polymer’s diameter  $d$  by comparing the tangent-tangent correlation, we obtain good quantitative agreement between experiments and simulations with diameter estimates from polyelectrolyte theory. The finite thickness leads to an apparent stiffening and an increase of the principal axes of the polymers configurations as observed by the mean square radius of gyration. In contrast to Flory’s prediction, the asphericity as a shape measure proves the growth to be anisotropic, resulting in a change of shape.

The DNA rings without superhelicity were produced from nicked plasmids pSH1, pBR322, and pUC19 with flexibilities of  $L/l_p = 40, 30,$  and  $18.3$ , respectively. Plasmid pUC19 was treated with restriction enzyme RsaI to

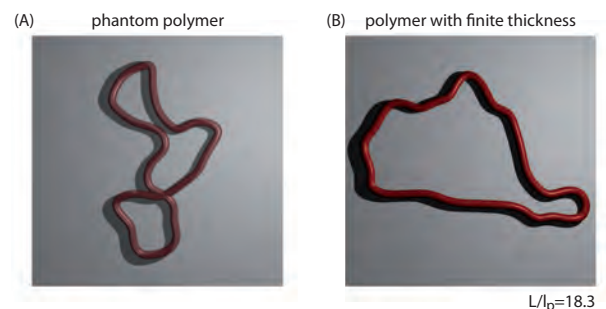


FIG. 1: Simulation snap-shot of a phantom polymer (A) and a polymer with finite thickness (B) on a plane. Phantom polymers bear overlaps and kink-like bending resulting in smaller configurations with more aspherical shapes than polymers with finite thickness.

produce three different linear fragments, and using T4 DNA ligase, minicircles of different flexibilities were obtained  $L/l_p = 12.4, 4.6$ . In order to access the trajectory of the DNA rings by Atomic Force Microscopy, the sample was deposited on mica, see supplementary material for details. Previous analysis of us [15] proofed the tangent-tangent correlation and the mean square radius of gyration to obey two dimensional statistics of the polymer rings.

For the Monte Carlo simulation of a semiflexible polymer rings with persistence length  $l_p$ , preceding simulation methods were customized to describe two dimensional polymers and extended to incorporate finite thickness as outlined in the supplementary material. In the simulations with finite thickness configurations including intersections of tubes of the diameter  $d$  around each segment are rejected. Uncorrelated data sets are obtained by taking configurations every  $10^6$  Monte Carlo steps for phantom polymers and every  $10^8$  steps for simulations with finite thickness. Large ensembles are sampled such that the statistical error based on a normal distribution of the observable is of the size of the symbols in all figures shown.

Semiflexible polymers are well described by the worm-like chain model, where the polymer is modeled as an elastic rod with bending modulus  $\kappa$  [13]. Representing the polymer by a differential space curve  $\mathbf{r}(\mathbf{s})$  of length  $L$  parametrized by an arc length  $s$ , its statistical properties are determined by the elastic energy  $\mathcal{H} = \kappa/2 \int_0^L ds [\partial\mathbf{t}(s)/\partial s]^2$ , where  $\mathbf{t}(s) = \partial\mathbf{r}(s)/\partial s$  is the tangent vector. The persistence length  $l_p$  as a measure of the stiffness is defined by the initial decay of the mean tangent-tangent correlation  $\langle \mathbf{t}(s)\mathbf{t}(s') \rangle = \exp(-|s - s'|/l_p)$ , given by  $l_p = \frac{2\kappa}{k_B T}$  for a polymer embedded in two dimensions.

Size and shape of a polymer are comprised in the radius of gyration tensor,

$$Q_{ij} = \frac{1}{L} \int ds \mathbf{r}_i(s)\mathbf{r}_j(s) - \frac{1}{L^2} \int ds \mathbf{r}_i(s) \int d\tilde{s} \mathbf{r}_j(\tilde{s}), \quad (1)$$

whose eigenvalues  $\lambda_1$  and  $\lambda_2$  define the spatial extent of the polymer along its principal axes. The squared radius of gyration measures the total size of an object and hence is given by the sum of the two eigenvalues,

$$R_g^2 = \lambda_1 + \lambda_2. \quad (2)$$

The criterion for the shape of a polymer is the asphericity, which is given by the normalized variance of  $\lambda_1$  and  $\lambda_2$  [20], yielding in two dimensions,

$$\Delta = \frac{(\lambda_1 - \lambda_2)^2}{(\lambda_1 + \lambda_2)^2}. \quad (3)$$

The asphericity ranges between 0 and 1;  $\Delta = 0$  for the most spherical object in two dimensions, the ring, and  $\Delta = 1$  for the most aspherical configuration, a rod.

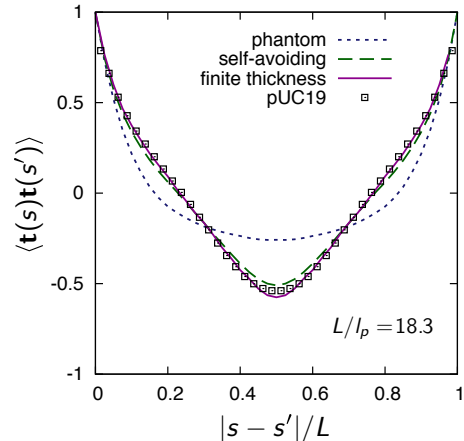


FIG. 2: Tangent-tangent correlation of a semiflexible polymer ring for different theoretical models and for DNA (pUC19). The finite thickness is calibrated to  $d/l_p = 0.13$ . Incorporating the same persistence length models with higher self-exclusion show enhanced correlations.

To model real polymers, two internal parameters are required, the persistence length  $l_p$  and the diameter  $d$  of the filament. For the persistence length of DNA we use the widely accepted value of  $l_p = 50nm$ . The effective diameter of DNA, being a polyelectrolyte, changes in a predictable manner in response to its surrounding ionic solution, as it has been determined theoretically [21] and experimentally [22]. For our experimental conditions the ratio of diameter to persistence length is  $d/l_p = 0.13$ . To calibrate the simulation parameters to the experimental data, the tangent-tangent correlation is an ideal observable reflecting the statistics along the whole contour of the polymer. The agreement between simulation with finite thickness and experimental data is exemplified for the tangent-tangent correlation for a flexibility of  $L/l_p = 18.3$  considering plasmid pUC19 in Fig. 2. Included in the graph are also results for a phantom polymer, where self-intersecting configurations are permitted, and for reasons of comparison the trivial limit of vanishing thickness  $d \rightarrow 0$  denoted self-avoiding polymer. In the latter case, only intersections of the polymer backbone are rejected. This limit does not describe the experimental data quantitatively as good as the simulations with a thickness of  $d/l_p = 0.13$  (7% increase of the reduced chi-square). Hence, the diameter estimate based on polyelectrolyte theory yields good quantitative agreement.

In the tangent-tangent correlation function of Fig. 2, two effects are evidenced if comparison is made between a polymer with finite thickness and a phantom chain of same persistence length (solid and dashed line in Fig. 2, respectively), one due to the finite thickness of the polymer and the other to the circular topology. On short distances, the finite thickness restricts the available con-

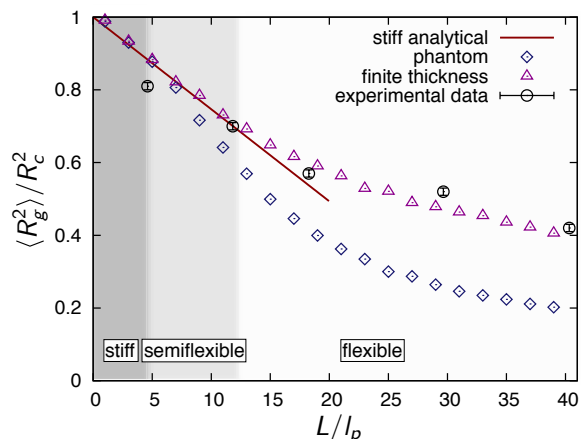


FIG. 3: Squared radius of gyration  $\langle R_g^2 \rangle$  compared to the size of the corresponding rigid ring  $R_c^2 = (L/2\pi)^2$  vs.  $L/l_p$ . The influence of finite thickness arises in the semiflexible regime after an effective stiffening in accordance with analytical predictions for stiff rings. In the flexible regime, the increase in size is required to model the experimental data. Error bars indicate the statistical errors.

formational space, thus increasing the directional correlation. In order to respect the circular topology, the correlation function must become more negative on distances  $s \approx L/2$ . In summary, the polymer with finite thickness appears effectively stiffer.

Similarly, this effective stiffening also affects the overall size of the polymer as measured by the squared radius of gyration  $\langle R_g^2 \rangle$ . In Fig. 3  $\langle R_g^2 \rangle$  normalized with the radius of gyration of a rigid circle, namely  $\langle R_g^2 \rangle / R_c^2$ , is plotted versus the flexibility parameter  $L/l_p$  for the considered models together with the data. Three regimes are discerned; in the stiff regime all simulation data for the radius of gyration normalized by total polymer length versus flexibility  $L/l_p$  follow the predicted linear decay [23]. The stiff regime extends up to high flexibilities compared to open chains. For phantom polymers this effect can be accounted for by an effective stiffening due to the topological constraint of a ring [23]. For polymers with finite thickness the squared radius of gyration follows the analytic result for the stiff limit up to even higher flexibilities of approximately  $L/l_p = 12$  indicating a further effective stiffening due to the polymer's thickness i.e. as a result of excluded volume. This is in agreement with the observation of enhanced correlations in the tangent-tangent correlation. The semiflexible regime is a crossover region, where departing from the analytically determined stiff limit, phantom polymers show a linear decay as flexibility increases suggesting an initial step by step excitation of higher modes. In contrast, for polymers with finite thickness these initial higher modes are suppressed, resulting in a direct transition from the linear decay in the stiff limit to the power law decay in

the flexible regime. Such polymers with finite thickness deviate from the stiff limit to larger sizes as is also observed for three-dimensional phantom polymer rings [23]. Finally, in the flexible regime both models have substantially different radii of gyration. In contrast to phantom polymers, polymers with finite thickness show notably larger sizes recovering Flory's swelling effect. The scaling exponent agrees with Flory's predicted exponent (data not shown). The segments of phantom polymers overlap strongly to maximize entropy as flexibility permits. Precisely those modes are, however, forbidden for polymers with finite thickness yielding a larger mean squared radius of gyration. Flory's argument oversimplifies a semiflexible chain of segments to an ideal gas and assumes that all chain segments overlap with an equal probability with each other. This results in a growth in size that is equally large along all principal axes of the polymer. Hence, Flory's description predicts an *isotropic increase of the principal axes*, which will be tested below when considering the asphericity. The experimental data in Fig. 3 are in agreement with the finite thickness polymers, providing solid evidence that a description of DNA as a semiflexible polymer with persistence length  $l_p = 50$  nm and effective diameter  $d/l_p = 1.3$  is a faithful description of DNA conformations. Indicated in the graph (Fig. 3) are only statistical errors of a Gaussian distributed observable as a lower estimate of the statistical error. Furthermore, systematic errors may arise, first, due to the limited resolution of the AFM images, and second, due to the fact that the minicircles are not nicked and may thus experience a slight distortion.

In order to test Flory's prediction, the asphericity  $\langle \Delta \rangle$  (Eq. 3) is plotted in Fig. 4 as a function of the flexibility parameter  $L/l_p$  and the three regimes appear again. Starting from a ring configuration with  $\Delta = 0$  for infinite stiffness  $L/l_p = 0$ , the asphericity grows linearly for both models in the stiff region due to the fact that polymers have an elliptical shape of increasing eccentricity, as it has been recently predicted by scaling arguments [11]. Self-exclusion plays no role in these configurations because the segments are well separated from each other due to the high bending energy of stiff polymers. The increase in asphericity is continued in the semiflexible regime until it starts to decrease slowly for flexible polymers, clarifying ambiguous simulations [24, 25]. For phantom polymers the asphericity decreases down to  $\langle \Delta \rangle = 0.2625$  in the Gaussian limit [26]. The three regimes of the phantom polymer resemble results for three-dimensional phantom rings, which, however, show a more pronounced decrease in asphericity in the flexible regime as the third spatial dimension enables more compact configurations.

Focussing on the magnitude of the asphericity in the two dimensional models of phantom polymers and polymers with finite thickness, we find that the curves commence to deviate from each other in the semiflexible regime, showing fundamentally different values of as-

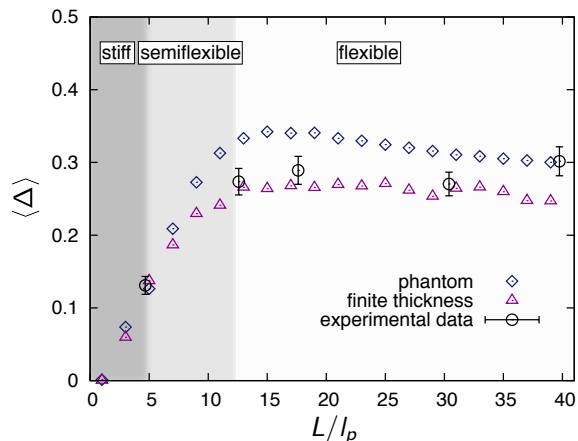


FIG. 4: The asphericities of the two models deviate in the semiflexible regime due to the influence of finite thickness. Through enhanced correlations between adjacent segments and prominent growth of the minor principal axis forced by pushing overlapping segments apart finite thickness makes the elliptical shape of ring polymers rounder.

phericity in the flexible region. Hence, the ratio of the principal axes is strikingly different and the growth in size induced by the polymer's thickness is anisotropic along the principal axes yielding more spherical configurations compared to a phantom polymer. This is opposite to simulation results for open random walks in three dimensions, where self-avoidance has been found to lead to slightly more aspherical configurations [27, 28]. In fact in three dimensions, a random walk is rarely intersecting its own trajectory. Then our present work suggests the remaining governing impact of self-avoidance in three dimensions to be an effective stiffening. Such a stiffening yields more aspherical shapes for open semiflexible polymers in three dimensions.

Confinement, like in the present case of two dimensional ring polymers, on the other hand, forces polymer segments to overlap much more frequently. Concerning two dimensional polymer rings, the notion of an aspherical shape indicates that one principal axis is much longer than the other like in an ellipse. In the apices of the ellipse, the segments are prone to overlap with neighboring segments on a local level, while segments in the convex part of the ellipse tend to overlap with segment being separated approximately half the total length along the contour. The finite thickness now effectively stiffens the polymer inducing less bending at the apices and it increases the minor principal axis by pushing segments in the convex region apart, see Fig. 1. This results in a more spherical configuration for polymer rings with finite thickness, as observed in Fig. 4. As the asphericity distribution is highly skewed our statistical errors underestimate the actual error justifying slight deviations between our sets of data. Considering two dimensional

polymer rings the good agreement between simulations and experimental data over the broad range of flexibilities manifests the role of finite thickness and its effects of effective stiffening and anisotropic change in shape.

In conclusion, we have analyzed the impact of excluded volume caused by the finite thickness of polymer rings in two dimensions over the whole range of flexibility, both by observing DNA rings on mica surface and by computer simulations of phantom and finite thickness polymers. We find that the experimental data can only be explained by the latter, where each segment of the polymer is represented by an impenetrable tube. From the comparison of the different models, we determine two effects of finite thickness. Firstly, tangent-tangent correlation shows an enhanced correlation due to the steric constraints of the neighboring segments, leading to an effective stiffening observed in the semiflexible regime of the mean-square radius of gyration. Secondly, in the flexible regime Flory's swelling is recovered. However, the asphericity discloses an anisotropic change in shape. Manifesting these properties should enable a new understanding of the conformation statistics of biopolymers such as DNA and F-actin. A basis on which biopolymer assemblies can be designed to develop new nanomaterials.

F.D., K.A. and E.F. acknowledge financial support of the German Excellence Initiative via the program "Nanosystems Initiative Munich (NIM)", of the DFG through SFB 486, and of the LMUinnovativ project "Functional Nanosystems (FuNS)". K.A. acknowledges funding by the Studienstiftung des deutschen Volkes. G.W. and G.D. acknowledge the support by the Swiss National Science Foundation through grants Nr. 200020-116515 and 200020-125159.

- 
- [1] Seeman, N. C. *Nature* **2003**, *421*, 427–31.
  - [2] Chen, J.; Seeman, N. *Nature* **1991**, *350*, 631–633.
  - [3] Bloomfield, V. A. *Biopolymers* **1991**, *31*, 1471–81.
  - [4] Hud, N. V.; Downing, K. H. *P Natl Acad Sci USA* **2001**, *98*, 14925–30.
  - [5] Lodish, H. F.; Berk, A.; Kaiser, C. A. *Molecular cell biology*; Palgrave Macmillan: London, 2008; p 973.
  - [6] Tang, J.; Käs, J.; Shah, J.; Janmey, P. *Eur Biophys J* **2001**, *30*, 477–484.
  - [7] Limozin, L.; Sackmann, E. *Phys Rev Lett* **2002**, *89*, 168103.
  - [8] Claessens, M. M. A. E.; Bathe, M.; Frey, E.; Bausch, A. R. *Nat Mater* **2006**, *5*, 748–753.
  - [9] Cohen, A.; Mahadevan, L. *P Natl Acad Sci USA* **2003**, *100*, 12141–12146.
  - [10] Lau, A. W. C.; Prasad, A.; Dogic, Z. *Europhys Lett* **2009**, *87*, 48006.
  - [11] Alim, K.; Frey, E. *Phys. Rev. Lett.* **2007**, *99*, 198102.
  - [12] Flory, P. J. *Principles of polymer chemistry*; Cornell Univ. Press: Ithaca, N.Y., 1953; p 672.
  - [13] Rubinstein, M.; Colby, R. H. *Polymer Physics*; Oxford



- Univ. Press: Oxford, 2003; p 440.
- [14] Rivetti, C.; Guthold, M.; Bustamante, C. *J. Mol. Biol.* **1996**, *264*, 919–32.
- [15] Witz, G.; Rechendorff, K.; Adamcik, J.; Dietler, G. *Phys. Rev. Lett.* **2008**, *101*, 4.
- [16] Maier, B.; Rädler, J. *Phys. Rev. Lett.* **1999**, *82*, 1911–1914.
- [17] Valle, F.; Favre, M.; De Los Rios, P.; Rosa, A.; Dietler, G. *Phys. Rev. Lett.* **2005**, *95*, 158105.
- [18] Ercolini, E.; Valle, F.; Adamcik, J.; Witz, G.; Metzler, R.; De Los Rios, P.; Roca, J.; Dietler, G. *Phys. Rev. Lett.* **2007**, *98*, 058102.
- [19] DesCloizeaux, J.; Jannink, G. *Polymers in solution*; Clarendon Press: Oxford, 1990; p 896.
- [20] Aronovitz, J.; Nelson, D. *J. Phys. (France)* **1986**, *47*, 1445–1456.
- [21] Stigter, D. *Biopolymers* **1977**, *16*, 1435–1448.
- [22] Rybenkov, V.; Cozzarelli, N.; Vologodskii, A. *P. Natl. Acad. Sci. U.S.A.* **1993**, *90*, 5307–5311.
- [23] Alim, K.; Frey, E. *Eur. Phys. J. E* **2007**, *24*, 185–191.
- [24] Camacho, C.; Fisher, M.; Singh, R. *J. Chem. Phys.* **1991**, *94*, 5693–5700.
- [25] Norman, R.; Barker, G.; Sluckin, T. *J. Phys. II* **1992**, *2*, 1363–1376.
- [26] Diehl, H.; Eisenriegler, E. *J. Phys. A* **1989**, *22*, L87–L91.
- [27] Cannon, J.; Aronovitz, J.; Goldbart, P. *J. Phys. I* **1991**, *1*, 629–645.
- [28] Bishop, M.; Saltiel, C. *J. Chem. Phys.* **1988**, *88*, 3976.

# Supplementary Information: Excluded volume effects on semiflexible ring polymers

Fabian Drube,<sup>†</sup> Karen Alim,<sup>†</sup> Guillaume Witz,<sup>‡</sup> Giovanni Dietler,<sup>‡</sup> and Erwin Frey<sup>\*,†</sup>

*Arnold Sommerfeld Center for Theoretical Physics and Center for NanoScience, Department of Physics,*

*Ludwig-Maximilians-Universität München, Theresienstraße 37, D-80333 München, Germany , and Laboratoire de Physique de la Matière Vivante, Ecole Polytechnique Fédérale de Lausanne (EPFL), CH-1015 Lausanne, Switzerland*

E-mail: frey@lmu.de

## Experimental Preparation

Atomic force microscopy was used to image DNA molecules of different lengths. The three longest chains with with flexibilities  $L/l_p=18.3$ , 30 and 40 were standard plasmids pUC19 (2686 bp), pBR322 (4361 bp), and pSH1 (5930 bp). The shorter chains with  $L/l_p=12.4$  and 4.6 were generated by using T4 DNA ligase to circularize DNA fragments (676 bp and 1769 bp) obtained from the restriction of pUC19 by endonuclease RsaI. The three largest rings were nicked to suppress any supercoiling  $\sigma$ . The two mini-circles were not nicked but their short size ensures that most of them are at their elastic energy minimum without supercoiling  $\sigma = 0$ . pUC19 and pBR322 plasmids as

---

\*To whom correspondence should be addressed

<sup>†</sup>Arnold Sommerfeld Center for Theoretical Physics and Center for NanoScience, Department of Physics, Ludwig-Maximilians-Universität München, Theresienstraße 37, D-80333 München, Germany

<sup>‡</sup>Laboratoire de Physique de la Matière Vivante, Ecole Polytechnique Fédérale de Lausanne (EPFL), CH-1015 Lausanne, Switzerland

well as enzymes were purchased from Fermentas, plasmid pSH1 was provided by S.M Lewis. All DNA preparations were diluted in 1 mM Tris-HCl buffer, pH 7.8, to a final DNA concentration of 1  $\mu\text{g/ml}$ , and  $\text{MgCl}_2$  was added in the DNA solution to a final concentration of 5 mM. For imaging, 10  $\mu\text{l}$  solution were deposited for 10 minutes on a freshly cleave mica surface, rinsed with 3 ml deionized water, and dried under air flow. Images were taken with a Nanoscope III (Veeco) operated in tapping mode (150 to 300 kHz) in air with silicon ultrasharp non-contact tips of a nominal tip radius of  $<10$  nm (NT-MDT Co., Zelenograd, Moscow, Russia). The images were only flattened using the Nanoscope III program. Finally, the two dimensional coordinates of the molecules were recorded using the tracing module of *Ellipse*.<sup>1</sup> The tracked positions  $\vec{r}_i$ ,  $i \in [1, N]$ , along the polymer's contour are then used to calculate size and shape parameters based on the discretized version of the radius of gyration tensor

$$Q_{ij} = \frac{1}{N} \sum_{i=1}^N \vec{r}_i \vec{r}_i - \frac{1}{N^2} \sum_{i=1}^N \vec{r}_i \sum_{j=1}^N \vec{r}_j. \quad (1)$$

## Simulations

To sample the conformations of two dimensional, semiflexible ring polymers Metropolis Monte Carlo simulations is employed. The polymer ring of length  $L$  and persistence length  $l_p$  is discretized as a two dimensional closed polygon of  $N$  segments of length  $a$ ,  $L = Na$ , and direction  $\vec{t}_i$ . The energy associated with each single configuration is given by the discretized version of the wormlike chain model

$$\mathcal{H} = Nk_B T \frac{l_p}{L} \sum_{i=1}^N (1 - \vec{t}_i \vec{t}_{i+1}), \quad (2)$$

with imposed periodic boundary conditions  $\vec{t}_{N+1} = \vec{t}_1$ . The persistence length  $l_p$  is chosen to be the established value for DNA of  $l_p = 50\text{nm}$ .

New configurations are obtained by standard crankshaft move<sup>2</sup> as follows: Two arbitrary vertices of the polymer are selected randomly. A pivot axis is drawn between these two vertices and all segments between them are rotated by 180 degrees around the axis. Finite thickness is imple-

mented by discarding conformations in which tubes of diameter  $d$  around each segment overlap.

The correlation between subsequent polymer configurations is estimated by using the autocorrelation function for the polymer's squared radius of gyration

$$\chi(t) = \frac{1}{t_{max} - t} \sum_{t'=0}^{t_{max}-t} R_g^2(t' - t) R_g^2(t) - \left( \frac{1}{t_{max} - t} \right)^2 \left( \sum_{t'=0}^{t_{max}-t} R_g^2(t + t') \right) \left( \sum_{t'=0}^{t_{max}-t} R_g^2(t) \right), \quad (3)$$

resulting in a correlation time of

$$\tau = \frac{\chi(0)}{\chi(t_{max})}. \quad (4)$$

In our simulations the correlation time has been largely overestimated by values of  $10^6$  for phantom chain simulations and  $10^8$  for simulations with finite thickness.

## References

- (1) Marek, J.; Demjénová, E.; Tomori, Z.; Janáček, J.; Zolotová, I.; Valle, F.; Favre, M.; Dietler, G. *Cytometry A* **2005**, *63*, 87–93.
- (2) Escobedo, F. A.; Pablo, J. J. D. *J. Chem. Phys.* **1995**, *102*, 2636–2652.

### 3 Structuring tissue by mechanics and signals

It is the intriguing puzzle of the development of higher organisms that a single cell, a fertilized egg, gives rise to a multicellular structure of different cell types arranged to form organs of specified shape and function. The whole progress of development is a sequence of coordinated cell proliferation and differentiation making use of development's toolbox. The mechanisms include cell division, cell rearrangement, death and growth as well as change of individual cell shape and cell differentiation. These processes are controlled by the differential expression of genes generating a cascade of signals, which control cell division rates and planes, adhesion to cell neighbors, and cell fate. Hence, on the one hand, development is the result of an ingenious network of feedback in gene expression including apparent redundancies and negative feedback to turn the whole progress reliable. On the other hand, purely mechanical forces govern the execution of cell migration, shape and arrangement. The interplay of both optimized feedback networks and physical laws behind the mechanics persists throughout development resulting in specified cell fate and function.

A signaling molecule impressing by its multitude of functions and almost omnipotent structuring during the development of plants is the plant hormone auxin. Sites of auxin accumulation guide plant development from the initial shoot root polarity in the embryo towards the final positioning of leaves around the stem, also guiding the pattern of veins within growing leaves [42, 147]. These patterns of auxin are not stationary distributions of the molecule, rather, the dynamic, directed auxin flow lies at the origin of these patterns. The direction of auxin flow arises by the oriented, polar accumulation of efflux facilitator proteins from the PIN family. Only these PIN proteins enable the successful transport of auxin from one cell to the next. Now auxin and its own efflux protein PIN are connected via positive feedback, thereby, auxin induces the polar accumulation of PIN proteins and thus orients its own direction of flow.

We investigate the character of the feedback between auxin and PIN proteins during the initiation of vein structures in leaves. The initiation of veins is a processes that can be abstracted enough to subject its dynamics to a thorough theoretical analysis by means of non-linear dynamics and pattern formation. Thereby our work characterizes the role of contributing dynamics and provides both qualitative and quantitative predictions to assess the character of auxin and PIN feedback and to determine at least estimates of the governing kinetic parameters.

Mechanical forces most notably govern the cellular structure of adherent tissue. The prime example of such a tissue of interconnected cells are the monolayers of epithelia. This tissue type is ubiquitous in animal kingdom as it forms the boundaries of compartments within organisms. The mechanical forces that orchestrate tissue structure by determining cell packing geometry, topology, and individual cell shape can be abstracted to three different kinds [111, 128]: The bulk elasticity of the cell body resisting deformations, the contractile force by a cortical meshwork of cytoskeleton contracting the cells perimeter and the adhesive force between cells increasing their contact. Although all process themselves are highly dynamic at the microscopic level, together they build a homeostatic state that can be described by the balance of the contributing forces.

We study how these mechanical forces determine cell packing in a tissue model with well-defined boundary conditions in collaboration with experiments performed by Alicia Piera Aberola and Anna-Kristina Marel in the group of Joachim O. Rädler, LMU Munich. Theoretical analysis of the observed cell packing geometries shows that in addition to the antagonistic action of cell cortex contractility and cell-cell adhesion, elastic forces against cell shape anisotropy drive cell organization.

### 3.1 Plant development

The study of developmental processes in plants is particularly interesting as the by far largest part of organ development takes place after embryogenesis. Therefore, the plant is already subjected to environmental conditions and evolves without the maternal guidance of, *e.g.*, an egg shell. Plants exhibit a robust circuit of hormonal signals that orients the plant axes and guides the initiation and structuring of most plant organs. The model organism to investigate these developmental processes is *Arabidopsis thaliana* (Ackerschmalwand), see photograph in Fig. 3.1 (G). This small flowering plant has a fast life cycle and responds well visible to genetic modifications.

The mechanisms of plant development are more limited in contrast to animals as their cells possess a rigid cell wall which excludes cell movement, rendering differential cell division and directed cell elongation especially important. Plant growth starts with a single fertilized egg, first establishing a shoot (apical) versus root (basal) polarity by oriented cell division [207], see Fig. 3.1 (A). The basal end then goes through a series of highly conserved cell divisions generating a heart-like outgrowth, see Fig. 3.1 (B). At the tip of the heart a so-called root apical meristem forms while a shoot apical meristem is established at the indent of the heart. These meristems at the opposing ends of a plant are the key to plant development as they constitute undifferentiated tissue that continuously undergoes cell divisions. Thereby, the shoot apical meristem gives rise to shoots, stalks, leaves and flowers while roots are generated by the root apical meristem. Plants are an example where cell fate is believed to be determined by relative position. All organs display a radial symmetry of tissue types with epidermal cells outmost, followed by ground tissue

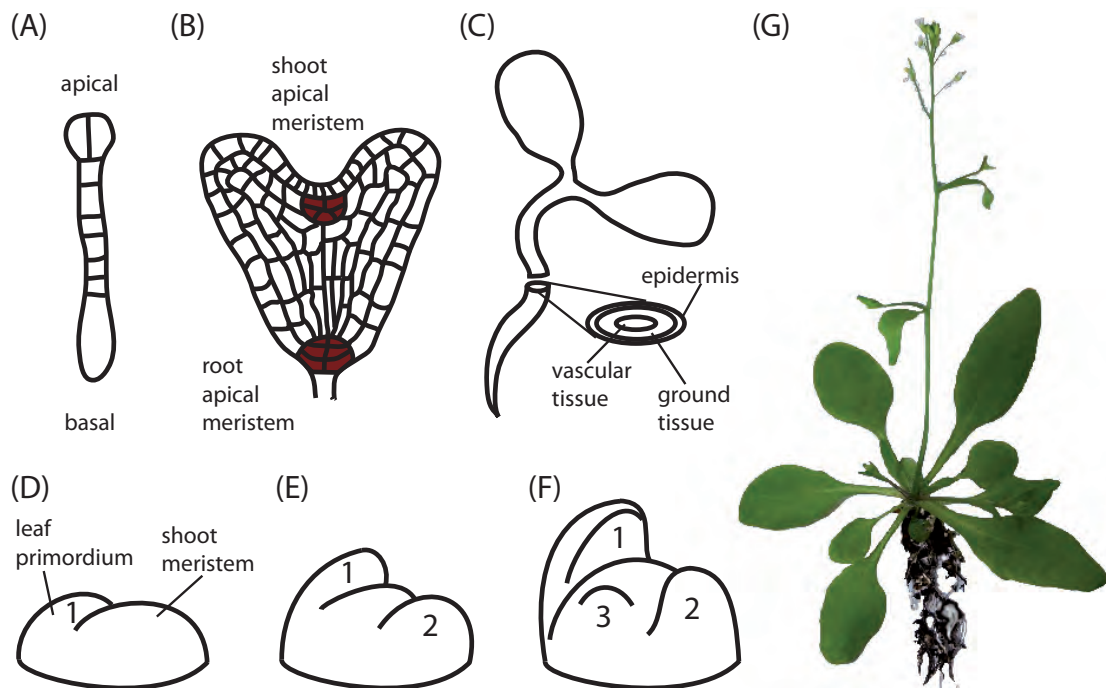


**Figure 3.1:** Development of the model organism *Arabidopsis thaliana*. (A) After the first round of conserved cell divisions the shoot-root direction is established. (B) At the heart stage several cell divisions later, shoot and root apical meristem are established, that guide the development of all future organs. (C) Tissue fate is position dependent, radial identification of tissue type from outmost epidermal to innermost vascular tissue. (D-F) Successive leaf outgrowth at the shoot apex in spiral order, phyllotaxis. Adapted from Wolpert et al. [207]. (G) Photograph of a fully grown plant including roots, rosette leaves and flowers. Courtesy of Karlheinz Knoch, Botanic Garden Karlsruhe.

that encloses vascular tissue as depicted in Fig. 3.1 (C). Also the decision of whether cells at the tip of the shoot will contribute to lateral outgrowths like leaves or not is believed to be position dependent. The onset of lateral organs is first visible by bulges at the shoot, so-called primordia. These form subsequently along a spiral staircase around the shoot, as observable in the series of sketches of the shoot apex in Fig. 3.1 (D-F). This highly conserved pattern, termed phyllotaxis, seems to arise from a local inhibition between emerging primordia causing a specific distance between neighbors [125]. However, recent investigations suggest a competition for the growth factor auxin to lie at the heart of phyllotactic patterns [87, 103, 156].

Leaves develop as a lateral outgrowth from a group of founder cells within the peripheral zone at the shoot apical meristem [43]. Already in the primordium, the first noticeable swelling, the axes of a leaf are established. An adaxial-abaxial axis from the upper to the lower surface and a proximal-distal axis reaching from the leaf base to its tip. The in cross-section crescent shaped primordium continues to proliferate establishing several layers of tissue that comprise the leaf from lower to upper epidermis. In the simple leaves

with entire margin observed in *Arabidopsis thaliana* the proliferation rate is dominantly uniform throughout the leaf blade [50]. However, cell division rate is suggested to vary for the formation of leaflets, lobes and marginal serration. Towards the end of leaf formation the proliferation phase ceases from leaf tip to base [50, 131] followed by a phase where the arrested cells increase their cell volume tremendously. Finally, the fully sized leaf is grown. During the entire development of a leaf the individual growth of all tissue layers is supposedly highly regulated to prevent buckling and curling but build a planar cell arrangement.

The differentiation of cells into specific tissue identities occurs parallel to leaf growth. Already after a fifth of the total time for leaf formation the provascular tissue is formed that will later give rise to the primary vein which extends from the petiole at the leaf base through the center of the leaf blade to its tip [173, 174]. Subsequently, the vascular tissue of the second and higher order veins forms, starting from already grown veins in a hierarchical manner. Eventually, after the formation of the provascular cells of second order, also the ground tissue between the upper and lower layer starts to differentiate [174] building the mesophyll tissue of the inner leaf.

Together, differentiation and tissue mechanics build the developing plant. Both are intertwined and a successful understanding of the full processes can only be reached by examining both underlying mechanisms, the physical laws of mechanics and the role of feedback and signals one at a time.

## 3.2 Tissue mechanics

Mechanical forces arising within tissues are the key to a huge variety of processes. On the one hand, mechanics govern active restructuring like cell division, growth and death [92, 180] as well as tissue migration and spreading [65, 138, 151, 194]. On the other hand, the geometry of cellular arrangement and individual cell shape is the result of the balance of forces within tissues [111, 128]. The impact of mechanics is especially strong in tissues, where cells are constantly connected to each other. There are two different implementations of such cohesive tissues: Epithelial tissues, where cell membranes are interconnected by adherence junctions, and plant cells, where neighboring cells share a common, rigid cell wall. The first is often modeled as a viscous body [17, 64, 120], the latter as a plastic elastic network [35, 44, 83].

Epithelial tissues are monolayers of interconnected cells that dominate the anatomy of “higher” animals as they typically build the boundaries of compartments. Epithelia are the first specialized tissue forming during the embryogenesis of metazoa indicating the importance of this tissue type in development [40]. As usually epithelia tissues derive from a few number of cells by generations of cell divisions, all cells within a tissue bear almost identical properties. Epithelia cells are connected by adherence junction that in most cases



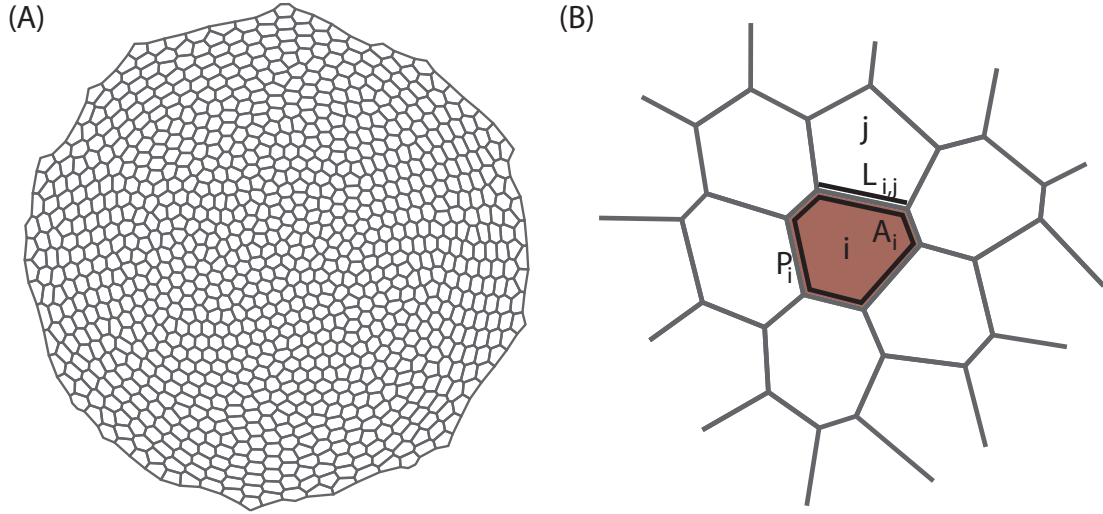


**Figure 3.2:** Vertex model of a full (A) and part (B) of a tissue. The cells are represented by their cell junctions (vertices) and cell-cell contact lines (edges). The structure of a tissue state is given by the force balance state. Contributing forces arise from the cell's bulk elasticity, regulating cell area  $A_i$ , cell cortex contractility, reducing cell perimeter  $P_i$ , and cell-cell adhesion, favoring long cell-cell contact  $L_{ij}$ .

form by the reinforcing action of both cadherin based adhesion and actin cytoskeleton reorganization and stabilize into a homeostatic state [28].

This stationary state is the result of the trade-off of contractile forces from the cell cortex, the adhesive forces between cells and the elastic forces against deformation of the cell body. Differential changes in these properties drive large scale cell rearrangements during development. For example differing cell adhesion governs cells sorting [14, 186, 187] and the packing geometries of retinal epithelia cells observed in the individual units, ommatidia, of *Drosophila* compound eyes [85, 89, 98]. Restructuring of cell cortex, hence, modifying its contractility, takes an active part in cell intercalation during germ-band elongation in *Drosophila* [13, 111, 153].

All these processes of internal modification happen on long time scales compared to the relaxation of the mechanical forces. Thus, the geometric structure of the tissue and the individual cell shape itself can be regarded as equilibrated force balance state. Above the level of pure topological modeling [73], the polygonal geometry of cell packing states can, therefore, successfully be described as the minimum of an energy functional [59, 89, 92, 98, 153]. Modeling the epithelial monolayer as two dimensional sheet of individual cells  $i = 1 \dots N$  with area  $A$ , perimeter  $P$  and cell-cell contact line  $L$ , as shown in Fig. 3.2, the elastic, contractile and adhesive forces can be cast in the following energy functional,

$$E = \sum_{i=1}^N \left\{ (A_i - A^0)^2 + \phi P_i^2 - v \sum_{j \sim i} L_{ij} \right\} \quad (3.1)$$

where  $\kappa$ ,  $\phi$  and  $v$  denote the bulk elastic modulus, the contractility and the adhesion

strength, respectively. To describe the structure and shape of extended tissues these kind of energy functionals are employed in computer simulation of vertex models of cells. In a vertex model the topology and geometry of tissues is abstracted to the positions of cell junctions (vertices) and straight cell-cell contact lines (edges) between them. This approach led to the quantification of the ensemble average of the governing forces in *Drosophila* germ-band [153] and wing disk [59]. In vivo cell structures depend on a variety of factors such as supporting and surrounding tissue type and their history during development. To understand and individually quantify the cell mechanics that govern multicellular structures it is, therefore, desirable to study cell packing geometries under well-defined boundary conditions. This approach has been pursued by us in collaboration with the group of Joachim O. Rädler, LMU Munich.

Plant cells display different mechanical mechanisms as they are surrounded by a cell wall built of cellulose microfibrils [191]. The cell itself exerts a turgor pressure against the walls, which builds up due to the osmotic pressure caused by the large concentration of solute inside the cell. It is assumed that the stress formed by the turgor pressure induces a plastic elongation of the cell walls [117, 155]. As microfibrils build highly parallel structures the elastic modulus of the cell walls can be anisotropic favoring certain directions. Therefore, plant tissues are assumed to behave like a plastic medium that undergoes irreversible deformations. However, there is evidence that cellulose microfibril deposition is guided by cortical microtubules [38, 80, 144], which themselves are observed to align to the axis of main stress in the plant tissue [35, 83]. Hence, plant tissue is not simply an elastic network, moreover the anisotropy of the elastic modulus is subjected to biological feedback rules. The feedback regulation supposedly modifies the elastic modulus such that cells preferentially grow perpendicular to the main stress. The elastic modulus is also affected by biochemical signals such as expansin or auxin [105] which in their course of action loosen the cell wall and may therefore locally increase volume growth.

Similarly also animal cells have been found to react to stress by inducing gene expression [45, 58, 208] or performing tension-sensitive signaling [55, 189]. Thus stress profiles may act as morphogenetic fields that provide positional information to determine size and shape of organs in cooperation with biochemical profiles. The most powerful biochemical substance in plants orchestrating numerous developmental processes is the hormone auxin.

### 3.3 Auxin dynamics

The plant hormone auxin takes a multifunctional role throughout plant development. This multiple influence does not arise by pre-patterning the plant with distinct concentration gradients. But auxin is rather continuously transported and accumulated within plant tissues. The peculiarity is that this auxin transport is polar, a polarity that is both induced and expressed by an oriented flow of auxin.

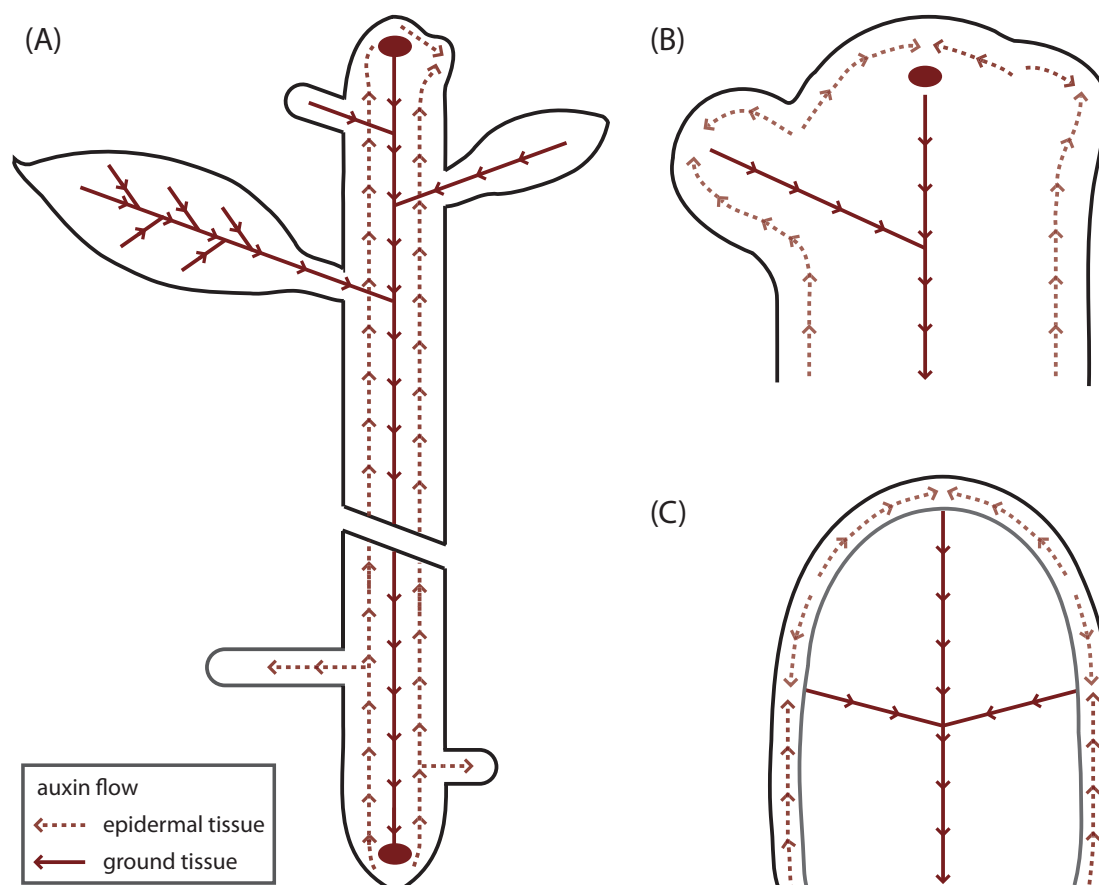


**Figure 3.3:** Patterns of auxin flow in plants. (A) A sketch of the overall plant including both root (lower part) and stem (upper part) and detailed cartoons of the shoot apex (B) and the leaf primordium (C). The continuous flow of auxin from leaves and shoot tip to root tip orients the plants and patterns root initiation sites, leaf position along the stem, and veins within leaves. In the shoot apex the site of a new leaf is marked by auxin in flow into the epidermal layer followed by the initiation of vein formation into the ground tissue. In leaves auxin accumulates in so called auxin convergence points in the epidermal layer from which it flows into the ground meristem tissue triggering vein initiation.

Early on in plant development an auxin flow from shoot to root [67] establishes an auxin maximum which designates and maintains the root apical meristem [166]. Later auxin produced in the developing organs, for example in leaves, is transported along cell files associated with the plant vascular system down the stem in the root apical meristem to maintain the auxin accumulation [71, 114], see illustration in Fig. 3.3 (A). At the root the amount of auxin shipped from the leaves induces the growth of lateral roots to ensure an appropriate root-shoot balance [15]. Auxin is cycled at the root tip upwards into the epidermis [79], thereby controlling cell elongation and initiation of root hairs [18]. Similarly, at the shoot tip auxin is cycled from the meristem tissue to the epidermis, where

its accumulation designates sites of leaf initiation [87, 156], see the schematic drawing in Fig. 3.3 (B). These initiation sites form areas of high auxin production, which subsequently become the site of auxin outflow towards the existing vascular system in the stem. Thereby, the development of the vascular system of the developing leaf is induced [173, 174], see Fig. 3.3 (C). On top of the leading role of auxin in plant construction, auxin is also an important factor in plant adaptation to light (phototropism) or gravity (gravitropism) stimuli by locally enhancing growth [68, 190].

Unfortunately auxin can yet only be radioactively labeled. Therefore, our understanding of auxin triggered processes relies on application of synthetical auxin or on the observation of the mediator of polar auxin transport, proteins from the PIN family. These PIN proteins polarly localize within cells with their majority facing the direction of auxin transport [148, 205]. Hence, imaging of GFP fused PIN proteins gives a valid estimate of the routes of auxin. The course of auxin is now considered in the particular cases of the leaf initiation at the the shoot apical meristem and in the developing leaves.

### **Auxin flow in the shoot apical meristem**

Auxin regulated leaf primordia initiation mainly occurs in the epidermal layer of the peripheral zone of the shoot apical meristem. Auxin flows from the internal tissue layers to the epidermal layer [8, 156], where it accumulates in maxima at the position of incipient leaf primordia [11, 87, 183] as depicted in Fig. 3.3 (B). PIN1 proteins are dominantly polarized towards the tip of the developing primordia, thereby, depleting the next adjacent region from auxin. Thus, the region surrounding the primordium is deprived of the growth hormone auxin and the next primordium forms only a distance away, the cause for phyllotactic patterns.

During the successive growth of the leaf primordium gradually a new PIN1 dependent auxin flow route builds up from the tip of the bulge towards the inner stem. This designates the new route of yet to develop vascular tissue that connects the new organ to the pre-existing vascular network [11, 87]. This scenario is similar to the vein initiation observed during leaf vascularization.

### **Auxin flow in the developing leaf**

At each step during the hierarchical vascularization of leaves [133] future vascular cell areas are marked by polar PIN1 distribution indicating auxin flow out of the leaf towards pre-existing veins [173, 174, 202]. That auxin is a key signal for vascular tissue formation has been shown by external auxin application [168], disruption of directed auxin transport [46, 71, 121, 181], auxin signaling [84, 90, 152] and auxin biosynthesis [32].

Vein formation is triggered by the inflow of auxin from auxin accumulation sites in the

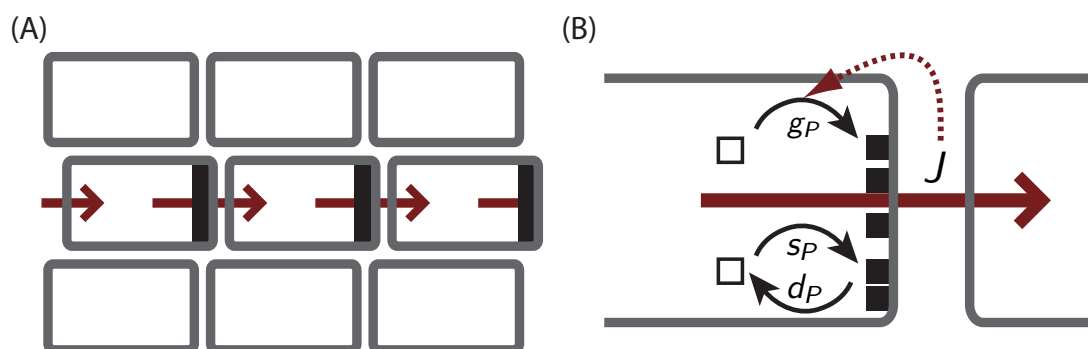


**Figure 3.4:** Auxin transport and canalization model. (A) Auxin flow (*red arrow*) is guided by the polar distribution of PIN proteins (*black boxes*) within cells. (B) The canalization model assumes, in addition to basal synthesis  $s_P$  and degradation  $d_P$  rates of PIN molecules on a membrane, a positive feedback of the auxin flow  $J$  on an enhanced synthesis rate  $g_P$  resulting in a polar distribution of PIN molecules.

epidermal rim of a leaf [5], see illustration in Fig. 3.3 (C). Close examination reveals that PIN1 proteins polarize first just at the site of auxin inflow. Only at later time steps does the PIN1 polarization extend up to pre-existing provascular tissue [174]. Hence, although differentiation of provascular tissue starts at pre-existing veins, vein initiation originates at the sites of auxin inflow. The vein initiation is a remarkable example of the feedback between auxin and its efflux facilitator PIN.

### Auxin transport and feedback

Auxin, indole-3-acetic acid (IAA), is itself a small weak acid. In the presence of the slightly acidic extracellular environment (pH 5.5) auxin is protonated and can easily penetrate a cell's membrane, as it is an uncharged, small molecule. Inside the cell the more alkaline environment (pH 7) leads to auxin ionization trapping the now charged molecule [154, 162]. Therefore, auxin accumulates within cells and can only travel to neighboring cells with help of efflux carriers located in the cell membrane [76, 77].

Membrane bound proteins from the PIN protein family have been identified to play the role of an auxin efflux mediator [137]. These proteins are polarly distributed within the cell membrane facilitating a directed transport of auxin along a file of cells, *e.g.*, down the center of the stem. Moreover, PIN is connected via multiple feedback loops to auxin, as auxin regulates PIN transcription [199] and most importantly PIN localization [142, 172, 174]. Hence, auxin not only exhibits but also induces its own polar transport via a feedback mechanism.

Auxin's feedback on its own efflux carrier has been hypothesized by Sachs [167] long before the discovery of PIN proteins. To explain venation patterns Sachs proposed that auxin flow itself enhances its own flow. Thereby, auxin locally activates its flow but on the other

hand also detracts flow from immediate neighbors and inhibits flow along parallel files of cells, see Fig. 3.4 (A). This scenario is similar to the flow of water on an eroding bed of sand giving rise to the name canalization model. Mitchison first formalized this hypothesis by describing the change of the concentration of auxin efflux carriers  $P_i(n)$  at a wall  $i$  in cell  $n$  due to basal synthesis  $s_P$ , degradation  $d_P$  and enhanced synthesis  $g_P$  [126, 127],

$$\frac{d}{dt}P_i(n) = -d_P P_i(n) + s_P + \begin{cases} g_P J_i^2(n) & \text{if } J_i(n) > 0 \\ 0 & \text{else} \end{cases}, \quad (3.2)$$

as sketched in Fig. 3.4 (B). Positive outflow towards the neighboring membrane  $j$  of cell  $m$  increases the efflux carrier synthesis rate proportional to the square of the auxin flow, which is itself proportional to the active efflux carriers:  $J_i(n) = P_i(n)A(n) - P_j(m)A(m)$ . Mitchison noted the necessity of a non-linear feedback and chose the square of the auxin flow. He and numerous other people [61, 69, 70, 100] confirmed in lattice simulations that these or similar dynamics do generate venation patterns. However, those models did not predict looped, closed veins. The puzzle of closed veins was attacked in simulations by introducing additional factors [60], pre-patterned auxin sinks [49] or patterned and/or moving auxin sources [160, 164].

To model auxin and PIN dynamics during phyllotactic pattern formation a new kind of feedback term was recently suggested [97, 183], where the auxin concentration in the neighboring cell increases the number of efflux carriers facing that neighbor. Simulations of these kind of concentration driven feedback dynamics reproduce phyllotactic patterns [41, 97, 183] and also show efflux carrier polarization fronts [123]. The debate between the different feedback mechanisms led to simulations that integrate both mechanisms [9, 52], simulations showing that pure canalization model produces phyllotactic patterns [188] and alternative approaches [101].

Common to all these investigations is a very limited knowledge of the model parameters' physical value. Except for a single very recent work considering the auxin concentration induced feedback [169] the plausibility of the feedback mechanism and the contributing terms chosen have only been assessed by computer simulations. Analytic investigations of the non-linear and pattern formation dynamics, however, offer predictions independent of the parameter choice. As our work shows, analytic calculations disclose the role and dominance of each term in the microscopic dynamics. Even quantitative predictions are possible, which may help to identify the magnitude of the physical parameters.

### 3.4 Pattern formation

Feedback and internal energy sources which are present in multiple biological and chemical processes create the basis for a huge variety of pattern formation. Considering a completely homogeneous medium that is relaxed into its stable, uniform, stationary state two distinct classes of dynamics can emerge: stable patterns or traveling waves. Which phenomenon

may occur depends on the characteristics of the medium [37, 124, 211]. If a stationary state is linearly unstable small fluctuations cause dissipative time-stationary patterns or sequences of circular waves. If on the other hand a system is linearly stable traveling waves may propagate without diminution when excited by an external impulse.

Both types of patterns, dissipative time-stationary or traveling waves, have numerous examples. In a first advance to explain the development of patterns during animal morphogenesis Turing [196] laid the foundations to explain various types of stationary spot and stripe patterns, similar to those observed in animal coats [129] and sea shells [122]. Also phyllotactic patterns in plants have been modeled as dissipative structures arising due to mechanical [179] and/or auxin based feedbacks [134].

The most prominent example for traveling waves propagating in so-called excitable media is nerve conduction. Based on the quantitative description of nerve excitations by Hodgkin and Huxley [91] more and more simplified and analytical tractable models have been developed to explain the excitation of a single wave pulse or a wave train [62, 130, 158]. Chemical reactions are a field where theoretical analysis of reaction equations and experimental observations can lead to vast agreement as is observed in the case of the famous chemical oscillator, the Belousov-Zhabotinsky reaction [10, 210].

In mathematical terms the patterns and waves observed are variations in the concentrations  $c_i$  of a set of reactants/hormones/morphogens  $i = \{1, \dots, n\}$ . As a simplification, their dynamics are homogeneous in space, such that the rate of change of concentration  $c_i(x)$  is governed by the same partial differential equation at every point  $x$  in space. The most general form for such a deterministic system of coupled equations is given by,

$$\frac{\partial c_i}{\partial t} = f_i(\nabla \mathbf{c}, \mathbf{c}) + \nabla(D_i \nabla c_i) + I_i(t). \quad (3.3)$$

The feedback may it be enhancing or antagonistic is subsumed in the nonlinear function  $f_i(\nabla \mathbf{c}, \mathbf{c})$ . Diffusion in space is reflected by the second term, while an external stimuli applied to the system is presented by  $I_i(t)$ . Apart from the generalized set of equations most systems considered display the following simpler structure,

$$\frac{\partial c_i}{\partial t} = f_i(\mathbf{c}) + D_i \nabla^2 c_i + I_i(t), \quad (3.4)$$

consisting of a space independent reaction term  $f_i(\mathbf{c})$ , external input  $I_i(t)$  and homogeneous diffusion  $D_i \nabla^2 c_i$  only.

The fundamental characteristics of such a system are identified by analyzing the so-called point system, where any spatial variance is neglected,

$$\frac{\partial c_i}{\partial t} = f_i(\mathbf{c}). \quad (3.5)$$

A point system can be prepared by carefully mixing all reactants. The roots of the functions  $f_i(\mathbf{c})$ ,  $i = 1, \dots, n$  determine the number of uniform stationary states, while the nullclines mark those lines along which one single reactant is stationary  $\partial c_i / \partial t = 0$ .

To observe traveling wave phenomena the reaction term has to display one minimum in at least a single reactant concentration. If this is the case, external excitations above a certain threshold relax via a deflected path back to the initial state. The exact shape of such a path is then determined by the system characteristics only and is independent of the excitation pulse form and duration.

The diffusion term plays an important role both in dissipative patterns and traveling waves. Diffusion is the cause for a propagating wave in space. By diffusion an excited point in space can infect its neighbor and excite this point as well. Since excitable media usually display a refractory period, to replenish substrate for example, waves can once started only travel in one direction. At the site of ignition, excitation of waves to multiple directions is however possible. This is a fact that becomes of importance concerning the formation of looped veins in our work.

While traveling wave systems exhibit linearly stable stationary states, it is just the diffusion term which may drive a stationary state of a dissipative system to become unstable such that small fluctuations can build up to form periodic patterns.

Despite the innocent appearance of the governing equations (3.3, 3.4) analytical solutions are very sparse and turn particularly hard if the number of reactants or the dimensions of space increases. One successful simplification is to discern fast and slow processes [27, 139]. Thereby, an entire wave pulse can be subdivided into a series of individual phases. In a phase where the fast variable changes, the slow ones are constant, while in a phase where the slow variable varies, the fast one can be approximated by its quasi-stationary values. This is an approach that leads to our success concerning polarization waves during the initiation of veins.

### 3.5 Vein initiation by polarization wave front

We investigate structuring of cell ensembles by feedback governed cell differentiation in the case of vein initiation by auxin and PIN dynamics. The corresponding manuscript [4] under the title “Quantitative predictions on auxin-induced polar distribution of PIN proteins during vein initiation in leaves” is accepted for publication in the special issue on “Physics of morphogenetic processes in animals and plants” in *European Physical Journal E* and reprinted together with its corresponding supplementary information in section 3.8 of this work. During leaf development auxin accumulates in the outer epidermal layer in so called convergence points. From these points auxin flows into the underlying ground meristem tissue. There auxin propagates the successive polarization of PIN distributions in cell membranes, locally initiated from the point of auxin influx [174], see reproductions in Fig. 3.5. This dominantly one dimensional process along a file of cells is amenable to a study of the underlying non-linear dynamics and enabling quantitative predictions.

To describe auxin  $A$  and PIN  $P$  concentration and their dynamics we consider a minimal canalization model. In addition to the initial description of Mitchison [126, 127] as stated



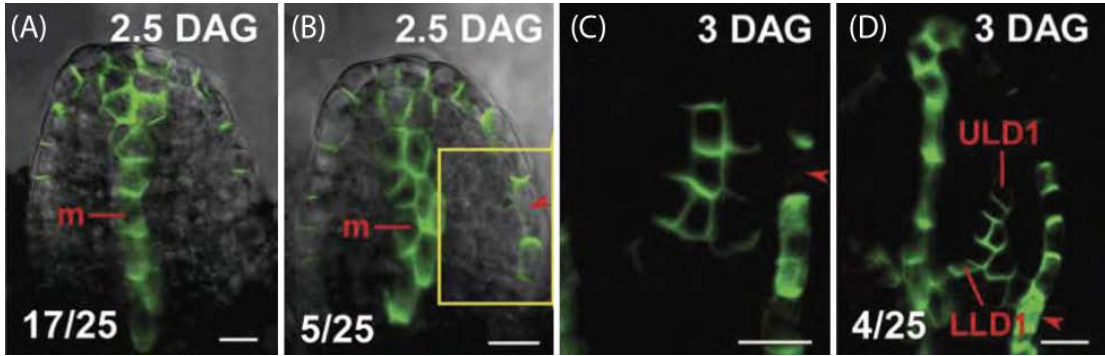


**Figure 3.5:** Patterns of polarly distributed GFP-marked PIN proteins during vein initiation in leaf primordia observed by light microscopy. During the earliest stage of leaf growth shown in (A) PIN is polarized towards the leaf tip in the epidermal layer. From there on PIN proteins are polarized towards the plant stem within the ground tissue. Successively, PINs in the epidermal layer reorganize to polarize towards a point further down the leaf rim, marked by the yellow box in (B). From this supposed auxin accumulation site onwards, figures (C)(zoom in) and (D) display the successive polarization of the ground tissue cells. Polarization initially starts at the site of auxin inflow from the epidermal layer. Scale bar 10  $\mu$ m. Reprinted with permission from [174].

in equation (3.2), we fully model auxin dynamics and discern PIN proteins in bulk and at the membrane. Except for the positive feedback term  $g_P$  all terms enter linearly, such as synthesis  $s_A$   $s_P$ , degradation  $d_A$   $d_P$  and transport  $e_A$  .

$$\frac{d}{dt}A(n) = s_A - d_A A(n) - \frac{e_A}{i} J_i(n) \quad (3.6)$$

$$\frac{d}{dt}P_i(n) = -d_P P_i(n) + s_P P_b(n) + \begin{cases} g_P P_b(n) J_i^2(n) & \text{if } J_i(n) > 0 \\ 0 & \text{else} \end{cases} \quad (3.7)$$

An illustration of this model is reprinted in our accompanying manuscript. Since the production of proteins such as PIN occurs on large time scales compared to the fast synthesis of auxin [150], we take the whole amount of PIN per cell to be constant. Thus  $s_P$ ,  $g_P$  and  $d_P$  describe the basal or enhanced attachment of bulk proteins  $P_b$  and the detachment of membrane bound proteins.

The analysis of our model along a one dimensional strand of cells reveals that each single cell is a bistable excitable medium. At rest a cell is in a non-polar state with no net auxin transport. However, cells can be excited into a polar constant flux state. This excitation is caused by a local auxin inflow and progresses in a traveling wave front. Depending on the auxin inflow gradient, full excitation pulses can also develop, in the course of these the excited cell relaxes back to its initial rest state. Form and velocity of traveling front or pulse on the contrary only depend on the underlying dynamic parameters and are not affected by the characteristics of auxin inflow. This observation is opposite to the

predictions that emerge from concentration driven feedbacks as such models only exhibit a single linearly unstable fixed point. Hence, in concentration feedback models auxin inflow can only transiently polarize PIN distributions. The amount of polarization then also strongly depends on the characteristics of auxin inflow.

Our analysis of the non-linear dynamics of auxin and PIN allows to identify the role of each microscopic process during PIN polarization. Heuristically polarization occurs due to the victory of directed, enhanced attachment over the undirected, basal attachment. However, the time scale of these attachment dynamics is a lot smaller than the time scale for the directional cue, which is the transport of auxin from one cell to the next. Hence, from a polar cell at a polarization front auxin is transported into the first non-polar cell just next to it. There auxin piles up as in a traffic jam because the cell has yet to become polarized by enhanced attachment before auxin can be transported onwards. Our rigorous mathematical results for the traveling pulse or front circumstantiate this heuristic picture. We give analytic results for the uniform stable states, the auxin amplitude in pulse and front and their velocity. Thereby, we relate macroscopic observables to the parameters of the contributing microscopic processes.

Finally, our description offers a simple explanation for the occurrence of bipolar cells, which represent the indispensable ingredient for the development of closed veins. At the site of auxin inflow the traveling polarization front can readily propagate in several directions. Depending on the initial conditions of PIN proteins in each membrane the competition for the bulk PIN proteins is biased and only a single membrane attains its polar stable state. But also two membranes could share the amount of PIN composing a bipolar cell. Experiments also suggest that mechanical cues could favor certain membranes [83].

### 3.6 Cell packing geometries in small groups of cells

We investigate how mechanical forces determine cellular structure under the condition of well-defined boundaries for small groups of cells. This work is based on a collaboration with experiments performed by Alicia Piera Aberola and Anna-Kristina Marel in the group of Joachim O. Rädler, LMU Munich. The manuscript under the title “Oligocellular arrays: A novel approach to explore cell tissue mechanics” is submitted for publication and reprinted with the accompanying supplementary information in this work in section 3.9. We model tissue mechanics by confining groups of up to four epithelial cells to quadratic adhesion patches. Cells reproducibly rearrange into distinct cellular structures, the most probable configurations are sketched in Fig. 3.6. The distribution of observed cell packing states depends only on the number of cells  $N$  per square and can be used to understand and even quantify mechanical forces within tissues.

The mechanical forces within epithelial tissues can be abstracted to bulk cell elasticity, resisting cell deformation, cell cortex contractility, driving the constriction to small perime-

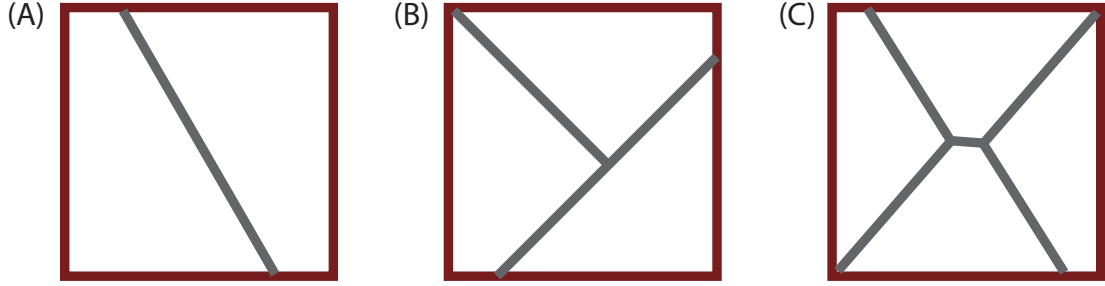


**Figure 3.6:** Most probable packing states for  $N = 2, 3,$  and  $4$  cells confined to a square adhesion patch. (A) In the trivial case of two cells the antagonism between cell cortex contractility and cell-cell adhesion determines the opening angle of the cell-cell contact line (*gray*) for two cells. (B) Additional elastic forces counteracting cell anisotropy then allow to favor the T-shaped arrangement of cells shown over a parallel ordering. (C) Four cells exhibit as an additional feature the loss of four-cell junctions in favor of two three-cell junctions a small distance apart.

ters, and cell-cell adhesion, favoring long cell-cell contact. In our experimental setting the total adhesive area is always distributed equally between all cells on a square, probably due to a dominating cell-surface interaction. This constrains the individual area of cells within their cellular organization and, therefore, initially diminishes the impact of cell elasticity. Hence, cell packing states are solely governed by the antagonistic action of cell cortex contractility and cell-cell adhesion. Minimizing the corresponding energy functional, see equation (3.1), is employed to model cell packing states for  $N = 2, 3,$  and  $4$  cells.

The congruent cell geometries for two cells on a square adhesion patch only differ in the angle the cell-cell contact line encloses with the confining square's edges. A parallel contact line satisfies minimal perimeter, *i.e.*, dominating cell cortex contractility, while a diagonal contact line allows for maximal contact line, *i.e.*, dominating adhesion. Competition between both results in intermediate angles as force balance state, as observed by us for epithelia Huh 7 cells. Comparison of the analytic prediction for the angle and experimental measurements yields the quantification of the ratio of cell cortex contractility to adhesion strength in the model. The symmetry of the adhesion squares generates eight mutually equivalent force balance states. Fluctuations of the cells drive transitions between and deviations around these states. The full distribution of states in ensembles and over time is in agreement with the model's prediction of the statistical weight of cell structures.

Three cells are by the geometry of the adhesion square forced to break the symmetry of equal area, perimeter and contact line as exhibited by two cells. Two classes of cell packing states with equally divided area are observed, parallel ordering and a T-shaped arrangement as shown in Fig. 3.6 (B). Based solely on the competition of cell cortex contractility and cell-cell adhesion parallel ordering of cell is energetically favorable over T-shaped in contrast to measured probabilities. However, the packing classes also differ fundamentally in cell anisotropy. Introducing an extended model by including an additional elastic

force counteracting cell shape anisotropy resolves this discrepancy and further consistently explains the high probability of additional Y-shaped cells.

The case of four cells serves as test case to assess the extended model initially introduced to explain the observed packing states of three cells. Indeed, the distribution of cell packing states of four cells on a square adhesion patch is bimodal, a characteristic only predicted by the extended model. Thus the notion that cell anisotropy is indeed a governing factor in cell mechanics is further substantiated. Moreover, four cells avoid four-cell junctions by forming two three cell junctions a small distance apart. This aspect is captured neither by the classic nor by our extended model. It is, however, intriguing to consider the statistical weight of states, directly related to their statistical entropy, which would clearly favor two three-cell junctions over the singular state of a four-cell junction.

Our work shows how a simplified tissue model enables direct evaluation and quantifications of tissue mechanics even on a single cell level. Observing the entire configuration space of a model tissue led us to the conclusion that elastic forces counteracting cell shape anisotropy are an important factor in cell tissue mechanics.

## 3.7 Outlook

Concerning cellular organization by differentiation our work focusses on the dynamics of the major regulator of plant development, the hormone auxin. The aim of this work was to derive both qualitative and quantitative predictions for the full physiologically reasonable space of parameters. Quantitative predictions are desirable as many of the kinetic processes involved in auxin dynamics are not accessible directly due to limitations in auxin labeling. At least estimates of the range of the kinetic parameters involved would be a huge step forward to assess the quality of theoretical predictions. But already qualitative predictions are indeed valuable, if they enable to discern between the different models of feedback. We hope that our predictions help to validate or falsify the kind of feedback governing auxin and PIN dynamics. Predictions and their validation should act as a precursor to universal understanding of auxin and PIN interactions. Indeed leaf site initiation at the shoot apex and vein initiation progressing from the leaf tip bear huge resemblances in their stages and processes suggesting common auxin and PIN dynamics at their origin. Several recent attempts targeted this issue [9, 52, 123, 188] but all are yet missing an unequivocal uniform formulation.

In addition to its role during differentiation, auxin acts as a growth hormone regulating cell division and volume growth. Thus, differential auxin concentrations can promote differential growth, which generates stresses in the elastic tissue. To explore the mechanism of development it is, therefore, mandatory to investigate how stress fields are generated and how they may orchestrate the growth of tissues into form. A recent initiative of us in this field is a study on the effect of stress on cell shape.

Concerning cell mechanics we took the promising approach to study one specific aspect in a well designed *in vitro* setup, where input and control parameter are much more regulated. Thus, the quantification of cell mechanics in individual cells becomes amenable. A concept that can be transferred to study the interaction between different cell types, an important aspect in cell therapy. Also the reduction to a small number of cells bears the advantage of turning the theoretical analysis a pure analytical or at most numerical investigation. Our investigation of a finite system reveals principles of cellular organization that should be transferred to the analysis of larger tissues. Modifying the boundary conditions in *in vitro* setups may also provide insight into the interaction between different tissue types. Following tissue growth over longer periods may clarify how cell mechanics control cell growth, death and the axis of cell division. An important aspect here seems to be to follow the generation of stresses and their relaxation.

Ultimately both auxin patterning and mechanics have to be studied in unison to understand plant development. The origins of the remarkable diversity of leaf shapes can only be revealed when integrating patterning of growth hormones and the plastic growth of plant cells. The development of plants offers a magnificent playground to investigate how the laws of physics and biologically optimized feedback enrich each other to generate form and structure.



# Quantitative predictions on auxin-induced polar distribution of PIN proteins during vein formation in leaves\*

K. Alim<sup>a</sup> and E. Frey

Arnold Sommerfeld Center for Theoretical Physics and Center for NanoScience, Ludwig-Maximilians-Universität, Theresienstr. 37, D-80333 München, Germany

Received 7 December 2009 and Received in final form 29 March 2010  
© EDP Sciences / Società Italiana di Fisica / Springer-Verlag 2010

**Abstract.** The dynamic patterning of the plant hormone auxin and its efflux facilitator the PIN protein are the key regulators for the spatial and temporal organization of plant development. In particular auxin induces the polar localization of its own efflux facilitator. Due to this positive feedback, auxin flow is directed and patterns of auxin and PIN arise. During the earliest stage of vein initiation in leaves auxin accumulates in a single cell in a rim of epidermal cells from which it flows into the ground meristem tissue of the leaf blade. There the localized auxin supply yields the successive polarization of PIN distribution along a strand of cells. We model the auxin and PIN dynamics within cells with a minimal canalization model. Solving the model analytically we uncover an excitable polarization front that triggers a polar distribution of PIN proteins in cells. As polarization fronts may extend to opposing directions from their initiation site, we suggest a possible resolution to the puzzling occurrence of bipolar cells, thus we offer an explanation for the development of closed, looped veins. Employing non-linear analysis, we identify the role of the contributing microscopic processes during polarization. Furthermore, we deduce quantitative predictions on polarization fronts establishing a route to determine the up to now largely unknown kinetic rates of auxin and PIN dynamics.

## 1 Introduction

The polar transport of the plant hormone auxin is the key regulator of many processes in the spatial and temporal organization of development and growth of plants. As the indole-3-acetic acid, in short auxin, induces the polar localization of its own efflux facilitator, a member of the family of PIN proteins, a variety of auxin and PIN patterns arise [1]. Those distributions change dynamically as plants orient in response to environmental stimuli denoted as tropism [2,3]. During the morphogenesis of plants PIN and auxin rearrangements lie at the heart of organ positioning via phyllotaxis [4] and vein patterning in leaves [5].

The notion that auxin is transported in a polar, directed, manner inspired researchers since its discovery by Went in 1933 [6]. Early works already suggested the participation of a polar localized efflux carrier in the transport of auxin [7–9], well before its discovery in the form of membrane bound PIN proteins a decade ago [10]. Since then numerous experiments confirmed that PIN proteins facilitate the efflux of auxin from cells in plants [11,2,12,13,4], yeast and mammalian cells, which had been supplied with

auxin and PIN [14]. A feedback between auxin and its efflux facilitator localization was proposed by Sachs in his canalization hypothesis [15], later formalized by Mitchison [16,17]. Canalization predicts a feedback of auxin flow between neighboring cells on the amount of efflux facilitators favoring the direction of auxin flow. Experiments confirmed a definite feedback between auxin and PIN distribution [18,19], the cause of which is reported to lie in auxin affecting the clathrin-dependent endocytotic cycling of PIN [20,21]. Late investigations also identified biochemical processes taking part in the PIN localization in response to auxin, see ref. [22] for a review.

A variety of microscopic models for the dynamics of auxin and PIN proteins have been developed to describe their patterns during phyllotaxis [23] and leaf vein formation [24], see [25] for a review. Extensive simulations of these microscopic models describe qualitative aspects of plant development. However, the role of the underlying biological processes and their kinetic rates still remain elusive to a large extent. Quantitative predictions based on analytical solutions of the microscopic equations in a simple scenario might on the one hand help to estimate kinetic parameters and on the other hand give insight into the impact of certain processes. A scenario amenable to such an investigation is the polarization of the, in this particular case, PIN1 distribution due to auxin flow in the

\* Supplementary material in the form of a .pdf file available from the Journal web page at

<http://dx.doi.org/10.1140/epje/i2010-10604-5>

<sup>a</sup> e-mail: karen.alim@physik.lmu.de

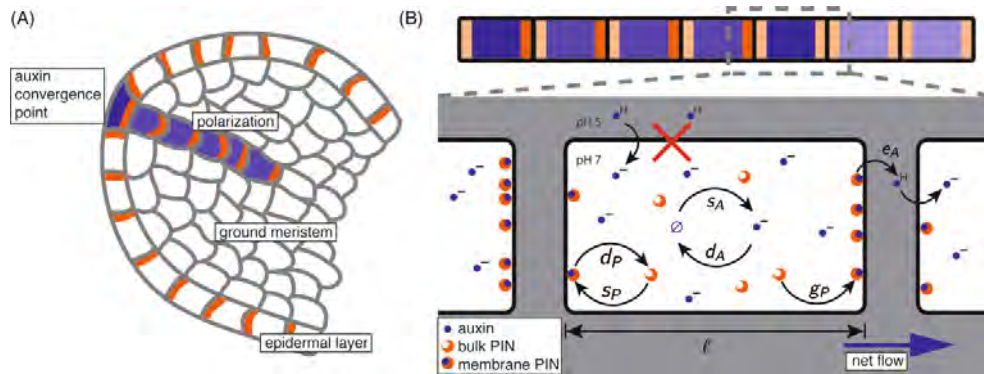


**Fig. 1.** (Colour on-line) Illustration of the dynamics of auxin and its efflux facilitator PIN. (A) Schematic drawing of vein initiation in a leaf primordium. Auxin (blue) accumulates at convergence points in the outer epidermal layer (*rim*), from which it is transported into the ground meristem. Due to this inflow of auxin, ground meristem cells become polarized in their PIN distribution (orange). (B) Polarization of PIN distribution in a strand of cell due to auxin inflow from the left, indicating details of auxin and PIN dynamics. The weak acid auxin accumulates in the interior of a plant cell due to a gradient in  $pH$ . In the inner cell the charged anion is trapped and can only be transported outwards by the help of efflux facilitators in the form of PIN proteins. The auxin transport from cell to cell has an efficiency  $e_A$ . Auxin synthesis  $s_A$  and degradation  $d_A$  takes place in the inner cell. PIN proteins cycle between the bulk and the cell membrane by basal attachment  $s_P$  and detachment rates  $d_P$ . In addition, positive auxin net flow is modeled to feed back on these rates increasing the PIN attachment by  $g_P$ . Along the strand of cells the color shading indicates relative concentration of auxin and PIN on either membrane.

earliest stage of vein formation [26], see fig. 1. Vein initiation itself takes place in the ground meristem tissue of leaf primordia. The positions of vein initiation sites are determined by auxin accumulation in “convergence” points, which lie in a rim of epidermal cells around the ground meristem tissue [19, 27–29]. These single cells with high auxin concentration polarize towards the ground meristem and locally transport their auxin into a cell in the ground meristem tissue. This localized inflow triggers the successive polarization of PIN distributions along a strand of cells starting from the cell with auxin inflow [19]. The strand of polarized cells finally extends up to a previously existing strand of polarized cells, building the pre-pattern for the vascular network. Starting from the petiole of the leaf primordium the polarized cells differentiate then into vascular cells [30]. In particular, second-order veins in *Arabidopsis thaliana* exhibit PIN polarization in opposite directions starting from a single bipolar cell, which lies in the ground meristem below the auxin convergence point in the epidermal layer [19]. This yet unresolved behavior gives rise to the formation of closed vein loops when both oppositely polarized strands connect to already formed veins.

A resolution on the origin of bipolar cells is postulated by examination of a minimal canalization model for the polarization of PIN distribution due to auxin supply in a one-dimensional strand of cells. Performing a non-linear analysis of the model reveals for each single cell two uniform stable states considering polarization. One resting state, where efflux facilitators are symmetrically distributed within the cell, and one polar state characterized by a constant net transport of auxin due to a polar localization of PIN proteins. The model predicts auxin triggered polarization pulses and fronts as a consequence

of a dynamic rearrangement of PIN efflux facilitators towards the polar state. Cells with continuous auxin supply can be in a dynamic bipolar state, from which polarization fronts travel to both ends of a strand of cells. The role of the underlying kinetic processes becomes explicit in the course of the non-linear analysis of the polarization. An analytic solution results in quantitative predictions on the pulse’s and front’s auxin amplitude depending on the kinetic parameters, establishing a basis for detailed experimental determination.

## 2 Model

To describe how auxin polarizes the distribution of PIN during vein formation, we focus on a one-dimensional strand of cells, see fig. 1(B), assuming that there is no net auxin flow perpendicular to the direction of polarization. The strand is subdivided into cells of length  $\ell$  numbered by  $n$ . Every cell is characterized by a single auxin concentration  $A(n)$  and the concentration of membrane bound PIN proteins. We distinguish between PIN proteins in the bulk of the cell  $P_b(n)$  and adsorbed to the cell membrane either on the right-hand side or on the left-hand side of the cell,  $P_r(n)$ , and  $P_l(n)$ , respectively. The auxin concentration per cell changes due to synthesis and degradation with rates  $s_A$  and  $d_A$ . Furthermore, the amount of auxin changes due to a net flow to neighboring cells facilitated by PIN proteins embedded in the cell membranes of the corresponding cell-cell interface. The net flow from cell  $n$  to cell  $n + 1$  is, hence, given by  $J(n) = e_A[A(n)P_r(n) - A(n + 1)P_l(n + 1)]$ , where  $e_A$  denotes the transport efficiency rate across the cell-cell



interface. The full auxin dynamics is then described by

$$\frac{d}{dt}A(n) = s_A - d_A A(n) - \frac{1}{\ell} [J(n) - J(n-1)]. \quad (1)$$

Stating these dynamics for auxin we assume that auxin transport is dominantly from one inner cell to the other. Auxin is known to accumulate in cell interiors [7, 31] since auxin is a lipophilic weak acid which easily enters cells as undissociated acid, its prevailing form at the pH of 5 in extracellular space. In the interior of plant cells ion pumps keep the pH at 7, leading to the ionization of auxin and building a concentration gradient that accumulates auxin inside cells. As lipid membranes are impenetrable for the now charged molecule, auxin is trapped in the cell's interior rendering efflux facilitator necessary. Being exported by PIN proteins, auxin is free to diffuse in the extracellular space, the apoplast. However, the distance between neighboring cells is so small that almost all auxin molecules have entered any cell again within one millisecond<sup>1</sup>. Furthermore, auxin can be assumed to be approximately uniformly distributed within typical cells because the diffusion of the small molecule auxin is very large. In aqueous solutions  $D = 670 \mu\text{m}^2/\text{s}$  has been measured [34] which has been confirmed by indirect measurements of the diffusion constant in auxin transport experiments [35]. Distinct auxin gradient would therefore only arise for large plant cells of about  $100 \mu\text{m}$  or larger. It is not entirely clear that this reasoning holds under the condition of highly effective auxin transport [36], however, the time scale of auxin transport by mere diffusion through a cell of typical  $50 \mu\text{m}$  is 4 s, faster than other process contributing to the polarization of PIN, substantiating the neglect of auxin gradients within cells during PIN polarization. Hence, we can approximate auxin flow to be dominated by cell-to-cell transport. Synthesis and degradation of auxin are considered since they take place on fast time scales as the majority of auxin is stored in its conjugated form inside the cell which is readily hydrolyzed in less than seconds [37]. This is in contrast to the production and degradation of PIN proteins, which takes place on much larger time scales of several minutes. We therefore model the total amount of PIN proteins  $P_{\text{tot}}$  to be constant per cell, yielding the following equality for the number of free PIN proteins in the bulk  $P_b(n) = P_{\text{tot}} - P_r(n) - P_l(n)$ . Hence, we only consider the dynamics of PIN proteins embedded in a cell membrane. Their concentration changes first of all by a basal adsorption rate  $s_P$  and a basal desorption rate  $d_P$ . Addi-

<sup>1</sup> The importance of extracellular diffusion of auxin can be assessed by estimating the residence time of auxin in extracellular space. Assuming an auxin molecule diffuses with diffusion constant  $D = 67 \mu\text{m}^2/\text{s}$  [32] in a typical cell-cell interface of  $0.5 \mu\text{m}$ . If it comes close to either of the cells the molecule may re-enter. Taking into account that not all extracellular auxin molecules are protonated and hence able to penetrate the membrane, we assume the probability to enter a cell to be of 10% [31, 8]. Considering these assumptions already 97% of all auxin molecules have re-entered any cell including the one they were delivered from after a time duration of one millisecond [33].

tionally, the net auxin flow over a cell-cell interface is modeled to feed back onto the amount of PIN proteins favoring the flow direction. This is cast in an enhanced attachment or equally a decreased desorption rate:  $g_P J^2(n) \theta(J(n))$  as proposed by canalization models [15–17, 24, 38–40, 26]. By imposing the Heaviside step function  $\theta$ , the feedback reacts to positive net flow only. For the following analysis the feedback is proportional to the square of the net auxin flow as stated below. In the discussion we explain that any exponent larger than one yields analogous results. Different feedback mechanisms proposed recently [23, 41–43] are also compared to our approach in the discussion. Incorporating the positive feedback on auxin flow, the PIN dynamics are given by

$$\begin{aligned} \frac{d}{dt}P_r(n) &= -d_P P_r(n) + s_P P_b(n) \\ &\quad + g_P J^2(n) \theta(J(n)) P_b(n), \end{aligned} \quad (2)$$

$$\begin{aligned} \frac{d}{dt}P_l(n) &= -d_P P_l(n) + s_P P_b(n) \\ &\quad + g_P J^2(n-1) \theta(-J(n-1)) P_b(n). \end{aligned} \quad (3)$$

Except for the non-linear feedback term, we assumed throughout the model setup linear relationships as a first-order expansion to the yet elusive detailed underlying dynamics. We refer to the discussion for an analysis of model modifications confirming the robustness of our assumptions. In contrast to many existing canalization models [16, 17, 38–40, 26] we account for the detailed PIN cycling by endosomes similar to ref. [24], however, we discard the explicit dynamics of a putative auxin synthesizer used in that work.

Up to now our model involves six kinetic rates, however, rescaling the concentration of auxin  $a = A/A_{\text{eq}}$ , where  $A_{\text{eq}} = s_A/d_A$ , and PIN proteins,  $p_{r,l} = P_{r,l}/P_{\text{tot}}$ , as well as time  $\tau = t d_P$  reveals that only four independent, dimensionless parameters govern the behavior of auxin and PIN dynamics, namely  $\delta_a = d_A/d_P$ ,  $\sigma_p = s_P/d_P$ ,  $\gamma_p = g_P A_{\text{eq}}^2 P_{\text{tot}}^2/d_P$ , and  $\epsilon_a = e_A P_{\text{tot}}/\ell d_P$ . Quantitative knowledge of the kinetic rates is very sparse. Half-life measurements of auxin yield estimates for its degradation rate,  $d_A = 2 \cdot 10^{-4} - 2 \cdot 10^{-5} 1/\text{s}$  [44], which is however strongly affected by environmental conditions such as light, wind, and temperature. Permeability measurements [45, 32] of PIN-assisted auxin anion transport are found to be  $e_A P_{\text{tot}} = 1.4 \mu\text{m}/\text{s}$ . For the other kinetic rates no experimental estimates are available to the best of our knowledge although various rates have been assumed in simulations. This limited knowledge of the kinetic rates underlying auxin and PIN dynamics demonstrates how desired an intuition of their relation and role is, which can be obtained from mathematical analysis, opening up new approaches for experimental measurements.

## 3 Results

### 3.1 Observations from numerics

During vein formation auxin supplied from the outer epidermis enters a single cell initiating the polarization of a

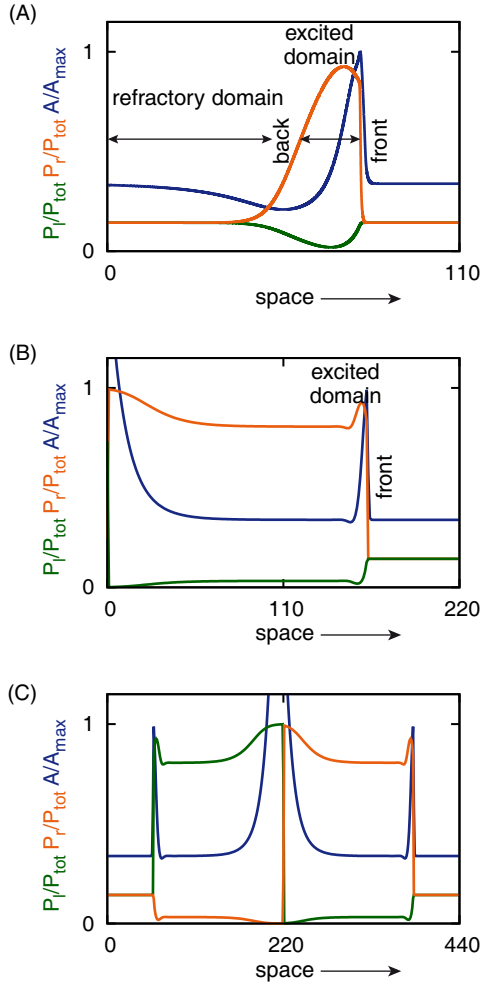


**Fig. 2.** (Colour on-line) Spatial trajectory of polarization pulse and fronts. Auxin (blue) and PIN concentration on the left- (green) and right- (orange) hand side of a cell are displayed along a strand of cells numbered by their distance in cells from the site of initiation. (A) A short, initial supply of auxin to a single cell yields a single polarization pulse, while (B) a continuous, high inflow of auxin from one end (left) yields a polarization front. (C) Continuous supply at a center cell results in two opposite polarization fronts originating from a single bipolar cell. Trajectories arise from the numerical integration of our mathematical model for parameters values  $d_A/d_P = 0.2$ ,  $s_P/d_P = 0.2$ ,  $e_A P_{tot}/ld_P = 2$ , and  $g_P A_{eq}^2 P_{tot}^2/d_P = 8$ . Initial and continuous auxin supply of  $A = 20A_{eq}$ .

cell strand [19]. We simulated this scenario by integrating the microscopic equations (1)-(3) numerically for different kinds of auxin supply, see fig. 2. Starting from a strand of cell with evenly distributed PIN proteins and an equilibrated amount of auxin, we shortly applied auxin by increasing the initial auxin concentration in a single cell. This triggers a polarization pulse which shortly polarizes the PIN proteins in each cell before all cells relax back to their initial non-polar state, fig. 2(A). Subsequent pulses can only be excited when the cells are almost relaxed back to their non-polar state, therefore a certain lag time is required (data not shown). If the auxin is supplied con-

tinuously by keeping the amount of auxin in a single cell at high level a polarization front forms. The front causes all cells which it passed to become permanently polarized, fig. 2(B). If a cell in the center of a strand of cells is continuously supplied with auxin, two fronts arise traveling to opposite directions along the strand, fig. 2(C). The latter two observations resemble those from vein formation [19].

As the polarization pulse and front bear a lot of characteristics in common, deriving analytic solutions for the first gives also quantitative insight into the second. In the following our non-linear analysis explains the formation of a polarization pulse, we derive quantitative results for pulse and front properties. Observations in fig. 2(A) and (B) indicate that changes in concentration of PIN proteins on the left,  $P_l$ , facing adverse to the direction of transport, are very small. We therefore assumed in our following analysis  $dP_l(n)/dt = 0$ , *i.e.*, considering the stationary state value  $P_l(n) = \sigma_p(1 - P_r(n))/(1 + \sigma_p)$  for a polarization traveling to the right.

### 3.2 Static state of a single cell

Assuming a uniform state for a whole strand of cells, each single cell itself has two stable and one unstable equilibrium state, as shown in fig. 3(A). The first stable fixed point at

$$\begin{aligned} a^{\text{RES}} &= 1, \\ p^{\text{RES}} &= \frac{\sigma_p}{1 + 2\sigma_p}, \end{aligned} \quad (4)$$

is a resting state, where PIN proteins are evenly distributed and no net auxin flow occurs. For parameters beyond  $\gamma_p \geq 4(1 + 2\sigma_p)$  two further crossings of the nullclines  $dA/dt = 0$  and  $dP_r/dt = 0$  occur in a saddle-node bifurcation, a pair of one unstable and one stable fixed point at

$$\begin{aligned} a^{\text{POL}\mp} &= 1, \\ p^{\text{POL}\mp}(a^{\text{POL}\mp}) &= \frac{1 + 3\sigma_p \mp (1 + \sigma_p)\sqrt{1 - \frac{4(1+2\sigma_p)}{\gamma_p(a^{\text{POL}\mp})^2}}}{2(1 + 2\sigma_p)}, \end{aligned} \quad (5)$$

respectively. At the second stable fixed point the PIN distribution is polar as  $P_r$  outnumbers  $P_l$  by at least  $P_{tot}/2$ , yielding a constant net flow of auxin to the right. The resting state originates from synthesis and degradation terms in eqs. (1)-(3), while the second pair of fixed points arises due to the feedback. As both the resting and the polar state are linearly stable, a uniform set of cells decays into one of them depending on the cells initial state. To the left of the unstable manifold embedding the unstable fixed point, depicted as dashed line in fig. 3(A), all cells relax to the resting state while to the right of this separatrix all states decay to the polar fixed point. This is true for a homogeneous set of cells, however, in a spatially inhomogeneous system complex scenarios such as waves and fronts arise [46, 47].

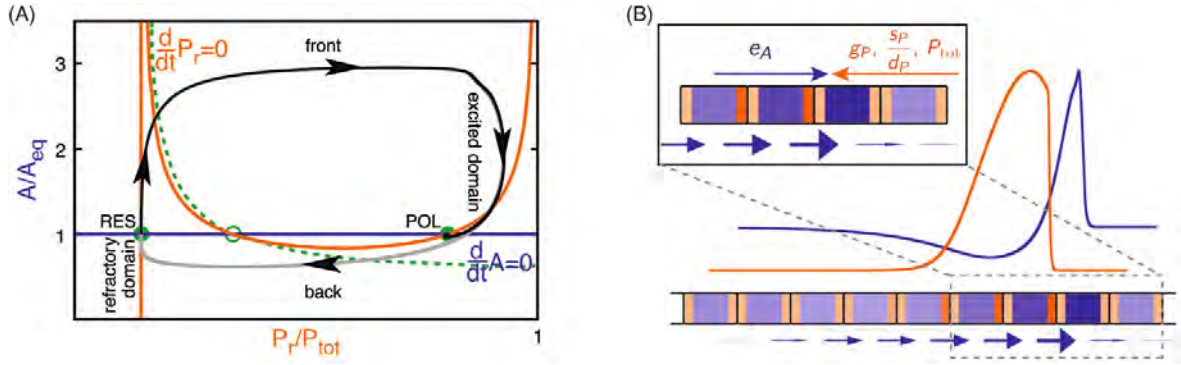


**Fig. 3.** (Colour on-line) Illustration of the non-linear characteristics of auxin-induced polarization. (A) Trajectory of a polarization pulse (grey) and front (black) in the nullcline graph obtained from integrating the microscopic equations. Each single cell has two linearly stable fixed points (solid green circle), a resting state with symmetric PIN distribution (RES) and a polar state with constant auxin flux (POL). Their areas of attraction are separated by an unstable manifold (green dashed line) embedding the unstable fixed point (open green circle). Parameters as in fig. 2. (B) Heuristic mapping of the numerical polarization pulse along a strand of cells. Auxin is piled up in a cell with even distribution of PIN on both cell membranes at the front of the pulse. Due to the slow attachment rates of PIN proteins  $g_P, s_P/d_P$  the cell is still non-polar. Increasing the attachment rates due to the positive feedback of auxin flow reduces the auxin amplitude. Growing cell-to-cell transport efficiencies  $e_A$  increase the auxin amplitude as more auxin reaches the peak per time step.

### 3.3 Dynamic transition

Due to spatial inhomogeneities passed on along a strand of cells from a cell with auxin supply, the state of a cell changes over time as a polarization pulse or front travels through. The trajectory of states of a single cell in time, fig. 3(A), maps onto the trajectory of a polarization pulse over a strand of cells in space, see fig. 3(B), allowing for a heuristic interpretation of the polarization dynamics. To investigate these dynamics, we performed the continuum limit of the microscopic equations (1), (2), see Supplementary material I for details. This gives rise to a set of partial differential equations, which describe the change of  $a$  and  $p_r$  at one point in space over time,

$$\begin{aligned} \frac{\partial}{\partial \tau} a(x, t) &= \delta_a (1 - a(x, t)) \\ &- \epsilon_a \frac{1 + 2\sigma_p}{1 + \sigma_p} \frac{\ell \partial}{\partial x} [(p_r(x, t) - p^{\text{RES}}) a(x, t)], \end{aligned} \quad (6)$$

$$\begin{aligned} \frac{\partial}{\partial \tau} p_r(x, t) &= -\gamma_p \frac{(1 + 2\sigma_p)^2}{(1 + \sigma_p)^3} a^2(x, t) (p_r(x, t) - p^{\text{RES}}) \\ &\times (p_r(x, t) - p^{\text{POL-}}(a)) (p_r(x, t) - p^{\text{POL+}}(a)) \\ &- \gamma_p \frac{\sigma_p^2}{(1 + \sigma_p)^3} (p_r(x, t) - 1) \left\{ \frac{\ell \partial}{\partial x} [(p_r(x, t) - 1) a(x, t)] \right\}^2. \end{aligned} \quad (7)$$

This time evolution depends on reaction terms, including only auxin and PIN concentration at the same specific point in space, and gradient terms which account for the influence of neighboring sites. The reaction terms cause the system to relax to its stable fixed points as described in the previous section. The gradient terms, however, drive the system along its pulse trajectory.

The following explains the dynamic transition and the role of reaction and gradient terms in it starting from a

cell in the non-polar resting state (RES). If the gradient in auxin and PIN to the neighboring cell is large enough the cell is forced out of its stable resting state to larger values of auxin entering the domain of attraction of the polar state (POL). If a neighboring cell has accumulated more auxin and has a higher amount of PIN facing the direction of the polarization pulse,  $p_r$ , it is very effective in transporting auxin onwards into a cell, raising the auxin content well above the equilibrium value. As the now auxin-supplied cell has itself more auxin to transport onwards, the net flux increases starting off the positive feedback which results in PIN polarization. The then fully polarized cell is very efficient in moving its excess auxin onwards, finally decreasing its auxin content towards the polar stable state. The neighboring cell that has been polar and transporting onwards auxin for a bit longer has less auxin, reversing the direction of the auxin gradient. If this auxin gradient is large enough, it drives the cell past its polar state into the domain of attraction of the resting state. Hence, if the amount of auxin in the neighboring cell is very low, the auxin supply breaks down and with it the onward flux of auxin. The positive feedback is decreasing and with it polarization towards the non-polar resting state. Subsequent polarization pulses can only be triggered if the polarization already saturated down to almost resting state values, otherwise the remaining polarization would just transport the applied auxin onwards before the positive feedback can build up an enhanced polarization of PIN proteins. The phenomenon that a system has to relax back to its resting state before a new pulse can be excited is denoted refractory phase in excitable media.

We find that the gradient terms in the auxin and PIN dynamics have unequal analytic structures that lead to their different functions. In the PIN dynamics the squared gradient increases spatial inhomogeneities in PIN distribution by augmenting  $p_r$  up to saturation. In the auxin

dynamics the signs of auxin and PIN gradients decide the direction of change in auxin concentration. In front of an excitation pulse the gradient induces a growth of auxin content, while it decreases the amount of auxin at the rear of the pulse. The magnitude of the auxin gradient also decides between the formation of a polarization pulse or front. If the auxin content in the neighboring cell is only slightly smaller due to continuous or only slowly varying auxin supply a constant flux of auxin through polar cells is established, a polarization front forms. If, however, the auxin gradient is large and the auxin inflow decreases drastically the feedback breaks down and the cells in the polarization pulse relax back to their resting state. In summary the polarization of PIN distribution by auxin flow is initially a bistable system that behaves like an excitable medium depending on the amount and continuity of auxin supply.

### 3.4 Analytical results

Identifying polarization dynamics as an excitable medium enables us to go beyond numerical integration of the microscopic equations and analytically compute the auxin amplitude of a polarization pulse or front. To this end, we employed singular perturbation theory [49, 50] on a polarization pulse. Here we explain the outline of the calculation, a detailed derivation is provided in Supplementary material I. The whole polarization pulse can be subdivided into four regions as shown in fig. 2(A) and fig. 3(A). First the front and back where the auxin concentration is nearly constant and only the number of PIN proteins changes significantly. Second the excited and the refractory domain during which the efflux facilitator concentration follows approximately the nullcline and hence only changes according to the nullclines' variation with the auxin concentration while the auxin concentration itself varies profoundly. Therefore, all four regions are governed to good approximation by just a single non-linear equation, the one of the PIN protein dynamics or the one of auxin dynamics, respectively. Unfortunately, even each single continuum equation is not analytically solvable. The model equations (6), (7) are therefore linearized around the stable nullclines yielding two sets of equations, one left to the unstable manifold and one right to it. By this linearization we overestimated the PIN dynamics close to the unstable manifold which leads to smaller auxin amplitudes than those resulting from the integration of the microscopic equations (1)-(3). An algebraic solution is obtained by imposing a traveling wave Ansatz  $A(x-vt)$ ,  $P_r(x-vt)$  and solving all four equations under the condition of differential continuity at their intersections. The calculation yields a closed expression for the auxin amplitude which captures the role of the underlying kinetic parameters:

$$\frac{A_{\max}^2}{A_{\text{eq}}^2} = \frac{\rho}{2} \left( 1 + \sqrt{1 + \frac{4^2}{\beta^2} \left[ 1 + \sin\left(\frac{\phi}{3}\right) - \frac{\cos\left(\frac{\phi}{3}\right)}{\sqrt{3}} \right]} \right), \quad (8)$$

where we abbreviated  $\rho = 4(1 + 2\sigma_p)/\gamma_p$ ,  $\beta = 16 \frac{1}{\epsilon_a} \frac{\sigma_p}{(1+\sigma_p)}$ ,

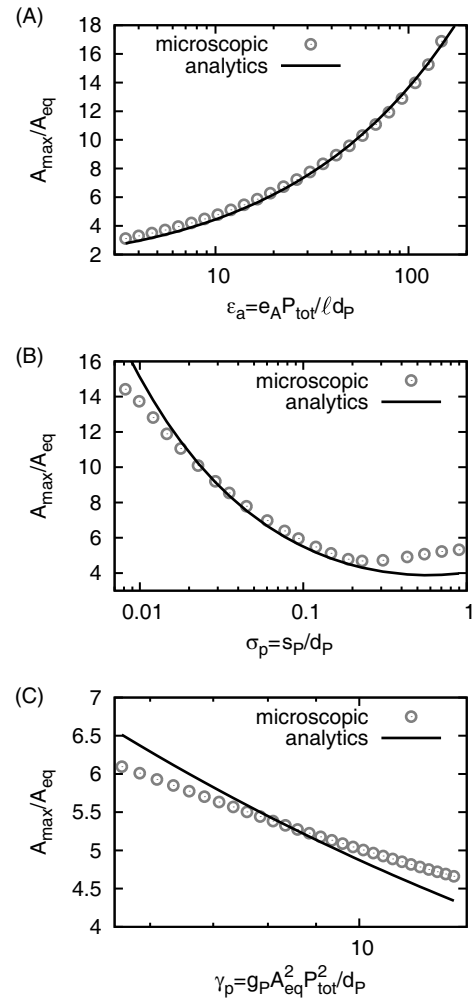


**Fig. 4.** Results for the auxin amplitude  $A_{\max}$ . The auxin amplitude  $A_{\max}$  varies during a polarization pulse or front with its independent kinetic parameters (A) transport efficiency of auxin  $\epsilon_a = e_A P_{\text{tot}} / l d_P$ , (B) basal attachment rate  $\sigma_p = s_P / d_P$  and, (C) enhanced attachment rate  $\gamma_p = g_P A_{\text{eq}}^2 P_{\text{tot}}^2 / d_P$ . Shown are results from the numerical integration of the microscopic equations and the analytic expression multiplied by an overall factor of 2.3. We considered  $\sigma_p = s_P / d_P \ll 1$ , such that only less than a third of all PIN proteins occupy each membrane in the resting state.  $\epsilon_p = e_A P_{\text{tot}} / l d_P > 1$  as auxin permeability  $e_A P_{\text{tot}} = 1.4 \mu\text{m/s}$  [45, 32] is roughly larger than endosome cycling by active transport along a cell's cytoskeleton  $l s_P$  [48]. We suggest  $\gamma_p = g_P A_{\text{eq}}^2 P_{\text{tot}}^2 / d_P > 1$ , as protein and auxin numbers might be very large. Finally, assuming literature values of  $d_A$  [44], endosome cycling, and taking cell length of tens of  $\mu\text{m}$ , we used  $d_A / d_P = 0.2$  to compare our results. Each graph shows the variation of a single parameter, while the remaining are kept constant at  $d_A / d_P = 0.2$ ,  $e_A P_{\text{tot}} / l d_P = 10$ ,  $g_P A_{\text{eq}}^2 P_{\text{tot}}^2 / d_P = 12$ , and  $s_P / d_P = 0.2$ .

and  $\phi = \tan^{-1}(-3\sqrt{3}\beta^2, \sqrt{2^{14} - 3^3\beta^4})$ . The analytic result is compared to the numeric integration of the microscopic equations (1)-(3) over a broad range of the kinetic parameters in fig. 4. Due to the linearization of the equations, the algebraic amplitudes are too low. Fitting the

analytic to the numeric results yields an overall factor 2.3. This constant factor does not depend on the specific parameter range. Considering the amount of approximations that entered the calculation, the analytic result captures very well the dependence on the kinetic parameters over orders of magnitudes. To obtain insight in how the magnitude of the kinetic parameters determines the amplitude, we simplified eq. (8) further. Following our considerations on the size of the kinetic parameters in fig. 4,  $\beta$  is smaller than one. Hence, expanding for small  $\beta$  gives

$$A_{\max}^2 \propto \frac{2\rho}{\beta} \propto \frac{e_A P_{\text{tot}}}{\ell d_P} \frac{1}{\frac{g_P P_{\text{tot}}^2 A_{\text{eq}}^2}{d_P}} \frac{(1 + \frac{s_P}{d_P})(1 + 2\frac{s_P}{d_P})}{\frac{s_P}{d_P}}. \quad (9)$$

As the amplitude arises due to auxin inflow from neighboring cells,  $A_{\max}$  increases with the rescaled transport efficiency  $e_A P_{\text{tot}}/\ell d_P$ . Auxin is accumulated in a cell until the cell reaches its almost fully polarized state and can efficiently transport auxin onwards, see fig. 3(B). Hence, accumulation time and auxin amplitude  $A_{\max}$  inversely depend on the basal PIN cycling rate  $s_P/d_P$  and the enhanced attachment rate  $g_P P_{\text{tot}}^2 A_{\text{eq}}^2/d_P$ . Synthesis and degradation of auxin do not contribute to the amplitude in this first-order approximation as their impact on the transport is very small. Note that the amplitude, like all other pulse and front characteristics, is independent of the amount of supplied auxin, a general property of excitable media. Applying the above simplification to the resulting analytic expressions for the velocity of the auxin pulse, see supplemental eqs. (S7), (S8), yields

$$v \propto e_A P_{\text{tot}}. \quad (10)$$

This result reveals that the pulse of front velocity is dominated by membrane permeability of auxin facilitated by PIN proteins which is just the product of transport efficiency and number of PIN proteins per cell. The prefactor in eq. (10)  $v/e_A P_{\text{tot}}$  can be estimated from comparison with numeric integration of the microscopic equations as shown in fig. 4 to be in the range of  $6 \cdot 10^{-5}$ – $6 \cdot 10^{-4}$  depending on the remaining kinetic parameters.

## 4 Discussion

We have shown that some prominent aspects of auxin and PIN dynamics can be inferred from a simple mathematical model. Our model predicts the transition of ground meristem cells from a non-polarized stable state to a polarized stable state of constant auxin flow. This development occurs by a traveling wave front triggered by a continuous inflow of auxin from the outer epidermal layer, in accordance with experimental observations [19]. Each cell is a bistable excitable medium. Excitations from one state to the other can be induced by supply of auxin and crucially depend on the spatial gradients in auxin and polar PIN concentrations between cells. The amplitude of auxin in the wave front and the polarization of the stable states is cast in analytical expressions concordant with numerical integration of our microscopic equations.

The microscopic equations underlying our model for auxin and PIN dynamics are defined such that all relevant biological processes are included while a minimum of assumptions on their actual kinetics entered. To this end only linear synthesis, degradation and transport etc. is considered as a first-order approximation of any kind of kinetics. However, the model is robust against alteration of the linear relationships, as is illustrated in Supplementary material II. For example, extending the cell-to-cell auxin transport to account for Michaelis-Menten kinetics preserves the form of the nullclines and the dynamics of the wave. In our model only the feedback of auxin flow on the attachment of PIN proteins enters non-linearly. A linear growth of the enhanced attachment rate with the auxin flow cannot lead to a propagating front, as such a model does not exhibit two stable fixed points. Only auxin flow exponents higher than one show these properties. However, the exact value of the exponent does not affect the form and dynamics of the traveling wave, again confirming the robustness of our assumptions.

Recently, models for auxin and PIN dynamics were developed proposing that the auxin concentration in the neighboring cell feeds back onto an enhanced attachment rate of PIN proteins [23,41–43] in contrast to canalization models, where the net auxin flux governs the feedback. These concentration driven models exhibit a static state of spatially ordered auxin maxima with PIN proteins polarized towards these auxin maxima [23]. This behavior arises as concentration driven feedback changes the non-linear character of auxin and PIN dynamics. These models generally exhibit only a single stable, resting fixed point [51,52]. The polarization due to auxin supply observed in these models [42] arises due to an evolved relaxation into the stable, resting state. Hence, the polarization is only temporary and, for instance, the amount of polarization and the velocity of the polarization front depend crucially on the amount of auxin supply. This is in contrast to our minimal canalization model, where all polarization characteristics are only governed by the kinetic parameters. The amount of auxin supply in an excitable medium only regulates if a pulse or front is excited or not. Hence, these qualitative differences may help to distinguish between the different models experimentally.

The role of all kinetic processes during the dynamic rearrangement of PIN and auxin in cells becomes explicit when examining the very front of the polarization in a microscopic scenario as illustrated in fig. 3(B). The almost fully polarized cell at the peak of the front carries a lot of auxin molecules that are invading the next yet non-polar cell in the direction of polarization with a rate mainly governed by the cell-to-cell transport efficiency  $e_A$ . To successfully transfer the accumulating auxin onwards the PIN proteins in the yet non-polar cell have to rearrange to facilitate directed transport. However, the endosome cycling  $s_P, g_P$  by which the membrane bound PIN proteins reach the cell membrane is very slow. Hence, the attachment rate of the efflux facilitators forms a bottleneck that piles up more and more auxin in a cell, that is slowly increasing

the amount of PIN proteins facing the direction of transport. Heuristically, an auxin pulse forms due to a traffic jam caused by the slow cycling of the efflux facilitators, as given by eq. (9). As an equilibrium concentration of PIN proteins is always embedded in each membrane ready to transport auxin, the magnitude of the velocity of a polarization front or pulse is set by the cell-to-cell transport efficiency, see eq. (10). The other kinetic parameters only slightly modulate the velocity. The PIN attachment rates,  $g_P$ ,  $s_P$ , and detachment rate,  $d_P$ , on the other hand, determine the number of PIN proteins accumulated at the membrane in the polar stable state, see eq. (5). The polarization grows with the enhanced attachment rate, the strength of the feedback,  $g_P$ . On the contrary, basal PIN cycling  $s_P/d_P$  intensifies the competition between opposing membranes decreasing the amount of PIN proteins in the direction of polarization.

The result of our analytic expressions for the PIN concentration in the polar state with constant auxin flux in eq. (5) and the auxin amplitude at the very head of the polarization front eq. (8) enable estimates of the underlying kinetic rates by identifying and measuring these observables in future experiments. Existing experimental results by Scarpella *et al.* [19] permit an estimate of the polarization front velocity in the range  $v = 10^{-4} - 10^{-3} \mu\text{m/s}$ , in accordance with our estimate for the velocity  $v = 8 \cdot 10^{-5} - 8 \cdot 10^{-4} \mu\text{m/s}$ , resulting from the fitted pre-factor in eq. (10) and the literature value of auxin permeability  $e_A P_{\text{tot}}$  [45,32]. An quantitative estimate of PIN polarity from the same existing data is to best of our knowledge yet unfeasible as a reference for the protein number is absent. This could be overcome by new experiments, which could also aim at the auxin kinetic rates. Unlike PIN which is readily GFP tagged, auxin is not directly detectable and quantification of its amount can only occur via indirect methods. Recently, measurements of deuterated auxin improved [53], making experiments with exogenously applied auxin conceivable. In such setups one should, however, keep in mind that exogenous auxin mixes with endogenous, non-labelled auxin, decreasing the observed amplitude. The position of the auxin peak can easily be located as it should be accumulated in front of those cells with the largest amount of PIN proteins at the corresponding membrane. Measurements of the amount of PIN proteins in polarized cells via GFP tagging could not only disclose the basal endosome cycling rate but also the magnitude of the feedback between auxin flow and PIN dynamics.

The occurrence of bipolar cells has stimulated previous theoretical models introducing a hypothetical new molecule [54] or moving auxin sources [38]. Our model, however, readily predicts the occurrence of bipolar cells along a one-dimensional strand of cells at the site of continuous auxin inflow. These cells show a high concentration of PIN proteins on either membrane, a balanced outcome of the competition for PIN between both membranes. This state is not a statically stable but dynamically driven by the supply of auxin. Transferring this observation to the two-dimensional layer of ground meris-

tem cells during vein initiation may explain the bipolar cells observed experimentally [19,27–29]. In two dimensions several membranes can compete, yielding also triple polar cells or theoretically higher orders of polarity. However, in biological cells not all cell membranes may have the same number of PIN proteins to enter the competition. Those with fewer initial PIN proteins will become the site of PIN drain, decreasing the number of successful polarization fronts. Experiments indicate that mechanical cues might favor certain membranes [55], paving the way of a polarization front and hence the position of veins and vein loops.

In summary we analyzed a canalization model to explain how auxin and PIN dynamics polarize the distribution of PIN proteins during early vein initiation in the ground meristem. Each cell is found to be bistable considering their PIN distribution in the membrane. Polarization occurs in a traveling front as auxin is supplied to a single cell mimicking the auxin inflow from the outer epidermal cell layer. The driver in this transition is the spatial gradient of auxin and polar PIN concentration between cells. The key idea in this polarization is the positive feedback between hormone auxin and its own efflux facilitator PIN. An idea that might be inspiring in other developmental processes in animals where tissue is polarized as, for example, in planar cell polarity [56]. As the polarization front can travel in opposite directions from its initiation site, a bipolar cell, the up to now puzzling occurrence of closed vein loops can be resolved. Furthermore, our nonlinear analysis enables the calculation of exact analytical expression for the polarization front. Therefore, our new quantitative predictions for the PIN polarization driven by auxin flow establishes a basis to determine the kinetic parameters underlying the transport of auxin and may therewith have far-reaching impacts on the understanding of the developmental processes and their differences in plant species, to perceive the fundamental patterns of leaf veins or phyllotaxis and learn how environmental conditions alter these.

The authors thank Eric M. Kramer for fruitful discussions. Financial support of the German Excellence Initiative via the program “Nanosystems Initiative Munich (NIM)” and of the LMUinnovativ project “Functional Nanosystems (FuNS)” is gratefully acknowledged. K.A. acknowledges funding by the Studienstiftung des deutschen Volkes.

## References

1. J. Petrasek, J. Friml, *Development* **136**, 2675 (2009).
2. J. Friml, J. Wiśniewska, E. Benková, K. Mendgen, K. Palme, *Nature* **415**, 806 (2002).
3. A. Marchant, J. Kargul, S.T. May, P. Muller, A. Delbarre, C. Perrot-Rechenmann, M.J. Bennett, *EMBO J.* **18**, 2066 (1999).
4. D. Reinhardt, E.R. Pesce, P. Stieger, T. Mandel, K. Baltesperger, M. Bennett, J. Traas, J. Friml, C. Kuhlemeier, *Nature* **426**, 255 (2003).

5. L.E. Sieburth, *Plant Physiol.* **121**, 1179 (1999).
6. F.A.F.C. Went, *Naturwiss.* **21**, 1 (1933).
7. P.H. Rubery, A.R. Sheldrake, *Nature New Biol.* **244**, 285 (1973).
8. M.H.M. Goldsmith, T.H. Goldsmith, M.H. Martin, *Proc. Natl. Acad. Sci. U.S.A.* **78**, 976 (1981).
9. G.J. Mitchison, *Proc. R. Soc. London, Ser. B Bio.* **209**, 489 (1980).
10. L. Gälweiler, C.H. Guan, A. Müller, E. Wisman, K. Mendgen, A. Yephremov, K. Palme, *Science* **282**, 2226 (1998).
11. K. Okada, J. Ueda, M.K. Komaki, C.J. Bell, Y. Shimura, *Plant Cell* **3**, 677 (1991).
12. E. Benková, M. Michniewicz, M. Sauer, T. Teichmann, D. Seifertová, G. Jürgens, J. Friml, *Cell* **115**, 591 (2003).
13. J. Friml, A. Vieten, M. Sauer, D. Weijers, H. Schwarz, T. Hamann, R. Offringa, G. Jürgens, *Nature* **426**, 147 (2003).
14. J. Petrášek, J. Mravec, R. Bouchard, J.J. Blakeslee, M. Abas, D. Seifertová, J. Wiśniewska, Z. Tadele, M. Kubeš, M. Čovanová *et al.*, *Science* **312**, 914 (2006).
15. T. Sachs, *Annu. Bot. London* **33**, 263 (1969).
16. G.J. Mitchison, *Proc. R. Soc. London, Ser. B Bio.* **207**, 79 (1980).
17. G.J. Mitchison, *Philos. Trans. Roy. Soc. B* **295**, 461 (1981).
18. M. Sauer, J. Balla, C. Luschnig, J. Wisniewska, V. Reinohl, J. Friml, E. Benkova, *Genes Dev.* **20**, 2902 (2006).
19. E. Scarpella, D. Marcos, J. Friml, T. Berleth, *Genes Dev.* **20**, 1015 (2006).
20. T. Paciorek, E. Zážimalová, N. Ruthardt, J. Petrášek, Y.D. Stierhof, J. Kleine-Vehn, D.A. Morris, N. Emans, G. Jürgens, N. Geldner *et al.*, *Nature* **435**, 1251 (2005).
21. P. Dhonukshe, I. Grigoriev, R. Fischer, M. Tominaga, D.G. Robinson, J. Hasek, T. Paciorek, J. Petrášek, D. Seifertová, R. Tejos *et al.*, *Proc. Natl. Acad. Sci. U.S.A.* **105**, 4489 (2008).
22. R. Benjamins, B. Scheres, *Annu. Rev. Plant Biol.* **59**, 443 (2008).
23. H. Jönsson, M.G. Heisler, B.E. Shapiro, E.M. Meyerowitz, E. Mjolsness, *Proc. Natl. Acad. Sci. U.S.A.* **103**, 1633 (2006).
24. F.G. Feugier, A. Mochizuki, Y. Iwasa, *J. Theor. Biol.* **236**, 366 (2005).
25. T. Berleth, E. Scarpella, P. Prusinkiewicz, *Trends Plant Sci.* **12**, 151 (2007).
26. R.S. Smith, E.M. Bayer, *Plant Cell Environ.* **32**, 1258 (2009).
27. C.L. Wenzel, M. Schuetz, Q. Yu, J. Mattsson, *Plant J.* **49**, 387 (2007).
28. E.M. Bayer, R.S. Smith, T. Mandel, N. Nakayama, M. Sauer, P. Prusinkiewicz, C. Kuhlemeier, *Genes Dev.* **23**, 373 (2009).
29. D. Koenig, E. Bayer, J. Kang, C. Kuhlemeier, N. Sinha, *Development* **136**, 2997 (2009).
30. M.G. Sawchuk, P. Head, T.J. Donner, E. Scarpella, *New Phytol.* **176**, 560 (2007).
31. J.A. Raven, *New Phytol.* **74**, 163 (1975).
32. R. Swarup, E.M. Kramer, P. Perry, K. Knox, H.M.O. Leyser, J. Haseloff, G.T.S. Beemster, R. Bhalerao, M.J. Bennett, *Nat. Cell. Biol.* **7**, 1057 (2005).
33. A.S. Usenko, A.G. Zagorodny, *Mol. Phys.* **61**, 1213 (1987).
34. P. Larsen, *Growth substances in higher plants*, Vol. **3** of *Modern Methods of Plant Physiology* (Springer, Berlin, 1955).
35. E. Wangermann, G.J. Mitchison, *Plant Cell Environ.* **4**, 141 (1981).
36. E.M. Kramer, *J. Exp. Bot.* **59**, 45 (2007).
37. S. Pollmann, A. Müller, M. Piotrowski, E.W. Weiler, *Planta* **216**, 155 (2002).
38. A.G. Rolland-Lagan, P. Prusinkiewicz, *Plant J.* **44**, 854 (2005).
39. S. Stoma, M. Lucas, J. Chopard, M. Schaedel, J. Traas, C. Godin, *PLoS Comput. Biol.* **4**, e1000207 (2008).
40. E.M. Kramer, *Trends Plant Sci.* **14**, 242 (2009).
41. R.S. Smith, S. Guyomarc'h, T. Mandel, D. Reinhardt, C. Kuhlemeier, P. Prusinkiewicz, *Proc. Natl. Acad. Sci. U.S.A.* **103**, 1301 (2006).
42. R.M.H. Merks, Y.V. de Peer, D. Inzé, G.T.S. Beemster, *Trends Plant Sci.* **12**, 384 (2007).
43. M. Ibañes, N. Fàbregas, J. Chory, A. Caño-Delgado, *Proc. Natl. Acad. Sci. U.S.A.* **106**, 13630 (2009).
44. F. Rapparini, Y.Y. Tam, J.D. Cohen, J.P. Slovin, *Plant Physiol.* **128**, 1410 (2002).
45. A. Delbarre, P. Muller, V. Imhoff, J. Guern, *Planta* **198**, 532 (1996).
46. V.S. Zykov, A.T. Winfree, *Simulation of Wave Processes in Excitable Media* (Manchester University Press, Manchester, 1987).
47. A.S. Mikhailov, A.Y. Loskutov, *Foundations of Synergetics I: Distributed Active Systems* (Springer Verlag, New York, 1991).
48. C.L. Howe, W.C. Mobley, *J. Neurobiol.* **58**, 207 (2004).
49. P. Ortoleva, J. Ross, *J. Chem. Phys.* **63**, 3398 (1975).
50. R.G. Casten, H. Cohen, P.A. Lagerstrom, *Q. Appl. Math.* **32**, 365 (1975).
51. A. Newell, P. Shipman, Z. Sun, *J. Theor. Biol.* **251**, 421 (2008).
52. P. Sahlin, B. Söderberg, H. Jönsson, *J. Theor. Biol.* **258**, 60 (2009).
53. K. Ljung, A.K. Hull, J. Celenza, M. Yamada, M. Estelle, J. Normanly, G. Sandberg, *Plant Cell* **17**, 1090 (2005).
54. F. Feugier, Y. Iwasa, *J. Theor. Biol.* **243**, 235 (2006).
55. O. Hamant, M.G. Heisler, H. Jonsson, P. Krupinski, M. Uyttewaal, P. Bokov, F. Corson, P. Sahlin, A. Boudaoud, E.M. Meyerowitz *et al.*, *Science* **322**, 1650 (2008).
56. P.A. Lawrence, G. Struhl, J. Casal, *Nat. Rev. Genet.* **8**, 555 (2007).

# Supplementary Information: Quantitative Predictions on Auxin-Induced Polar Distribution of PIN Proteins during Vein Formation in Leaves

Karen Alim and Erwin Frey

*Arnold Sommerfeld Center for Theoretical Physics and Center for NanoScience,  
Ludwig-Maximilians-Universität, Theresienstr. 37, D-80333 München, Germany*

## I. AUXIN AMPLITUDE COMPUTATION

Starting from the microscopic definition of a model for the polarization of PIN distributions by auxin flow, see Eq. (1), (2) and (3), an exact analytical expression for the auxin amplitude and the velocity of the polarization pulse is derived. To this end a continuum limit is performed and singular perturbation theory is employed as described in the following.

Initially, polarization is defined by three equations governing the dynamics of auxin concentration  $A$  and the amount of PIN efflux facilitators on the membrane on the right  $P_r$  or on the left  $P_l$  hand side of the cell. Assuming the symmetry of the system is broken such that polarization evolves to the right, the concentration of efflux facilitators on the left hand side membrane of every cell does not change significantly with time if  $s_P/(d_P + 2s_P) \ll 1$ , we therefore assume  $dP_l(n)/dt = 0$ . As flow proceeds to the right  $J(n) > 0 \forall n$ , the amount of PIN proteins on the left hand side membrane amounts in its stationary state to  $P_l(n) = s_P(1 - P_r(n))/(d_P + s_P)$ . Substituting this result in the remaining dynamic equations the system is described by two components only,  $A(n)$  and  $P_r(n)$ . We derive continuum equations by setting  $n \rightarrow x$ ,  $n + 1 \rightarrow x + \ell$ , and  $n - 1 \rightarrow x - \ell$ . When the wavelength as the length scale on which the pulse evolves is considerably larger than the cell length  $\ell$ , a time scale separation occurs which makes higher order terms negligible small. As observed in the simulations shown in Fig. 2 the wavelength of a single pulse is of the order of tens of cells justifying a Taylor expansion in  $x$ . To describe the characteristics observed in the microscopic equations with continuous equations only zeroth order terms and a single second order term in the PIN dynamics are required,

$$\frac{\partial}{\partial t} \frac{A(x, t)}{A_{\text{eq}}} = d_A \left( 1 - \frac{A(x, t)}{A_{\text{eq}}} \right) - \frac{e_A P_{\text{tot}}}{\ell} \frac{1 + 2\frac{s_P}{d_P}}{1 + \frac{s_P}{d_P}} \ell \frac{\partial}{\partial x} \left[ \left( \frac{P_r(x, t)}{P_{\text{tot}}} - \frac{\frac{s_P}{d_P}}{1 + 2\frac{s_P}{d_P}} \right) \frac{A(x, t)}{A_{\text{eq}}} \right], \quad (\text{S1})$$



$$\begin{aligned}
\frac{\partial}{\partial t} \frac{P_r(x, t)}{P_{\text{tot}}} &= -\frac{g_P P_{\text{tot}}^2 (1 + 2\frac{s_P}{d_P})^2 A^2(x, t)}{(1 + \frac{s_P}{d_P})^3} \left( \frac{P_r(x, t)}{P_{\text{tot}}} - \frac{\frac{s_P}{d_P}}{1 + 2\frac{s_P}{d_P}} \right) \\
&\times \left( \frac{P_r(x, t)}{P_{\text{tot}}} - \frac{1 + 3\frac{s_P}{d_P} - (1 + \frac{s_P}{d_P}) \sqrt{1 - \frac{4(d_P + 2s_P)}{g_P P_{\text{tot}}^2 A^2(x)}}}{2(1 + 2\frac{s_P}{d_P})} \right) \\
&\times \left( \frac{P_r(x, t)}{P_{\text{tot}}} - \frac{1 + 3\frac{s_P}{d_P} + (1 + \frac{s_P}{d_P}) \sqrt{1 - \frac{4(d_P + 2s_P)}{g_P P_{\text{tot}}^2 A^2(x, t)}}}{2(1 + 2\frac{s_P}{d_P})} \right) \\
&- \frac{g_P P_{\text{tot}}^2 \frac{s_P^2}{d_P^2}}{(1 + \frac{s_P}{d_P})^3} \left( \frac{P_r(x, t)}{P_{\text{tot}}} - 1 \right) \left\{ \ell \frac{\partial}{\partial x} \left[ \left( \frac{P_r(x, t)}{P_{\text{tot}}} - 1 \right) A(x, t) \right] \right\}^2. \quad (\text{S2})
\end{aligned}$$

In these expressions the degree of nonlinearity is still too high to obtain analytical results by use of singular perturbation theory. Therefore, the continuum equations are further simplified by approximating them right and left of the nullcline embedding the unstable fixed point,  $P_r(x) = \frac{d_P + 3s_P}{2(d_P + 2s_P)} - \frac{d_P + s_P}{2(d_P + 2s_P)} \sqrt{1 - \frac{4(d_P + 2s_P)}{g_P P_{\text{tot}} A^2(x)}}$ , which to good approximation resembles the separatrix between the areas of attraction of the stable fixed points.

Left of the nullcline the reaction terms of the continuum equations, those terms without spatial or temporal derivatives, are expanded around the stable nullcline embedding the stable resting state ( $A/A_{\text{eq}} = 1, P_r/P_{\text{tot}} = s_P/(d_P + 2s_P)$ ). The spatial derivative terms are simplified by discarding the spatial derivative of auxin whose factor  $P_r(x)/P_{\text{tot}} - s_P/(d_P + 2s_P)$  turns the whole term negligible small close to the stable nullcline, resulting in,

$$\frac{\partial}{\partial t} \frac{A(x, t)}{A_{\text{eq}}} = d_A \left( 1 - \frac{A(x, t)}{A_{\text{eq}}} \right) - \frac{e_A P_{\text{tot}}}{\ell} \frac{1 + 2\frac{s_P}{d_P}}{1 + \frac{s_P}{d_P}} \frac{A(x, t)}{A_{\text{eq}}} \ell \frac{\partial}{\partial x} \frac{P_r(x, t)}{P_{\text{tot}}}, \quad (\text{S3})$$

$$\begin{aligned}
\frac{\partial}{\partial t} \frac{P_r(x, t)}{P_{\text{tot}}} &= -\frac{(d_P + 2s_P)}{(1 + \frac{s_P}{d_P})} \left( \frac{P_r(x, t)}{P_{\text{tot}}} - \frac{\frac{s_P}{d_P}}{1 + 2\frac{s_P}{d_P}} \right) \\
&- \frac{g_P P_{\text{tot}}^2 \frac{s_P^2}{d_P^2}}{(1 + \frac{s_P}{d_P})^3} \left( \frac{P_r(x, t)}{P_{\text{tot}}} - 1 \right) \left\{ \ell \frac{\partial}{\partial x} \left[ \left( \frac{P_r(x, t)}{P_{\text{tot}}} - 1 \right) A(x, t) \right] \right\}^2. \quad (\text{S4})
\end{aligned}$$

Right of the nullcline embedding the unstable fixed point the reaction term of the efflux facilitator dynamics is expanded around the polar fixed point ( $A/A_{\text{eq}} = 1, P_r/P_{\text{tot}} = \frac{d_P + 3s_P}{2(d_P + 2s_P)} + \frac{d_P + s_P}{2(d_P + 2s_P)} \sqrt{1 - \frac{4(d_P + 2s_P)}{g_P A_{\text{eq}}^2 P_{\text{tot}}^2}}$ ). Here, the spatial derivative terms contributing to the PIN protein dy-

namics become negligible small and are therefore discarded, yielding,

$$\frac{\partial}{\partial t} \frac{A(x, t)}{A_{\text{eq}}} = d_A \left( 1 - \frac{A(x, t)}{A_{\text{eq}}} \right) - \frac{e_A P_{\text{tot}}}{\ell} \frac{1 + 2\frac{s_P}{d_P}}{1 + \frac{s_P}{d_P}} \ell \frac{\partial}{\partial x} \left[ \left( \frac{P_r(x, t)}{P_{\text{tot}}} - \frac{\frac{s_P}{d_P}}{1 + 2\frac{s_P}{d_P}} \right) \frac{A(x, t)}{A_{\text{eq}}} \right] \quad (\text{S5})$$

$$\begin{aligned} \frac{\partial}{\partial t} \frac{P_r(x, t)}{P_{\text{tot}}} = & -\frac{g_P P_{\text{tot}}^2 A^2(x, t)}{2(1 + \frac{s_P}{d_P})} \left( 1 - \frac{4(d_P + 2s_P)}{g_P P_{\text{tot}}^2 A^2(x, t)} + \sqrt{1 - \frac{4(d_P + 2s_P)}{g_P P_{\text{tot}}^2 A^2(x, t)}} \right) \\ & \times \left( \frac{P_r(x, t)}{P_{\text{tot}}} - \frac{1 + 3\frac{s_P}{d_P} + (1 + \frac{s_P}{d_P}) \sqrt{1 - \frac{4(d_P + 2s_P)}{g_P P_{\text{tot}}^2 A^2(x, t)}}}{2(1 + 2\frac{s_P}{d_P})} \right). \end{aligned} \quad (\text{S6})$$

Based on these sets of equations the amplitude and the velocity of a polarization pulse are calculated employing singular perturbation theory [1, 2]. The singular perturbation approach becomes applicable to a two component system performing a pulse if the pulse can be separated in different regions which comply either of the following restrictions. Either to good approximation one component is constant while the other changes rapidly. Or if both components change simultaneously one of the components should follow a nullcline. Then the two coupled nonlinear equations decouple in each region and only one differential equation remains to be solved. Assuming a traveling wave ansatz  $z = x - vt$ , where  $v$  defines the velocity of the wave, the partial differential equations simplify to ordinary differential equations. These differential equations remain to be solved under the condition of continuity and differential continuity at the nullcline embedding the unstable fixed point which separates the two cases Eqs. (S3, S4) and Eqs. (S5, S6).

The trajectory of an auxin pulse can be subdivided into four regions, first a wave front and back, where the auxin concentration is approximately constant  $A_{\text{max, min}}$ , while the PIN protein concentration changes rapidly and second an excited and a refractory region during which the PIN concentration follows the stable nullclines. Several boundary conditions arise from the requirement of continuity and differential continuity. Considering the efflux facilitator dynamics continuity requires that PIN concentrations during pulse front and back governed by Eqs. (S4) and (S6) merge into the nullclines defining refractory and excited domain  $P_{r, \text{front}}(z \rightarrow \infty) = P_{r, \text{refrac}}$ ,  $P_{r, \text{front}}(z \rightarrow -\infty) = P_{r, \text{excite}}$  and  $P_{r, \text{back}}(z \rightarrow -\infty) = P_{r, \text{refrac}}$ ,  $P_{r, \text{back}}(z \rightarrow \infty) = P_{r, \text{excite}}$ . As the separating nullcline is crossed during wave front and back additionally continuity and differential continuity is compulsory for efflux facilitators at the position of the nullcline embedding the unstable fixed point  $z_{\text{sep}}$ . The auxin concentration evolving during excited Eq. (S5) and refractory region Eq. (S3) has to reach the constant auxin concentration of pulse front and back  $A_{\text{max}}$ ,  $A_{\text{min}}$  at distinct points

in evolution  $z = z_{\text{front}}$  and  $z_{\text{back}}$ , resulting in the boundary conditions  $A_{\text{refrac}}(z_{\text{front}}) = A_{\text{max}} = A_{\text{excite}}(z_{\text{front}})$ ,  $A_{\text{refrac}}(z_{\text{back}}) = A_{\text{min}} = A_{\text{excite}}(z_{\text{back}})$ ,  $dA_{\text{refrac}}(z_{\text{front}})/dz = dA_{\text{excite}}(z_{\text{front}})/dz$ , and  $dA_{\text{refrac}}(z_{\text{back}})/dz = dA_{\text{excite}}(z_{\text{back}})/dz$ . Two of those boundary conditions yield equations that solve for the auxin amplitude  $A_{\text{max}}$  and the pulse velocity  $v$ . First the condition of differential continuity of the PIN concentration at the separatrix  $\partial P_r(z_{\text{sep}})/\partial z$  results in,

$$v = \frac{4\ell d_P \frac{s_P}{d_P}}{1 + \frac{s_P}{d_P}} \sqrt{\frac{\frac{A_{\text{max}}^8}{\rho^4} \left(1 + \frac{\rho}{A_{\text{max}}^2}\right)^2 \left(1 + \sqrt{1 - \frac{\rho}{A_{\text{max}}^2}}\right)^4}{1 + \frac{4A_{\text{max}}^4}{\rho^2} \left(1 + \frac{\rho}{A_{\text{max}}^2}\right) \left(1 + \sqrt{1 - \frac{\rho}{A_{\text{max}}^2}}\right)^2}}, \quad (\text{S7})$$

where we abbreviated  $\rho = 4(d_P + 2s_P)/g_P P_{\text{tot}}^2$ . Second differential continuity of auxin left and right of a wave front or back  $A_{\text{refrac}}(z_{\text{front}}) = A_{\text{max}} = A_{\text{excite}}(z_{\text{front}})$  yields,

$$v = \frac{e_A P_{\text{tot}}}{4} \left(1 + \sqrt{1 - \frac{\rho}{A_{\text{max}}^2}}\right). \quad (\text{S8})$$

These two equations together result in a quartic equation for the amplitude of the auxin pulse, evaluated to the expression given in eq. (8). Reentering this result into one of the defining equations above yields an analytic result for the velocity of an auxin pulse.

## II. COMPARISON TO ALTERNATIVE MICROSCOPIC TRANSPORT MODELS

When defining our microscopic equations Eqs. (1 - 3) we included all contributing processes but considered a minimum of assumptions on the kinetics. In this spirit all processes are modeled by linear relations as the first order term of any kind of underlying kinetics. The only exception is the enhanced attachment of PIN proteins, which is the point where non-linearity enters the microscopic model triggering the non-linear effect of a traveling pulse or front. Including further non-linearities renders the microscopic models intractable for analytical calculations. However, the analysis of our minimal model has revealed the key characteristics for polarization to be two stable fixed points accompanied by an unstable manifold. Excitations beyond this unstable manifold then lead to the development of a wave pulse or the relaxation to the polar stable fixed point. With this knowledge we can assess more evolved microscopic models by comparing their non-linear characteristics such as the nullclines to the minimal model. As is shown in the following,

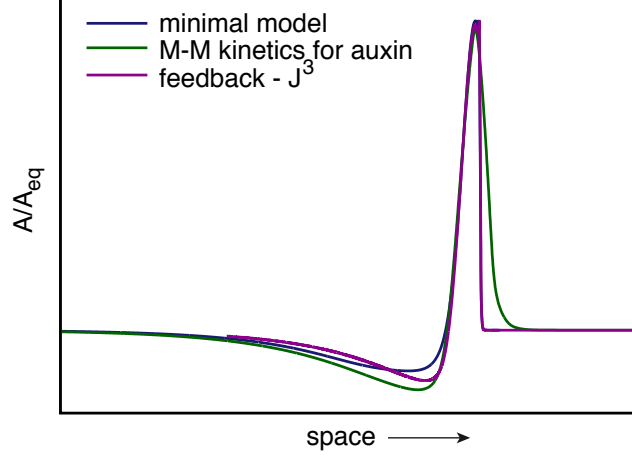


FIG. S1: Comparing the polarization pulse for different extended models to our minimal model yields no difference in their characteristics confirming the robustness of our linear approximations. Parameters values as follows. Minimal model  $d_A/d_P = 0.2$ ,  $s_P/d_P = 0.2$ ,  $e_A P_{\text{tot}}/\ell d_P = 10$ , and  $g_P A_{\text{eq}}^2 P_{\text{tot}}^2/d_P = 12$ . Michaelis-Menten kinetics for active auxin transport  $d_A/d_P = 0.2$ ,  $s_P/d_P = 0.2$ ,  $e_A P_{\text{tot}}/\ell d_P A_{\text{eq}} = 8$ ,  $g_P P_{\text{tot}}^2/d_P = 70$ , and  $k_A/A_{\text{eq}} = 1.6$ . Feedback to the power of three  $d_A/d_P = 0.2$ ,  $s_P/d_P = 0.2$ ,  $e_A P_{\text{tot}}/\ell d_P A_{\text{eq}} = 10$ , and  $g_P P_{\text{tot}}^3 A_{\text{eq}}^3/d_P = 18$ .

exemplarily changing linear terms of the minimal model into non-linear terms results only in slight changes of the characteristics confirming the robustness of a first order assumption in the minimal model. If not explicitly stated otherwise we assumed  $dP_l(n)/dt = 0$  to calculate the fixed points.

### A. Michaelis-Menten kinetics for active auxin transport

One may assume that a Michaelis-Menten mechanism describes the active transport of a substrate auxin by an enzyme presented by the PIN proteins [3, 4]. Then, in the definition of the net auxin flow the number of transported auxin molecules is represented by a Hill function with Michaelis-Menten constant  $k_A$ . For reasons of completeness we state the full set of microscopic equations:

$$\frac{d}{dt}A(n) = s_A - d_A A(n) - \frac{e_A}{\ell} [J(n) - J(n-1)], \quad (\text{S9})$$

$$\frac{d}{dt}P_r(n) = -d_P P_r(n) + s_P P_b(n) + g_P J^2(n) \theta(J(n)) P_b(n), \quad (\text{S10})$$

$$\frac{d}{dt}P_l(n) = -d_P P_l(n) + s_P P_b(n) + g_P J^2(n-1) \theta(-J(n-1)) P_b(n), \quad (\text{S11})$$

$$J(n) = \frac{A(n)}{A(n) + k_A} P_r(n) - \frac{A(n+1)}{A(n+1) + k_A} P_l(n+1). \quad (\text{S12})$$

These equations yield in accordance with the minimal model three fixed points, one resting state at  $(A/A_{\text{eq}} = 1, P_r/P_{\text{tot}} = s_P/(d_P + 2s_P))$  and a pair of stable and unstable constant current fixed points at  $(A/A_{\text{eq}} = 1, P_r/P_{\text{tot}} = \frac{d_P + 3s_P}{2(d_P + 2s_P)} \mp \frac{d_P + s_P}{2(d_P + 2s_P)} \sqrt{1 - (1 + k_A)^2 \frac{4(d_P + 2s_P)}{g_P P_{\text{tot}}^2}})$ . The model displays very similar nullclines and the same dynamics as the minimal model as exemplified in Fig. S1. If the new parameter  $k_A$  lies outside its range  $k_A \leq -1 - \sqrt{\frac{g_P P_{\text{tot}}^2}{4(d_P + 2s_P)}}$  and  $k_A \geq -1 + \sqrt{\frac{g_P P_{\text{tot}}^2}{4(d_P + 2s_P)}}$  only a single stable fixed point occurs and no polarization can be observed.

### B. Feedback - power of the current

In the minimal model we take the feedback of auxin flow on the enhanced attachment of PIN proteins to enter with a power of two. In general one could assume any kind of power,

$$\frac{d}{dt}A(n) = s_A - d_A A(n) - \frac{e_A}{\ell} [J(n) - J(n-1)], \quad (\text{S13})$$

$$\frac{d}{dt}P_r(n) = -d_P P_r(n) + s_P P_b(n) + g_P J^k(n) \theta(J(n)) P_b(n), \quad (\text{S14})$$

$$\frac{d}{dt}P_l(n) = -d_P P_l(n) + s_P P_b(n) + g_P J^k(n-1) \theta(-J(n-1)) P_b(n), \quad (\text{S15})$$

$$J(n) = A(n)P_r(n) - A(n+1)P_l(n+1). \quad (\text{S16})$$

Considering only integer powers for simplicity, we find the following. For  $k = 1$  the above equations display the resting fixed point at  $(A/A_{\text{eq}} = 1, P_r/P_{\text{tot}} = P_l/P_{\text{tot}} = s_P/(d_P + 2s_P))$  and a polar fixed point at  $(A/A_{\text{eq}} = 1, P_l/P_{\text{tot}} = s_P/g_P A_{\text{eq}} P_{\text{tot}}, P_r/P_{\text{tot}} = 1 - (s_P + d_P)/g_P A_{\text{eq}} P_{\text{tot}})$ . The resting state is the only fixed point and stable for  $g_P A_{\text{eq}} P_{\text{tot}} < d_P + 2s_P$ , otherwise the polar fixed point is stable and the resting state turns unstable. No excited polarization can occur in either case. However, if  $k > 1$  the equations display a set of stable and unstable fixed points in addition to the resting stable fixed point. For any  $k > 1$  one recovers the dynamics observed for  $k = 2$  in the minimal model as exemplified in Fig. S1 for the cases  $k = 3$ . This observation is in accordance with results of Ref. [5], which stated vein patterns for any feedback function obeying to first order a higher power than  $k = 1$ . For  $k = 2$  we observed that the pair of a stable and an unstable polar fixed point occurs only for  $g_P A_{\text{eq}}^2 P_{\text{tot}}^2 / d_P \geq 4(1 + 2s_P/d_P)$ , similar rules apply for  $k = 3$  or higher.

### III. MODEL PARAMETERS

Our model depends on four dimensionless parameters  $\delta_a = d_A/d_P$ ,  $\sigma_p = s_P/d_P$ ,  $\gamma_p = g_P A_{\text{eq}}^2 P_{\text{tot}}^2/d_P$ , and  $\epsilon_a = e_A P_{\text{tot}}/\ell d_P$ . As quantitative knowledge is very sparse, i.e., only  $d_A = 2 \cdot 10^{-4} - 2 \cdot 10^{-5} 1/s$  and  $e_A P_{\text{tot}} = 1.4 \mu m/s$  are experimentally verified, their values have been varied over large ranges within conceptual limits, see table below. As only less than a third of all PIN protein can occupy each membrane in the resting state given by  $P_{r,l}/P_{\text{tot}} = \sigma_p/(1 + 2\sigma_p)$ ,  $\sigma_p$  is limited to values considerably smaller than one. Furthermore, it is reasonable to assume that  $e_A P_{\text{tot}}/\ell d_P > 1$  as auxin permeability  $e_A P_{\text{tot}} = 1.4 \mu m/s$  [6, 7] is roughly larger than endosome cycling by active transport along a cell's cytoskeleton  $\ell s_P$  [8]. In addition, we suggest  $g_P A_{\text{eq}}^2 P_{\text{tot}}^2/d_P > 1$  as protein and auxin numbers might be very large. Finally, assuming literature values of  $d_A$  [9], endosome cycling, and taking cell length of tens of  $\mu m$ , we took  $d_A/d_P < 1$ . The parameter assumed in our simulation presented in Fig. 5 are summarized in the following.

Parameter	$\delta_a = d_A/d_P$	$\sigma_p = s_P/d_P$	$\gamma_p = g_P A_{\text{eq}}^2 P_{\text{tot}}^2/d_P$	$\epsilon_a = e_A P_{\text{tot}}/\ell d_P$
Values	0.1-1	0.05 -1	1-10	1- 100

- 
- [1] P. Ortoleva and J. Ross, J. Chem. Phys. **63**, 3398 (1975).
- [2] R. G. Casten, H. Cohen, and P. A. Lagerstrom, Q. Appl. Math. **32**, 365 (1975).
- [3] H. Jönsson, M. G. Heisler, B. E. Shapiro, E. M. Meyerowitz, and E. Mjolsness, Proc. Natl. Acad. Sci. USA **103**, 1633 (2006).
- [4] R. M. H. Merks, Y. V. de Peer, D. Inzé, and G. T. S. Beemster, Trends Plant Sci **12**, 384 (2007).
- [5] F. G. Feugier, A. Mochizuki, and Y. Iwasa, J. Theor. Biol. **236**, 366 (2005).
- [6] A. Delbarre, P. Muller, V. Imhoff, and J. Guern, Planta **198**, 532 (1996).
- [7] R. Swarup, E. M. Kramer, P. Perry, K. Knox, H. M. O. Leyser, J. Haseloff, G. T. S. Beemster, R. Bhalerao, and M. J. Bennett, Nat. Cell. Biol. **7**, 1057 (2005).
- [8] C. L. Howe and W. C. Mobley, J Neurobiol **58**, 207 (2004).
- [9] F. Rapparini, Y. Y. Tam, J. D. Cohen, and J. P. Slovin, Plant Physiol. **128**, 1410 (2002).

# Oligocellular arrays: A novel approach to explore cell tissue mechanics

Alicia Piera Alberola<sup>1†</sup>, Karen Alim<sup>2†</sup>, Anna-Kristina Marel<sup>1</sup>,  
Erwin Frey<sup>2\*</sup> and Joachim O. Rädler<sup>1\*</sup>

1. Faculty of Physics and Center for NanoScience (CeNS), Ludwig-Maximilians-Universität,  
Geschwister Scholl Platz 1, D-80539 München, Germany

2. Arnold Sommerfeld Center for Theoretical Physics (ASC) and Center for NanoScience (CeNS),  
Faculty of Physics, Ludwig-Maximilians-Universität München,  
Theresienstraße 37, D-80333 München, Germany

†Authors contributed equally to this work.

\*To whom correspondence should be addressed.

Email: frey@lmu.de

Email: joachim.raedler@physik.uni-muenchen.de

Telephone number: +49 89 2180 2438

## Abstract

The prospect that local cell mechanics underlies the formation of large-scale tissue structures has tremendous impact on our understanding of tissue remodeling, developmental morphogenesis and tumor growth. Yet quantitative measurements and predictable modeling of the homeostatic balance of tensional inter- and intracellular forces are scarce. Here we investigate, as basic tissue units, small sets of Huh7 epithelia cells on arrays of micro-fabricated square adhesion patches. Beyond single cell and full tissue level, these oligocellular tissues enforce well-defined boundary conditions and hence give access to mechanisms governing tissue mechanics not revealed previously. We observe cell arrangement into distinct packing states, which we categorize according to their geometry and relative abundance. The standard mechanical model, previously proposed for extended tissues, fails to fully explain the packing states. We propose an extended model including cell shape anisotropy in addition to cell-cortex contractility and cell-cell adhesion. This extended model fully captures the statistics of oligocellular tissues and allows quantification of tissue mechanics. The reproducibility of cell states suggests that these tissues may be used as quantitative cell mechanics assays, in order to explore underlying cellular processes.

## Introduction

In recent years, it became increasingly obvious that cell mechanics plays an important role in tissue formation during development, growth, wound healing and tumorigenesis. The interplay between mechanical forces in epithelial cells has been found to organize tissue sorting<sup>1</sup>, govern the surprisingly regular polygonal packing of cells within tissues<sup>2-5</sup>, and their rearrangement during development<sup>6-11</sup>. Cell mechanics may also play an important part in cell dynamics such as tissue growth<sup>12, 13</sup> and tissue spreading<sup>14-19</sup>. The polygonal arrangement of cells within tissues has recently been described with vertex models<sup>3, 4, 10, 13, 20</sup>. These models explain a homeostatic tissue state to be determined by the interplay of cortical actin contractile forces, contact favoring adhesion forces and elastic forces. Regulation of these balancing forces determines cell packing geometry<sup>2, 3, 5</sup> and drives large scale reordering of cells within tissues during development<sup>6, 9</sup>. First quantitative comparison of *Drosophila* tissue structures and vertex model simulation by Farhadifar *et al.*<sup>4</sup> and Rauzi *et al.*<sup>10</sup> allowed to estimate the force parameters. In this context it is very promising to apply a bottom-up approach by designing artificial cell arrangements as model tissue with defined boundary conditions. Employing such experiments in a hypothesis driven manner can establish and validate mechanical models of cell tissue mechanics.

The emerging field of cell micropatterning techniques allows control of adhesion patches, which determine shape, size and location of cultured cells. Micropatterns have been employed in precise biophysical single cell studies concerning mechanical forces<sup>21, 22</sup> established by cell contact points to the extracellular matrix (ECM), and the influence of their geometrical distribution on fundamental biological functions<sup>23-25</sup> and internal organization of cells<sup>26</sup>. An important, and not yet fully appreciated advantage of micropatterning based cell studies, is the fact that settings consisting of a small number of cells reduce the degrees of freedom for cell arrangements for given cell-contact and intracellular parameters and, hence, give access to cell mechanical quantities that are neither empirically observable at the single cell level nor at the full tissue level.



In this article, we study the packing states for an ensemble of small groups of cells in defined micropatterned growth areas. We observe epithelial Huh 7 cells within micron-scale square adhesion patches and find that cells relax into distinct cell packing states, depending on the number of cells per adhesion patch. These stable cell arrangements cannot be explained within the standard mechanical model. A qualitative analysis of the geometry and relative abundance of oligocellular packing states provides strong evidence for an additional elastic term beyond the competition between cell cortex contractility and cell-cell adhesion. We show that an extended mechanical model including a term that counteracts cell anisotropy encompasses all oligocellular states in accordance with the experimental data. Following the dynamics of a single cell packing state, we also show that transitions occur between energetically equivalent states over time. Finally, we outline that oligocellular arrays have great potential as quantitative assays for cellular interactions.

## Results

### Cells living in confinement.

We describe experiments on Huh 7 cells growing on structured thin PDMS films. Using plasma induced hydrophilisation, defined micro-patterns are created, as described in the materials and methods section. The hydrophilic squares (side length  $\ell = 57 \mu\text{m}$ ) provide preferred adhesion areas that artificially constrain a small number of cells to a limited surface area (Figure 1a).

When cells are seeded onto the micro-structured surface, they are found to distribute and spread onto the adhesive square patches (Figure 1b). The number of cells per adhesive area,  $N$ , depends on the total cell concentration, which in the experiments was chosen such that typically between one to four cells are settled per patch. A single cell per patch tends to wet and fill the entire square. In the competitive situation with more than one cell per square, cells are found to arrange themselves into configurations with the total adhesive area being equally shared between cells. These packing states are long lasting compared to the time of cell state formation. When with proceeding time cells divide, new packing states of higher cell number form by rearrangement of cells, as schematically shown in Figure 1c. This cycle continues until the patches become overpopulated and cells are expelled from the adhesion “islands”. This occurs at an average number of more than four cells per area. However, now and again, squares occupied by up to seven cells are found. If cells are expelled, they are able to migrate to neighboring empty adhesive patches crawling over the hydrophobic parts of the surface. In the following, we will describe in more detail the characteristic packing states that appear for a small number of cells per patch ( $N < 5$ ). These long lasting cell packing states exhibit high symmetry as indicated by the tracked cell-cell contact lines in Figure 1b. Note that the emergence of relaxed packing states is not synchronized over the entire assay as can be seen in Figure 1b. The formation of relaxed stable states is a reproducible hallmark of the cell arrangement after cell division. In the following section we classify the stable cell packing states into distinct classes and discuss their relative abundance.

### Stable cell packing states.

For each number of cells per square patch we observe with high reproducibility a distribution of symmetric packing states (see histograms and fluorescent micrographs of the most prominent geometries in [Figure 2](#)). The packing states are characterized by cells sharing the available adhesive area equally, nuclei displacement towards the centre of the structure, and circumferential actin stress fibers surrounding the perimeter of the squares. We use the symmetry of the packing states to define “classes” for the cell arrangements within square adhesion patches.

There is only one class of packing states for two cells, namely two cells aligned in parallel, denoted  $2^{\parallel}$ . Two cells congruently divide the square area, sharing one cell-cell contact line and exhibiting the same area and length of circumference. In this class, packing states may vary in the angle  $\vartheta$  that the cell-cell contact line encloses with the boundary, see [Figure 2a](#). The ensemble average cell-contact angle of  $2^{\parallel}$  states in the experiment is found to be broadly distributed around a mean value of  $\langle \vartheta \rangle = (21 \pm 13)^{\circ}$ .

Due to elementary laws of geometry three cells on a square are obliged to break symmetry and arrange into states non-congruent in cell-cell contact. We find two classes of stable cell packing states, denoted  $3^{\parallel}$  and  $3^{\top}$ . The  $3^{\parallel}$  state, in which the three cells are aligned in parallel, does not occur as often as the  $3^{\top}$  packing state, where cells arrange in a T shape ([Figure 2b](#)). Within both classes ( $3^{\parallel}$  and  $3^{\top}$ ), the packing states differ in their orientation relative to the adhesion square's edges. The horizontal arrangement within the  $3^{\top}$  class is often rearranged into a fork state  $3^{\vee}$ . In the case of four cells per area, symmetry permits again cells to arrange in congruent packing states. Obviously, there are two high symmetry classes,  $4^{\parallel}$ , for parallel, and  $4^{\times}$ , for quadratic arrangement. However, neither of these classes is found in experiment. While the  $4^{\parallel}$  class is not observed at all, the  $4^{\times}$  class exists only in a distorted form that avoids the formation of a four-cell contact point. In the latter class, which we denote  $4_{\delta}^{\times}$ , symmetry is broken, as two cells are in contact with only two neighbors while the remaining two cells have three neighboring cells each. The length  $\delta$  of the contact line with the additional third neighbor is short compared to the

square length. The experiments show indeed a rather sharp distribution of  $\delta$  centered on  $\delta = (0.12 \pm 0.04)\ell \approx 7\mu m$  (see also supplementary [Figure S6](#)). The rare arrangements where the length  $\delta$  is below the resolution limit and could not be estimated are grouped into a class denoted  $4_0^x$ . Packing states within the  $4_0^x$  symmetry class differ again in their orientation relative to the adhesion square's edges. Since in all geometries cells equally share the available area, different cell packing states only vary in cell-cell contact length and individual cell perimeter, suggesting mechanical forces to regulate especially cell-cell contact length and cell perimeter.

### **Internal organization of cells.**

Polarity is an essential property of columnar epithelial cells which is attributed to the spatial orientation of the cell-cell and cell-ECM contacts<sup>26</sup>. The result is a polar positioning of the cell nucleus in the vicinity of cell-cell and cell-ECM contacts as depicted in [Figure 3a](#). Recent experiments of single cells<sup>27</sup> or tissues<sup>28, 29</sup> in confining geometries indicate nucleus position adverse to high focal adhesion density and close to cell-cell contacts. We investigate the internal organization of the cell packing states by labeling actin and cell nuclei, see [Figure 2](#) and [Figure 3b](#). Among the dense network of actin fibers throughout individual cells, actin stress fibers are pronounced along the edges of the square patches, probably due to the accumulation of focal adhesion points at the rim and especially at the corners of adhesion squares<sup>27</sup>. Also cell-cell contact lines show distinct actin density, which can be attributed to the actin cortex that establishes the contractile force within cells<sup>7</sup>. The cell nucleus position, relative to the cell centre, and its form evolve with the number of cells per patch. While a roundish nucleus is placed almost in the cell centre for a single cell per square, it is off-centered towards cell-cell contact lines for several cells per square. Nucleus shape is often observed to be deformed to assimilate a form dictated by the contour of cell-cell contact lines, thereby taking an elongated shape for N=2 and even a triangular shape for N=4, see [Figure 3b](#) and supplementary [Figure S5](#). Nucleus position is independent of cell shape. For example in the diagonal oriented state of  $3^T$  class, see [Figure 2b](#), the nucleus is always off-centered towards cell-cell contact, being

placed in the corner of a triangular cell in one case and along the edge of a triangular cell in the neighboring one. Nucleus position is also independent of the geometry of the adhesive patch, e.g., on square, circle or hexagon, nuclei are always off-centered towards cell-cell contact lines, often acquiring the shape of these lines (see Supplementary [Figure S4](#)).

### **Mechanical equilibrium model of cell packing states.**

We now analyze the geometry of all observed packing states in a mechanical model to infer the governing mechanical forces. We first follow current modeling approaches, which assume that cell arrangements are determined by three interactions namely cell-cell adhesion, cell cortex contractility and cell elasticity<sup>3, 4, 10, 13</sup>. In our experiments, however, the adhesion area is fixed by the preformed surface micropattern. From this boundary condition and taking into account that cell-surface interactions dominate, it follows that cells equally divide the available adhesion area  $\ell^2$  among each other as observed in experiment. Hence, we reduce model and parameters by introducing the constraint of equal area per cell,  $A_i = \text{const}$ . Cell arrangements on the adhesive squares are thus ruled by cell cortex contractility and cell-cell adhesion only. Cell contractility decreases the perimeter  $P_i$  of a cell  $i$ , while cell-cell adhesion favors long cell-cell contact lines  $L_{i,j}$  between neighboring cells  $j \in \nu(i)$ , see [Figure 4a](#). Stable arrangements of  $N$  cells are then described by the minimum of the energy function

$$E = \sum_{i \in \text{cells}}^N \left\{ \kappa P_i^2 - \alpha \sum_{j \in \nu(i)} L_{i,j} \right\}, \text{ with } A_i = \ell^2 / N = \text{const}. \quad (1)$$

where  $\kappa$  denotes the cell cortex contractility and  $\alpha$  the cell-cell adhesion parameter. Here we have neglected cell shape undulations and discuss cell states with straight cell boundaries only; fluctuations in cell boundaries are incorporated in  $\alpha$  and  $\kappa$  as effective parameters. Predictions of the energy function are discussed in ascending order for the cases  $N=2,3$ , and 4.

Arrangements of  $N=2$  cells on a square are described by just a single parameter, the angle  $\vartheta$ , between the horizontal axis through the square's centre and the contact line between the two cells, as shown in [Figure 4b](#). Minimization of the energy function shows that  $\vartheta = 0, \pm \frac{\pi}{2}, \pi$  is the

stable configuration for dominating contractility, which minimizes the perimeter, while

$\vartheta = \pm \frac{\pi}{4}, \pm \frac{3}{4}\pi$  is the solution for prevailing cell-cell adhesion, which maximizes the length of the

contact line. In general the competition between both contributions is given by the ratio  $\alpha/\ell\kappa$

and the energy minimization leads to a stable configuration with  $\cos \vartheta = \frac{1}{\frac{1}{2} \frac{\alpha}{\ell\kappa} - 2}$ .

Hence, the characteristic angle in cell packing states is directly related to the ratio of cell-cell adhesion and cell cortex contractility strength. Therefore, the experiment presented in [Figure 2a](#)

showing  $\langle \vartheta \rangle \approx 21^\circ$  for the Huh7 cells, yields a ratio of cell-cell adhesion strength versus cell cortex contractility of about  $\alpha/\kappa = 6.14\ell = 350\mu m$ .

Since the experiments show a broad distribution of angles  $\vartheta$ , we extend our model by introducing a statistical weight  $\rho$  for packing states in analogy to the statistical Boltzmann

weight  $\rho(\vartheta) = e^{-\beta E(\vartheta)} / \int d\vartheta e^{-\beta E(\vartheta)}$ . Fitting now the experimental distribution shown in [Figure 2a](#)

using the statistical weight function, we consistently find  $\alpha/\kappa = 6.08\ell = 347\mu m$  and effective temperature scale  $\beta = 7.7\kappa\ell^2$ . The theoretical distribution function shows a mean value of

$\langle \vartheta \rangle = 20.3^\circ$  in agreement with experimental data.

In the case of N=3 cells, cell packings break the symmetry of the adhesion square and cells arrange into non-congruent states. We observe two classes of cell packing: parallel,  $3^{\parallel}$ , and, T-shaped,  $3^{\top}$ , as shown in [Figure 2b](#). Using the parameter range identified from the case N=2, the parallel ordering  $3^{\parallel}$  exhibits a 10% lower total energy than the T-shaped packing. Indeed, the mechanical model in Eq. (1) predicts parallel ordering to be more probable than T-shaped, in contrast to observations. Thus our model assumption that cell states are governed by cell-cell contact and *isotropic* contractility is too restrictive to describe the prevalence of  $3^{\top}$  states. A solution to this puzzling situation arises from the experimental observation that the two classes display substantially different aspect ratios for individual cells as  $3^{\parallel}$  cells are very elongated and  $3^{\top}$  cells are rather roundish; see [Figure 4c](#) and [Figure S3](#). This suggests that the current standard model should be extended to account for cell *anisotropy*. Defining the size-

independent anisotropy of an individual cell as the normalized variance of the eigenvalues  $\lambda_{1,2}$  of the second moment of area<sup>\*</sup>, the standard model is extended by an additional term proportional to cell anisotropy with elastic constant  $\varepsilon$ :

$$E = \sum_{i \in \text{cells}}^N \left\{ \kappa P_i^2 - \alpha \sum_{j \in v(i)} L_{i,j} + \frac{\varepsilon}{N} \left( \frac{\lambda_{i,1} - \lambda_{i,2}}{\lambda_{i,1} + \lambda_{i,2}} \right)^2 \right\}, \text{ with } A_i = \ell^2 / N = \text{const.} \quad (2)$$

While positive  $\varepsilon$  favors cell isotropy, negative  $\varepsilon$  promotes elongated cell shape. A considerably small, positive  $\varepsilon$  renders parallel ordering less probable than T-shaped in agreement with experiments. As an independent control, the relatively frequent occurrence of the fork state  $3^Y$ , described in [Figure 2b](#), compared to the T-shaped  $3^T$  state is captured by the extended model, substantiating our notion. Within the  $3^T$  class itself the extended model predicts the minimal energy state to be diagonally oriented as observed with highest probability, see [Figure 2b](#) and [Figure S3](#).

Turning to an arrangement of  $N=4$  cells we may now assess the validity of the extended model Eq.(2). While the current standard model would predict parallel ordering  $4^{\parallel}$ , the elastic anisotropy term in our extended model strongly disfavors it. This is in accordance with the fact that  $4^{\parallel}$  states are not observed experimentally. Typically,  $N=4$  cells arrange in a  $4^{\times}$  class, where two 3-cell junctions are separated by a small distance  $\delta$ , see [Figure 4d](#). These cell packing states exhibit a *bimodal distribution* centered around states with maximal cell-cell contact and states with minimal perimeter; see [Figure 2c](#). The current standard model always predicts a *single stable state*; for the measured  $\alpha/\ell\kappa$  this state is characterized by maximal cell-cell contact. In contrast, our extended model correctly captures a *bimodal distribution* as it energetically favors both configurations with maximal cell-cell contact and those with minimal perimeter due to their lower anisotropy, see [Figure S3](#). Remarkably our experiments reveal a strongly peaked distribution of  $\delta$  centered around  $\delta = 0.12\ell$  (see supplementary [Figure S6](#)). This can neither be explained with the current standard model nor with our extended model, which both energetically promote a 4-cell junction instead of the observed two 3-cell junctions. This suggests that further factors need to be incorporated. One intriguing hypothesis is to

consider the statistical weight of states, directly related to their statistical entropy, which would clearly favor two 3-cell junctions over the singular state of a 4-cell junction.

### **Transitions between equivalent stable cell packings.**

So far we have described the stationary distribution of packing states according to a mechanical energy landscape. Experiments show that the cell arrangements are broadly distributed and also fluctuate with time. We show a 18h time lapse movie of a two-cell arrangement in [Figure 5](#). Due to the rotational symmetry of the adhesion patch, and the mirror symmetry of the two cells, the energy function has eight equivalent minima, according to eight degenerate stable packing states per patch. As a function of time, we observe transitions between these states, as can be seen in the time course of the cell-contact angle in [Figure 5b](#). Tracking the angle of N=2 packing states over time, we observe fluctuations around the mean and transitions past the corners of the adhesion patch. The distribution of angles over time is tracked and exhibits one distinct maximum in each quadrant, see [Figure 5c](#), corresponding to the mean angle as extracted from the cell packing ensemble in [Figure 2a](#). The probability of states matches the prediction from our model (red line in [Figure 5c](#)), only states with contact lines extending from corner to corner, i.e.,  $\vartheta = 45^\circ$ , occur more often than predicted. This could be arising as cells might take more time to reorder their stress fibers when passing a corner than when moving along edges, increasing the time sampling density of corner versus edge configurations. The fitted time distribution of angles yields  $\langle \vartheta \rangle = 17.4^\circ$  and  $\alpha/\kappa = 6.07\ell = 346\mu\text{m}$  for  $\beta = 24.3\kappa\ell^2$ . It is noteworthy that the ratio  $\alpha/\kappa$  agrees with the previous considerations. Apparently, however, without overstressing the analogy, the effective temperatures in the ensemble and time average differ. As both averages cover different scales in time, the difference might well reflect distinct stochastic dynamics of the underlying cytoskeletal network.



## Discussion

The behavior of a small number of cells on micropatterned substrates is a novel field for experiment and theoretical analysis. The finite size of the system allows for the full assessment of the entire configuration space. The very observation of distinct classes of highly regular homeostatic cell arrangements led us to extend the current model of cell mechanics in tissues. In particular we measured and calculated for two, three, and four cells on a square adhesion patch a characteristic distribution of cell packing states. The trivial case of two cells is charming because it is characterized by the contact angle as the single and easily quantifiable parameter. This case is well described by the standard vertex model<sup>3, 4, 10, 13, 18</sup>. In contrast, the arrangement of three cells on a square is more evolved and adopts non-trivial geometries. Here the abundance of T-states could not be explained consistently within the standard model. We, hence, have generalized the standard model by introducing an elastic anisotropy term, which in turn was corroborated by the correct predictions of the three cell fork states and the bimodal distribution of four cell states.

An important aspect of our analysis is that all homeostatic states in the different packing classes are subject to considerable fluctuations. We found that a Boltzmann distribution captures the experimentally observed distribution of states. This yields an “effective temperature” as a measure for the strength of fluctuations. Similar approaches are frequently encountered in the physics literature in the context of various driven and active systems far from equilibrium<sup>30, 31</sup>. In the case of living cells the effective temperature can be attributed to stochastic dynamics of the cytoskeleton caused by the underlying activity of molecular motors. Our modeling suggests the intriguing hypothesis that the stochastic fluctuations are strong enough to counteract the elastic forces, thus rendering 4-cell junctions non-existent. However, we cannot exclude that internal cell structure determines the distance between 3-cell junctions. Probable candidates are elastic forces due to the presence of cell nuclei in the proximity of cell contact lines.

The oligocellular packing states also exhibit distinct polarization of cells within an adhesion patch. Cell nuclei are off-centered towards neighboring cells and often are even deformed to

assimilate the shape of the cell-cell contact line. As recently noted by Desai *et al.*<sup>28</sup> and Dupin *et al.*<sup>29</sup> cell polarization is induced by asymmetric cell-cell adhesion via cadherins. Furthermore, the shape of adhesion sites has an influence on cell polarization as reported by Thery *et al.*<sup>27</sup>. Remarkably all oligocellular arrangements observed here are indeed oriented from cell-cell adhesion sites towards the boundaries of the adhesive patch. This aspect renders oligocellular arrays distinct from locally isotropic polygonal tissue structures and possibly allows to study epithelia polarization in more detail.

Oligocellular packing states on micro-patterns may have biotechnological relevance, similar to recent advances on single cell studies<sup>27</sup>. In vivo cell packing is influenced by a variety of factors such as supporting cell layers, surrounding tissue type, and its history during tissue development. Artificial cell arrays allow to study cell mechanics in ensembles of small groups of cells in a well-defined cell-cell contact geometry and chemically biofunctionalized environment. In combination with mechanical modeling this opens up novel approaches for quantitative analysis. There are many possibilities to extend oligocellular arrays by using various geometries<sup>27</sup>, different surfaces chemistry, or by fine-tuning biological interactions with genetic manipulation. Oligocellular tissues could furthermore be applied to study mechanical changes during cell differentiation, an important aspect for cell therapy, or differential cell adhesion<sup>32</sup>. From a cell biology perspective, it is desirable to specifically relate structures and processes at the intracellular level with the elastic forces governing cell mechanics at a tissue level. In particular future studies should reveal how cell anisotropy is regulated and how it facilitates the emergence of tissue shape and function. In summary, we believe that given the complexity of cellular interactions oligocellular arrays are a promising assay whose simplicity may promote our understanding of tissue formation by quantifiable measures.

## Methods

### Cell culture.

Huh-7 cells were grown in MEM-F12 medium supplemented with 10% FBS and 5 mM L-Glutamine at 37°C in a humidified atmosphere, 5% CO<sub>2</sub> level. Cells were maintained at 85% confluence, trypsinized, washed with PBS, re-suspended in cell medium and counted using a Neubauer counting chamber.

### Hydrophilic/hydrophobic patterns.

We use the patterning technique reported by Hsieh *et al.*<sup>33</sup> with some modifications.

PDMS (Sylgard 184, Dow Corning, Midland, MI, U.S.A.) was prepared in a 10/1 w/w ratio. The mixture was stirred and degassed for ten minutes. This mixture was spin coated on an Ibidi  $\mu$ -slide (Ibidi-GmbH, München, Germany) at 2000 rpm for 10 s followed by 4000 rpm for 30 s. The coated slides were degassed again and the PDMS was cured in the oven overnight at 50°C. The copper TEM grids were pre-exposed to water vapour for 30 s, to create a water bridge between the grid and the PDMS surface as described by Andruzzi<sup>34</sup>, and immediately placed onto the PDMS surface. The samples were exposed to low pressure oxygen plasma for 2 min (40W 5 cm<sup>3</sup>/min at 25°C and 2 bar, Femto, Diener) and, afterwards, sonicated 1 min in 80% ethanol to remove the copper grids and 3 min in water to clean them. Samples were sterilized in 80% ethanol, submerged 15 min in sterile Millipore water to remove ethanol residues and used immediately. In contrast with the results obtained by Hsieh *et al.*<sup>33</sup>, the sample regions that were protected from the plasma remained hydrophobic while the rest of the sample became hydrophilic, as we expected.

### Cell patterning.

Cells were re-suspended in MEM-F12 medium supplemented with 10% FBS and 5 mM L-Glutamine, seeded on the plasma treated surfaces and incubated at 37°C in a humidified atmosphere, 5% CO<sub>2</sub> level. After 20 min, chambers were rinsed with cell medium in order to remove non-attached cells. At this point, patterns formed accordingly to surface wettability were already visible.

### **Cell nuclei staining.**

Cells were fixed during 20 min with 10% of formaldehyde in cell culture medium and rinsed thrice with PBS buffer. Then, they were incubated 5 min in a 2 µg/ml 4'6-diamidino-2-phenylindole (DAPI, Sigma) in PBS and rinsed again thrice with PBS buffer.

### **Microscopy.**

Images were acquired using a motorized Nikon Eclipse Ti microscope equipped with a temperature-controlled mounting frame, 10x and 40x Plan Fluor objectives and a CCD CoolSNAP HQ monochrome camera. Acquisitions were controlled through µ-Manager open source software. Fluorescence illumination was generated using an Intensilight lamp and fluorescent signals were detected using the following filter sets: GFP, BP470/40, FT495, BP525/50 and DAPI, BP360/40, 400DCLP, BP360/50. For living cell image acquisition, the temperature of the mounting frame temperature was set to 37°C and CO<sub>2</sub> independent Leibovitz's L15 cell culture medium, supplemented with 10% FBS and 1 mM extra L-Glutamine, was used. The time interval for time lapse acquisition was 10 min.

### **Acknowledgements**

The authors would like to thank Manfred Ogris for providing the actin-GFP expressing Huh 7 cell line. This work was supported by the EU FP6 project NanoInteract (contract 033231) and by the Deutsche Forschungsgemeinschaft through the Excellence Cluster "Nanosystems Initiative Munich (NIM)" and of the LMUinnovativ project "Functional Nanosystems (FuNS)". K.A. acknowledges funding by the "Studienstiftung des deutschen Volkes".

### **Footnotes**

\*The normalization by the mean of the eigenvalues ensures that the anisotropy measure is independent of the total cell area.

## Figures

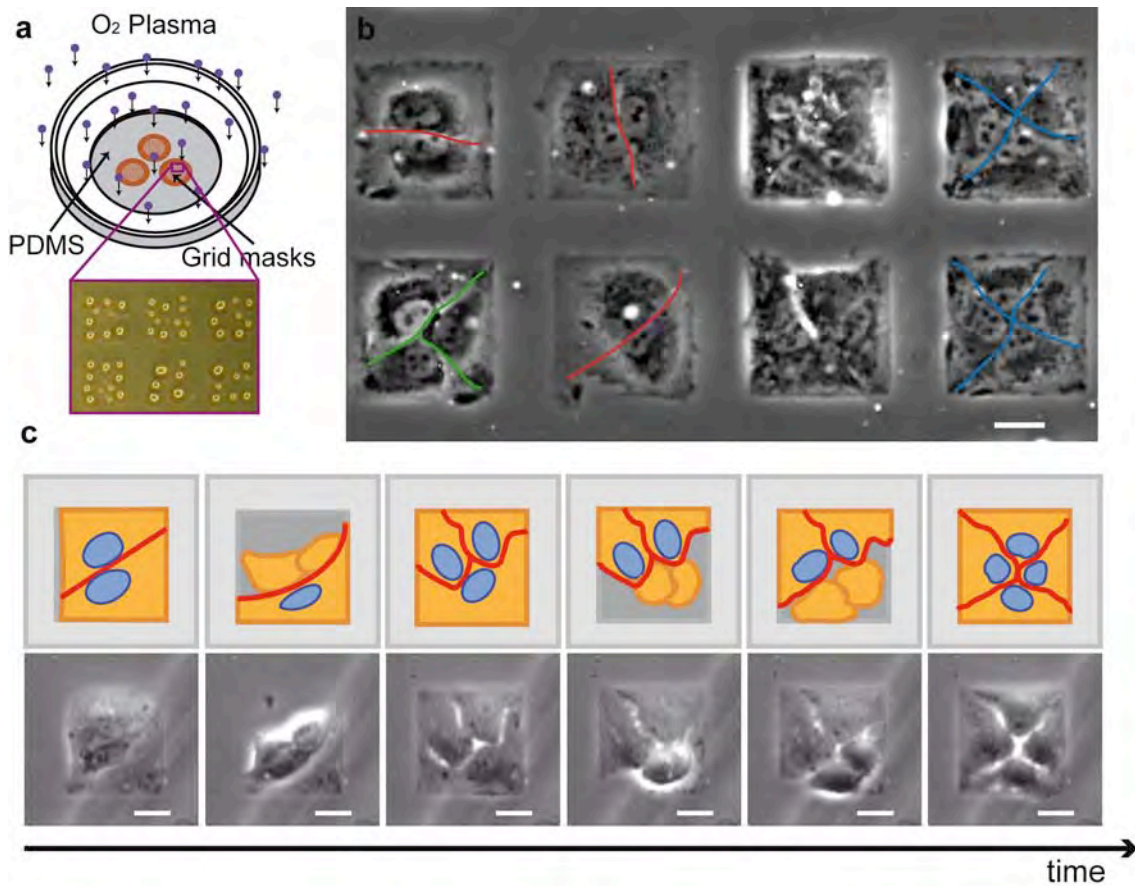


**Figure 1. Cells living in confinement.** **a.** Hydrophilic/Hydrophobic surface patterning is achieved through oxygen plasma treatment of PDMS using a TEM grid as a mask. Removing the grid reveals patterned squares as shown by water vapor condensation in the inset. **b.** Cells seeded onto the patterned area are confined to the hydrophilic adhesive patches, tend to wet them completely and adopt in majority highly symmetric cell packing states. **c.** Time evolution of a group of cells seeded on an adhesive square. Cells arrive to the adhesive patch, spread, relax and are able to divide. After cell division, cells reorganize and relax into a new cell arrangement. Relaxed cell packing states divide the available area equally among all cells. The geometry of the cell-cell contact lines displays high reproducibility, which enables statistical data analysis and model building. Scale bars correspond to 20  $\mu\text{m}$ .

Piera et al. Figure 1

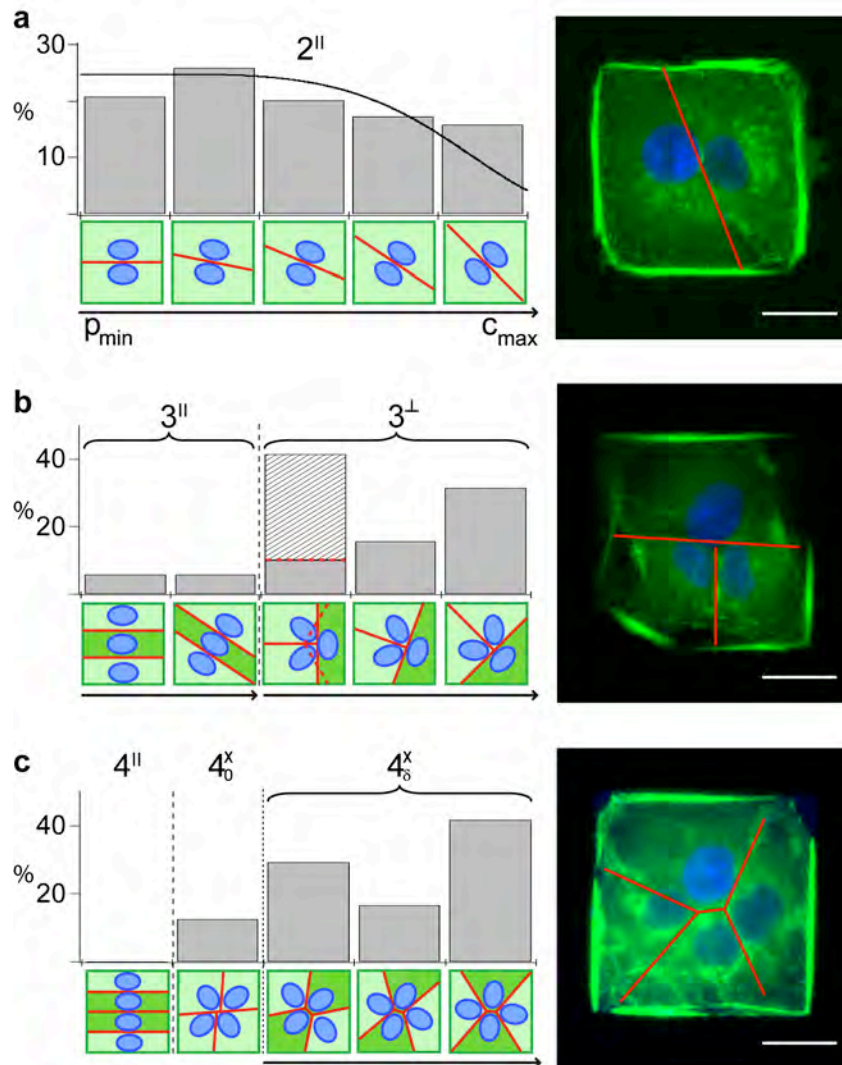


**Figure 2. Relative abundance of packing states classified by number of cells and symmetry.** Cells relax into homeostatic states characterized by symmetric geometry, cell nuclei displacement towards the centre and an actin belt at its perimeter. Histograms show the relative abundance of each of the different configurations for two, three and four cells on a square. Different states in a class are sorted from minimal cell perimeter ( $p_{\min}$ ), to maximal cell-cell contact ( $c_{\max}$ ), as indicated by the arrows. **a.** Two cells divide a square in two congruent areas with varying relative orientation of the contact line with respect to the square. This class is denoted  $2^{\text{II}}$ . Each column encompasses a successive range of nine degrees, from horizontal ( $0^\circ$ ) to diagonal ( $45^\circ$ ). The full line corresponds to a theoretical fit of the distribution. **b.** A square cannot be divided into three parts having equal area, perimeter and cell-cell contact lines, as those marked in light green. Three cells show two classes of cell arrangements denoted  $3^{\text{II}}$  and  $3^{\text{I}}$ . Within the first of the  $3^{\text{I}}$  states, we make a distinction between the regular and the rearranged fork state  $3^{\text{Y}}$  cases as indicated by the dashed lines. **c.** In the case of four cells, the  $4^{\text{X}}$  symmetry is preferred over  $4^{\text{II}}$ . In general, however, the  $4^{\text{X}}$  symmetry is broken because cells avoid the formation of 4-cell junctions, adopting states with two 3-cell junctions ( $4^{\text{X}}_\delta$ ) separated by small distance  $\delta$  instead. Fluorescence micrographs show examples of the dominant packing states for two, three and four cells. The GFP-expressing actin cytoskeleton of modified Huh 7 cells is shown in green, while the DAPI-stained cell nuclei are in blue. Scale bars correspond to 20  $\mu\text{m}$ .

Piera et al. Figure 2

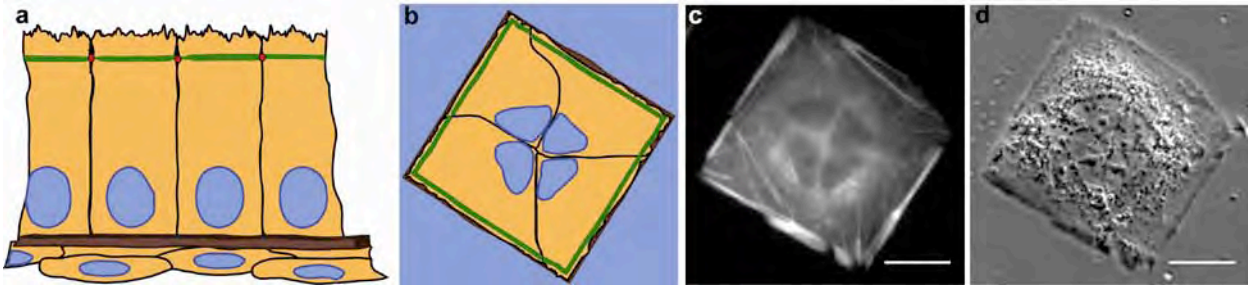


**Figure 3. Induced cell polarization.** **a.** In a normal polarized epithelial sheet the apical membranes face the upper “adhesion-site-free” surface. The nuclei are displaced towards the areas of accumulation of cell-ECM adhesion sites. The adhesion belt is located just below the apical membrane, linking the cells, and the cortical actin ring encircling each of the interacting cells in the sheet. **b-d.** Our artificial environment introduces an asymmetry in the distribution of adhesion sites, the rims of squares are cell-cell “adhesion-site-free” surfaces. Just beneath these surfaces, actin stress fibers form a belt surrounding the perimeter of the adhesion patch, while cortical actin is observed encircling each cell in the square, as can be seen in **c**. The nuclei appear off-centered towards the cell-cell contact lines and very often they are deformed to assimilate the shape of the cell-cell contact line contour, acquiring a triangular shape, as can be observed in the phase contrast, **d**, and fluorescence, **c**, micrographs. Scale bars correspond to 20  $\mu\text{m}$ .

Piera et al. Figure 3

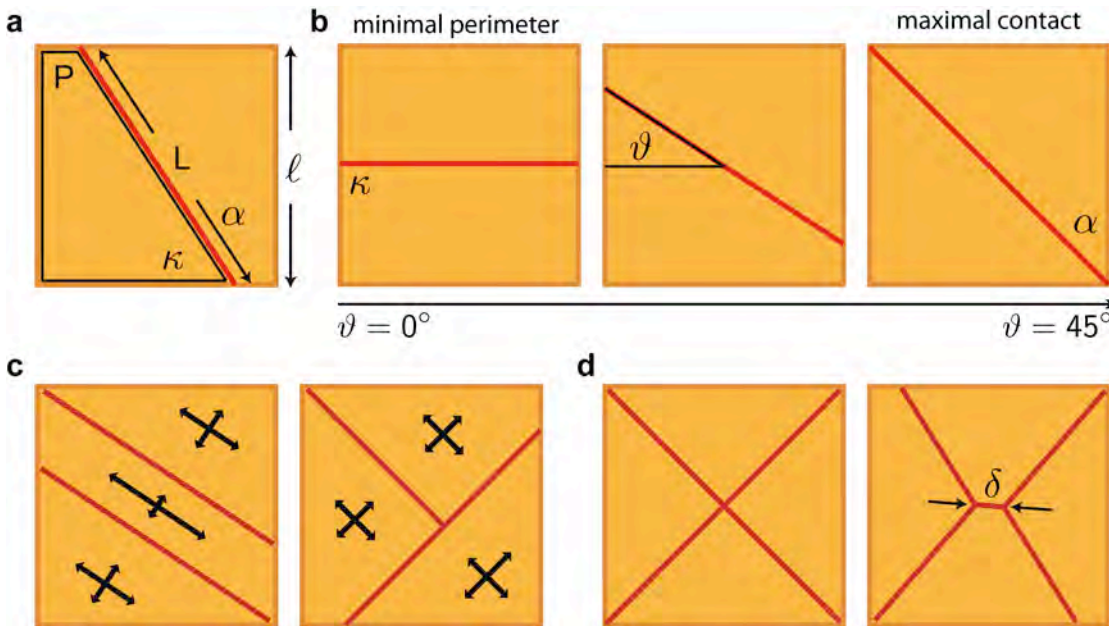


**Figure 4. Mechanical equilibrium model for cell packing states.** **a.** The geometry of a cell packing is described by each cell’s perimeter  $P$  and the cell-cell contact line  $L$ . Both measure the contributing mechanical forces. While cell cortex contractility  $\kappa$  promotes small perimeters  $P$  the opposing cell-cell adhesion  $\alpha$  favors large cell-cell contact  $L$ . **b.** In the symmetric cell packing of two cells on a square a single angle  $\vartheta$  classifies the competition between minimal perimeter caused by cell cortex contractility and maximal cell-cell contact line favored by cell-cell adhesion. The resulting angle depends on the ratio of both contributions only. **c.** While in the  $3^{\text{II}}$  class cells are highly elongated they are rather roundish in the  $3^{\text{T}}$  class. Only additional elastic forces that counteract cell anisotropy are able to explain the dominance of the  $3^{\text{T}}$  class consistently. **d.** Four cells on a square arrange asymmetrically with two 3-cell junctions separated a distance  $\delta$  apart, see main text. The graphics for  $N=3,4$  cells depict the maximal contact state only.

Piera et al. Figure 4

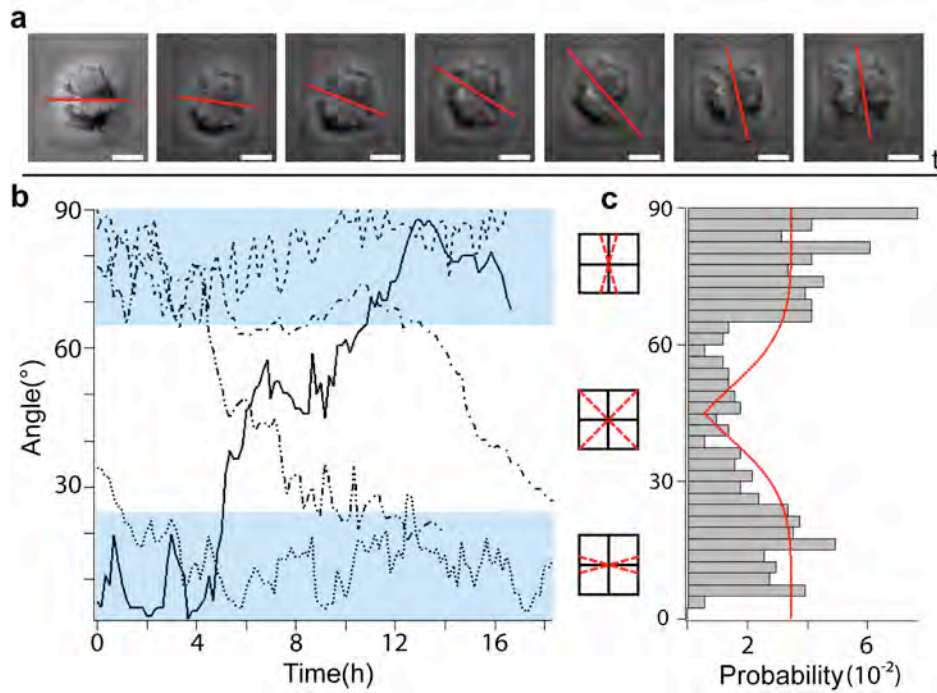


**Figure 5. Fluctuations around and transitions between equally stable cell packing states.** Over the course of time cell arrangements fluctuate around their stable state and also transition to mutually equal stable states related by mirror symmetry along the diagonal of the square as shown by the timeline of phase contrast micrographs **a** and by angle tracking in **b**. The rotational and mirror symmetry of two cells on a square allows for in total eight equivalent stable cell packing states. Following the timeline of the angle the cell-cell contact line encloses with the horizontal axis enables the quantification of angle distributions **c**. The observed distribution is in agreement with model predictions, fit shown in red. Scale bars correspond to 20  $\mu\text{m}$ .

Piera et al. Figure 5



## References

1. Steinberg, M.S. Reconstruction of tissues by dissociated cells. *Science* **141**, 401-408 (1963).
2. Hayashi, T. & Carthew, R.W. Surface mechanics mediate pattern formation in the developing retina. *Nature* **431**, 647-652 (2004).
3. Käfer, J., Hayashi, T., Marée, A.F.M., Carthew, R.W. & Graner, F. Cell adhesion and cortex contractility determine cell patterning in the *Drosophila* retina. *Proc. Natl. Acad. Sci. U.S.A.* **104**, 18549-18554 (2007).
4. Farhadifar, R., Roper, J.C., Algouy, B., Eaton, S. & Jülicher, F. The influence of cell mechanics, cell-cell interactions, and proliferation on epithelial packing. *Curr. Biol.* **17**, 2095-2104 (2007).
5. Hilgenfeldt, S., Eriskens, S. & Carthew, R.W. Physical modeling of cell geometric order in an epithelial tissue. *Proc. Natl. Acad. Sci. U.S.A.* **105**, 907-911 (2008).
6. Bertet, C., Sulak, L. & Lecuit, T. Myosin-dependent junction remodelling controls planar cell intercalation and axis elongation. *Nature* **429**, 667-671 (2004).
7. Paluch, E. & Heisenberg, C.P. Biology and physics of cell shape changes in development. *Curr. Biol.* **19**, R790-R799 (2009).
8. Krieg, M. *et al.* Tensile forces govern germ-layer organization in zebrafish. *Nat. Cell Biol.* **10**, 429-U122 (2008).
9. Lecuit, T. & Lenne, P.-F. Cell surface mechanics and the control of cell shape, tissue patterns and morphogenesis. *Nat. Rev. Mol. Cell Biol.* **8**, 633-644 (2007).
10. Rauzi, M., Verant, P., Lecuit, T. & Lenne, P.-F. Nature and anisotropy of cortical forces orienting *Drosophila* tissue morphogenesis. *Nat. Cell Biol.* **10**, 1401-U1457 (2008).
11. Blanchard, G.B. *et al.* Tissue tectonics: morphogenetic strain rates, cell shape change and intercalation. *Nat. Meth.* **6**, 458-U486 (2009).
12. Shraiman, B.I. Mechanical feedback as a possible regulator of tissue growth. *Proc. Natl. Acad. Sci. U.S.A.* **102**, 3318-3323 (2005).
13. Hufnagel, L., Teleman, A.A., Rouault, H., Cohen, S.M. & Shraiman, B.I. On the mechanism of wing size determination in fly development. *Proc. Natl. Acad. Sci. U.S.A.* **104**, 3835-3840 (2007).
14. Omelchenko, T., Vasiliev, J.M., Gelfand, I.M., Feder, H.H. & Bonder, E.M. Rho-dependent formation of epithelial "leader" cells during wound healing. *Proc. Natl. Acad. Sci. U.S.A.* **100**, 10788-10793 (2003).
15. Safran, S.A., Gov, N., Nicolas, A., Schwarz, U.S. & Tlusty, T. Physics of cell elasticity, shape and adhesion. *Physica A* **352**, 171-201 (2005).
16. Angelini, T.E., Hannezo, E., Trepat, X., Fredberg, J.J. & Weitz, D.A. Cell migration driven by cooperative substrate deformation patterns. *Phys. Rev. Lett.* **104**, 168104 (2010).
17. Poujade, M. *et al.* Collective migration of an epithelial monolayer in response to a model wound. *Proc. Natl. Acad. Sci. U.S.A.* **104**, 15988-15993 (2007).
18. Trepat, X. *et al.* Physical forces during collective cell migration. *Nat. Phys.* **5**, 426-430 (2009).
19. Friedl, P. & Gilmour, D. Collective cell migration in morphogenesis, regeneration and cancer. *Nat. Rev. Mol. Cell Biol.* **10**, 445-457 (2009).
20. Chen, H.H. & Brodland, G.W. Cell-level finite element studies of viscous cells in planar aggregates. *J. Biomech. Eng.* **122**, 394-401 (2000).
21. Balaban, N.Q. *et al.* Force and focal adhesion assembly: a close relationship studied using elastic micropatterned substrates. *Nat. Cell Biol.* **3**, 466-472 (2001).

22. Bischofs, I.B., Klein, F., Lehnert, D., Bastmeyer, M. & Schwarz, U.S. Filamentous network mechanics and active contractility determine cell and tissue shape. *Biophys. J.* **95**, 3488-3496 (2008).
23. Chen, C.S., Mrksich, M., Huang, S., Whitesides, G.M. & Ingber, D.E. Geometric control of cell life and death. *Science* **276**, 1425-1428 (1997).
24. Théry, M. *et al.* The extracellular matrix guides the orientation of the cell division axis. *Nat. Cell Biol.* **7**, 947-U929 (2005).
25. Jiang, X.Y., Bruzewicz, D.A., Wong, A.P., Piel, M. & Whitesides, G.M. Directing cell migration with asymmetric micropatterns. *Proc. Natl. Acad. Sci. U.S.A.* **102**, 975-978 (2005).
26. Eaton, S. & Simons, K. Apical, basal, and lateral cues for epithelial polarization. *Cell* **82**, 5-8 (1995).
27. Théry, M. *et al.* Anisotropy of cell adhesive microenvironment governs cell internal organization and orientation of polarity. *Proc. Natl. Acad. Sci. U.S.A.* **103**, 19771-19776 (2006).
28. Desai, R.A., Gao, L., Raghavan, S., Liu, W.F. & Chen, C.S. Cell polarity triggered by cell-cell adhesion via E-cadherin. *J. Cell Sci.* **122**, 905-911 (2009).
29. Dupin, I., Camand, E. & Etienne-Manneville, S. Classical cadherins control nucleus and centrosome position and cell polarity. *J. Cell Biol.* **185**, 779-786 (2009).
30. Ono, I.K. *et al.* Effective temperatures of a driven system near jamming. *Phys. Rev. Lett.* **89**, - (2002).
31. Ojha, R.P., Lemieux, P.-A., Dixon, P.K., Liu, A.J. & Durian, D.J. Statistical mechanics of a gas-fluidized particle. *Nature* **427**, 521-523 (2004).
32. Pedrotty, D.M. *et al.* Structural coupling of cardiomyocytes and noncardiomyocytes: quantitative comparisons using a novel micropatterned cell pair assay. *Am. J. Physiol. Hearth Circ. Physiol.* **295**, H390-H400 (2008).
33. Hsieh, S., Cheng, Y.-A., Hsieh, C.-W. & Liu, Y. Plasma induced patterning of polydimethylsiloxane surfaces. *Mater. Sci. Eng. B* **156**, 18-23 (2009).
34. Andruzzi, L. *et al.* Bio-selective surfaces by chemically amplified constructive microlithography. *Surf. Sci.* **601**, 4984-4992 (2007).

# Supplementary information: Oligocellular arrays: A novel approach to explore cell tissue mechanics

Alicia Piera Alberola<sup>1†</sup>, Karen Alim<sup>2†</sup>, Anna-Kristina Marel<sup>1</sup>,  
Erwin Frey<sup>2\*</sup> and Joachim O. Rädler<sup>1\*</sup>

1. Faculty of Physics and Center for NanoScience (CeNS), Ludwig-Maximilians-Universität,  
Geschwister Scholl Platz 1, D-80539 München, Germany

2. Arnold Sommerfeld Center for Theoretical Physics (ASC) and Center for NanoScience (CeNS),  
Faculty of Physics, Ludwig-Maximilians-Universität München,  
Theresienstraße 37, D-80333 München, Germany

†Authors contributed equally to this work.

\*To whom correspondence should be addressed.

Email: frey@lmu.de

Email: joachim.raedler@physik.uni-muenchen.de

Telephone number: +49 89 2180 2438

## Calculation of cell packing states and corresponding mechanical energy

Cell packing states for  $N=2,3,4$  cells per square adhesion patch of side length  $\ell$  are calculated according to the vertex positions given for all geometries in [Figures S1/S2](#). States within a packing class vary with respect to the angle  $\vartheta$  enclosed with the confining patch as depicted for each class in [Figures S1/S2](#). Due to the fourfold rotational symmetry of the square only angles  $0^\circ \leq \vartheta \leq 45^\circ$  denote mutually different states.

Given all  $n$  vertices  $\{x_i, y_i\}$  of a cell, its corresponding perimeter is given by

$$P = \sum_i \sqrt{(x_i - x_{i-1})^2 + (y_i - y_{i-1})^2},$$

the contact length  $L$  forms the according subset. The anisotropy  $\Delta$  of a cell is based on the

second moment of area matrix  $M = \begin{pmatrix} m_{xx} & m_{xy} \\ m_{xy} & m_{yy} \end{pmatrix}$  of a polygon defined by

$$m_{xx} = \frac{1}{12} \sum_{i=1}^n (y_i^2 + y_i y_{i+1} + y_{i+1}^2)(x_i y_{i+1} - x_{i+1} y_i),$$

$$m_{xy} = \frac{1}{24} \sum_{i=1}^n (x_i y_{i+1} + 2x_i y_i + 2x_{i+1} y_{i+1} + x_{i+1} y_i) (x_i y_{i+1} - x_{i+1} y_i),$$

$$m_{yy} = \frac{1}{12} \sum_{i=1}^n (x_i^2 + x_i x_{i+1} + x_{i+1}^2) (x_i y_{i+1} - x_{i+1} y_i).$$

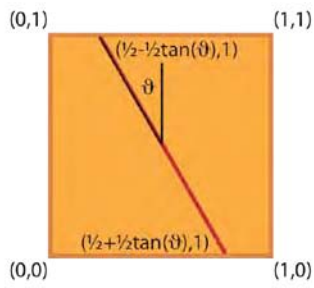
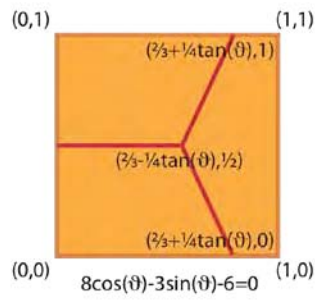
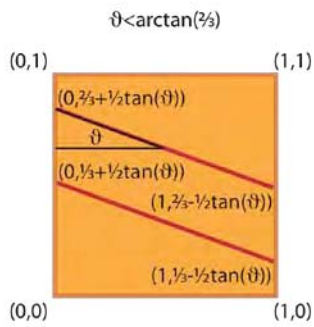
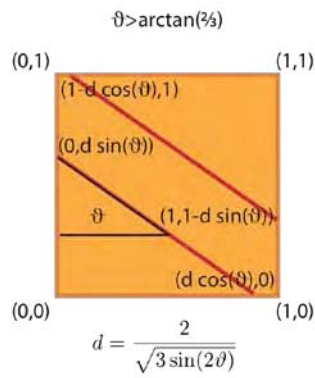
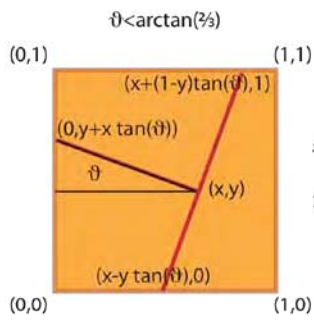
The cell anisotropy is then given by the normalized mean variance of the eigenvalues  $\lambda_1, \lambda_2$  of

$M$ , i.e.  $\Delta = \left( \frac{\lambda_1 - \lambda_2}{\lambda_1 + \lambda_2} \right)^2$ . Here the normalization ensures that the cell anisotropy is independent

of cell size.

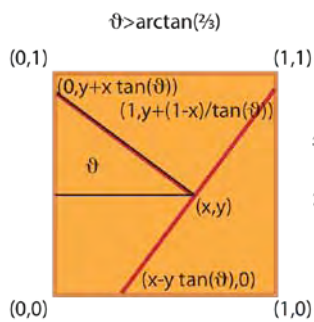
Fitting the current standard model Eq. (1) to our experimental data for the ensemble and time distribution of cells in the 2<sup>ll</sup> class we consistently obtain  $\alpha_{\kappa\ell} = 6.1$ . Including cell anisotropy in our extended model given in Eq. (2) a valid choice of parameters based on the 2<sup>ll</sup> data is  $\alpha_{\kappa\ell} = 5.1$  and  $\epsilon_{\kappa\ell^2} = 2$ . Given these parameters the extended model predicts a higher energy for 3<sup>ll</sup> than for 3<sup>T</sup> and a bimodal distribution for 4 <sub>$\delta$</sub> <sup>x</sup> cells close to  $\vartheta = 0^\circ, 45^\circ$ . Also the fork state 3<sup>Y</sup> consistently exhibits lower energy than the corresponding 3<sup>T</sup> state. Note that the additional term gives only a small but important correction to the previous value of  $\alpha_{\kappa\ell} = 6.1$  considering cell cortex contractility and cell-cell adhesion only.

Figure S3 displays for all cell packing states the energy landscape in the current standard model, their corresponding cell anisotropy, and the energy landscape in our extended model for the parameter choice given above.

**2<sup>II</sup>****3<sup>Y</sup>****3<sup>II</sup>****3<sup>II</sup>****3<sup>T</sup>**

$$x = \frac{1}{6} \cos^2(\vartheta) \sqrt{\sec^2(\vartheta)(7 + 9 \sec^2(\vartheta))}$$

$$y = \frac{1}{6} \cos^2(\vartheta) \left[ 3 \sec^2(\vartheta) + \cot(\vartheta) (-4 + \sqrt{\sec^2(\vartheta)(7 + 9 \sec^2(\vartheta))}) - 4 \tan(\vartheta) \right]$$

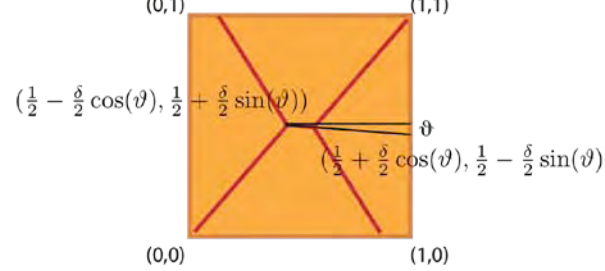
**3<sup>T</sup>**

$$x = \frac{1}{\sqrt{3}} \sqrt{\sin(\vartheta) \cos^3(\vartheta) \left[ \tan(\vartheta)(4 \tan(\vartheta) + 3) + 3 \cot(\vartheta) - 2\sqrt{6 \csc(\vartheta) \sec^3(\vartheta)} + 4 \right]}$$

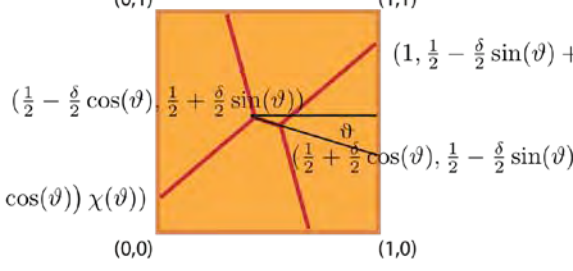
$$y = \frac{1}{6} \cot(\vartheta) \left( \sin(2\vartheta) \sqrt{6 \csc(\vartheta) \sec^3(\vartheta)} + \sqrt{6 \cos(\vartheta) \left[ 6 \cos(\vartheta) + \sin(\vartheta) \left( 8 - \sqrt{6 \csc(\vartheta) \sec^3(\vartheta)} \right) - \sin(3\vartheta) \sqrt{6 \csc(\vartheta) \sec^3(\vartheta)} \right]} - 6 \right)$$

**Figure S1. Calculation of cell packing states for N=2,3.** In a square normalized to side length  $\ell = 1$  the formula for the coordinates are indicated next to the corresponding vertex for the packing classes  $2^{II}$ ,  $3^Y$ ,  $3^{II}$ , and  $3^T$ .

$4_{\delta}^{\times}$

$$\begin{aligned}
 & \left( \frac{1}{2} - \frac{\delta}{2} \cos(\vartheta) - \left( \frac{1}{2} - \frac{\delta}{2} \sin(\vartheta) \right) \frac{\cot(2\vartheta) - \chi(\vartheta)}{\chi(\vartheta) \cot(2\vartheta) + 1}, 1 \right) \\
 & \qquad \qquad \qquad \left( \frac{1}{2} + \frac{\delta}{2} \cos(\vartheta) + \left( \frac{1}{2} + \frac{\delta}{2} \sin(\vartheta) \right) \frac{1}{\chi(\vartheta)}, 1 \right) \\
 & (0,1) \qquad \qquad \qquad (1,1) \\
 & \left( \frac{1}{2} - \frac{\delta}{2} \cos(\vartheta), \frac{1}{2} + \frac{\delta}{2} \sin(\vartheta) \right) \\
 & \qquad \qquad \qquad \left( \frac{1}{2} + \frac{\delta}{2} \cos(\vartheta), \frac{1}{2} - \frac{\delta}{2} \sin(\vartheta) \right) \\
 & (0,0) \qquad \qquad \qquad (1,0) \\
 & \left( \frac{1}{2} - \frac{\delta}{2} \cos(\vartheta) - \left( \frac{1}{2} + \frac{\delta}{2} \sin(\vartheta) \right) \frac{1}{\chi(\vartheta)}, 0 \right) \\
 & \qquad \qquad \qquad \left( \frac{1}{2} + \frac{\delta}{2} \cos(\vartheta) + \left( \frac{1}{2} - \frac{\delta}{2} \sin(\vartheta) \right) \frac{\cot(2\vartheta) - \chi(\vartheta)}{\chi(\vartheta) \cot(2\vartheta) + 1}, 0 \right)
 \end{aligned}$$


$$\chi(\vartheta) = \frac{2 \left( \delta^2 \cos(2\vartheta) \tan(\vartheta) + \sqrt{-\delta^4 + (\delta^2 + 1)^2 \sec^2(\vartheta) - 8\delta \sec(\vartheta) + \csc^2(\vartheta) + 4 + 2 \cot(2\vartheta) - 2} \right) + 8\delta \cos(\vartheta)}{4(\delta^2 \sin^2(\vartheta) - 2\delta \cos(\vartheta) \cot(\vartheta) - \tan(\vartheta) + \cot(\vartheta) + 1)}$$

$$\begin{aligned}
 & \left( \frac{1}{2} - \frac{\delta}{2} \cos(\vartheta) - \left( \frac{1}{2} - \frac{\delta}{2} \sin(\vartheta) \right) \frac{\cot(2\vartheta) - \chi(\vartheta)}{\chi(\vartheta) \cot(2\vartheta) + 1}, 1 \right) \\
 & (0,1) \qquad \qquad \qquad (1,1) \\
 & \left( \frac{1}{2} - \frac{\delta}{2} \cos(\vartheta), \frac{1}{2} + \frac{\delta}{2} \sin(\vartheta) \right) \\
 & \qquad \qquad \qquad \left( \frac{1}{2} + \frac{\delta}{2} \cos(\vartheta), \frac{1}{2} - \frac{\delta}{2} \sin(\vartheta) \right) \\
 & \left( 0, \frac{1}{2} + \frac{\delta}{2} \sin(\vartheta) - \left( \frac{1}{2} - \frac{\delta}{2} \cos(\vartheta) \right) \chi(\vartheta) \right) \\
 & (0,0) \qquad \qquad \qquad (1,0) \\
 & \left( \frac{1}{2} + \frac{\delta}{2} \cos(\vartheta) + \left( \frac{1}{2} - \frac{\delta}{2} \sin(\vartheta) \right) \frac{\cot(2\vartheta) - \chi(\vartheta)}{\chi(\vartheta) \cot(2\vartheta) + 1}, 0 \right)
 \end{aligned}$$


$$\begin{aligned}
 \chi(\vartheta) &= \frac{\delta \sec(2\vartheta) [-2\delta \sin(\vartheta) \cos^3(\vartheta) + \sin(3\vartheta) + \cos(\vartheta)]}{(\delta \cos(\vartheta) - 1)^2} \\
 &+ \frac{\tan(2\vartheta) \sqrt{2} \csc(2\vartheta) [\csc(2\vartheta) (-\delta^4 \cos(4\vartheta) + \delta^4 + 4\delta^3 \cos(3\vartheta) - 4(\delta^2 + 4)\delta \cos(\vartheta) + 16\delta^2)]}{4(\delta \cos(\vartheta) - 1)^2} \\
 &+ \frac{\tan(2\vartheta) \left( \sqrt{2} \csc(2\vartheta) [\csc(2\vartheta) (-16\delta \sin(\vartheta) + 8) - 8\delta^2(\delta \cos(\vartheta) - 1)] - 4 \right)}{4(\delta \cos(\vartheta) - 1)^2}
 \end{aligned}$$

**Figure S2. Calculation of cell packing states for N=4.** In a square normalized to side length  $\ell = 1$  the formula for the coordinates are indicated next to the corresponding vertex for the packing class  $4_{\delta}^{\times}$ .

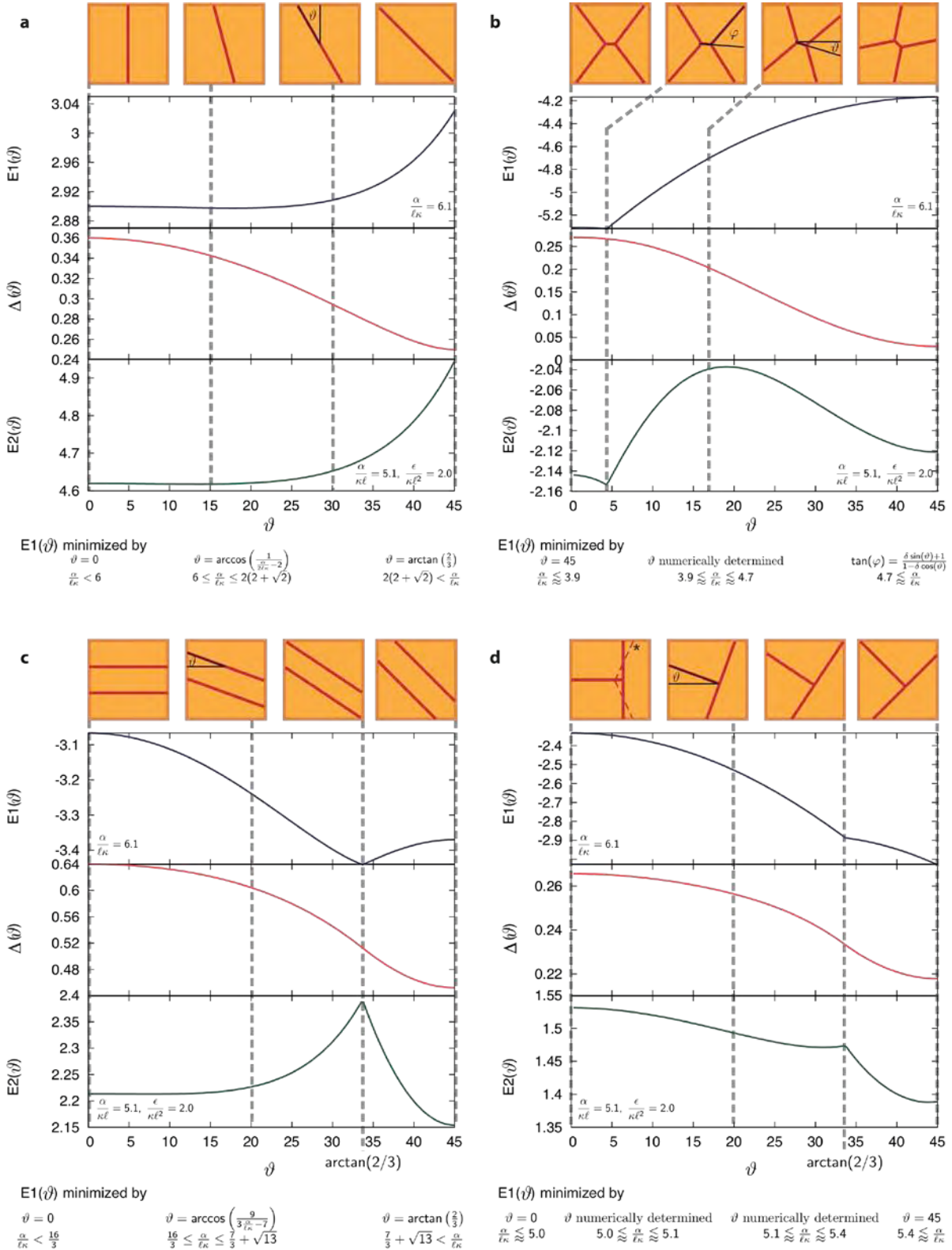


**Figure S3. Cell anisotropy and energy landscapes of cell packing states in the current standard and the extended model.** For  $2^{\text{II}}$  **a**,  $4^{\text{X}}$  **b**,  $3^{\text{II}}$  **c** and  $3^{\text{T}}$  class **d** the graphs display the energy landscape versus angle  $\vartheta$  for the current standard model given in Eq. (1) with measured parameter value  $\alpha/\kappa\ell = 6.1$ ,  $E1(\vartheta)$ , and subsequently the cell anisotropy of the state  $\Delta(\vartheta)$  and the extended model presented in Eq. (2) with parameter values  $\alpha/\kappa\ell = 5.1$  and  $\epsilon/\kappa\ell^2 = 2$ ,  $E2(\vartheta)$ . Note that although the qualitative behavior of the anisotropy is similar in all cases, the scale is strongly different. *Piera et al. Figure S3*

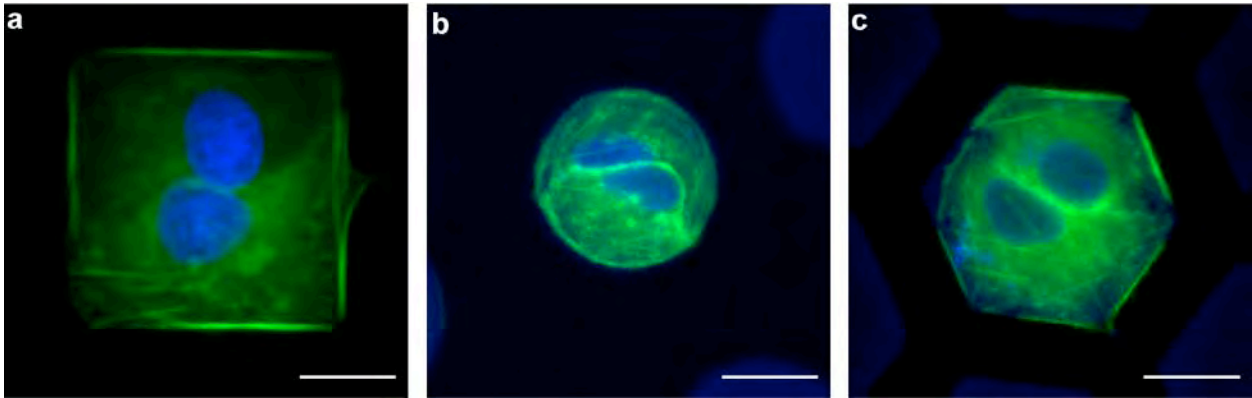


**Figure S4. Nuclear position is independent of patch geometry.** Fluorescence micrographs show that on square **a**, circle **b** or hexagon **c**, nuclei are always off-centered towards cell-cell contact lines. In green the actin cytoskeleton of gene modified Huh 7 cells can be seen. The cell nucleus has been stained with DAPI (blue). Scale bars correspond to 20  $\mu\text{m}$ .

Piera et al. Figure S4

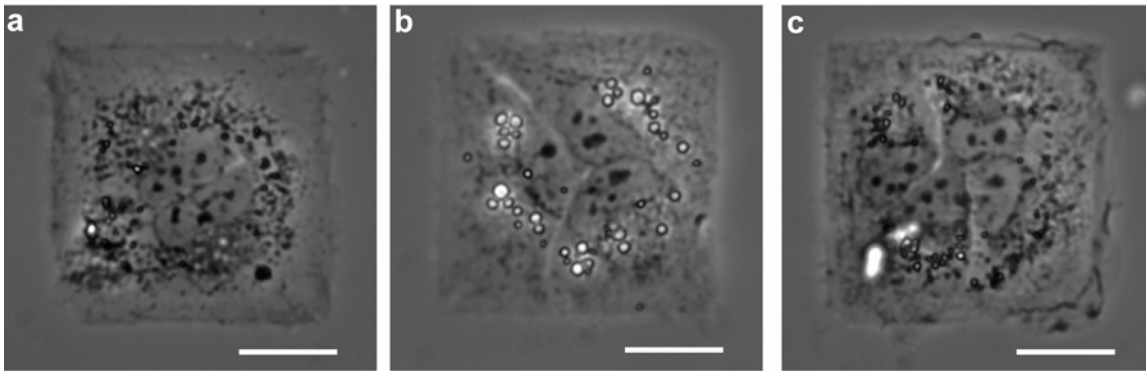


**Figure S5. Nuclear shape.** Phase contrast micrographs showing nuclei deformation following the distribution of cell-cell contact lines for two **a**, three **b** and four cells **c** on a square adhesive patch. Scale bars correspond to 20  $\mu\text{m}$ .

Piera et al. Figure S5

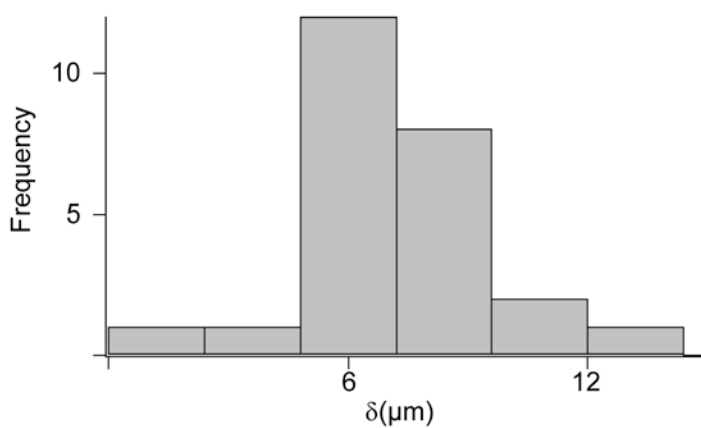


**Figure S6. Distribution of distances ( $\delta$ ) between 3-cell junctions.**

Piera et al. Figure S6



# A Perturbation expansion for finite flexibility

Concerning the asphericity of a semiflexible polymer ring in the flexible regime there exist ambiguous simulation results on how the asphericity approaches its flexible limit of a gaussian chain in two dimensions [24, 135]. Our simulation results in three dimensions as well as in two dimensions showed a clear decay from larger values of asphericity to the limit. We clarified our simulation outcome by calculating the effect of finite flexibility to the exact calculation of the gaussian chain asphericity in a perturbation expansion. The calculation outlined in the following is along the lines of the work of Diehl and Eisenriegler [47, 95, 96].

Starting from the average shape of a closed Gaussian chain we include bending stiffness as perturbation from infinite flexibility  $L/l_p$  in adding a bending term  $\mathcal{H}_{\text{bend}}$  to the Hamiltonian of a discretized, closed Gaussian chain  $\mathcal{H}_{\text{GC}}$ ,

$$\begin{aligned} \mathcal{H} &= \mathcal{H}_{\text{GC}} + \mathcal{H}_{\text{bend}} \\ &= \sum_{\alpha=1}^d \frac{1}{(2l)^2} \sum_{j=1}^N (x_{j,\alpha} - x_{j-1,\alpha})^2 + \sum_{\alpha=1}^d \frac{l_p}{L} \frac{2N}{(2l)^2} \sum_{j=1}^N (x_{j+1,\alpha} - 2x_{j,\alpha} + x_{j-1,\alpha})^2, \end{aligned} \quad (\text{A.1})$$

where  $x_{j,\alpha}$  denote the  $\alpha^{\text{th}}$  component of the position vector of the  $j^{\text{th}}$  segment. This Hamiltonian is used to calculate the expectation value of the asphericity  $\Delta$ , where we apply an identity as first addressed in Ref. [3], yielding the following formula,

$$\langle \Delta_d \rangle_{\mathcal{H}} = \frac{d}{d-1} \left\langle \frac{\text{Tr}(\widehat{Q}^2)}{(\text{Tr}Q)^2} \right\rangle_{\mathcal{H}} = \frac{d}{d-1} \int_0^\infty dy y \langle \text{Tr}\widehat{Q}^2 \rangle_{\mathcal{H}_y} \langle e^{-y\text{Tr}Q} \rangle_{\mathcal{H}_y}, \quad (\text{A.2})$$

where  $\mathcal{H}_y$  is defined by:

$$\mathcal{H}_y = \mathcal{H} + \sum_{\alpha=1}^d \frac{1}{2} \frac{y}{N^2} \sum_{i,j} (x_{i,\alpha} - x_{j,\alpha})^2. \quad (\text{A.3})$$

To calculate the expectation value  $\langle e^{-y\text{Tr}Q} \rangle_{\mathcal{H}_y}$  we introduce normal coordinates for the position vectors with eigenfunctions  $\phi_\nu(j) = N^{-1/2} \exp(i2\pi\nu j/N)$ , for  $\nu = \pm 1, \dots, \pm(N-1)/2$  and eigenvalues,

$$\epsilon_\nu(y) = \frac{1}{l^2} \sin^2 \left( \frac{\pi\nu}{N} \right) \left\{ 1 + 8 \frac{l_p}{L} N \sin^2 \left( \frac{\pi\nu}{N} \right) \right\} + \frac{y}{N}. \quad (\text{A.4})$$

Expanding the fraction  $\epsilon_\nu(y)/\epsilon_\nu(0)$  for large number of segments  $N$  yields,

$$\epsilon_\nu(y)/\epsilon_\nu(0) = 1 + \frac{y\langle R^2 \rangle}{(\pi\nu)^2} - 8\frac{l_p}{L}\frac{y\langle R^2 \rangle}{N} + \mathcal{O}(1/N^2), \quad (\text{A.5})$$

where  $\langle R^2 \rangle = Nl^2$  denotes the mean square end to end distance of a truly gaussian chain. Using result Eq. A.5 the second expectation value in Eq. A.2 is readily calculated in the limit of  $N$  to infinity and  $l \rightarrow 0$ , while keeping  $\langle R^2 \rangle = Nl^2$  fixed.

$$\begin{aligned} \langle e^{-y\text{Tr}Q} \rangle_{\mathcal{H}_{y,\text{RP}}}^{d/2} &= \lim_{N \rightarrow \infty} \prod_{\nu=\pm 1}^{\pm \frac{N-1}{2}} \frac{\epsilon_\nu(y)}{\epsilon_\nu(0)} \\ &= \lim_{N \rightarrow \infty} \left\{ \prod_{\nu=\pm 1}^{\pm \frac{N-1}{2}} \left( 1 + \frac{y\langle R^2 \rangle}{(\pi\nu)^2} \right) - 8\frac{l_p}{L}\frac{y\langle R^2 \rangle}{N} \sum_{l=\pm 1}^{\pm \frac{N-1}{2}} \prod_{\nu \neq l} \left( 1 + \frac{y\langle R^2 \rangle}{(\pi\nu)^2} \right) + \mathcal{O}\left(\frac{1}{N^2}\right) \right\} \\ &= \lim_{N \rightarrow \infty} \left\{ \prod_{\nu=\pm 1}^{\pm \frac{N-1}{2}} \left( 1 + \frac{y\langle R^2 \rangle}{(\pi\nu)^2} \right) \left[ 1 - 16\frac{l_p}{L}\frac{y\langle R^2 \rangle}{N} \sum_{l=1}^{\frac{N-1}{2}} \frac{1}{1 + \frac{y\langle R^2 \rangle}{(\pi\nu)^2}} + \mathcal{O}\left(\frac{1}{N^2}\right) \right] \right\} \\ &= \frac{\sinh^2(\sqrt{y\langle R^2 \rangle})}{y\langle R^2 \rangle} \left( 1 - 8\frac{l_p}{L}y\langle R^2 \rangle \right). \end{aligned} \quad (\text{A.6})$$

Higher order terms in  $1/N^2$  vanish in this limit. Now we treat the bending term in the Hamiltonian Eq. A.2 only as a perturbation to the original Gaussian chain, therefore we assume  $l_p/L \ll 1$  and simplify the result for the second expectation value in Eq. A.2 even further,

$$\langle e^{-y\text{Tr}Q} \rangle_{\mathcal{H}_y} = \left( \frac{\sqrt{y\langle R^2 \rangle}}{\sinh(\sqrt{y\langle R^2 \rangle})} \right)^d \left\{ \left( 1 + 4d\frac{l_p}{L}y\langle R^2 \rangle \right) + \mathcal{O}\left(\left(\frac{l_p}{L}\right)^2\right) \right\}. \quad (\text{A.7})$$

The remaining task to calculate the asphericity is solving for the expectation value of the trace of the reduced matrix  $\widehat{Q}$ . Using Wick's theorem one finds the trace is given by,

$$\langle \text{Tr}\widehat{Q}^2 \rangle_{\mathcal{H}_y} = \frac{(d-1)(d+2)}{4\langle R^2 \rangle^4} \int_0^{\langle R^2 \rangle} dt dt' ds ds' \langle [x_i(t) - x_i(t')] [x_j(s) - x_j(s')] \rangle_{\mathcal{H}_y}^2. \quad (\text{A.8})$$

These two-point functions are themselves related to the propagator  $G(s, t)$  by

$$\langle \widehat{Q}^2 \rangle = \frac{(d-1)(d+2)}{4\langle R^2 \rangle^4} \int_0^{\langle R^2 \rangle} dt dt' ds ds' [G(t, s) + G(t', s') - G(t, s') - G(t', s)] \quad (\text{A.9})$$

which is itself defined by

$$G(t, s) = \langle [x_i(t) - x_i(0)] [x_i(s) - x_i(0)] \rangle. \quad (\text{A.10})$$

The propagator itself can be calculated by solving for the two point correlation functions in normal coordinates by evaluating,

$$\langle x_i(t)x_j(s) \rangle_{\mathcal{H}_y} = \delta_{t,s} \sum_{\nu} \frac{\phi_{\nu}(i)\phi_{\nu}(j)}{2\epsilon_{\nu}(y)}. \quad (\text{A.11})$$

Evaluating the propagator in the limit of infinite  $N$ , we find,

$$G(t, s) = G_G(t, s) - 4\frac{l_p}{L}\langle R^2 \rangle, \quad (\text{A.12})$$

where  $G_G(t, s)$  denotes the propagator of a truly Gaussian ring polymer.

$$G_G(t, s) = \frac{\langle R^2 \rangle}{2\sqrt{y\langle R^2 \rangle} \sinh(\sqrt{y\langle R^2 \rangle})} \left\{ \cosh \left( 2\sqrt{y\langle R^2 \rangle} \left( \frac{1}{2} - \frac{|t-s|}{\langle R^2 \rangle} \right) \right) + \cosh(\sqrt{y\langle R^2 \rangle}) \right. \\ \left. - \cosh \left( 2\sqrt{y\langle R^2 \rangle} \left( \frac{1}{2} - \frac{t}{\langle R^2 \rangle} \right) \right) - \cosh \left( 2\sqrt{y\langle R^2 \rangle} \left( \frac{1}{2} - \frac{s}{\langle R^2 \rangle} \right) \right) \right\}, \quad (\text{A.13})$$

Hence, we find the expectation value for the trace  $\langle \text{Tr} \widehat{Q}^2 \rangle_{\mathcal{H}_y}$ ,

$$\langle \text{Tr} \widehat{Q}^2 \rangle_{\mathcal{H}_y} = \frac{(d+2)(d-1)}{16y^2 \sinh^2(\sqrt{y\langle R^2 \rangle})} \left\{ 2y\langle R^2 \rangle - 4 \sinh^2(\sqrt{y\langle R^2 \rangle}) \right. \\ \left. + 2\sqrt{y\langle R^2 \rangle} \sinh(\sqrt{y\langle R^2 \rangle}) \cosh(\sqrt{y\langle R^2 \rangle}) \right\}. \quad (\text{A.14})$$

The second factor in the integral defining the asphericity in Eq. A.2 is altered by a factor due to the finite flexibility,  $\langle e^{-y\text{Tr}Q} \rangle_{\mathcal{H}_y} = \langle e^{-y\text{Tr}Q} \rangle_{\mathcal{H}_{\text{GC},y}} (1 + 4d\frac{l_p}{L}y\langle R^2 \rangle)$ . Then the  $d$ -dimensional asphericity results in,

$$\langle \Delta_d \rangle = \frac{d(d+2)}{4(d+1)} \left( 3 + \frac{2}{d} - dF_d \right) + \frac{l_p}{L}d^2(d+2) \left( F_{d+2} + \frac{d-2}{d}F_d \right) \\ = \langle \Delta_d \rangle_G + \frac{l_p}{L}d^2(d+2) \left( F_{d+2} + \frac{d-2}{d}F_d \right). \quad (\text{A.15})$$

with

$$F_d = \int_0^{\infty} dy y^{d+1} \sinh^{-d}(y) \quad (\text{A.16})$$

Evaluating this expression for  $d = 2$  and  $d = 3$  yields a positive correction due to finite flexibility. Hence, the asphericity of a polymer ring approaches its flexible limit from above.



# Bibliography

- [1] B. Alberts, A. Johnson, P. Walter, J. Lewis, M. Raff, et al., “Molecular biology of the cell”, (Taylor & Francis, 2008), 5th edition
- [2] K. Alim and E. Frey, “Fluctuating semiflexible polymer ribbon constrained to a ring”, *Eur Phys J E*, **24**, 185 (2007)
- [3] K. Alim and E. Frey, “Shapes of semiflexible polymer rings”, *Phys Rev Lett*, **99**, 198102 (2007)
- [4] K. Alim and E. Frey, “Quantitative predictions on auxin-induced polar distribution of PIN proteins during vein formation in leaves”, *Eur Phys J E*, in press (2010)
- [5] R. Aloni, K. Schwalm, M. Langhans, and C. I. Ullrich, “Gradual shifts in sites of free-auxin production during leaf-primordium development and their role in vascular differentiation and leaf morphogenesis in *Arabidopsis*”, *Planta*, **216**, 841 (2003)
- [6] S. R. Aragon and R. Pecora, “Dynamics of wormlike chains”, *Macromolecules*, **18**, 1868 (1985)
- [7] J. A. Aronovitz and D. R. Nelson, “Universal features of polymer shapes”, *J Phys (Paris)*, **47**, 1445 (1986)
- [8] K. Bainbridge, S. Guyomarc’h, E. Bayer, R. Swarup, M. Bennett, et al., “Auxin influx carriers stabilize phyllotactic patterning”, *Genes Dev*, **22**, 810 (2008)
- [9] E. M. Bayer, R. S. Smith, T. Mandel, N. Nakayama, M. Sauer, et al., “Integration of transport-based models for phyllotaxis and midvein formation”, *Genes Dev*, **23**, 373 (2009)
- [10] B. P. Belousov, “A periodic reaction and its mechanism”, in *Collection of short papers on radiation medicine for 1958*, Med Publ (1959)
- [11] E. Benková, M. Michniewicz, M. Sauer, T. Teichmann, D. Seifertová, et al., “Local, efflux-dependent auxin gradients as a common module for plant organ formation”, *Cell*, **115**, 591 (2003)

- 
- [12] O. G. Berg, R. B. Winter, and P. H. von Hippel, “Diffusion-driven mechanisms of protein translocation on nucleic acids. 1. Models and theory”, *Biochemistry*, **20**, 6929 (1981)
- [13] C. Bertet, L. Sulak, and T. Lecuit, “Myosin-dependent junction remodelling controls planar cell intercalation and axis elongation”, *Nature*, **429**, 667 (2004)
- [14] D. A. Beysens, G. Forgacs, and J. A. Glazier, “Cell sorting is analogous to phase ordering in fluids”, *P Natl Acad Sci USA*, **97**, 9467 (2000)
- [15] R. P. Bhalerao, J. Eklöf, K. Ljung, A. Marchant, M. Bennett, et al., “Shoot-derived auxin is essential for early lateral root emergence in *Arabidopsis* seedlings”, *Plant J*, **29**, 325 (2002)
- [16] M. Bishop and C. J. Saltiel, “The shapes of two-dimensional, four-dimensional, and five-dimensional linear and ring polymers”, *J Chem Phys*, **85**, 6728 (1986)
- [17] T. Bittig, O. Wartlick, A. Kicheva, M. González-Gaitán, and F. Jülicher, “Dynamics of anisotropic tissue growth”, *New J Phys*, **10**, 063001 (2008)
- [18] I. Blilou, J. Xu, M. Wildwater, V. Willemsen, I. Paponov, et al., “The PIN auxin efflux facilitator network controls growth and patterning in *Arabidopsis* roots”, *Nature*, **433**, 39 (2005)
- [19] D. J. Bonthuis, C. Meyer, D. Stein, and C. Dekker, “Conformation and dynamics of DNA confined in slitlike nanofluidic channels”, *Phys Rev Lett*, **101**, 4 (2008)
- [20] C. P. Brangwynne, G. H. Koenderink, E. Barry, Z. Dogic, F. C. MacKintosh, et al., “Bending dynamics of fluctuating biopolymers probed by automated high-resolution filament tracking”, *Biophys J*, **93**, 346 (2007)
- [21] D. Bray, “Cell Movements: From Molecules to Mobility”, (Garland Science, 2000), 2nd edition
- [22] H. Bruus, “Theoretical microfluidics?”, (Oxford University Press, 2007)
- [23] C. Bustamante, J. F. Marko, E. D. Siggia, and S. Smith, “Entropic elasticity of lambda-phage DNA”, *Science*, **265**, 1599 (1994)
- [24] C. J. Camacho, M. E. Fisher, and R. R. P. Singh, “Semiflexible planar polymeric loops”, *J Chem Phys*, **94**, 5693 (1991)
- [25] P. B. Canham, “The minimum energy of bending as a possible explanation of the biconcave shape of the human red blood cell”, *J Theor Biol*, **26**, 61 (1970)
- [26] J. W. Cannon, J. A. Aronovitz, and P. Goldbart, “Equilibrium distribution of shapes for linear and star macromolecules”, *J Phys I*, **1**, 629 (1991)

- [27] R. G. Casten, H. Cohen, and P. A. Lagerstrom, “Perturbation analysis of an approximation to Hodgkin-Huxley theory”, *Q Appl Math*, **32**, 365 (1975)
- [28] M. Cavey and T. Lecuit, “Molecular bases of cell-cell junctions stability and dynamics”, *Cold Spring Harbor Perspect Biol*, **1**, a002998 (2009)
- [29] M. E. Cerritelli, N. Cheng, A. H. Rosenberg, C. E. McPherson, F. P. Booy, et al., “Encapsidated conformation of bacteriophage T7 DNA”, *Cell*, **91**, 271 (1997)
- [30] M. Chalfie, Y. Tu, G. Euskirchen, W. W. Ward, and D. C. Prasher, “Green fluorescent protein as a marker for gene expression”, *Science*, **263**, 802 (1994)
- [31] J. H. Chen and N. C. Seeman, “Synthesis from DNA of a molecule with the connectivity of a cube”, *Nature*, **350**, 631 (1991)
- [32] Y. Cheng, X. Dai, and Y. Zhao, “Auxin synthesized by the YUCCA flavin monooxygenases is essential for embryogenesis and leaf formation in *Arabidopsis*”, *Plant Cell*, **19**, 2430 (2007)
- [33] M. M. A. E. Claessens, R. Tharmann, K. Kroy, and A. R. Bausch, “Microstructure and viscoelasticity of confined semiflexible polymer networks”, *Nat Phys*, **2**, 186 (2006)
- [34] A. E. Cohen and L. Mahadevan, “Kinks, rings, and rackets in filamentous structures”, *P Natl Acad Sci USA*, **100**, 12141 (2003)
- [35] F. Corson, O. Hamant, S. Bohn, J. Traas, A. Boudaoud, et al., “Turning a plant tissue into a living cell froth through isotropic growth”, *P Natl Acad Sci USA* (2009)
- [36] H. Craighead, “Future lab-on-a-chip technologies for interrogating individual molecules”, *Nature*, **442**, 387 (2006)
- [37] M. Cross and H. Greenside, “Pattern Formation and Dynamics in Nonequilibrium Systems”, (Cambridge University Press, 2009)
- [38] E. F. Crowell, V. Bischoff, T. Desprez, A. Rolland, Y.-D. Stierhof, et al., “Pausing of golgi bodies on microtubules regulates secretion of cellulose synthase complexes in *arabidopsis*”, *Plant Cell*, **21**, 1141 (2009)
- [39] H. E. Daniels, “The statistical theory of stiff chains”, *Proc R Soc Edinburgh*, **63A**, 290 (1952)
- [40] J. A. Davies, “Mechanisms of morphogenesis”, (Academic Press, 2005)
- [41] P. B. de Reuille, I. Bohn-Courseau, K. Ljung, H. Morin, N. Carraro, et al., “Computer simulations reveal properties of the cell-cell signaling network at the shoot apex in *Arabidopsis*”, *P Natl Acad Sci USA*, **103**, 1627 (2006)

- [42] C. Delker, A. Raschke, and M. Quint, “Auxin dynamics: The dazzling complexity of a small molecule’s message”, *Planta*, **227**, 929 (2008)
- [43] N. G. Dengler and H. Tsukaya, “Leaf morphogenesis in dicotyledons: Current issues”, *Int J Plant Sci*, **162**, 459 (2001)
- [44] J. Dervaux and M. B. Amar, “Morphogenesis of growing soft tissues”, *Phys Rev Lett*, **101**, 4 (2008)
- [45] N. Desprat, W. Supatto, P.-A. Pouille, E. Beaurepaire, and E. Farge, “Tissue deformation modulates twist expression to determine anterior midgut differentiation in *Drosophila* embryos”, *Dev Cell*, **15**, 470 (2008)
- [46] M. K. Deyholos, G. Cordner, D. Beebe, and L. E. Sieburth, “The SCARFACE gene is required for cotyledon and leaf vein patterning”, *Development*, **127**, 3205 (2000)
- [47] H. W. Diehl and E. Eisenriegler, “Universal shape ratios for open and closed random walks: Exact results for all d”, *J Phys A: Math Gen*, **22**, L87 (1989)
- [48] S. Digiuni, S. Schellmann, F. Geier, B. Greese, M. Pesch, et al., “A competitive complex formation mechanism underlies trichome patterning on *Arabidopsis* leaves”, *Mol Syst Biol*, **4**, 217 (2008)
- [49] P. Dimitrov and S. W. Zucker, “A constant production hypothesis guides leaf venation patterning”, *P Natl Acad Sci USA*, **103**, 9363 (2006)
- [50] P. M. Donnelly, D. Bonetta, H. Tsukaya, R. E. Dengler, and N. G. Dengler, “Cell cycling and cell enlargement in developing leaves of *Arabidopsis*”, *Dev Biol*, **215**, 407 (1999)
- [51] F. Drube, K. Alim, G. Witz, G. Dietler, and E. Frey, “Excluded volume effects on semiflexible ring polymers”, *Nano Lett*, **10**, 1445 (2010)
- [52] L. Dupuy, J. Mackenzie, T. Rudge, and J. Haseloff, “A system for modelling cell-cell interactions during plant morphogenesis”, *Ann Bot*, **101**, 1255 (2008)
- [53] W. C. Earnshaw and S. C. Harrison, “DNA arrangement in isometric phage heads”, *Nature*, **268**, 598 (1977)
- [54] M. Elbaum, D. K. Fygenson, and A. Libchaber, “Buckling microtubules in vesicles”, *Phys Rev Lett*, **76**, 4078 (1996)
- [55] N. D. Epstein and J. S. Davis, “Sensing stretch is fundamental”, *Cell*, **112**, 147 (2003)
- [56] E. A. Evans, “Bending resistance and chemically induced moments in membrane bilayers”, *Biophys J*, **14**, 923 (1974)



- [57] F. Family, T. Vicsek, and P. Meakin, “Are random fractal clusters isotropic?”, *Phys Rev Lett*, **55**, 641 (1985)
- [58] E. Farge, “Mechanical induction of twist in the *Drosophila* foregut/stomodaeal primordium”, *Curr Biol*, **13**, 1365 (2003)
- [59] R. Farhadifar, J.-C. Röper, B. Aigouy, S. Eaton, and F. Jülicher, “The influence of cell mechanics, cell-cell interactions, and proliferation on epithelial packing”, *Curr Biol*, **17**, 2095 (2007)
- [60] F. G. Feugier and Y. Iwasa, “How canalization can make loops: A new model of reticulated leaf vascular pattern formation”, *J Theor Biol*, **243**, 235 (2006)
- [61] F. G. Feugier, A. Mochizuki, and Y. Iwasa, “Self-organization of the vascular system in plant leaves: Inter-dependent dynamics of auxin flux and carrier proteins”, *J Theor Biol*, **236**, 366 (2005)
- [62] R. Fitzhugh, “Impulses and physiological states in theoretical models of nerve membrane”, *Biophys J*, **1**, 445 (1961)
- [63] P. J. Flory, “Principles of polymer chemistry”, (Cornell Univ. Press, Ithaca, N.Y., 1953)
- [64] G. Forgacs, R. A. Foty, Y. Shafrir, and M. S. Steinberg, “Viscoelastic properties of living embryonic tissues: A quantitative study”, *Biophys J*, **74**, 2227 (1998)
- [65] P. Friedl and D. Gilmour, “Collective cell migration in morphogenesis, regeneration and cancer”, *Nat Rev Mol Cell Biol*, **10**, 445 (2009)
- [66] J. Friml, “Auxin transport - shaping the plant”, *Curr Opin Plant Biol*, **6**, 7 (2003)
- [67] J. Friml, A. Vieten, M. Sauer, D. Weijers, H. Schwarz, et al., “Efflux-dependent auxin gradients establish the apical-basal axis of *Arabidopsis*”, *Nature*, **426**, 147 (2003)
- [68] J. Friml, J. Wiśniewska, E. Benková, K. Mendgen, and K. Palme, “Lateral relocation of auxin efflux regulator PIN3 mediates tropism in *Arabidopsis*”, *Nature*, **415**, 806 (2002)
- [69] H. Fujita and A. Mochizuki, “The origin of the diversity of leaf venation pattern”, *Dev Dyn*, **235**, 2710 (2006)
- [70] H. Fujita and A. Mochizuki, “Pattern formation of leaf veins by the positive feedback regulation between auxin flow and auxin efflux carrier”, *J Theor Biol*, **241**, 541 (2006)
- [71] L. Gälweiler, C. Guan, A. Müller, E. Wisman, K. Mendgen, et al., “Regulation of polar auxin transport by AtPIN1 in *Arabidopsis* vascular tissue”, *Science*, **282**, 2226 (1998)

- [72] G. Gaspari, J. Rudnick, and A. Beldjenna, “The shapes of open and closed random-walks: A  $1/d$  expansion”, *J Phys A: Math Gen*, **20**, 3393 (1987)
- [73] M. C. Gibson, A. B. Patel, R. Nagpal, and N. Perrimon, “The emergence of geometric order in proliferating metazoan epithelia”, *Nature*, **442**, 1038 (2006)
- [74] S. F. Gilbert, “Developmental biology”, (Palgrave Macmillan, 1985), 7th edition
- [75] F. Gittes, B. Mickey, J. Nettleton, and J. Howard, “Flexural rigidity of microtubules and actin filaments measured from thermal fluctuations in shape”, *J Cell Biol*, **120**, 923 (1993)
- [76] M. H. M. Goldsmith, “The polar transport of auxin”, *Annu Rev Plant Physiol*, **28**, 439 (1977)
- [77] M. H. M. Goldsmith, T. H. Goldsmith, and M. H. Martin, “Mathematical analysis of the chemosmotic polar diffusion of auxin through plant tissues”, *P Natl Acad Sci USA*, **78**, 976 (1981)
- [78] R. E. Goldstein and S. A. Langer, “Nonlinear dynamics of stiff polymers”, *Phys Rev Lett*, **75**, 1094 (1995)
- [79] V. A. Grieneisen, J. Xu, A. F. M. Marée, P. Hogeweg, and B. Scheres, “Auxin transport is sufficient to generate a maximum and gradient guiding root growth”, *Nature*, **449**, 1008 (2007)
- [80] R. Gutierrez, J. J. Lindeboom, A. R. Paredez, A. M. C. Emons, and D. W. Ehrhardt, “*Arabidopsis* cortical microtubules position cellulose synthase delivery to the plasma membrane and interact with cellulose synthase trafficking compartments”, *Nat Cell Biol*, **11**, 797 (2009)
- [81] C. Haber, S. A. Ruiz, and D. Wirtz, “Shape anisotropy of a single random-walk polymer”, *Proc Natl Acad Sci USA*, **97**, 10792 (2000)
- [82] O. Hallatschek, E. Frey, and K. Kroy, “Propagation and relaxation of tension in stiff polymers”, *Phys Rev Lett*, **94**, 077804 (2005)
- [83] O. Hamant, M. G. Heisler, H. Jönsson, P. Krupinski, M. Uyttewaal, et al., “Developmental patterning by mechanical signals in *Arabidopsis*”, *Science*, **322**, 1650 (2008)
- [84] C. S. Hardtke and T. Berleth, “The *Arabidopsis* gene MONOPTEROS encodes a transcription factor mediating embryo axis formation and vascular development”, *EMBO J*, **17**, 1405 (1998)
- [85] T. Hayashi and R. W. Carthew, “Surface mechanics mediate pattern formation in the developing retina”, *Nature*, **431**, 647 (2004)

- [86] R. Heim, A. B. Cubitt, and R. Y. Tsien, “Improved green fluorescence”, *Nature*, **373**, 663 (1995)
- [87] M. G. Heisler, C. Ohno, P. Das, P. Sieber, G. V. Reddy, et al., “Patterns of auxin transport and gene expression during primordium development revealed by live imaging of the *Arabidopsis* inflorescence meristem”, *Curr Biol*, **15**, 1899 (2005)
- [88] W. Helfrich, “Elastic properties of lipid bilayers: Theory and possible experiments”, *Z Naturforsch C*, **28**, 693 (1973)
- [89] S. Hilgenfeldt, S. Eriskien, and R. W. Carthew, “Physical modeling of cell geometric order in an epithelial tissue”, *P Natl Acad Sci USA*, **105**, 907 (2008)
- [90] L. Hobbie, M. McGovern, L. R. Hurwitz, A. Pierro, N. Y. Liu, et al., “The *axr6* mutants of *Arabidopsis thaliana* define a gene involved in auxin response and early development”, *Development*, **127**, 23 (2000)
- [91] A. L. Hodgkin and A. F. Huxley, “A quantitative description of membrane current and its application to conduction and excitation in nerve”, *J Physiol*, **117**, 500 (1952)
- [92] L. Hufnagel, A. A. Teleman, H. Rouault, S. M. Cohen, and B. I. Shraiman, “On the mechanism of wing size determination in fly development”, *P Natl Acad Sci USA*, **104**, 3835 (2007)
- [93] M. Hülskamp, “Plant trichomes: A model for cell differentiation”, *Nat Rev Mol Cell Biol*, **5**, 471 (2004)
- [94] J. N. Israelachvili, “Intermolecular and surface forces: With Applications to Colloidal and Biological Systems”, (Academic Press, 1991), 2nd edition
- [95] O. Jagodzinski, “The asphericity of star polymers: A renormalization-group study”, *J Phys A: Math Gen*, **27**, 1471 (1994)
- [96] O. Jagodzinski, E. Eisenriegler, and K. Kremer, “Universal shape properties of open and closed polymer chains: Renormalization-group analysis and Monte-Carlo experiments”, *J Phys I*, **2**, 2243 (1992)
- [97] H. Jönsson, M. G. Heisler, B. E. Shapiro, E. M. Meyerowitz, and E. Mjolsness, “An auxin-driven polarized transport model for phyllotaxis”, *P Natl Acad Sci USA*, **103**, 1633 (2006)
- [98] J. Käfer, T. Hayashi, A. F. M. Marée, R. W. Carthew, and F. Graner, “Cell adhesion and cortex contractility determine cell patterning in the *Drosophila* retina”, *P Natl Acad Sci USA*, **104**, 18549 (2007)
- [99] S. Köster, J. Kierfeld, and T. Pfohl, “Characterization of single semiflexible filaments under geometric constraints”, *Eur Phys J E*, **25**, 439 (2008)

- [100] E. M. Kramer, “PIN and AUX/LAX proteins: Their role in auxin accumulation”, *Trends Plant Sci*, **9**, 578 (2004)
- [101] E. M. Kramer, “Auxin-regulated cell polarity: An inside job?”, *Trends Plant Sci*, **14**, 242 (2009)
- [102] O. Kratky and G. Porod, “Röntgenuntersuchung gelöster Fadenmoleküle”, *Recl Trav Chim Pay B*, **68**, 1106 (1949)
- [103] C. Kuhlemeier, “Phyllotaxis”, *Trends Plant Sci*, **12**, 143 (2007)
- [104] W. Kuhn, “Über die Gestalt von Fadenmolekülen in Lösung”, *Kolloid Z*, **68**, 2 (1934)
- [105] U. Kutschera and K. Niklas, “The epidermal-growth-control theory of stem elongation: An old and a new perspective”, *J Plant Physiol*, **164**, 1395 (2007)
- [106] L. Landau and E. Lifschitz, “Theory of Elasticity”, (Pergamon Press, Oxford, 1970)
- [107] J. S. Langer, “Instabilities and pattern-formation in crystal-growth”, *Rev Mod Phys*, **52**, 1 (1980)
- [108] J. S. Langer, R. F. Sekerka, and T. Fujioka, “Evidence for a universal law of dendritic growth-rates”, *J Cryst Growth*, **44**, 414 (1978)
- [109] A. W. C. Lau, A. Prasad, and Z. Dogic, “Condensation of isolated semi-flexible filaments driven by depletion interactions”, *Eur Phys Lett*, **87**, 48006 (2009)
- [110] L. Le Goff, O. Hallatschek, E. Frey, and F. Amblard, “Tracer studies on F-Actin fluctuations”, *Phys Rev Lett*, **89**, 258101 (2002)
- [111] T. Lecuit and P.-F. Lenne, “Cell surface mechanics and the control of cell shape, tissue patterns and morphogenesis”, *Nat Rev Mol Cell Biol*, **8**, 633 (2007)
- [112] N.-K. Lee, A. Johner, and S.-C. Hong, “Compressing a rigid filament: Buckling and cyclization”, *Eur Phys J E*, **24**, 229 (2007)
- [113] J. Lepault, J. Dubochet, W. Baschong, and E. Kellenberger, “Organization of double-stranded DNA in bacteriophages: A study by cryo-electron microscopy of vitrified samples”, *EMBO J*, **6**, 1507 (1987)
- [114] O. Leyser, “Dynamic integration of auxin transport and signalling”, *Curr Biol*, **16**, R424 (2006)
- [115] L. Limozin and E. Sackmann, “Polymorphism of cross-linked actin networks in giant vesicles”, *Phys Rev Lett*, **89**, 168103 (2002)
- [116] I. Linhartová, B. Novotná, V. Sulimenko, E. Dráberová, and P. Dráber, “Gamma-tubulin in chicken erythrocytes: Changes in localization during cell differentiation and characterization of cytoplasmatic complexes”, *Dev Dyn*, **223**, 229 (2002)

- [117] J. A. Lockhart, “An analysis of irreversible plant cell elongation”, *J Theor Biol*, **8**, 264 (1965)
- [118] B. Maier and J. O. Rädler, “Conformation and self-diffusion of single DNA molecules confined to two dimensions”, *Phys Rev Lett*, **82**, 1911 (1999)
- [119] B. Maier and J. O. Rädler, “Shape of self-avoiding walks in two dimensions”, *Macromolecules*, **34**, 5723 (2001)
- [120] P. Marmottant, A. Mgharbel, J. Käfer, B. Audren, J.-P. Rieu, et al., “The role of fluctuations and stress on the effective viscosity of cell aggregates”, *P Natl Acad Sci USA* (2009)
- [121] J. Mattsson, Z. R. Sung, and T. Berleth, “Responses of plant vascular systems to auxin transport inhibition”, *Development*, **126**, 2979 (1999)
- [122] H. Meinhardt, “The Algorithmic Beauty of Sea Shells”, (Springer, 2009), 4th edition
- [123] R. M. H. Merks, Y. V. de Peer, D. Inzé, and G. T. S. Beemster, “Canalization without flux sensors: A traveling-wave hypothesis”, *Trends Plant Sci*, **12**, 384 (2007)
- [124] A. S. Mikhailov, “Foundations of Synergetics I: Distributed Active Systems”, (Springer, 1991)
- [125] G. J. Mitchison, “Phyllotaxis and the fibonacci series”, *Science*, **196**, 270 (1977)
- [126] G. J. Mitchison, “Model for vein formation in higher-plants”, *Proc R Soc Lond B*, **207**, 79 (1980)
- [127] G. J. Mitchison, “The polar transport of auxin and vein patterns in plants”, *Phil Trans R Soc Lond B*, **295**, 461 (1981)
- [128] D. J. Montell, “Morphogenetic cell movements: Diversity from modular mechanical properties”, *Science*, **322**, 1502 (2008)
- [129] J. D. Murray, “Mathematical Biology: II: Spatial Models and Biomedical Applications”, (Springer, 2008), 3rd edition
- [130] J. Nagumo, S. Arimoto, and S. Yoshizawa, “Active pulse transmission line simulating nerve axon”, *Proc IRE*, **50**, 2061 (1962)
- [131] U. Nath, B. C. W. Crawford, R. Carpenter, and E. Coen, “Genetic control of surface curvature”, *Science*, **299**, 1404 (2003)
- [132] F. J. Nedelec, T. Surrey, A. C. Maggs, and S. Leibler, “Self-organization of microtubules and motors”, *Nature*, **389**, 305 (1997)
- [133] T. Nelson and N. Dengler, “Leaf vascular pattern formation”, *Plant Cell*, **9**, 1121 (1997)

- [134] A. C. Newell, P. D. Shipman, and Z. Sun, “Phyllotaxis: Cooperation and competition between mechanical and biochemical processes”, *J Theor Biol*, **251**, 421 (2008)
- [135] R. E. Norman, G. C. Barker, and T. J. Sluckin, “Statistical mechanics of 2-dimensional vesicles”, *J Phys. II*, **2**, 1363 (1992)
- [136] T. Odijk, “DNA in liquid-crystalline environment: Tight bends, rings, supercoils”, *J Chem Phys*, **105**, 1270 (1996)
- [137] K. Okada, J. Ueda, M. K. Komaki, C. J. Bell, and Y. Shimura, “Requirement of the auxin polar transport system in early stages of *Arabidopsis* floral bud formation”, *Plant Cell*, **3**, 677 (1991)
- [138] T. Omelchenko, J. M. Vasiliev, I. M. Gelfand, H. H. Feder, and E. M. Bonder, “Rho-dependent formation of epithelial “leader” cells during wound healing”, *P Natl Acad Sci USA*, **100**, 10788 (2003)
- [139] P. Ortoleva and J. Ross, “Theory of propagation of discontinuities in kinetic systems with multiple time scales: Fronts, front multiplicity, and pulses”, *J Chem Phys*, **63**, 3398 (1975)
- [140] K. Ostermeir, K. Alim, and E. Frey, “Buckling of stiff polymer rings in weak spherical confinement”, *Phys Rev E*, **81**, 061802 (2010)
- [141] K. Ostermeir, K. Alim, and E. Frey, “Confinement induces conformational transition of semiflexible polymer rings to figure eight form”, *Soft Matter*, **6**, 3467 (2010)
- [142] T. Paciorek, E. Zažimalová, N. Ruthardt, J. Petrášek, Y. D. Stierhof, et al., “Auxin inhibits endocytosis and promotes its own efflux from cells”, *Nature*, **435**, 1251 (2005)
- [143] F. Pampaloni, G. Lattanzi, A. Jonás, T. Surrey, E. Frey, et al., “Thermal fluctuations of grafted microtubules provide evidence of a length-dependent persistence length”, *P Natl Acad Sci USA*, **103**, 10248 (2006)
- [144] A. R. Paredez, C. R. Somerville, and D. W. Ehrhardt, “Visualization of cellulose synthase demonstrates functional association with microtubules”, *Science*, **312**, 1491 (2006)
- [145] M. Pesch and M. Hülskamp, “Creating a two-dimensional pattern de novo during *Arabidopsis* trichome and root hair initiation”, *Curr Opin Genet Dev*, **14**, 422 (2004)
- [146] M. Pesch and M. Hülskamp, “One, two, three... models for trichome patterning in *Arabidopsis*?”, *Curr Opin Plant Biol*, **12**, 587 (2009)
- [147] J. Petrášek and J. Friml, “Auxin transport routes in plant development”, *Development*, **136**, 2675 (2009)

- [148] J. Petrášek, J. Mravec, R. Bouchard, J. J. Blakeslee, M. Abas, et al., “PIN proteins perform a rate-limiting function in cellular auxin efflux”, *Science*, **312**, 914 (2006)
- [149] J. A. F. Plateau, “Statique expérimentale de liquides soumis aux seules forces moléculaires”, (Gauthiers-Villars, 1873)
- [150] S. Pollmann, A. Müller, M. Piotrowski, and E. W. Weiler, “Occurrence and formation of indole-3-acetamide in *Arabidopsis thaliana*”, *Planta*, **216**, 155 (2002)
- [151] M. Poujade, E. Grasland-Mongrain, A. Hertzog, J. Jouanneau, P. Chavier, et al., “Collective migration of an epithelial monolayer in response to a model wound”, *P Natl Acad Sci USA*, **104**, 15988 (2007)
- [152] G. K. Przemeck, J. Mattsson, C. S. Hardtke, Z. R. Sung, and T. Berleth, “Studies on the role of the *Arabidopsis* gene MONOPTEROS in vascular development and plant cell axialization”, *Planta*, **200**, 229 (1996)
- [153] M. Rauzi, P. Verant, T. Lecuit, and P.-F. Lenne, “Nature and anisotropy of cortical forces orienting *Drosophila* tissue morphogenesis”, *Nat Cell Biol*, **10**, 1401 (2008)
- [154] J. A. Raven, “Transport of indoleacetic-acid in plant-cells in relation to pH and electrical potential gradients, and its significance for polar IAA transport”, *New Phytol*, **74**, 163 (1975)
- [155] P. M. Ray, P. B. Green, and R. Cleland, “Role of turgor in plant-cell growth”, *Nature*, **239**, 163 (1972)
- [156] D. Reinhardt, E.-R. Pesce, P. Stieger, T. Mandel, K. Baltensperger, et al., “Regulation of phyllotaxis by polar auxin transport”, *Nature*, **426**, 255 (2003)
- [157] W. Reisner, K. J. Morton, R. Riehn, Y. M. Wang, Z. N. Yu, et al., “Statics and dynamics of single DNA molecules confined in nanochannels”, *Phys Rev Lett*, **94**, 196101 (2005)
- [158] J. Rinzel and J. B. Keller, “Traveling wave solutions of a nerve conduction equation”, *Biophys J*, **13**, 1313 (1973)
- [159] C. Rivetti, M. Guthold, and C. Bustamante, “Scanning force microscopy of DNA deposited onto mica: Equilibration versus kinetic trapping studied by statistical polymer chain analysis”, *J Mol Biol*, **264**, 919 (1996)
- [160] A.-G. Rolland-Lagan and P. Prusinkiewicz, “Reviewing models of auxin canalization in the context of leaf vein pattern formation in *Arabidopsis*”, *Plant J*, **44**, 854 (2005)
- [161] M. Romanowska, H. Hinsch, N. Kirchgerner, M. Giesen, M. Degawa, et al., “Direct observation of the tube model in F-actin solutions: Tube dimensions and curvatures”, *Eur Phys Lett*, **86**, 26003 (2009)

- [162] P. H. Rubery and A. R. Sheldrake, “Carrier-mediated auxin transport”, *Planta*, **118**, 101 (1974)
- [163] J. Rudnick and G. Gaspari, “The asphering of random walks”, *J Phys A: Math Gen*, **19**, L191 (1986)
- [164] A. Runions, M. Fuhrer, B. Lane, P. Federl, A. G. Rolland-Lagan, et al., “Modeling and visualization of leaf venation patterns”, *ACM T Graphic*, **24**, 702 (2005)
- [165] V. V. Rybenkov, N. R. Cozzarelli, and A. V. Vologodskii, “Probability of DNA knotting and the effective diameter of the DNA double helix”, *P Natl Acad Sci USA*, **90**, 5307 (1993)
- [166] S. Sabatini, D. Beis, H. Wolkenfelt, J. Murfett, T. Guilfoyle, et al., “An auxin-dependent distal organizer of pattern and polarity in the *Arabidopsis* root”, *Cell*, **99**, 463 (1999)
- [167] T. Sachs, “Polarity and induction of organized vascular tissues”, *Ann Bot*, **33**, 263 (1969)
- [168] T. Sachs, “Pattern formation in plant tissues”, (Cambridge University Press, 1991)
- [169] P. Sahlin, B. Söderberg, and H. Jönsson, “Regulated transport as a mechanism for pattern generation: Capabilities for phyllotaxis and beyond”, *J Theor Biol*, **258**, 60 (2009)
- [170] N. Saitô, K. Takahashi, and Y. Yunoki, “The statistical mechanical theory of stiff chains”, *J Phys Soc Jap*, **22**, 219 (1967)
- [171] T. Sanchez, I. M. Kucic, and Z. Dogic, “Circularization, photomechanical switching, and a supercoiling transition of actin filaments”, *Phys Rev Lett*, **104**, 098103 (2010)
- [172] M. Sauer, J. Balla, C. Luschnig, J. Wiśniewska, V. Reinöhl, et al., “Canalization of auxin flow by Aux/IAA-ARF-dependent feedback regulation of PIN polarity”, *Genes Dev*, **20**, 2902 (2006)
- [173] M. G. Sawchuk, P. Head, T. J. Donner, and E. Scarpella, “Time-lapse imaging of *Arabidopsis* leaf development shows dynamic patterns of procambium formation”, *New Phytol*, **176**, 560 (2007)
- [174] E. Scarpella, D. Marcos, J. Friml, and T. Berleth, “Control of leaf vascular patterning by polar auxin transport”, *Genes Dev*, **20**, 1015 (2006)
- [175] C. M. Schroeder, R. E. Teixeira, E. S. G. Shaqfeh, and S. Chu, “Characteristic periodic motion of polymers in shear flow”, *Phys Rev Lett*, **95**, 018301 (2005)
- [176] U. Seifert, “Configurations of fluid membranes and vesicles”, *Adv Phys*, **46**, 13 (1997)



- [177] J. Shimada and H. Yamakawa, “Moments for DNA topoisomers: The helical wormlike chain”, *Biopolymers*, **27**, 657 (1988)
- [178] O. Shimomura, F. H. Johnson, and Y. Saiga, “Extraction, purification and properties of aequorin, a bioluminescent protein from the luminous hydromedusan, aequorea”, *J Cell Comp Physiol*, **59**, 223 (1962)
- [179] P. D. Shipman and A. C. Newell, “Phyllotactic patterns on plants”, *Phys Rev Lett*, **92**, 168102 (2004)
- [180] B. I. Shraiman, “Mechanical feedback as a possible regulator of tissue growth”, *P Natl Acad Sci USA*, **102**, 3318 (2005)
- [181] L. E. Sieburth, “Auxin is required for leaf vein pattern in *Arabidopsis*”, *Plant Physiol*, **121**, 1179 (1999)
- [182] R. S. Smith and E. M. Bayer, “Auxin transport-feedback models of patterning in plants”, *Plant Cell Environ*, **32**, 1258 (2009)
- [183] R. S. Smith, S. Guyomarc’h, T. Mandel, D. Reinhardt, C. Kuhlemeier, et al., “A plausible model of phyllotaxis”, *P Natl Acad Sci USA*, **103**, 1301 (2006)
- [184] K. Šolc, “Shape of a random-flight chain”, *J Chem Phys*, **55**, 335 (1971)
- [185] D. Stein, F. H. J. van der Heyden, W. J. A. Koopmans, and C. Dekker, “Pressure-driven transport of confined DNA polymers in fluidic channels”, *P Natl Acad Sci USA*, **103**, 15853 (2006)
- [186] M. S. Steinberg, “Reconstruction of tissues by dissociated cells”, *Science*, **141**, 401 (1963)
- [187] M. S. Steinberg, “Adhesion in development: An historical overview”, *Dev Biol*, **180**, 377 (1996)
- [188] S. Stoma, M. Lucas, J. Chopard, M. Schaedel, J. Traas, et al., “Flux-based transport enhancement as a plausible unifying mechanism for auxin transport in meristem development”, *PLoS Comput Biol*, **4**, e1000207 (2008)
- [189] D. M. Suter and P. Forscher, “Transmission of growth cone traction force through apCAM-cytoskeletal linkages is regulated by Src family tyrosine kinase activity”, *J Cell Biol*, **155**, 427 (2001)
- [190] R. Swarup, E. M. Kramer, P. Perry, K. Knox, H. M. O. Leyser, et al., “Root gravitropism requires lateral root cap and epidermal cells for transport and response to a mobile auxin signal”, *Nat Cell Biol*, **7**, 1057 (2005)
- [191] D. B. Szymanski and D. J. Cosgrove, “Dynamic coordination of cytoskeletal and cell wall systems during plant cell morphogenesis”, *Curr Biol*, **19**, R800 (2009)

- [192] J. X. Tang and P. A. Janmey, “The polyelectrolyte nature of f-actin and the mechanism of actin bundle formation”, *J Biol Chem*, **271**, 8556 (1996)
- [193] J. X. Tang, J. A. Käs, J. V. Shah, and P. A. Janmey, “Counterion-induced actin ring formation”, *Eur Biophys J*, **30**, 477 (2001)
- [194] X. Trepats, M. R. Wasserman, T. E. Angelini, E. Millet, D. A. Weitz, et al., “Physical forces during collective cell migration”, *Nat Phys*, **5**, 426 (2009)
- [195] M. Triantafillou and R. D. Kamien, “Polymer shape anisotropy and the depletion interaction”, *Phys Rev E*, **59**, 5621 (1999)
- [196] A. M. Turing, “The chemical basis of morphogenesis. 1953”, *Bull Math Biol*, **52**, 153 (1990)
- [197] B. van den Broek, M. A. Lomholt, S.-M. J. Kalisch, R. Metzler, and G. J. L. Wuite, “How DNA coiling enhances target localization by proteins”, *P Natl Acad Sci USA*, **105**, 15738 (2008)
- [198] R. Verma, J. C. Crocker, T. C. Lubensky, and A. G. Yodh, “Entropic colloidal interactions in concentrated DNA solutions”, *Phys Rev Lett*, **81**, 4004 (1998)
- [199] A. Vieten, S. Vanneste, J. Wiśniewska, E. Benková, R. Benjamins, et al., “Functional redundancy of PIN proteins is accompanied by auxin-dependent cross-regulation of PIN expression”, *Development*, **132**, 4521 (2005)
- [200] J. D. Watson and F. H. C. Crick, “Molecular structure of nucleic acids - a structure for deoxyribose nucleic acid”, *Nature*, **171**, 737 (1953)
- [201] D. Weaire and S. Hutzler, “The physics of foams”, (Oxford University Press, 2001)
- [202] C. L. Wenzel, M. Schuetz, Q. Yu, and J. Mattsson, “Dynamics of MONOPTEROS and PIN-FORMED1 expression during leaf vein pattern formation in *Arabidopsis thaliana*”, *Plant J*, **49**, 387 (2007)
- [203] J. Wilhelm and E. Frey, “Radial distribution function of semiflexible polymers”, *Phys Rev Lett*, **77**, 2581 (1996)
- [204] E. Winfree, F. R. Liu, L. A. Wenzler, and N. C. Seeman, “Design and self-assembly of two-dimensional DNA crystals”, *Nature*, **394**, 539 (1998)
- [205] J. Wiśniewska, J. Xu, D. Seifertová, P. B. Brewer, K. Ružička, et al., “Polar PIN localization directs auxin flow in plants”, *Science*, **312**, 883 (2006)
- [206] G. Witz, K. Rechendorff, J. Adamcik, and G. Dietler, “Conformation of circular DNA in two dimensions”, *Phys Rev Lett*, **101**, 4 (2008)
- [207] L. Wolpert, “Principles of development”, (Oxford University Press, 2006), 3rd edition

- 
- [208] M. A. Wozniak and C. S. Chen, “Mechanotransduction in development: A growing role for contractility”, *Nat Rev Mol Cell Biol*, **10**, 34 (2009)
- [209] H. Yamakawa, “Helical Wormlike Chains in Polymer Solutions”, (Springer-Verlag, Berlin, 1997)
- [210] A. M. Zhabotinsky, “Periodical oxidation of malonic acid in solution (a study of the belousov reaction kinetics)”, *Biofizika*, **9**, 306 (1964)
- [211] V. S. Zykov, “Simulation of Wave Processes in Excitable Media”, (Palgrave Macmillan, 1988)



# Acknowledgements

Being at the verge of completing an intense stage in my life I would like to thank all those people who have been part of it.

First and foremost I would like to thank my supervisor Prof. Dr. Erwin Frey for stirring my interest in biological physics and being of continuous support during my ongoing journey in the field. He truly became a *Doktorvater* to me in giving me the guidance I needed, always encouraging my ideas and adventures and being an endless pool of motivation.

I very much enjoyed the opportunity to follow up on projects in polymers physics together with Katja Ostermeir and Fabian Drube. It was a pleasure to guide them and work with them. On the experimental side one project on polymer shapes was accompanied by Guillaume Witz and Prof. Dr. Giovanni Dietler. I would like to thank them for a fruitful collaboration and for fun discussions on how theoretical physicists tend to write publications.

Working on morphogenesis I am fortunate to be part of an inspiring collaboration with Alicia Piera Aberola, Anna-Kristina Marel and Prof. Dr. Joachim Rädler. I am enjoying very much the open atmosphere of our discussions, it is probably rare to be greeted that friendly as a theorist. I would also like to thank Robert Fink for help with simulations and Florian Thüroff for joining this endeavor.

Half of the last year of my PhD I spent as a Grad Fellow at the Kavli Institute for Theoretical Physics. I am very grateful to Erwin Frey for encouraging me to go and to Prof. Dr. Boris Shraiman for generously offering his hospitality. I am indebted to his scientific training. I would also like to thank Prof. Dr. Arezki Boudaoud for innumerable discussions and Richard Neher, Sid Goyal and Pierre Neveu for much more than sharing so many coffee and chocolate with me.

Throughout my time in Munich I enjoyed the wonderful atmosphere in our group. I will not only miss the annual retreats to the DPG or Antholz or the weekly cookies sessions but most of all the frank and dear colleagues which made it a special place for me. I have more than memorable skat evenings with Tobias Reichenbach, Anna Melbinger and Jonas Cremer and challenging hikes with Tobias Munk in mind. I am grateful to Prof. Dr. Ulrich Gerland for many more discussions than just polymer translocation with Severin Schink. A big thanks goes to endless conversations on life and science with Judith Megerle. I am also

happy that life won't part me too far from my long term office mates and friends Wolfram Möbius and Benedikt Obermayer.

Last but not least I would like to give my family, my brother and my parents a huge hug for all the encouragement and love. And my dear husband. Murad thanks for ... everything.

# Curriculum Vitae

## Address

Karen Alim  
Arnold-Sommerfeld-Center for Theoretical Physics,  
Ludwig-Maximilians-Universität München,  
Theresienstr. 37, 80333 Munich, Germany  
Email:karen.alim@physik.lmu.de

## Personal data

Date of birth: July 22nd, 1981  
Place of birth: Hannover, Germany  
Nationality: German

## Education

- 10/2006-04/2010: PhD student at the Ludwigs-Maximilians-Universität Munich.  
Thesis advisor: Prof. Dr. Erwin Frey.  
Thesis title: On Shape and Structure in Biological Systems.
- 08/2009-12/2009: Grad Fellow at the Kavli Institute for Theoretical Physics.
- 05/2006: Diploma in physics. With Distinction.  
Thesis advisor: Prof. Dr. Erwin Frey.  
Thesis title: Statistical Mechanics of Fluctuating Polymer Rings.
- 10/2002-05/2006: Studies of physics at the Ludwigs-Maximilians-Universität Munich.
- 09/2003-08/2004: Master of Science (MSc) in theoretical physics at the University of Manchester.  
Thesis advisor: Prof. Dr. Alan J. Bray.  
Thesis title: Vicious walkers in one-body potentials.
- 10/2000-09/2002: Studies of physics at the Universität Karlsruhe (TH). Prediploma.
- 07/2000: Secondary school certificate (Abitur) at Gymnasium Großburgwedel.